FLOW/ACOUSTIC INTERACTIONS IN POROUS MEDIA UNDER A TURBULENT WIND ENVIRONMENT

by

YING XU

B.S., Tongji University, 2000
M.S., Tongji University, 2003

AN ABSTRACT OF A DISSERTATION

submitted in partial fulfillment of the requirements for the degree

DOCTOR OF PHILOSOPHY

Department of Mechanical and Nuclear Engineering
College of Engineering

KANSAS STATE UNIVERSITY
Manhattan, Kansas

2010

Abstract

Windscreens are widely used in outdoor microphone measurement for acoustic sensing systems. In many cases of outdoor microphone applications, wind noise interferes with the signals. The performance of measurement microphones thus heavily depends on correct designs of windscreens that are used to maximize the signal to noise ratio of the sensing system. The purpose of the study is to investigate the wind noise reduction between the unscreened microphone and the screened microphone under different frequencies of incoming wind turbulence.

In this study, a modified immersed boundary method using the distributed forcing term has been applied to simulate the flow/acoustic interaction between air and the porous medium. Because of the high accuracy requirement in the vicinity of the interface between air and the porous medium, spatial derivatives of flux need to be discretized using high order schemes. In this study, several different schemes have been tested in the vicinity of the interface including a second-order upwind scheme, a third-order upwind scheme, and a fifth-order Weighted Essentially Non-Oscillatory (WENO) scheme. Based on the test results, the fifth-order WENO scheme is selected for most of the simulation cases. The model equations for flow outside the windscreen are the Navier-Stokes equations; flow inside the windscreen (porous medium) uses the modified Zwikker-Kosten equation.

The wind turbulence in this study is generated by two different ways. The first is to place different sizes of solid cylinders and spheres in the upstream of the microphone under two-dimensional and three-dimensional conditions. The second is to use a Quasi-Wavelet method to generate the background atmospheric turbulence to simulate the real physical phenomena. Both

two-dimensional and three-dimensional simulations for the flow over the unscreened and the screened microphone are presented and discussed under both low Reynolds number and high Reynolds number flow conditions.

The results show that the windscreen effect is significant and the wind noise reduction level between the unscreened and the screened microphone can reach around 20dB either for low Reynolds number cases or for high Reynolds number cases. For low Reynolds number cases, Low flow resistivity windscreens are more effective for low frequency turbulence; high flow resistivity windscreens are more effective for high frequency turbulence. For high Reynolds number cases, the medium flow resistivity windscreens perform better compared to low flow resistivity windscreens and high flow resistivity windscreens.

FLOW/ACOUSTIC INTERACTIONS IN POROUS MEDIA UNDER A TURBULENT WIND ENVIRONMENT

by

YING XU

B.S., Tongji University, 2000
M.S., Tongji University, 2003

A DISSERTATION

submitted in partial fulfillment of the requirements for the degree

DOCTOR OF PHILOSOPHY

Department of Mechanical and Nuclear Engineering
College of Engineering

KANSAS STATE UNIVERSITY
Manhattan, Kansas

2010

Approved by:

Major Professor
Dr. Zhongquan Charlie Zheng

Abstract

Windscreens are widely used in outdoor microphone measurement for acoustic sensing systems. In many cases of outdoor microphone applications, wind noise interferes with the signals. The performance of measurement microphones thus heavily depends on correct designs of windscreens that are used to maximize the signal to noise ratio of the sensing system. The purpose of the study is to investigate the wind noise reduction between the unscreened microphone and the screened microphone under different frequencies of incoming wind turbulence.

In this study, a modified immersed boundary method using the distributed forcing term has been applied to simulate the flow/acoustic interaction between air and the porous medium. Because of the high accuracy requirement in the vicinity of the interface between air and the porous medium, spatial derivatives of flux need to be discretized using high order schemes. In this study, several different schemes have been tested in the vicinity of the interface including a second-order upwind scheme, a third-order upwind scheme, and a-fifth order Weighted Essentially Non-Oscillatory (WENO) scheme. Based on the test results, the fifth-order WENO scheme is selected for most of the simulation cases. The model equations for flow outside the windscreen are the Navier-Stokes equations; for flow inside the windscreen (porous medium) is the modified Zwikker-Kosten equation.

The wind turbulence in this study is generated by two different ways. The first is to place different sizes of solid cylinders and spheres in the upstream of the microphone under two-dimensional and three-dimensional conditions. The second is to use a Quasi-Wavelet method to generate the background atmospheric turbulence to simulate the real physical phenomena. Both

two-dimensional and three-dimensional simulations for the flow over the unscreened and the screened microphone are presented and discussed under both low Reynolds number and high Reynolds number flow conditions.

The results show that the windscreen effect is significant and the wind noise reduction level between the unscreened and the screened microphone can reach around 20dB either for low Reynolds number cases or for high Reynolds number cases. For low Reynolds number cases, Low flow resistivity windscreens are more effective for low frequency turbulence; high flow resistivity windscreens are more effective for high frequency turbulence. For high Reynolds number cases, the medium flow resistivity windscreens perform better compared to low flow resistivity windscreens and high flow resistivity windscreens.

Table of Contents

List of Figures

List of Tables

Acknowledgements

I would like to thank all of the people who made this dissertation possible. First and foremost, I thank my advisor, Professor Zhongquan Charlie Zheng, for his continuous support, patience, and guidance in my Ph.D. program.

Also, I would like to thank the members of my committee: Professor B. Terry Beck, Professor Daniel Swenson, Professor David R. Steward and Professor Michael J. O'Shea for their comments and encouragement.

This research has been funded partially under DOD US Army ERDC under contract W913E7-07-C-0004. I would like to thank Dr. Keith Wilson for his comments and discussions.

I have enjoyed working with people in our group. Specially, I received help from Dr. Ning Zhang and Dr. Wenhua Li. I also thank Xiaofan Yang for some good discussions.

I want to thank my parents for their unconditional love and incredible support. Last, but not least, I want to thank my wife, Xia Li, who has given me companionship, support and confidence always.

Nomenclature and Abbreviation

C_p = pressure coefficient

C_d = drag coefficient

D = cylinder diameter, m

D_a = Darcy number

dt = time step

dx, dy, dz = grid size in x, y, z direction, m

f = frequency, Hz

g = gravitational acceleration

h = grid size, m

K = specific permeability, m^2

L = length of distance, m

L_p = pressure level, dB

M_a = Mach number

p_s = stagnation pressure, Pa

P, p = pressure, Pa

R_e = Reynolds number

S_t = Strouhal number

u_* = friction speed, m/s

U = the speed of incoming flow, m/s

u, v, w = velocity component in x, y, z direction, m/s

u', v', w' = velocity fluctuation component in x, y, z direction, m/s

α = the size class of QW

a_α = the size of class α

β = smoothness indicator

φ = porosity

μ = dynamic viscosity, Pa·s

ν = kinematic viscosity, m^2/s

ρ = density, Kg/m^3

σ = flow resistivity, $Pa \cdot s/ m^2$

ω = unlinear weight

LES = Large Eddy Simulation

PSD = Power Spectral Density

QW = Quasi-Wavelet

SPL = Sound Pressure Level

WENO = Weighted Essentially Non-Oscillatory

WNR = Wind Noise Reduction

CHAPTER 1 - Introduction

In this first chapter, I will briefly introduce the main research and identify research motivation and objectives. I will also introduce basic techniques, and finally detail the thesis organization.

1.1 A Brief Introduction to Windscreen, Noise, and Atmospheric Turbulence

Windscreens used to protect microphones that would otherwise be buffeted by wind, typically are composed of one or more layers of soft, open-cell polyester or polyurethane foams. Typically, windscreens are widely used in outdoor microphone measurement for acoustic sensing systems. Windscreens reduce noise in the microphone signals from an intensity probe exposed to unsteady airflow.

Wind noise sensed by a microphone inside a windscreen is a complicated aerodynamic noise phenomenon because of the atmospheric turbulence and the porous property of the windscreen. Estimates of windscreen noise are presently based on experiments and measurements made with the given screen (Strasberg, 1988). There are different theories about the principle source of wind noise; for example, the turbulent wake in the air flow behind the windscreen (Strasberg, 1979, 1988). Another explanation is that the wind noise is due to the pressure fluctuations caused by velocity fluctuations of the outdoor incoming wind turbulence (Morgan and Raspet, 1992). Indeed Van den Berg (2006) shows that atmospheric turbulence is the cause of outdoor microphone wind noise.

The atmospheric boundary layer (ABL) is the turbulent layer of the atmosphere that interacts directly with the ground. Its exact description remains a challenging problem because turbulence is famously known as the last, great unsolved problem of classical mechanics.

Atmospheric turbulence is created by friction and thermal convection (thermal part will not be discussed here because it is not focused on the research). Turbulence due to friction is a result of wind shear. At the surface, the wind speed is zero, whereas, at high altitudes the geotropic wind is not influenced by the surface but is a result of large scale pressure differences as well as Coriolis forces resulting from the earth's rotation. In between, in the atmospheric boundary layer, wind speed increases with height z according to Garratt (1992)

$$V = \frac{u_*}{\kappa}\left(\ln\frac{z}{z_0} - \Psi\right) \tag{1.1}$$

where $\kappa = 0.4$ is the von Karman constant, z_0 is the roughness height and u_* is the friction velocity, defined by $u_*^2 = \tau / \rho$, where τ equals the momentum flux due to turbulent friction across a horizontal plane. Next, $\Psi = \Psi(\xi)$ is a function of $\xi = z/L$ which corresponds to atmospheric stability. Monin Obukhov length $L = -\frac{u_*^3 \theta_v}{\kappa g(\overline{w'\theta_v'})_s}$, is an important length scale for stability and can be expressed as the height above which thermal turbulence dominates over friction turbulence, θ_v is the mean virtual potential temperature, $\overline{w'\theta_v'}$ is the surface virtual potential temperature flux, g is the gravitational acceleration.

The friction created by wind shear produces eddies over a range of frequencies and lengths, their size determined by z and V. These eddies break up in ever smaller eddies and kinetic turbulent energy is cascaded to smaller sizes at higher frequencies until eddies reach the Kolmogorov size η_s (~1mm) and dissipate into heat by viscous friction.

A windscreen can be seen as a first order low pass filter for pressure variations due to atmospheric turbulence. Induced wind noise is thus determined by wind speed and windscreen diameter, but also by factors related to frictional and thermal turbulence (Van den Berg, 2006).

1.2 Research Motivation and Objectives

Windscreens are widely used in outdoor microphone measurement for acoustic sensing systems. However, in many cases of outdoor microphone applications, wind noise interferes with the signals. The performance of measurement microphones thus heavily depends on correct design of windscreens to maximize the signal to noise ratio of a sensing system. Current windscreen design theories are mostly heuristic in nature and by experiment. Therefore, a practical need exists to fully understand the mechanisms involved in flow/acoustic interaction around a screened microphone. Such understanding should lead to optimized designs of windscreens for measurement microphones.

Recently, numerical simulations of flow over porous media have aroused much interest and attention (Bhattacharyya et al., 2006). Specifically, the presence of porous media introduces discontinuity at the interface between the fluid and the porous media and also decreases computational accuracy; therefore, accuracy at the interface is a key issue in simulating such problems. Consequently, finding accurate and efficient ways to increase the accuracy and decrease the discontinuity at the interface is very important in simulations. One of the most effective ways to overcome this discontinuity is to apply high-order schemes such as upwind schemes or weighted essentially non-oscillatory (WENO) schemes (Harten et al. 1987, Shu and Osher, 1989). High-order schemes have been applied to viscous flow around steady and moving solid bodies (Berthelsen and Faltinsen, 2008) but not to the flow over porous media. Thus, in this research work, the high-order scheme will be used in the regions near the interface between fluid and porous media for the first time.

The research models the flow over the unscreened microphone and the screened microphone, to determine the flow field and study of wind noise reduction effects of the porous windscreen medium. In particular this study investigates effects of turbulence and windscreen

material properties represented by flow resistivity. Accordingly, time-domain computational techniques are developed to study the detailed flow field outside the windscreen as well as flow inside a windscreen that uses a porous material as the medium.

With the advent of time-domain methods (Ostashev et al. 2005), numerical simulations for acoustic problems can be combined with computational fluid dynamics. This provides new powerful tools to tackle acoustic problems. Recently, for instance, Wilson and White (2006) used the finite difference time-domain (FDTD) method to simulate turbulence-induced pressure fluctuations around a porous microphone windscreen.

In this study, the model equations for flow outside the windscreen are the incompressible Navier-Stokes equations; meanwhile, the model equation for flow inside the windscreen (porous medium) is the modified Zwikker-Kosten (ZK) equation.

The overall objective of the study is to identify the mechanism of flow/acoustic interaction between air and the porous media in turbulence conditions by addressing the following tasks.

a) Using 2D simulation, investigate the wind noise reduction between the unscreened microphone and the screened microphone at different frequencies of incoming wind turbulence. The wind turbulence is introduced by placing different sizes of solid cylinders in upstream of the microphone.
b) Using 3D simulation, investigate the wind noise reduction between the unscreened microphone and the screened microphone at different frequencies of incoming wind turbulence. The wind turbulence is introduced by placing a solid sphere in upstream of the microphone.

c) Using 2D simulation, investigate the wind noise reduction between the unscreened microphone and the screened microphone under realistic wind turbulence condition. For this reason, a Quasi-Wavelet (QW) method will be used to generate a background wind turbulence flow field to address the atmospheric effects on wake vortex behaviors.

d) In both 2D and 3D simulations, high-order schemes are used to improve the accuracy near the interface between air and the porous medium.

1.3 Selected Literature Review and Summary of Relevant Information

This section discusses Wind Noise, The Immersed Boundary Method, The High Order Scheme, and the Quasi-Wavelet Method.

1.3.1 Wind Noise

Strasberg (1988) did the dimensional analysis of windscreen noise and pointed out that the pressure within a spherical or cylindrical wind screen with diameter D in a flow with velocity V depends on the Reynolds number $\mathrm{Re} = DV/\nu$, the Strouhal number $S_r = fD/V$, and the Mach number $M = V/c$ (where ν is kinematic viscosity of air and c is the speed of sound). Thus, the data on windscreen noise can be put into non-dimensional form. Additionally, the spectrum of the noise is assumed to be given as a root-mean-square (RMS) sound pressure p_f in a relatively narrow band of width Δf centered at frequency f. Therefore, sound pressure in terms of a dimensionless sound pressure coefficient can be expressed as $p_f/(\rho V^2) = f(\mathrm{Re}, S_r, M)$ (where ρ is density of the air). Analyzing experimental data on 2.5~25 centimeter diameter windscreens, in air speeds ranging from 6 to 23 m/s, Strasberg found a curve fitting of a 1/3 octave frequency band pressure level:

$$L_{p,1/3} = 20\log_{10}(p_{1/3}/(\rho V^2)) = -81 - 23\log_{10}(f/(DV)) \quad (1.2)$$

For convenience, this equation may be rewritten as a numerical relation between the sound pressure level and the other variables expressed in commonly used units:

$$L_{1/3} = 61 + 63\log_{10}(\overline{V}) - 23\log_{10}(\bar{f}) - 23\log_{10}(\overline{D}) \quad (1.3)$$

where $\bar{f}$ is the frequency in Hz, $\overline{V}$ is the wind speed in m/s, $\overline{D}$ is the screen diameter in cm.

Next, Morgan and Raspet (1992) measured the wind noise and the instantaneous wind speed for bare and windscreened microphones outdoors. They stated that for high turbulence conditions the dominant source of pressure fluctuations at the microphone outdoors is the intrinsic turbulence in the incoming flow. Also, Morgan and Raspet pointed out that all measurements reported by Strasberg were made in low turbulence conditions, meaning the fluctuating wake of the screen is the dominant noise source. Then, Morgan and Raspet applied Bernoulli's equation by decomposing the wind velocity in the time-average velocity and the fluctuation velocity. Finally, they concluded that outdoors, the flow itself is turbulent and RMS flow velocity is large compared with the RMS fluctuation velocity of the wake.

An early model of windscreen noise reduction at very low wind turbulence frequency was that of a rigid, smooth sphere with an impermeable surface transmitting the pressure fluctuations to quiescent media inside the sphere (Zheng and Tan, 2003). The study was restricted to flow turbulence with scales much larger than the sphere diameter which determined that the mean flow across the sphere could thus be considered as a steady flow. Moreover, the pressure fluctuations induced on the spherical surface, whose distribution coincided mathematically with that of the corresponding steady surface pressure coefficient, were then used to obtain the pressure levels that could be sensed by a microphone placed at the center of the sphere, because pressure fluctuations inside the windscreen were assumed to satisfy the

Laplace equation. The justification of the use of steady-state flow model was based on experimental data by Morgan (1993) and Morgan and Raspet (1992), who showed that when the ratio between the sphere diameter and the wavelength was below 0.3 (the corresponding frequency was about 10 Hz), the pressure sensed at the center was almost constant. After that, a rapid rise with the decrease of wavelength appeared, because the scale of the turbulence became smaller and the steady-state assumption was no longer valid.

In Zheng's model, the wind noise is quantified by $\rho U u'$, where ρ is the density of the air, U is the speed of the incoming wind, and u' is the velocity fluctuation in the direction of the incoming wind. This is deduced from the Bernoulli relation for a stagnation pressure of

$$p_s = \frac{1}{2}\rho u^2 \tag{1.4}$$

where $u = U + u'$.

Van den Berg (2006) showed that atmospheric turbulence is indeed the cause of outdoor microphone wind noise and he used atmospheric boundary layer theory to model the effects of atmospheric turbulence on both a bare and a screened microphone. The induced wind noise is determined by average wind speed and wind screen diameter, and also by factors related to frictional and thermal turbulence.

Next, Raspet et al. (2006) pointed out another wind noise source due to interaction between the windscreen and the flow. In fact, the generated pressure fluctuations around the windscreen produce self noise. Earlier, Strasberg (1979, 1988) studied the cylindrical and spherical windscreen self noise in low turbulence flows and found that the measured windscreen noise data could be collapsed into a single curve based on dimensional analysis. However, there is no current theory for self noise in high turbulence flow.

1.3.2 Immersed Boundary Method

Immersed boundary (IB) methods for fluid-structure interaction problems typically discretize the equations of motion for the fluid (in this case, the incompressible Navier–Stokes equations) on a Cartesian grid, and such methods generally do not require that the geometry of the structure conform in any way to this Cartesian grid. Instead, the equations of motion for the fluid are augmented by an appropriately defined forcing term that typically is nonzero only in the vicinity of the structure.

The term ‘immersed boundary method’ was first used in reference to a method developed by Peskin (1972) to simulate cardiac mechanics and associated blood flow. Since Peskin introduced this method, numerous modifications and refinements have been proposed and a number of variants of this approach now exist. In addition, there is another class of methods, usually referred to as “Cartesian grid methods,” which were originally developed for simulating inviscid flows with complex embedded solid boundaries on Cartesian grids (Clarke et al. 1986). These methods have been extended to simulate unsteady viscous flows (Udaykumar et al. 1996, Ye et al. 1999) and thus have capabilities similar to those of IB methods.

1.3.3 High-Order Scheme

The finite difference scheme is based on interpolations of discrete data using polynomials or other simple functions. In approximation theory, it is well-known that the wider the stencil, the higher the order of accuracy of the interpolation, providing the function being interpolated is smooth inside the stencil. Thus, traditional finite difference methods are based on fixed stencil interpolations. For example, to obtain an interpolation for cell i to third order accuracy, the information of the three cells i-1, i, and i+1 can be used to build a second order interpolation polynomial. In other words, one always looks one cell to the left, one cell to the right, and at the

center cell itself, regardless of where in the domain one is situated. This works well for globally smooth problems. Since the resulting scheme is linear for linear partial differential equations; hence, stability can be easily analyzed by Fourier Transforms (for the uniform grid case). However, fixed stencil interpolation of second- or higher-order accuracy is necessarily oscillatory near a discontinuity. Such oscillations, which are called the Gibbs phenomena in spectral methods, do not decay in magnitude when the mesh is refined.

Next, the Essentially Non-Oscillatory (ENO) idea seems to be the first successful attempt to obtain a self similar, uniformly high order accurate, yet essentially non-oscillatory interpolation for piecewise smooth functions. The generic solution for hyperbolic conservation laws is in the class of piecewise smooth functions. ENO schemes were first introduced by Harten, Engquist, Osher and Chakravarthy in 1987. Weighted ENO (WENO) schemes were developed using a convex combination of all candidate stencils instead of just one as in the original ENO (Liu et al., 1994). ENO and WENO schemes have been used successfully to simulate shock turbulence interactions (Shu and Osher, 1989), to directly simulate the compressible turbulence (Ladeinde et al., 1995) and to develop relativistic hydrodynamics equations (Dolezal and Wong, 1995).

To date High-order schemes have been used in simulation for viscous flow around steady and moving solid bodies (Cho et al. 2007) but have not been applied to simulate flow fields in different media.

1.3.4 Quasi-Wavelet Method

During the last decade, several attempts to create turbulent flow have been made (Balaras, 2000; Kondo, 1997), the most widely used accurate method consists of conducting a preliminary computation of turbulent flow field, using Large Eddy Simulation (LES), such as boundary layer

flows (Koutmos and Mavridis, 1997), then using the results of the computations as inlet conditions. This precursor simulation method is successful; however, it entails a large computational load. The other popular approach uses a mean velocity profile and a level of turbulent kinetic energy. With these two data, random noise perturbations (based, for example, on a Gaussian distribution) are added to the velocity components to obtain the desired statistical quantities (mean velocity and turbulent energy) (Addad, 2002; Benhamadouche, 2003). This method, however, is known to be less suited for cases where inflow conditions play a major role in the development of a boundary layer.

Turbulence is generally understood as a collection of eddies of many different sizes (Hinze 1975). Moreover, Quasi-wavelets (QWs) are similar to customary wavelets in that they are based on translation and dilations of a parent function; however, their positions and orientations are random. An individual QW is roughly analogous to a turbulent eddy such that a random ensemble of QWs, with size distribution and rotation rates chosen in a manner consistent with Kolmogorov's hypothesis, produces a velocity field with realistic spectral properties (Goedecke et al, 2004).

QWs are derived from translations and dilatations of a dimensionless, spatially localized parent function $f(\xi)$. Here, ξ is the magnitude of the vector $\vec{\xi} \equiv (\vec{r} - \vec{b}^{\alpha n})/a_\alpha$, where $\vec{r}$ is the spatial coordinate, $\vec{b}^{\alpha n}$ is the center of the QW, and a_α is its size. The index a indicates the size class of the QW, with $\alpha = 1$ being the largest size and $\alpha = N$ the smallest, and n indicates a particular QW within that size class. The size a_1 is associated with the outer scale of the turbulence and a_N with the inner scale. By defining the velocity field $\vec{v}^{\alpha n}(\vec{r})$ as the curl of a vector potential $\vec{A}^{\alpha n}(\vec{r})$, we can assume that the turbulence will be a solenoidal field.

$$\vec{v}^{\alpha n}(\vec{r}) = \nabla \times \vec{A}^{\alpha n}(\vec{r}) \tag{1.5}$$

$$\vec{A}^{\alpha n}(\vec{r}) = \vec{\Omega}^{\alpha n} a_\alpha^2 f(\xi) \tag{1.6}$$

where $\vec{\Omega}^{\alpha n}$ is the angular velocity vector of the QW. The presence of a_α^2 in the definition provides dimensional consistency.

Writing out the curl of the vector potential leads to the following equation:

$$\vec{v}^{\alpha n}(\vec{r}) = \vec{\Omega}^{\alpha n} \times (\vec{r} - \vec{b}^{\alpha n})(-\xi^{-1} \partial f / \partial \xi) \tag{1.7}$$

Since turbulence and scattering processes are often studied in spectral domain, we will use the Fourier transformation of the velocity field. By definition,

$$\tilde{v}(\vec{\kappa}) = \frac{1}{(2\pi)^3} \int d^3 r e^{-i\vec{\kappa}\cdot\vec{r}} \vec{v}(\vec{r}) \tag{1.8}$$

where $\vec{\kappa}$ is the wave number vector for the turbulence. Thus, transformation of Eq. (13) yields:

$$\tilde{v}^{\alpha n}(\vec{\kappa}) = i\vec{\kappa} \times A^{\alpha n}(\vec{\kappa}) = i(\vec{\kappa} \times \vec{\Omega}^{\alpha n}) \exp(-i\vec{\kappa} \cdot \vec{b}^{\alpha n}) a_\alpha^5 F(\vec{\kappa} a_\alpha) \tag{1.9}$$

where F is the spectrally transformed parent function.

A key distinction between QWs and customary wavelets is that the orientation of the QWs, $\vec{\Omega}^{\alpha n}$ and their eddy center, $\vec{b}^{\alpha n}$, are random variables. For a homogeneous, isotropic model, the $\vec{\Omega}^{\alpha n}$ are statistically independent and distributed uniformly over all directions, and the $\vec{b}^{\alpha n}$ are statistically independent and distributed uniformly in a volume of interest V. The construction is illustrated in Figure 1-1. The total velocity field created by the QWs is the superposition of all the QW:

$$\vec{v}(\vec{r}) = \sum_{\alpha=1}^{N} \sum_{n=1}^{N_\alpha} \vec{v}^{\alpha n}(\vec{r}) \tag{1.10}$$

where N is the number of the size classes and N_α is the number of QWs for the size class α.

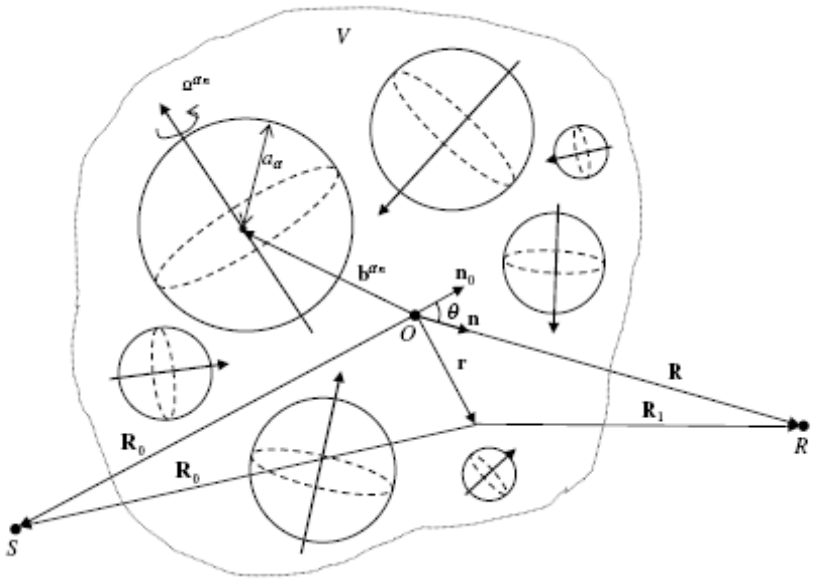

Figure 1-1 Distribution of the QWs in a volume of V

The basic procedure for generating a random field realization by the method of QW can now be outlined:

(1) Select the desired size classes a_α, α = 1, . . . , N . This might be done, for example, by deciding upon values a_1 and a_N based on the sizes of the largest and smallest entities in the field, and then selecting a value for the ratio $a_{\alpha+1}/a_\alpha = e^{-\mu}$.

(2) Define the packing fraction φ_α (Assume the packing fraction $\varphi_\alpha = N_\alpha a_\alpha^3 / V$ as a constant value φ, independent of the eddy size class α.) for each size class. Specify the desired volume V for the realization and calculate the number of QWs in each size class: N_α.

(3) For each size class α, generate N_α random QW positions ($\vec{b}_{\alpha N}$) and random coefficients (α_N). For the least complicated approach, the positions should have a random distribution in space.

(4) Calculate the field associated with QW Eq. (1.10) and sum to obtain the total field.

1.4 Research Method

Flow over porous media has been a critical subject in numerous environmental and engineering studies. When a flow encounters a porous cylinder, a complex flow field develops partially through and partially around the cylinder. The characteristics associated with the hybrid domain, involving both a porous region and a fluid region, are not fully understood primarily due to a lack of proper mathematical treatments of different regions and the fluid/porous interface. To solve the fluid/porous interface problem, the flow interactions outside and inside the porous medium and the transfer mechanisms across the interface need to be investigated in-depth.

First, Neale and Nader (1974) proposed the continuity of both the velocity and the shear stress at the fluid/porous interface, modeling the flow in the porous region using a semi-empirical Brinkman-Forchheimer's extended Darcy equation. The Brinkman term in this equation, representing the viscous effects, allows a no-slip boundary condition to be imposed at the impermeable wall and the matching of the momentum equations at the fluid/porous interface.

Then, Ochoatapia and Whitaker (1995) utilized macroscopic variables and transport equations to study the flow in a porous medium and obtained the volume-averaged fluid properties. They also imposed the interface shear stress jump condition between the flow region and the porous region using an empirical constant. Silva and de Lemos (2003) applied this shear stress jump condition to both laminar and turbulent flow over the porous medium. Next, Bhattacharyya et al. (2006) showed an application of a single-domain approach, which considers the porous layer as a pseudo-fluid and the composite region as a continuum. This leads to a single momentum equation, namely, a modified Navier-Stokes equation with an additional Darcy and Forchheimer term (Nield and Bejan, 1998).

Notably, most of the studies reviewed deal with low Reynolds number flows. However, much remains unknown about the physical mechanisms associated with the turbulent flow over a

porous medium. In fact, turbulence in a porous medium is a controversial issue. With very small permeability and fluid velocity, the flow is often dominated by the laminar flow regime. Nevertheless, some applications have been developed from the interaction between turbulent flow and the porous medium. For example, Shimizu et al. (1990) conducted some experiments and provide a mathematical model to describe the velocities within the porous medium under turbulent flow.

Later, Wilson et al. (2006, 2007) used the finite difference time-domain (FDTD) method to simulate sound propagation in rigid-frame porous medium, comparing the relaxation formulation to a widely applied model developed by Zwikker-Kosten (1949). The two models can be equivalent if the resistance constant, structure constant, and compression modulus in ZK model are allowed to be weakly frequency dependent.

The present study uses Navier-Stokes equations for incompressible flow outside the porous medium and a modified ZK equation for flow inside the porous medium. Notably, however, although we are studying acoustic phenomena and therefore the fluid is compressible, the significant pressure fluctuations are near the surface of an object or inside a porous medium. These pressure fluctuations are considered in the near field caused by flow fluctuations, such as the surface pressure fluctuations produced by turbulence boundary layers over the surface addressed by Kraichnan (1956), where the incompressible flow assumption is well-justified to study turbulence noise.

The flow fluctuations, both internal and external to the windscreen, are investigated based on coupled flow simulation between the outside and the inside of the windscreen. Accordingly, the research focused on developing a modified immersed boundary computational scheme

(Zhang and Zheng, 2007, Cho et al. 2007) suitable for simulation conditions when a windscreen is immersed in a background flow.

Moreover, the windscreen is considered a porous medium with the porosity and the structure constant set to 1 for simplicity. The air flow inside the windscreen is modeled to follow the ZK equation, which is the low frequency limit of more general forms of porous medium equations in Wilson et al. (2007). In addition, incompressibility is also assumed for flow inside the porous medium. The convection and diffusion terms omitted in the original ZK equation because the velocity is low in the porous medium are retained here so that the same solver used for the momentum equation can be used in the modified ZK equations. The effect of convection term and diffusion term automatically become small when the velocity is low. Moreover, we also want to test cases when the flow resistivity is small, when the convection effect may not be very small.

1.5 Organization of Thesis

In Chapter 2, the governing formulations for the air flow are introduced including the continuity equation and the Navier-Stokes equations. This chapter also covers the computational algorithm including the immersed boundary method and the high-order schemes and then offers a validation case.

Chapter 3 offers basic equations for flow over a porous medium and presents the scheme and computation techniques. Next, the chapter explains, executes and compares some verification results with those of analytical solutions, solutions from other authors and also from FLUENT software.

Chapter 4 investigates 2D flow/acoustic interaction between air and the porous windscreen. The wind turbulence is introduced by placing different sizes of solid cylinders in

upstream of the microphone. Both low Reynolds number cases (Re = 500) and high Reynolds number cases (Re = 5000) are studied and compared. Next the wind turbulence over different windscreen shapes are presented and discussed.

Chapter 5 investigates 3D flow/acoustic interaction between air and the porous windscreen. The wind turbulence is introduced by placing a solid sphere in upstream of the microphone. Both low Reynolds number cases (Re = 500) and high Reynolds number cases (Re = 5000) are subsequently presented and studied.

Chapter 6 uses a QW method to generate the atmospheric wind turbulence as background turbulence to address the atmospheric effects on wake vortex behaviors. Then wind noise reduction between the unscreened microphone and the screened microphone are studied and discussed.

Finally chapter 7 offers conclusions and future research potential.

CHAPTER 2 - Formulation and Algorithm

This chapter includes three main parts: the governing formulations for air flow, the computational algorithm including the immersed boundary method and high-order scheme, and a validation case.

2.1 Formulation

The flow of air may be analyzed mathematically using three equations: conservation of mass, conservation of momentum and conservation of energy. This study explores only the flow motion property, so conservation of energy is omitted here.

2.1.1 Conservation of Mass

The law of conservation of mass, often referred to as the continuity equation, is that the mass of a closed system will remain constant over time, regardless of the processes acting inside the system. A similar statement is that mass cannot be created or destroyed, although it may be rearranged in space and changed into different types of particles. This leads to a "mass balance" requirement posed in mathematical form and therefore a scalar equation.

The law of conservation of mass says that the rate of increase of mass within a fixed volume must equal the net rate of inflow through the boundaries, therefore:

$$\int_V \frac{\partial \rho}{\partial t} dV = -\int_A \rho \vec{u} \cdot \hat{n} dA \tag{2.1}$$

where $\vec{u}$ is the velocity vector, $\vec{u} = u\vec{i} + v\vec{j} + w\vec{k}$, u, v, w represents the velocity component of x, y, z direction separately. Additionally $\hat{n}dA$ is the normal area to the surface dA, $\rho\vec{u} \cdot \hat{n}dA$ is the outward flux through an area element dA.

The differential form can be obtained by transforming the surface integral on the right of Eq. (2.1) to a volume integral by means of the divergence theorem, which gives:

$$\int_V \left[\frac{\partial \rho}{\partial t} + \nabla \cdot (\rho \vec{u}) \right] dV = 0 \tag{2.2}$$

This requires that:

$$\frac{\partial \rho}{\partial t} + \nabla \cdot (\rho \vec{u}) = 0 \tag{2.3}$$

Eq. (2.3) is the continuity of flow equation and expresses the differential form of the law of conservation of mass.

For incompressible flow, the density ρ doesn't change with pressure, so the continuity equation (2.3) can be reduced to the incompressible form:

$$\nabla \cdot \vec{u} = 0 \tag{2.4}$$

2.1.2 Conservation of Momentum

The general Navier–Stokes equation for a compressible Newtonian fluid follows:

$$\frac{\partial (\rho \vec{u})}{\partial t} + \nabla \cdot (\rho \vec{u} \vec{u}) = -\nabla p + \nabla \cdot (\mu \cdot (\nabla \vec{u} + (\nabla \vec{u})^T)) + \nabla (\lambda \nabla \cdot \vec{u}) + \vec{g} \tag{2.5}$$

where μ is the first coefficient of viscosity, λ is the second coefficient of viscosity, T is the matrix transpose and $\vec{g}$ is the body force vector.

Then for incompressible flow, omitting the body force effects, the general incompressible Navier-Stokes Equation form can be written as:

$$\rho \left[\frac{\partial \vec{u}}{\partial t} + (\vec{u} \cdot \nabla) \cdot \vec{u} \right] = -\nabla p + \mu \nabla^2 \vec{u} \tag{2.6}$$

2.1.3 Nondimensionalization

The continuity equation (2.4) and Navier-Stokes equation (2.6) are both dimensional expressions. However, for most cases, using nondimensional form simplifies problems and comparisons. Therefore, to nondimensionalize Eq. (2.4) and (2.6) requires scaling parameters as in Table 2.1.

Table 2-1 Scaling parameters used to nondimensionalize the momentum equations

Scaling Parameter	Description	Primary Dimensions
D	Characteristic Length	D
U	Characteristic Speed	DT^{-1}
ρU^2	Characteristic Pressure Difference	$ML^{-1}T^{-2}$

In the research model problem, I normally define the diameter of windscreen cylinder or sphere as characteristic length, the speed of incoming flow as characteristic speed.

Defining nondimensional variables, $t^* = \frac{U}{D}t$, $\vec{x}^* = \frac{\vec{x}}{D}$, $\vec{u}^* = \frac{\vec{u}}{U}$, $p^* = \frac{p}{\rho U^2}$, substitute these variables into Eq. (2.4) and (2.6), and get:

$$\frac{U}{D}\nabla \cdot \vec{u}^* = 0 \tag{2.7}$$

$$\frac{\rho U^2}{D}\left[\frac{\partial \vec{u}^*}{\partial t^*} + (\vec{u}^* \cdot \nabla)\cdot \vec{u}^*\right] = -\frac{\rho U^2}{D}\nabla p^* + \frac{\mu U}{D^2}\nabla^2 \vec{u}^* \tag{2.8}$$

The continuity equation (2.4)， we easily get the nondimensional expression:

$$\nabla \cdot \vec{u}^* = 0 \tag{2.9}$$

To nondimensionalize momentum equation (2.6), multiply every term by a constant $D / \rho U^2$ to cancel the dimensions. After some rearrangement:

$$\frac{\partial \vec{u}^*}{\partial t^*} + (\vec{u}^* \cdot \nabla) \cdot \vec{u}^* = -\nabla p^* + \frac{\mu}{\rho UD} \nabla^2 \vec{u}^* \tag{2.10}$$

Defining $\mathrm{Re} = \rho UL / \mu$, generates the final nondimensional expression for an incompressible Navier-Stokes equation:

$$\frac{\partial \vec{u}^*}{\partial t^*} + (\vec{u}^* \cdot \nabla) \cdot \vec{u}^* = -\nabla p^* + \frac{1}{\mathrm{Re}} \nabla^2 \vec{u}^* \tag{2.11}$$

For incompressible flow problems, the continuity equation (2.9) and the Navier-Stokes equation (2.11) are basic governing equations. For convenience, in the following chapters, we remove the symbol * from Eq. (2.9) and (2.11). All equations are dimensionless forms without special explanation.

2.2 Algorithm

2.2.1 Modified Immersed Boundary Method

The two-dimensional basic problem is shown in Figure 2-1, where a stream of uniform flow approaches a solid cylinder. To model this, we have developed a modified immersed-boundary (IB) computational method (Zhang and Zheng, 2007, Cho et al. 2007) suitable for the simulation conditions when a body is immersed in a background flow.

The model equations are the continuity Equation (Eq. (2.9)) and the Navier-Stokes equations (Eq. (2.11)) for incompressible flow. For convenient numerical computation and characterization of flow, the governing equations are non-dimensionalized with the incoming wind speed, U, the diameter of the cylindrical windscreen, D, and the air density, ρ. The governing equations for the airflow for unsteady, incompressible flow can be generally written as:

$$\frac{\partial u_j}{\partial x_j} = 0 \tag{2.12}$$

and

$$\frac{\partial u_i}{\partial t} + \frac{\partial}{\partial x_j}(u_i u_j) = -\frac{\partial p}{\partial x_i} + \frac{1}{\mathrm{Re}}\frac{\partial^2 u_i}{\partial x_j \partial x_j} + f_i \tag{2.13}$$

where all the variables are dimensionless, and the Reynolds number, Re, is defined as $\rho UD/\mu$, f_i, the fictitious body force responsible for the flow to accommodate inside the solid cylinder (Cho et al. 2007).

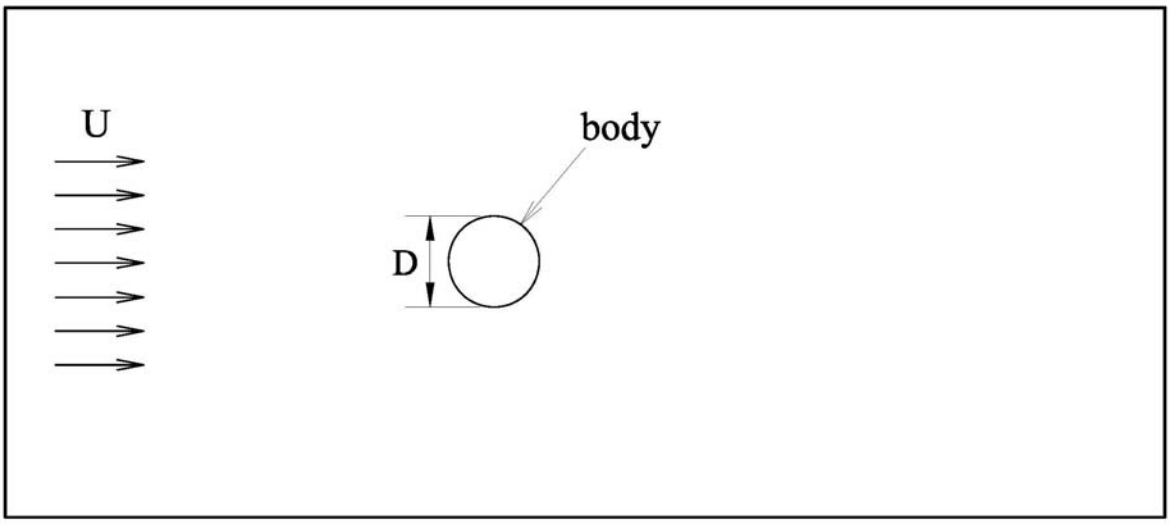

Figure 2-1 Illustration of the basic problem

Discretizing the momentum equation Eq. (2.13) as:

$$\frac{u_i^{n+1} - u_i^n}{\Delta t} = RHS_i + f_i \tag{2.14}$$

where $RHS_i = -\frac{\partial}{\partial x_j}(u_i u_j) - \frac{\partial p}{\partial x_i} + \frac{1}{\mathrm{Re}}\frac{\partial^2 u_i}{\partial x_j \partial x_j}$, and the f_i is given by,

$$f_i = \begin{cases} 0 & \text{outside the solid body} \\ -RHS_I + (v_{bi}^{n+1} - u_i^n)/\Delta t & \text{inside solid body} \end{cases} \tag{2.15}$$

where v_{bi}^{n+1} is the velocity of the solid body at the n+1 time step, therefore, the condition $u_{bi}^{n+1} = v_{bi}^{n+1}$ will be satisfied inside the solid body.

Applying a gradient on both sides of Eq. (2.13) and invoking the incompressibility condition of Eq. (2.12) generates a Poisson equation for the pressure

$$\nabla^2 p = -\frac{\partial}{\partial x_i \partial x_j}(u_i u_j) \tag{2.16}$$

Equation (2.14) is discretized using first-order time marching, with a semi-implicit scheme for the diffusion terms, the second-order Adams-Bashforth scheme for convection and central differencing for diffusion, and an implicit scheme for the resistivity term.

The procedure involves a two-step, predictor-corrector procedure. The velocity predictor equation is:

$$u_i^* = u_i^n + \delta t\left\{-\left(\frac{3}{2}S_i^n - \frac{1}{2}S_i^{n-1}\right) - p_{,i}^* + \frac{1}{2\,\mathrm{Re}}\nabla^2\left(u_i^n + S_i^*\right) + f_i\right\} \tag{2.17}$$

where the convection term defined as: $\vec{S} = (\vec{u}\cdot\nabla)\vec{u}$, p^* is an estimation to the pressure determined by:

$$\nabla^2\left(p^*\right) = -\nabla\cdot\left(\vec{S}^n\right) \tag{2.18}$$

where continuity is enforced by solving the Poisson equations for pressure.

Then, with the following correction step, the real time velocity and pressure are given by:

$$u_i^{n+1} = u_i^* - \nabla\phi \tag{2.19}$$

and

$$p_i^{n+1} = p_i^* + \phi \tag{2.20}$$

where ϕ is the solution of the modified pressure Poisson equation (PPE):

$$\nabla^2 \phi = \nabla \vec{u}^* \tag{2.21}$$

The Poisson equations (2.16) and (2.21) will be solved using MUDPACK Poisson solver (Adams, 1989).

The stability analysis of the scheme yields a stability criterion that is no more restrictive than that of an explicit scheme for a two-dimensional convection-diffusion equation (Zhang and Zheng, 2007)

$$\delta t < \min\left[\frac{h^2 \,\mathrm{Re}}{4}, \frac{2}{(u^2+v^2)\,\mathrm{Re}}\right] \tag{2.22}$$

where h is the grid size, u and v for x and y direction velocity, and Re for the Reynolds number. The first restriction in the minimum function is for diffusion and the second restriction is for convection. Therefore, the stability requirement for the current scheme is no more restrictive than this, because the semi-implicit scheme for diffusion should relax the first restriction and the Adams-Bashforth for convection should relax the second restriction.

The computational scheme is implemented on a staggered grid where the x-direction force is calculated on the u-grid, and the y-direction force is calculated on the v-grid.

2.2.2 High-Order Scheme

The presence of a porous media introduces a discontinuity in some flow variables, or in their derivatives, around the flow/porous interface and also arouses the numerical oscillation. Under these circumstances, most conventional finite difference schemes would generate some spurious numerical oscillations around the interface. However, the accuracy at the interface between flow and porous media is a key issue in simulating such problems. One of the most effective ways to overcome the unphysical oscillations and numerical instability is to apply high-order schemes including the upwind scheme and the WENO scheme (Harten et al. 1987, Shu and

Osher, 1988). High-order schemes have been used in simulation for viscous flow around steady and moving solid bodies (Cho et al. 2007), but still have not been applied to simulating flow field in different media.

The stability of a first-order upwind scheme is fine, but it has a strong diffusive effect similar to molecular viscosity. Therefore, the study will compare a second-order upwind scheme, a third-order upwind scheme, and a fifth-order WENO scheme.

2.2.2.1 Second-Order Upwind Scheme

Upwind schemes use an adaptive finite difference stencil to numerically simulate more properly the direction of propagation of information in a flow field. To outline this second order scheme, consider the simplified one dimensional wave equation:

$$\frac{\partial u}{\partial t} + a\frac{\partial u}{\partial x} = 0 \tag{2.23}$$

If we want to calculate the derivative $a\dfrac{\partial u}{\partial x}$ at X_i location (see Figure 2-2), if a is greater than 0, the wave propagation direction is from left to right. The derivative result will have more weight on left grids of X_i than that of right grids of X_i.

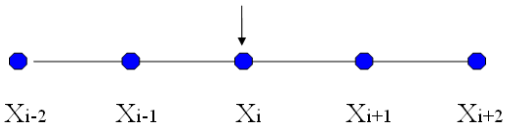

Figure 2-2 Illustration of the upwind scheme

Defining

$$a^+ = \max(a,0) \qquad a^- = \min(a,0)$$

$$u_x^- = \frac{3u_i - 4u_{i-1} + u_{i-2}}{2\Delta x} \tag{2.24}$$

$$u_x^+ = \frac{-u_{i+2} + 4u_{i+1} - 3u_i}{2\Delta x} \tag{2.25}$$

Discretizing the second term of Eq. (23), and we get:

$$a\frac{\partial u}{\partial x}\bigg|_{x=x_i^n} = a^+ u_x^- + a^- u_x^+ \tag{2.26}$$

2.2.2.2 Third-Order Upwind Scheme

$$u_x^- = \frac{2u_{i+1} + 3u_i - 6u_{i-1} + u_{i-2}}{6\Delta x} \tag{2.27}$$

$$u_x^+ = \frac{-u_{i+2} + 6u_{i+1} - 3u_i - 2u_{i-1}}{6\Delta x} \tag{2.28}$$

Substituting Eqs. (2.27) and (2.28) into Eq. (2.26), we can get the expression for the third-order upwind scheme.

2.2.2.3 Fifth-Order WENO Scheme

The philosophy of WENO scheme is similar to previous upwind scheme and it applies high-order interpolation using nonlinear weight to avoid numerical oscillations.

To outline this fifth-order scheme, consider the one dimensional wave equation,

$$\frac{\partial u}{\partial t} + \frac{\partial q(u)}{\partial x} = 0 \tag{2.29}$$

The derivative of any flux q is discretized as (see Figure 2-3):

$$\frac{\partial q}{\partial x}\bigg|_{x=x_i} = q_{x,i} = \frac{\hat{q}_{i+1/2} - \hat{q}_{i-1/2}}{\Delta x} \tag{2.30}$$

where $\hat{q}_{i+1/2}$ is an interpolated flux at the half-step location.

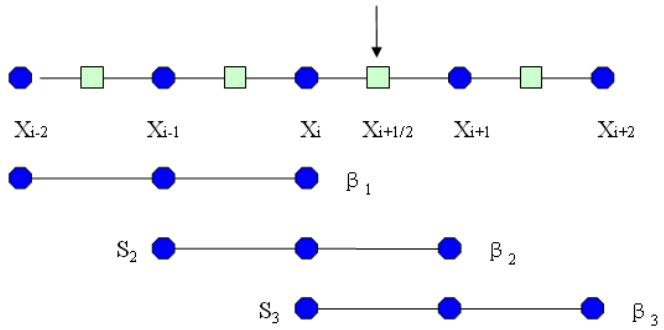

Figure 2-3 Illustration of the WENO scheme

If $\partial q / \partial u \geq 0$,

$$\hat{q}^{+}_{i+1/2} = \omega_1(\frac{1}{3}q_{i-2} - \frac{7}{6}q_{i-1} + \frac{11}{6}q_i) + \omega_2(-\frac{1}{6}q_{i-1} + \frac{5}{6}q_i + \frac{1}{3}q_{i+1}) + \omega_3(\frac{1}{3}q_i + \frac{5}{6}q_{i+1} - \frac{1}{6}q_{i+2}) \tag{2.31}$$

where:

$$\omega_j = \frac{\alpha_j}{\sum_{k=1}^{3}\alpha_k}, \qquad \alpha_k = \frac{d_k}{(\varepsilon + \beta_k)^2}$$

$$d_1 = \frac{1}{10,} d_2 = \frac{3}{5,} d_3 = \frac{3}{10}, \varepsilon = 10^{-6}$$

$$\beta_1 = \frac{13}{12}(q_{i-2} - 2q_{i-1} + q_i)^2 + \frac{1}{4}(q_{i-2} - 4q_{i-1} + 3q_i)^2$$

$$\beta_2 = \frac{13}{12}(q_{i-1} - 2q_i + q_{i+1})^2 + \frac{1}{4}(q_{i-1} - 4q_{i+1})^2$$

$$\beta_3 = \frac{13}{12}(q_i - 2q_{i+1} + q_{i+2})^2 + \frac{1}{4}(3q_i - 4q_{i+1} + q_{i+2})^2$$

The smoothness indicator β used here ensure that the stencil is given the least weight in the region of rapid change of flux q. More detail about the WENO scheme is in the reference

papers (Harten et al. 1987, Shu and Osher, 1988, Cho et al. 2007, Berthelsen and Faltinsen, 2008).

2.2.3 Comparison of High-order Schemes

Uniform flow over a stationary solid cylinder under low Reynolds number is used to test three high-order flux derivative schemes. The numerical model for flow over the cylinder case (see Figure 2-4) is two-dimensional and time dependant and nondimensionalized by the diameter of the cylinder D and the free-stream velocity U. The computation is performed on a staggered Cartesian grid mesh.

For the boundary conditions, at the inlet, $u = 1$, $v = 0$, and $\partial p / \partial x = 0$. For the bottom and top, $\partial u / \partial y = 0$, $v = 0$, and $\partial p / \partial y = 0$. For the outlet, $\partial u / \partial x = 0$, $\partial v / \partial x = 0$, and $p = 0$. The domain size is 25.6X12.8, the grid size is dx = dy = 0.0125, the Reynolds number is 40, the time step is dt = 0.004, the center of the solid cylinder is located an 8 unit length from the inlet boundary.

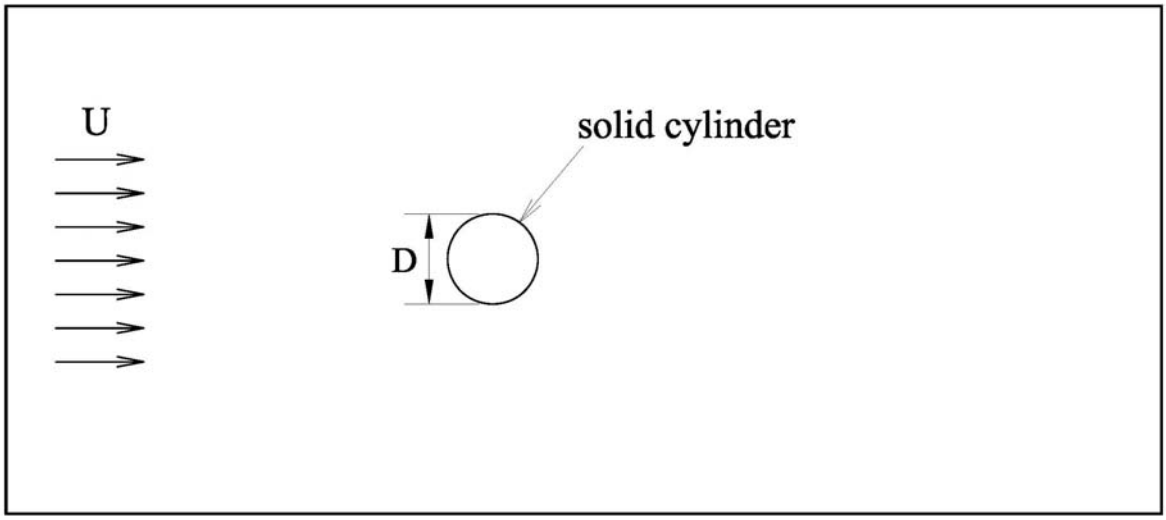

Figure 2-4 Illustration of the validation case: flow over solid cylinder

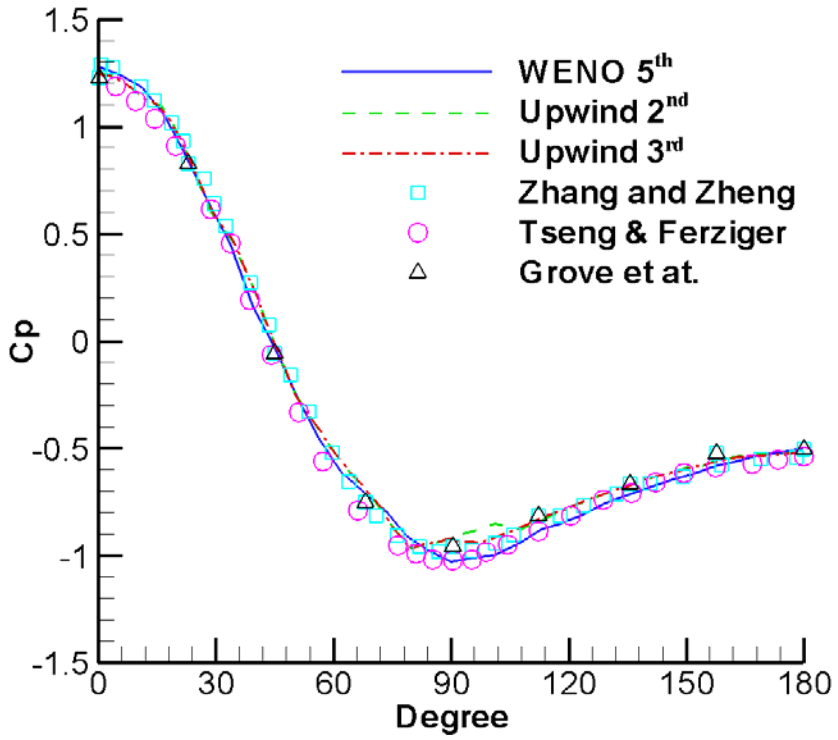

Figure 2-5 Cp comparison on the solid stationary cylinder surface (Re = 40)

The validation is done by investigating the surface-pressure distribution along the top half cylinder surface boundary (from upstream point (0 degree) to downstream point (180 degree)), which is most sensitive to different flux derivative schemes. In this test, several different schemes have been tested in the vicinity of the interface including a second- order upwind scheme, a third-order upwind scheme, and a fifth order WENO scheme. For a Reynolds number less than 50, a pair of attached, steady, and symmetric bubbles exists downstream of the cylinder. Since no vortex shedding has been formed, the pressure coefficient, Cp, on the surface is steady. Figure 2-3 shows the C_p on the cylinder surface at $Re = 40$. Next, three different schemes are implemented and their results are compared with the results of Zhang and Zheng (2007), Tseng and Ferziger (2003), and Silva et al. (2003). The results from the three schemes agree well with the reference results, but clearly the fifth-order WENO scheme result matches the reference

results best. The third-order and second-order schemes have very similar shape except for a few points around the position at 100 degrees. This validation case clearly shows that the high-order schemes are well-implemented. Therefore, the following chapters apply the fifth-order WENO scheme for the simulation cases because it has the best accuracy.

CHAPTER 3 - Flow over a Porous Medium

This chapter has three main parts: (1) governing formulations for the flow over a porous medium, (2) description of the computational algorithm, and (3) some basic verification and validation cases.

3.1 Basic Formulation

3.1.1 Darcy's Law

Henri Darcy's investigation of the hydrology of the fountains of Dijon and his experiments on steady-state flow in a uniform medium revealed proportionality between flow rate and the applied pressure difference. This one dimensional relation can be expressed as:

$$u = -\frac{K}{\mu}\frac{\partial P}{\partial x} \tag{3.1}$$

where u is the filtration velocity or darcy flux, $\partial P / \partial x$ is the pressure gradient in the flow direction, and μ is the dynamic viscosity of the fluid. The coefficient K is the specific permeability, which is independent of the nature of the fluid but depends on the geometry of the medium and the dimension of K is (Length)^2.

In three dimensions, for the case of an isotropic medium, Eq. (3.1) can be rewritten as:

$$\nabla P = -\frac{\mu}{K}\vec{\mathrm{v}} \tag{3.2}$$

Darcy's law has been verified by the results of many experiments. Moreover, theoretical backing for it has been obtained in various ways, with the aid of either deterministic or statistical models.

3.1.2 Extension of Darcy's Law

With unsteady term and the convection term added, Darcy's law can be extended as:

$$\rho\left[\frac{1}{\varphi}\frac{\partial \vec{\mathrm{v}}}{\partial t}+\frac{1}{\varphi^2}(\vec{\mathrm{v}}\cdot\nabla)\vec{\mathrm{v}}\right]=-\nabla P-\frac{\mu}{K}\vec{\mathrm{v}} \tag{3.3}$$

This equation was obtained by analogy with the Naiver-Stokes equation, where the porosity φ is defined as the fraction of the total volume of the medium that is occupied by the void space. Here the Dupuit-Forchheimer relationship is used (the fluid velocity assumed to not vary in direction normal to flow, a volume containing fluid only ($\vec{\mathrm{V}}$) and the filter velocity ($\vec{\mathrm{v}}$) are related to each other with $\vec{\mathrm{v}}=\varphi\vec{\mathrm{V}}$, Nield and Bejan, 1998).

An alternative to Darcy's equation is commonly known as Brinkman's equation:

$$\nabla P=-\frac{\mu}{K}\vec{\mathrm{v}}+\tilde{\mu}\nabla^2\vec{\mathrm{v}} \tag{3.4}$$

Now, two viscous terms appear; the first is the Darcy term, and the second is analogous to the Laplacian term that appears in the Navier-Stokes equation. Meanwhile, the coefficient $\tilde{\mu}$ is an effective viscosity. Brinkman set $\tilde{\mu}$ and μ equal to each other, but actually they are only approximately equal.

Joseph, Nield, and Papanicolaou (1982) modified the Darcy's Law and got:

$$\nabla P=-\frac{\mu}{K}\vec{\mathrm{v}}-c_F K^{-1/2}\rho\left|\vec{\mathrm{v}}\right|\vec{\mathrm{v}} \tag{3.5}$$

where c_F is a dimensionless form-drag constant. Meanwhile Eq. (3.5) is a modification of an equation associated with Dupuit and Forchheimer (Nield and Bejan, 1998); in fact, the last term of Eq. (3.5) is referred to the Forchheimer term.

Bhattacharyya, Dhinakaran and Khalili (2006) investigated the fluid motion around and through a porous cylinder. The governing equation for fluid through a porous cylinder is written as:

$$\frac{\partial \vec{\mathrm{v}}}{\partial t}+\frac{1}{\varphi}(\vec{\mathrm{v}}\cdot\nabla)\vec{\mathrm{v}}=-\varphi\nabla p+\frac{\varphi}{\mathrm{Re}}\nabla^2\vec{\mathrm{v}}-\frac{\varphi}{\mathrm{Re}\,D_a}\vec{\mathrm{v}}-\frac{0.13|\vec{\mathrm{v}}|}{\sqrt{D_a\varphi}}\vec{\mathrm{v}} \tag{3.6}$$

Here, the three authors combined the convection term, the diffusion term, the Darcy term and the Forchheimer term together, keeping the equation dimensionless. In the equation $D_a = K/a^2$, $\mathrm{Re}=\rho Ua/\mu$, where a is the characteristic length and U is characteristic velocity.

Chen, Yu and Winoto (2007) investigated the flow past a porous square cylinder, and they defined the governing equation for flow through porous medium as:

$$\rho\frac{\partial \vec{\mathrm{v}}}{\partial t}+\frac{1}{\varphi}(\vec{\mathrm{v}}\cdot\nabla)\vec{\mathrm{v}}=-\varphi\nabla p+\mu\nabla^2\vec{\mathrm{v}}-\frac{\mu\varphi}{K}\vec{\mathrm{v}}-\frac{\rho\varphi C_F|\vec{\mathrm{v}}|}{\sqrt{K}}\vec{\mathrm{v}} \tag{3.7}$$

Here, the equation is dimensional, and the only difference between Eq. (3.6) and Eq. (3.7) is that the diffusion term (in Eq. (3.6)) switches to the Brinkman term (in Eq. (3.7)).

Here shows many extended equations of Darcy's law. The widely used equation for unsteady flow over porous medium is the Darcy-Forchheimer equation (Eq. (3.6)).

3.1.3 Zwikker-Kosten Equation

The Zwikker-Kosten (ZK) phenomenological model has been used previously for numerical calculations of linear sound interactions with porous materials (Wilson et al. 2006, Salomons, Blumrich and Heimann, 2002). The original equation of motion for the ZK model is:

$$-\frac{\partial p}{\partial x}=\frac{k_s}{\varphi}\rho\frac{\partial u}{\partial t}+\sigma u \tag{3.8}$$

where k_s is the structure constant and σ is the resistance constant. Although Zwikker and Kosten allow these values to depend on frequency, they are normally assumed to be consistent in time-domain calculations.

Wilson et al. (2006, 2007) did the forerunner work on the application of the ZK equation for time-domain modeling of sound interaction with a porous surface. They also compared the ZK model with other sophisticated models (Relaxation Model etc.) and found good agreement between the rather simple ZK model and other more complex models.

In three dimensions, for the case of an isotropic medium, we can rewrite the ZK equation Eq. (2.8) as:

$$\rho \frac{\partial \vec{\mathrm{v}}}{\partial t} = -\frac{\varphi}{k_s} \nabla p - \sigma_s \vec{\mathrm{v}} \tag{3.9}$$

For simplicity, if we define the porosity φ and the structure constant k_s as unity ($\varphi = k_s = 1$), then Eq. (3.9) becomes:

$$\rho \frac{\partial \vec{\mathrm{v}}}{\partial t} = -\nabla p - \sigma_s \vec{\mathrm{v}} \tag{3.10}$$

Adding the convection term and the diffusion term into Eq. (3.10) and nondimensionlizing it, we get the modified ZK equation:

$$\frac{\partial \vec{\mathrm{v}}}{\partial t} + (\vec{\mathrm{v}} \cdot \nabla) \vec{\mathrm{v}} = -\nabla p + \frac{1}{\mathrm{Re}} \nabla^2 \vec{\mathrm{v}} - \sigma \vec{\mathrm{v}} \tag{3.11}$$

where σ is the dimensionless flow resistivity of the porous medium, non-dimensionalized by $\rho U / D$. The convection term and the diffusion term in Eq. (3.11) are omitted in the original ZK equation (Eq. (3.9)) because the velocity is low in the porous medium; however, including

them here enables the same Navier-Stokes equation solver to be used for Eq. (3.11). Additionally, we assume the effect of convection automatically becomes small when the velocity is low.

3.2 Numerical Scheme and Algorithm

The two-dimensional model problem is shown in Figure 3-1, where a stream of uniform flow approaches a porous cylinder. As discussed in Chapter 2.2, we have developed a modified IB computational method (Zhang and Zheng, 2007, Cho et al. 2007) suitable for the simulation conditions when a windscreen is immersed in a background flow.

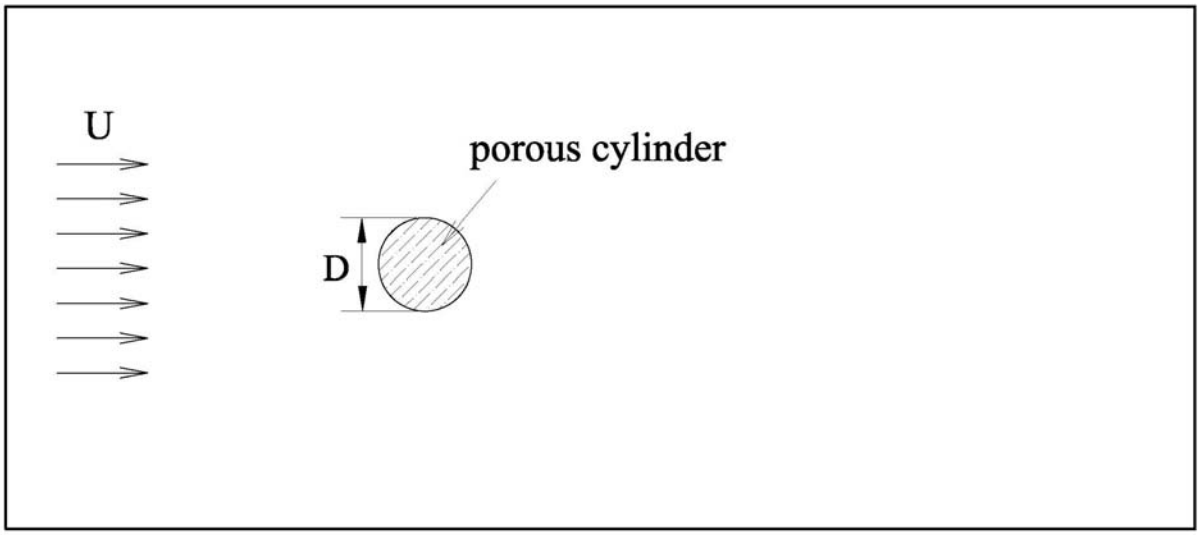

Figure 3-1 Illustration of the validation problem and the computational domain

The model equations are the Navier-Stokes equations for incompressible flow with a modified ZK equation for flow inside the porous medium.

For convenient numerical computation and characterization of flow, the governing equations are non-dimensionalized with the incoming wind speed, *U*, the diameter of the

cylindrical windscreen, D, and the air density, ρ. Thus, the governing equations for the airflow for unsteady, incompressible flow generally can be written as:

$$\frac{\partial u_i}{\partial t} + \frac{\partial}{\partial x_j}(u_i u_j) = -\frac{\partial p}{\partial x_i} + \frac{1}{\mathrm{Re}}\frac{\partial^2 u_i}{\partial x_j \partial x_j} + f_i \tag{3.12}$$

and

$$\frac{\partial u_j}{\partial x_j} = 0 \tag{3.13}$$

where all the variables are dimensionless, and the Reynolds number, Re, is defined as UD/ν, with ν being the kinematic viscosity of the air. Also f_i is the fictitious body force responsible for the flow to accommodate inside the porous or solid cylinder (Cho et al. 2007).

Discretizing the momentum equation Eq. (3.12) as:

$$\frac{u_i^{n+1} - u_i^n}{\Delta t} = RHS_i + f_i \tag{3.14}$$

where $RHS_i = -\frac{\partial}{\partial x_j}(u_i u_j) - \frac{\partial p}{\partial x_i} + \frac{1}{\mathrm{Re}}\frac{\partial^2 u_i}{\partial x_j \partial x_j}$, and the f_i is given by,

$$f_i = \begin{cases} 0 & \text{outside the porous body} \\ \sigma u_i & \text{inside the porous body} \\ -RHS_I + (v_{bi}^{n+1} - u_i^n)/\Delta t & \text{inside solid body} \end{cases} \tag{3.15}$$

where v_{bi}^{n+1} is the velocity of the solid body at the n+1 time step, the boundary condition $u_{bi}^{n+1} = v_{bi}^{n+1}$ will be automatically satisfied inside the solid body.

Eq. (3.15) shows that if $f_i = 0$, then Eq. (3.12) becomes the standard Navier-Stokes Equation for incompressible flow (this is the computational domain except for the porous zone and the solid zone); with $f_i = \sigma u_i$, then Eq. (3.12) becomes the modified ZK equation.

The air flow inside the windscreen is modeled to follow the modified ZK equation (Eq. (3.11)). In addition, incompressibility is also assumed for flow inside the porous medium. The governing equations for airflow inside the porous medium used in this study are expressed in Eq. (3.12) as $f_i = \sigma u_i$.

By applying a gradient on both sides of Eq. (3.12) and invoking the incompressibility condition of Eq. (3.13), a Poisson equation for the pressure can be obtained as

$$\nabla^2 p = -\frac{\partial}{\partial x_i \partial x_j}(u_i u_j) \tag{3.16}$$

The resulting computational scheme is implemented on a staggered grid with the x-direction force calculated on the u-grid and the y-direction force calculated on the v-grid. The whole numerical algorithm is in Chapter 2.2.

3.3 Basic Verification Cases

This section includes two main cases. One case is for uniform flow around and through a porous square. The other case is for uniform flow around and through a stationary porous cylinder under different Reynolds numbers.

3.3.1 Flow around and through a Porous Square

Clearly, the one-dimensional Darcy law is written as:

$$\frac{\partial p}{\partial x} = -\frac{\mu}{K} u_0 \tag{3.17}$$

As uniform flow around and through porous square illustrated in Figure 3-2, we can get analytical solution (assuming u_0, μ and K are constant):

$$\begin{aligned} p &= p_0 && x \le L \\ p &= p_0 - \frac{\mu}{K} u_0 x && x > L \end{aligned} \tag{3.18}$$

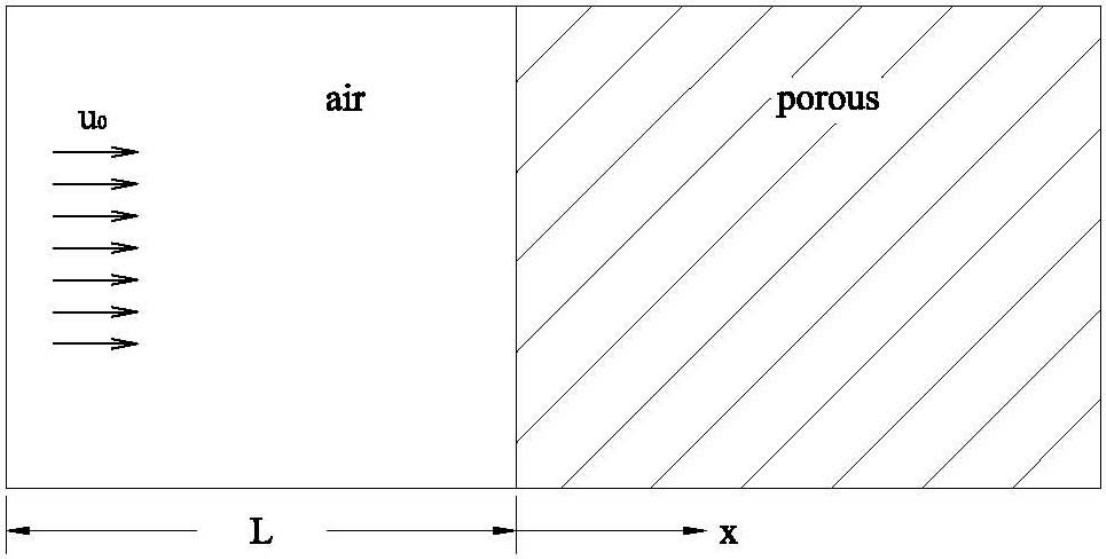

Figure 3-2 Illustration of uniform flow over porous square

We ran the simulation in FLUENT and also with our code. The same boundary conditions were set, at the inlet, $u = 0.1$, $v = 0$, and $\partial p / \partial x = 0$. For the bottom and top, $\partial u / \partial y = 0$, $v = 0$, and $\partial p / \partial y = 0$. For the outlet, $\partial u / \partial x = 0$, $\partial v / \partial x = 0$, and $p = 0$. The domain size is 25.6X12.8, L = 12, grid size dx = dy = 0.2, time step dt = 0.1. For simplicity we set air density $\rho = 1$ and the air viscosity $\mu = 0.01$. For comparison, the term μ / K in Darcy's law is comparable to the term σ in ZK equation (Eq. (3.11)), so the same parameter is set both in FLUENT and also in code by $\sigma = \mu / K$. We set two different σ values: 1 and 10, separately. The comparison of results among analytical, FLUENT and the code can be seen in Figure 3-3 and 3-4. Clearly, the

results show that the results from the code and also from FLUENT match the analytical solution very well.

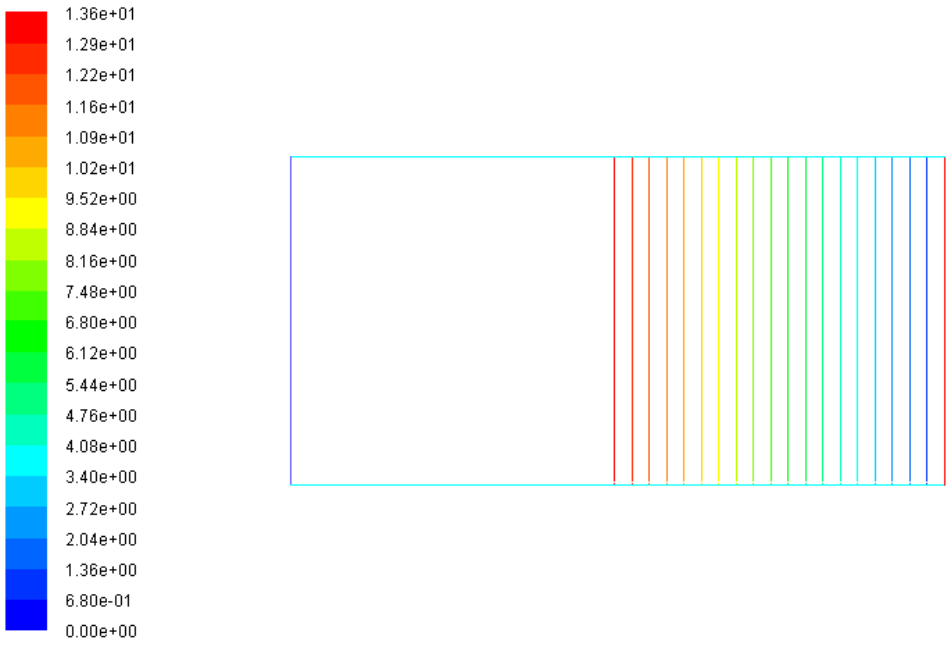

(a) FLUENT

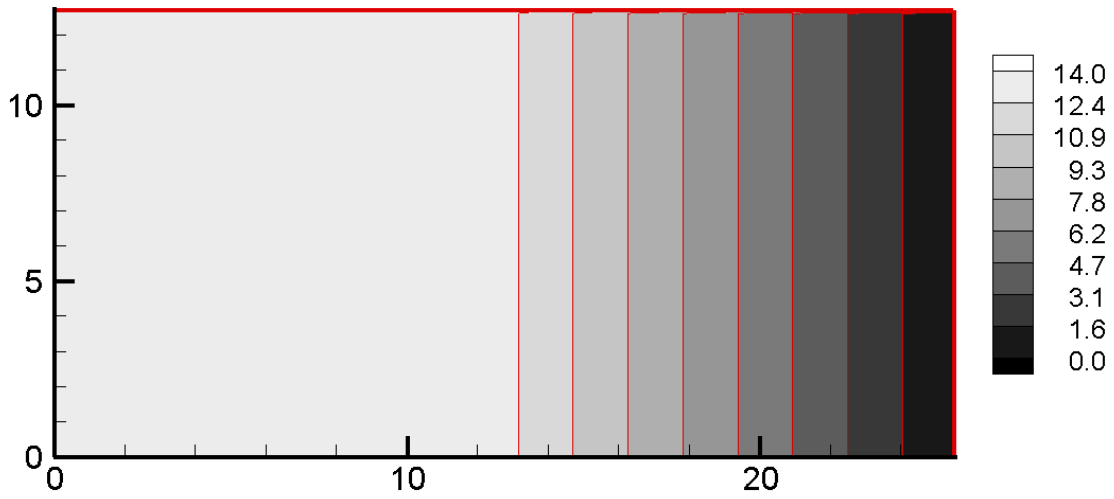

(b) Code

Figure 3-3 Pressure contour of flow field (σ = 10)

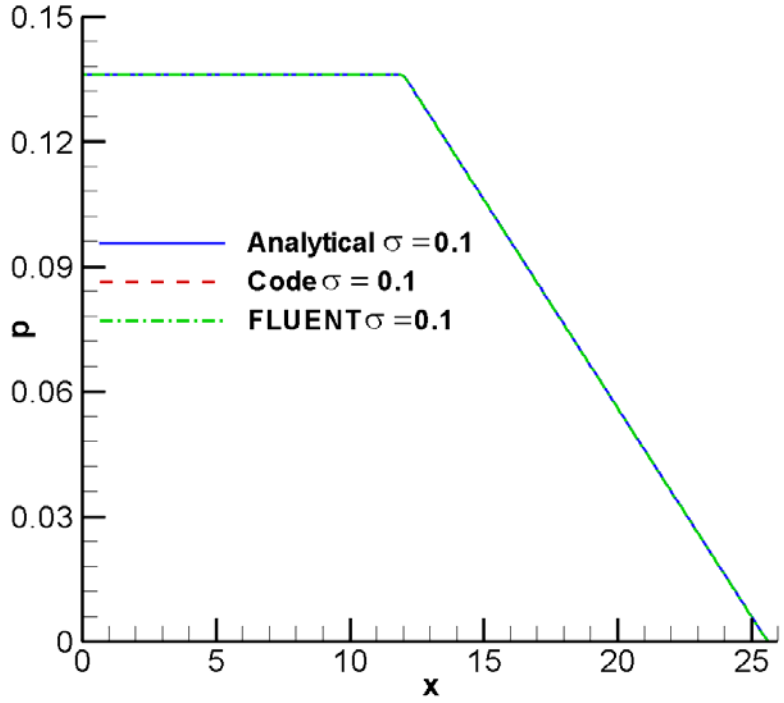

(a) $\sigma = 0.1$

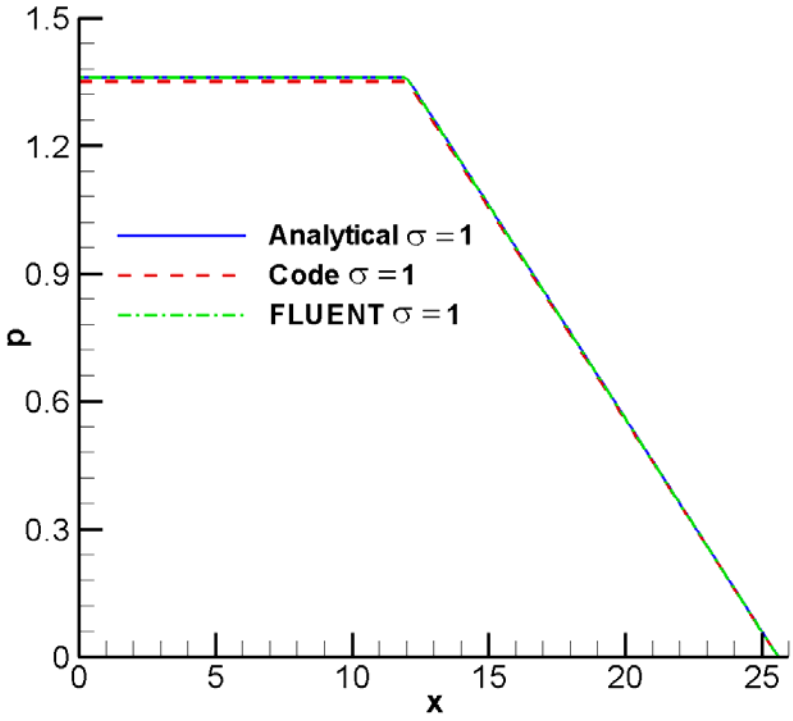

(b) $\sigma = 1$

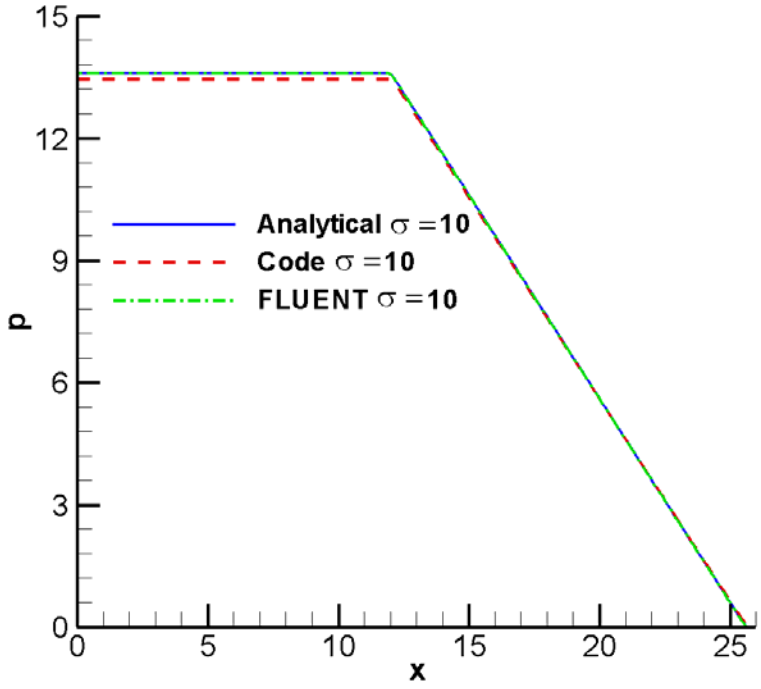

(c) σ = 10

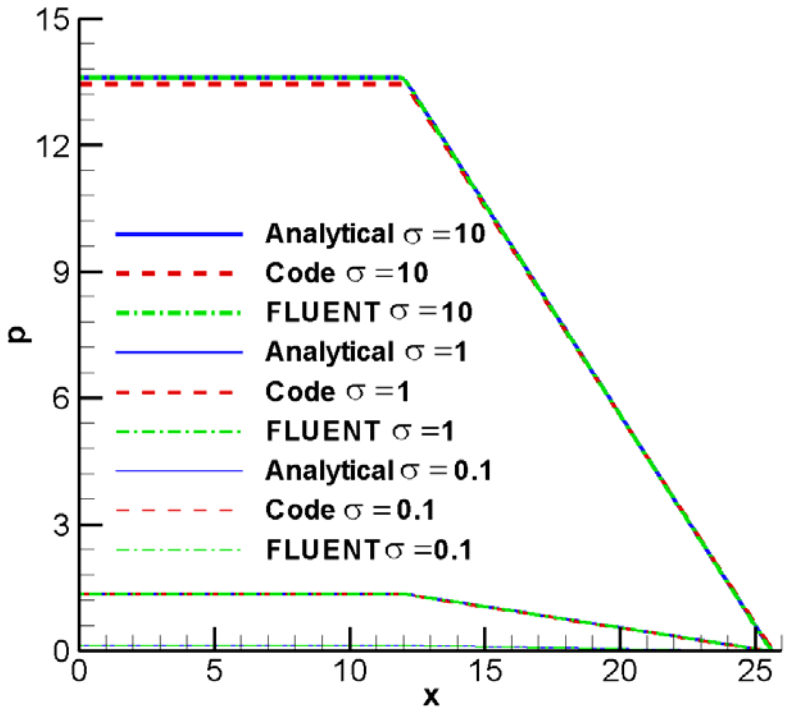

(d) total comparison

Figure 3-4 Pressure distribution along Y-center line

3.3.2 Flow around and through a Porous Cylinder

For the boundary conditions, at the inlet, $u = 1$, $v = 0$, and $\partial p / \partial x = 0$. For the bottom and top, $\partial u / \partial y = 0$, $v = 0$, and $\partial p / \partial y = 0$. For the outlet, $\partial u / \partial x = 0$, $\partial v / \partial x = 0$, and $p = 0$. The domain size is 25.6X12.8, the grid size dx = dy = 0.025, and the Reynolds numbers are 2, 5, 10, 20, 30 and 40 respectively. The time step is 0.002. The center of the porous cylinder is located an 8 unit length from the inlet boundary.

Bhattacharyya, Dhinakaran and Khalili (2006) investigated the flow through and around a porous cylinder numerically showing that the drag coefficient is similar to that of the numerical and experimental data (Sucker and Brauer, 1975, Braza et al, 1986) with porosity in the range $0.629 \le \varphi \le 0.999$ and Darcy number in the range $10^{-6} \le D_a \le 1.5$. Bhattacharyya et al. use Darcy-Forchheimer equation (Nield and Bejan, 1998) as governing equation for flow through and around porous media and implement the computation under cylindrical coordinate system. In the modified ZK equation, we define the flow resistivity term σ equals Darcy term $\frac{\mu\varphi}{K}$ for comparison purpose.

The vorticity contour of Z direction can be seen in Figure 3-5. The red color in the figures represents positive vorticity (in the counter clockwise sense, with the upper limit value of 2), the blue color represents negative vorticity (in the clockwise sense, with the lower limit value of -2). Cleary it shows that for the low flow resistivity case (σ = 5) much flow permeated the porous cylinder while for the high flow resistivity case (σ = 100) little flow permeated the porous cylinder, which makes sense for the porous medium property.

Subsequently, we plotted the drag coefficient C_d and compared it with results from Bhattacharyya et al. (see Figure 3-6). Also we compare the results from the results of flow over

solid cylinder (Sucker and Brauer, 1975, Braza et al., 1986 and Panton, 1996). This figure shows that most points are very similar to the results from Bhattacharyya et al., although there are some differences for C_d value at Reynolds number Re = 10 and Re = 40. The error in these two points is around 10% and this error may be due to the forcheheimer term (Nield and Bejan, 1998) which is neglected in the modified ZK equation.

These validation cases show that the governing equation for flow over porous problem has a fair agreement with the results from other authors. Therefore, the modified ZK equation can be utilized for simulation for flow over a porous medium.

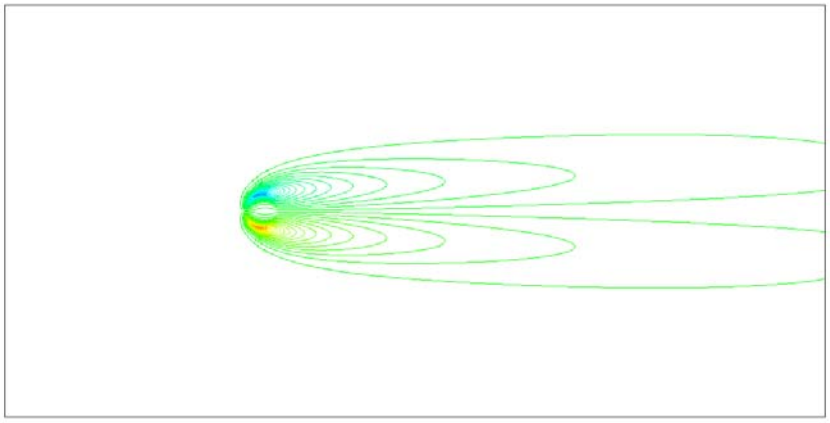

Porous case, Re = 40, σ = 5

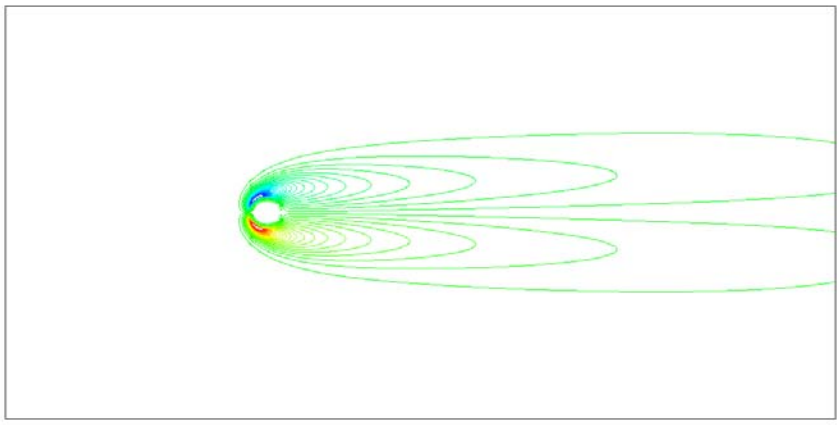

Porous case, Re = 2, σ = 100

Figure 3-5 Vorticity contour of the flow field

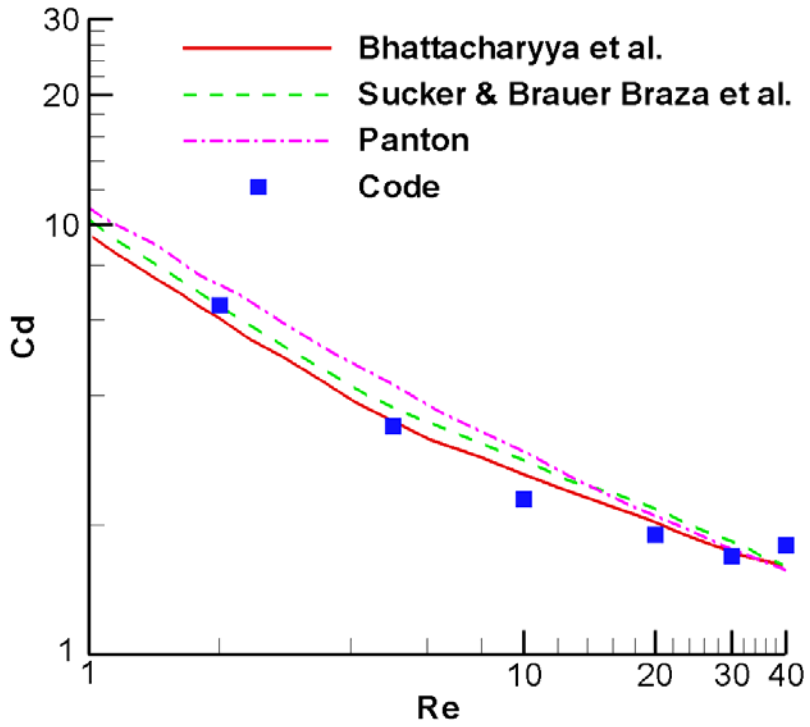

Figure 3-6 Drag coefficient (C_d) comparison

3.4 FLUENT Case Comparison

The computational fluid dynamics (CFD) software FLUENT is commonly used in industry and it contains a flow over porous medium package. We want to compare our results with those of FLUENT software.

The first comparison case is illustrated in Figure 2-4 (see Chapter 2.2), a uniform flow over a solid cylinder. We want to compare the pressure of a downstream point of the solid cylinder. Reynolds number is Re = 200. The boundary conditions are set as followings: at the inlet, $u = 1$, $v = 0$, and $\partial p / \partial x = 0$. For the bottom and top, $\partial u / \partial y = 0$, $v = 0$, and $\partial p / \partial y = 0$. For the outlet, $\partial u / \partial x = 0$, $\partial v / \partial x = 0$, and $p = 0$. The domain size is 25.6X12.8, the grid size dx = dy = 0.025, and the time step is 0.005. In FLUENT, the basic parameters and boundary condition settings are the same as for IB code. We apply the fifth-order WENO scheme in the area around

the interface between the air and the solid cylinder for convection term in IB code, while the second-order upwind scheme is applied in FLUENT.

For the downstream point pressure, the peak frequency from code is 0.41 and that from FLUENT is 0.39, the error is around 5%. Zhang and Zheng (2007) investigated the flow over stationary solid cylinder and found that the peak frequency under Reynolds number Re = 200 is around 0.41 which is much closer to IB code result than the FLUENT result.

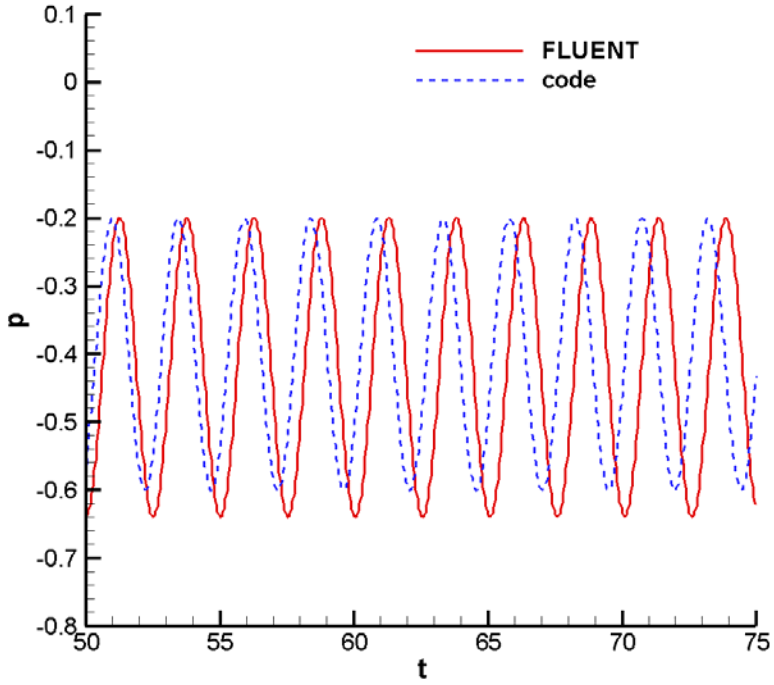

Figure 3-7 Pressure time histories of a downstream point of the solid cylinder (The downstream point is 4D away from the first solid cylinder center, all values are dimensionless, Re = 200)

The second comparison case is illustrated in Figure 3-7, a uniform flow over a solid cylinder and a stationary porous cylinder. We want to compare the results from both FLUENT and our code, including the vorticity contour of the flow field, the pressure time history of a

downstream point after the first solid cylinder, and also the pressure time history of the center point of the porous cylinder.

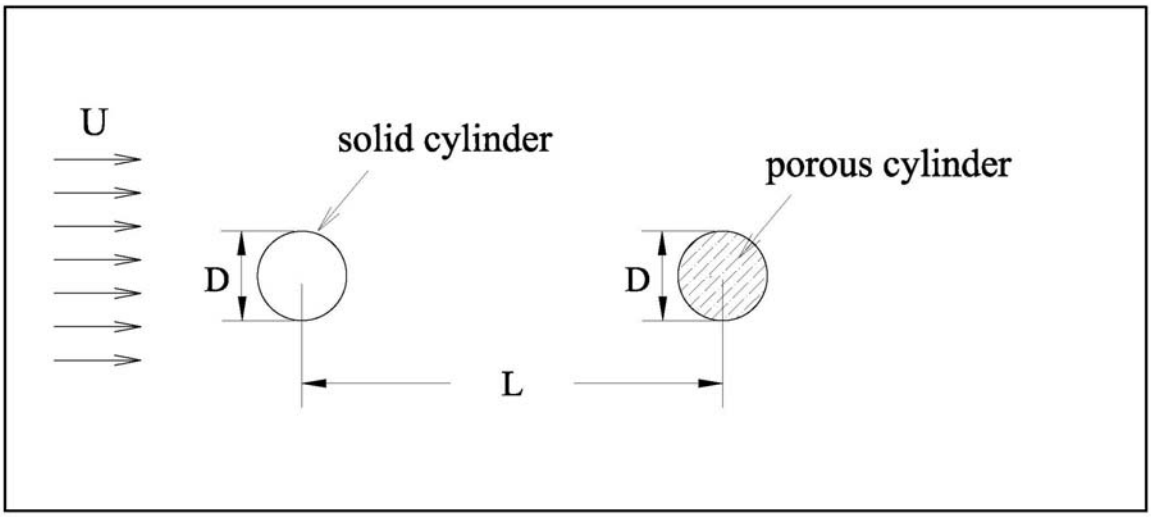

Figure 3-8 Illustration of the testing case

Accordingly, we set the Reynolds number as 500 both in IB code and FLUENT software. In the immersed boundary (IB) code, the boundary conditions are set as followings: at the inlet, $u = 1$, $v = 0$, and $\partial p / \partial x = 0$. For the bottom and top, $\partial u / \partial y = 0$, $v = 0$, and $\partial p / \partial y = 0$. For the outlet, $\partial u / \partial x = 0$, $\partial v / \partial x = 0$, and $p = 0$. The domain size is 25.6X12.8, the grid size dx = dy = 0.025, and the time step is 0.002. The center of the solid cylinder is located an 8 unit length from the inlet boundary and the diameters of the solid cylinder and porous cylinder are the same: D = 1. The distance between the solid cylinder center and porous cylinder center is set to L=8D. The flow resistivity for the porous medium is set as σ = 10. In FLUENT, the basic parameters and boundary condition settings are the same as for IB code. We apply the fifth-order WENO scheme in the interface zones between the air and the porous cylinder, and also the air and the solid cylinder for convection term in IB code, while the second-order upwind scheme is applied in FLUENT.

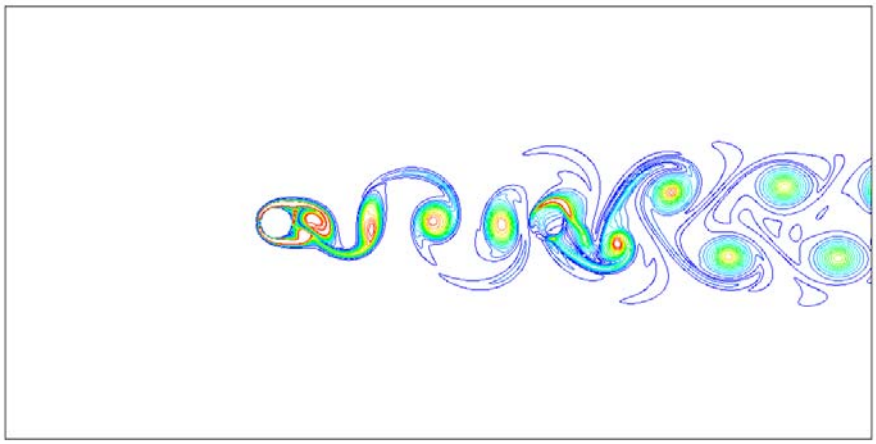

(a) IB code

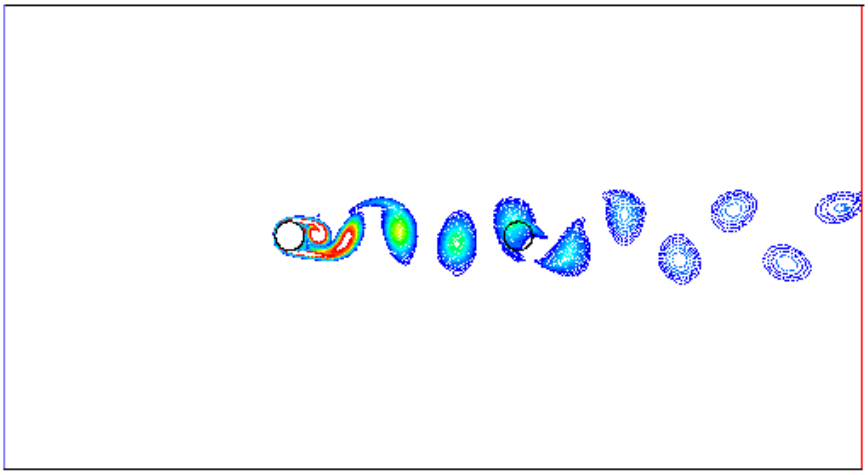

(b) FLUENT

Figure 3-9 Vorticity magnitude contour of flow field (Re = 500)

The vorticity magnitude contours of the flow field are in Figure 3-8 (the upper limit value of 5, the lower limit value of 0.5). The general vortex trend seems similar although there's some difference after the porous cylinder. The pressure time history of a downstream point after the first solid cylinder (the downstream point is 4D distance away from the first solid cylinder center) and the center point of the porous are in Figure 3-9 and 3-10. The results of the pressure time history show that the results from the immersed code are similar to the results from the FLUENT

software, although there are minor differences for magnitude and peak frequency. For the downstream point pressure, the peak frequency from code is 0.44 and that from FLUENT is 0.39, the error is around 7%. For the center point pressure, the peak frequency from code is 0.42 and that from FLUENT is 0.4, the error is around 5%. The peak frequencies (0.39 to 0.44) conform to the Strouhal number theory (f D/U ≈ 0.4, Kim and Durbin, 1988). Zhang and Zheng (2007) investigated the flow over stationary solid cylinder under Reynolds number Re = 500 and found that the peak frequency is around 0.43 which is closer to IB code result than the FLUENT result. The pressure fluctuation magnitude difference is mainly due to the numerical dissipation caused by fifth-order WENO scheme and second-order upwind scheme. From these two cases, we can see that FLUENT kind of underrates the peak frequency comparing to IB code. Ultimately, the comparisons show that the flow/porous equations are implemented well and can compare with results from other authors and software.

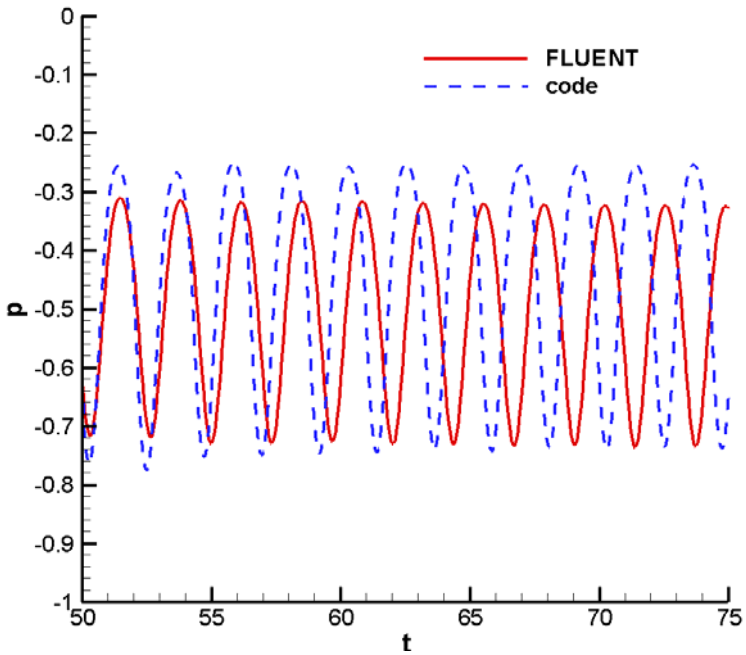

Figure 3-10 Pressure time histories of a downstream point of the first solid cylinder (The downstream point is 4D away from the first solid cylinder center, all values are dimensionless, Re = 500)

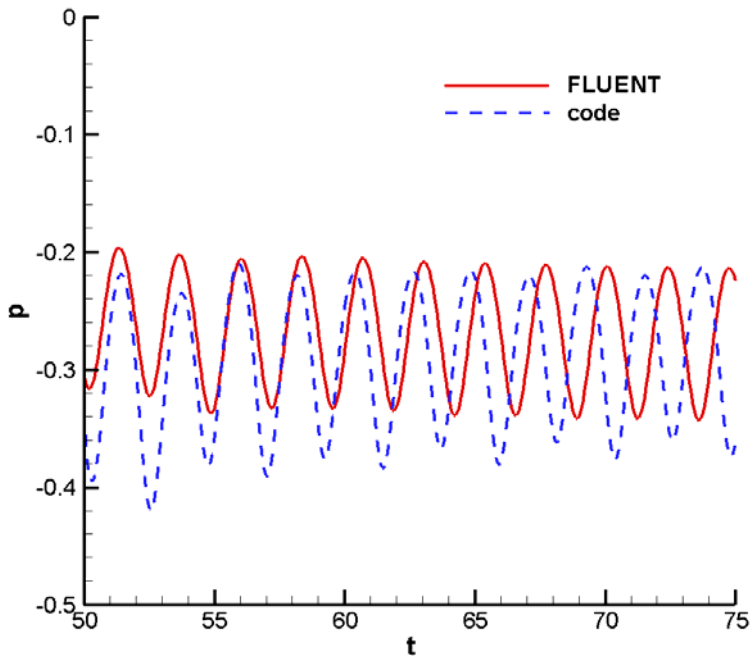

Figure 3-11 Pressure time histories of the center point of the porous cylinder (all values are dimensionless, Re = 500)

CHAPTER 4 - 2D Simulation and Results

The previous chapters describe the basic equations, numerical schemes and the validation cases. This chapter now simulates and describes two-dimensional cases. There are four main parts: (1) the flow over a windscreened microphone under a low Reynolds number (Re = 500); (2) the flow over a windscreened microphone under a high Reynolds number (Re = 5000); (3) a comparison between low and high Reynolds number cases; finally, (4) the flow over different shaped windscreens.

4.1 Problem Description

The two-dimensional model problem is shown in Figure 4-1, where a stream of unsteady and/or turbulent flow approaches a cylindrical unscreened or screened microphone. The windscreen, when present, is made of a porous material. Because of the unsteadiness and surface conditions, flow fluctuations and vortical structures are generated around the surface and in the wake region. The pressure fluctuations sensed by the microphone, which are assumed to be at the center of the screen, result from near-field, incompressible disturbances. The flow fluctuations, both internal and external to the windscreen, are investigated based on coupled flow simulation between the outside and inside of the windscreen. We have developed an immersed-boundary (IB) computational method suitable for simulations in which a windscreen is immersed in a background flow. While the IB methods for fluid-structure interaction problems typically discretize the equations of motion for fluid on a Cartesian grid, the methods generally do not require that the geometry of the structure to conform in any way to this Cartesian grid. The important issue is to study the wind noise reduction (WNR) effect of the windscreen. Specially, we want to know the sound pressure level (SPL) difference between the unscreened microphone

center (measurement point in the sub-figure (a) in Figure 4-1) and the screened microphone center (measurement point in the bottom sub-figure (b) in Figure 4-1) for different windscreen under different wind turbulence.

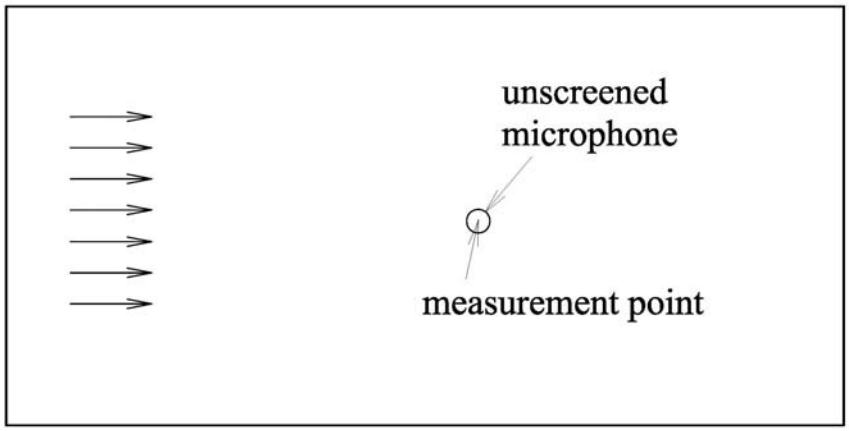

(a) an unscreened microphone

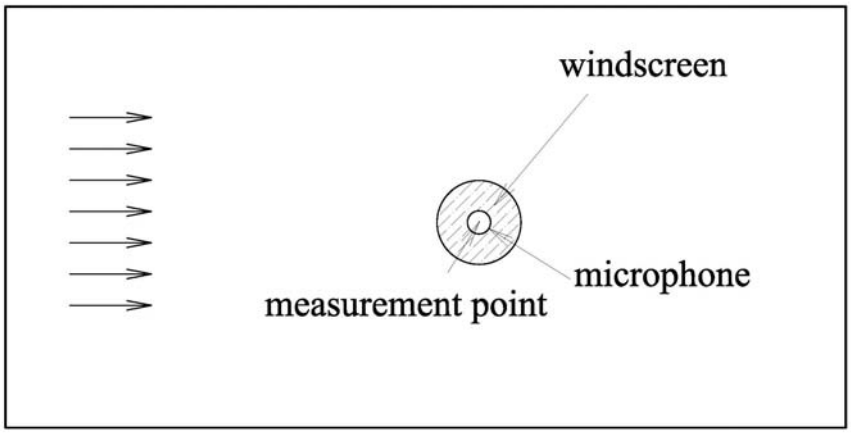

(b) a screened microphone

Figure 4-1 Illustration of the model problem and the computational domain: (a) an unscreened microphone; (b) a screened microphone.

The model equations used here are the Navier-Stokes (NS) equations for incompressible flow, with the modified ZK equation for flow inside the porous medium. The detailed computational equations and schemes are in Chapter 3. It should be noted that although

sound waves measured at a microphone are compressible disturbances, the wind noise interfering with the sound waves consist, in general, of incompressible turbulence. The pressure fluctuations of interest are near the surface of an object or inside a porous medium. These fluctuations are associated with near-field, as with the surface pressure fluctuations produced by a turbulent boundary layer over the surface as discussed by Kraichnan (1956), for which the incompressible flow assumption is well justified.

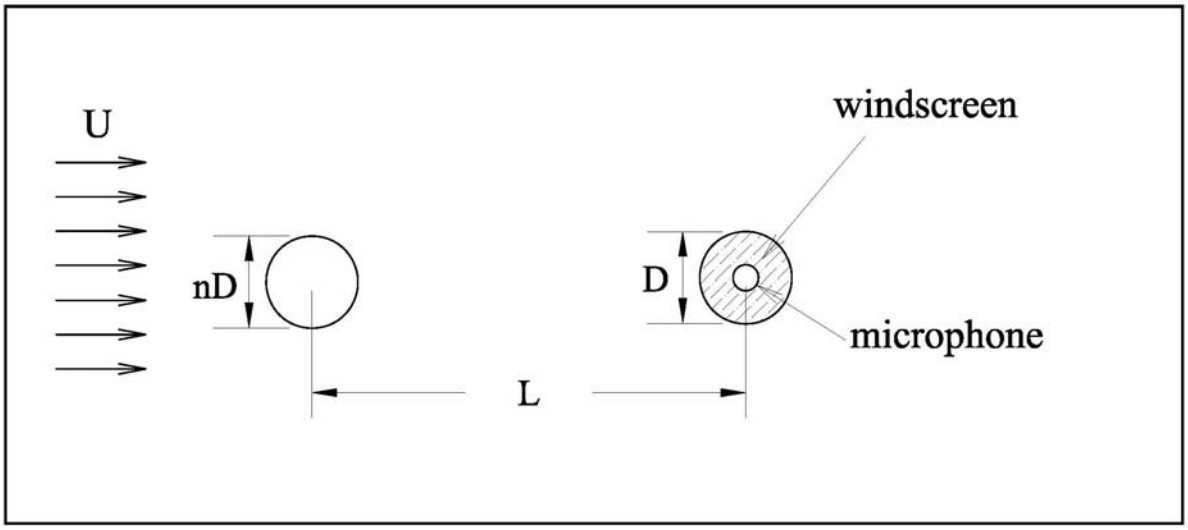

Figure 4-2 Illustration of the incoming wind turbulence generation with different sizes of upstream cylinders where n= 0.2, 0.5, 1.0, and 2.0.

As mentioned previously, this simulation uses time-domain computational fluid dynamics to solve for an acoustic problem.

To distinguish the noise reduction effect of the windscreen in different frequency ranges, we introduce wind turbulence by placing different sizes of solid cylinders upstream of the microphone (see Figure. 4-2). We selected cylinder of sizes 0.2D, 0.5D, 1.0D and 2.0D to generate different turbulent fields (where D is the diameter of the windscreen). The distance L, between the first cylinder center and the second windscreen center, is 8D. More realistic

atmospheric turbulence can be specified using other methods such as the quasi-wavelet method (Goedecke et al., 2004; Wilson, et al., 2004), and will be done in further studies (chapter 6). Meanwhile, the following section investigates the flow over the windscreen under first a low Reynolds number (Re = 500) and then a high Reynolds number (Re = 5000).

4.2 Low Reynolds Number (Re = 500) Cases

For the cases with a low Reynolds number, $\mathrm{Re} = \frac{UD}{\nu} = \frac{1m/s \cdot 0.0075m}{1.5 \times 10^{-5} m^2/s} = 500$, approximately characterizes a windscreen with a diameter of 0.75cm and wind speed of 1m/s for the incoming air. Also, the bare microphone (unscreened) has a diameter of 0.1875cm. Next, the four chosen values of dimensionless flow resistivity of the windscreen, 0.2, 2, 20 and 200, correspond to approximately 34, 340, 3400 and 34000 Pa·s/m^2 of dimensional flow resistivity, respectively ($1\sigma = \frac{\rho U}{D} = \frac{1.27kg/m^3 \cdot 1m/s}{0.0075m} = 170 P_a \cdot s/m^2$). In this simulation, the grid size is 0.025 in both the x and y direction, and the time step is 0.002, which satisfies the stability condition for the computational scheme (Zhang and Zheng 2007).

We first investigated the whole flow field as shown by vorticity contours in Figure 4-3 through Figure 4-6 for the flow resistivity (σ = 34, 340, 3400, 34000 Pa·s/m^2 and also unscreened) with different upstream cylinder sizes (0.2D, 0.5D, 1.0D and 2.0D case). The red color in the figures represents positive vorticity (in the counter clockwise sense, with the upper limit value of 5), the blue color represents negative vorticity (in the clockwise sense, with the lower limit value of -5). Clearly, smaller upstream cylinders generate smaller but denser vortical structures compared with larger upstream cylinders. Also, there is no flow inside the solid bare microphone, but some flow infiltrates the windscreened porous cylinder. Next, when the flow resistivity reaches high enough values (σ = 34000 Pa·s/m^2), little flow permeates the porous

cylinder, similar to flow over an unscreened bare cylinder. Finally, with very low flow resistivity, the flow permeates the porous cylinder as if the walls do not exist.

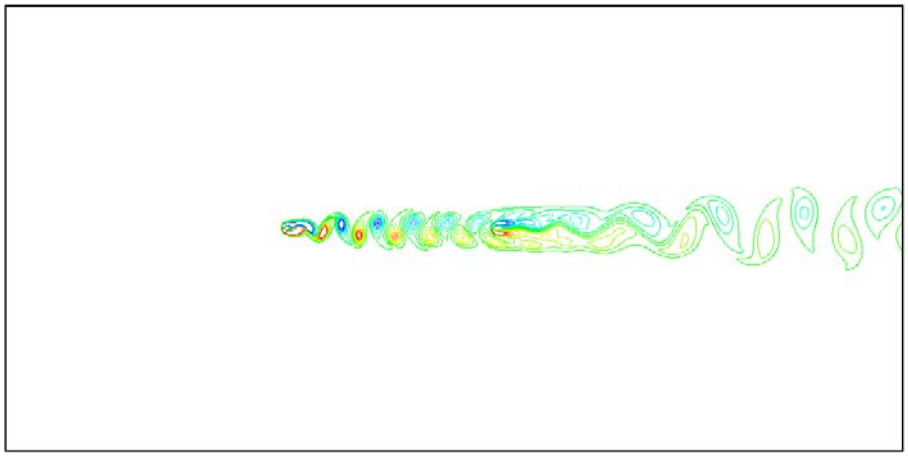

(a) σ = 34 Pa·s/m^2

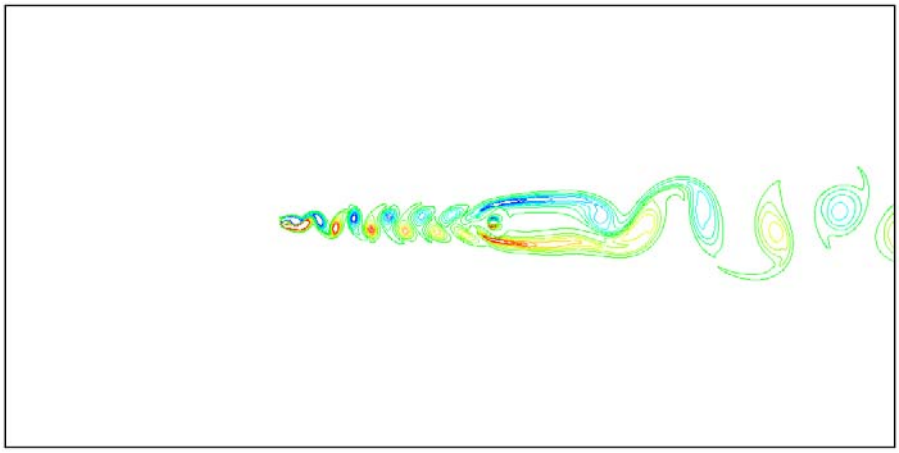

(b) σ = 340 Pa·s/m^2

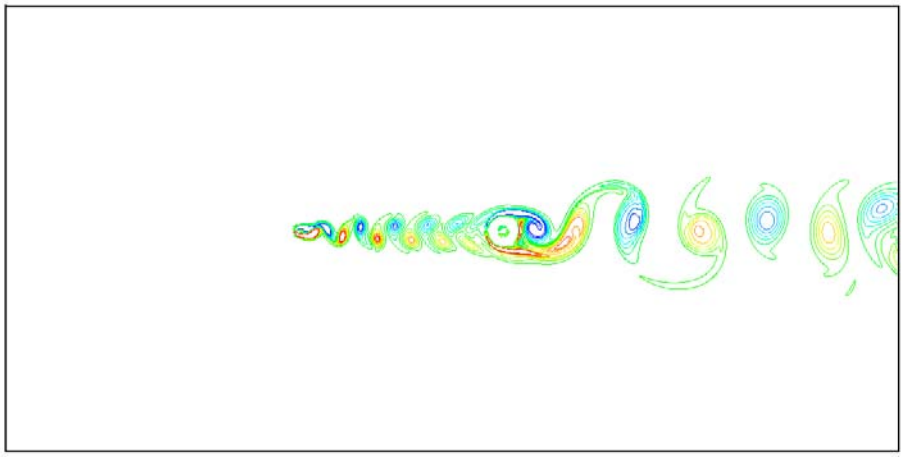

(c) σ = 3400 Pa·s/m^2

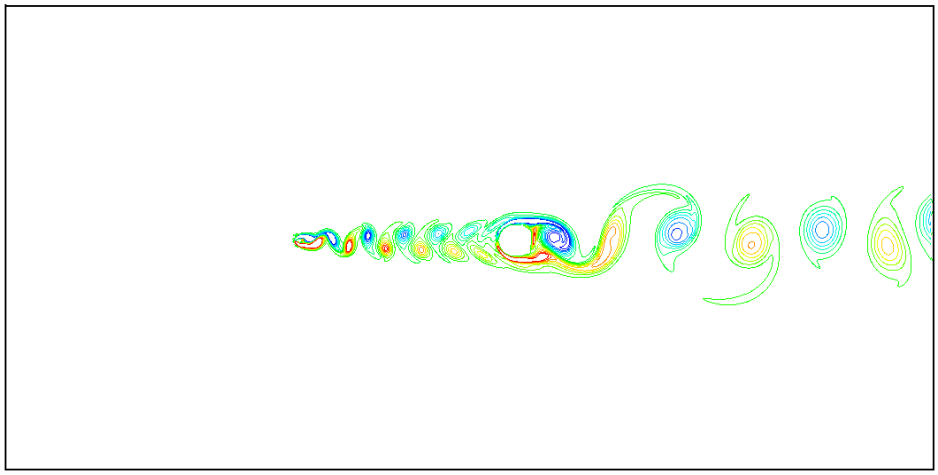

(d) σ = 34000 Pa·s/m^2

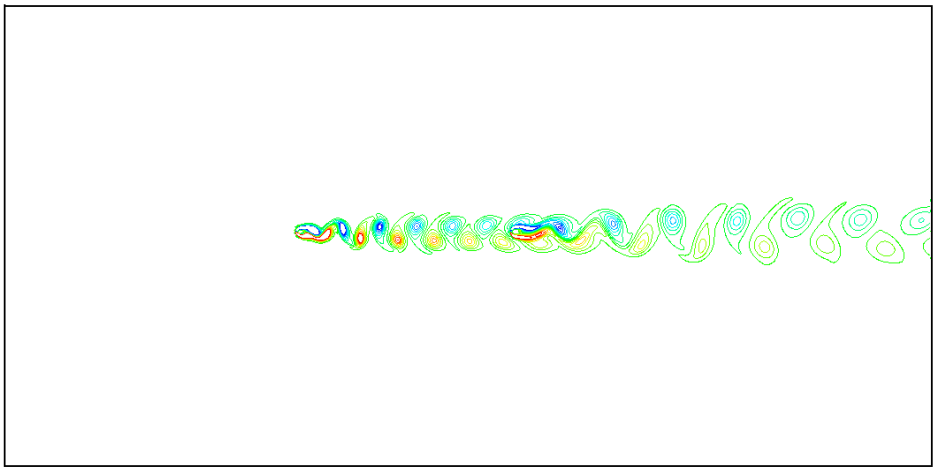

(e) unscreened

Figure 4-3 Vorticity contours of flow field (Re = 500, 0.2D case)

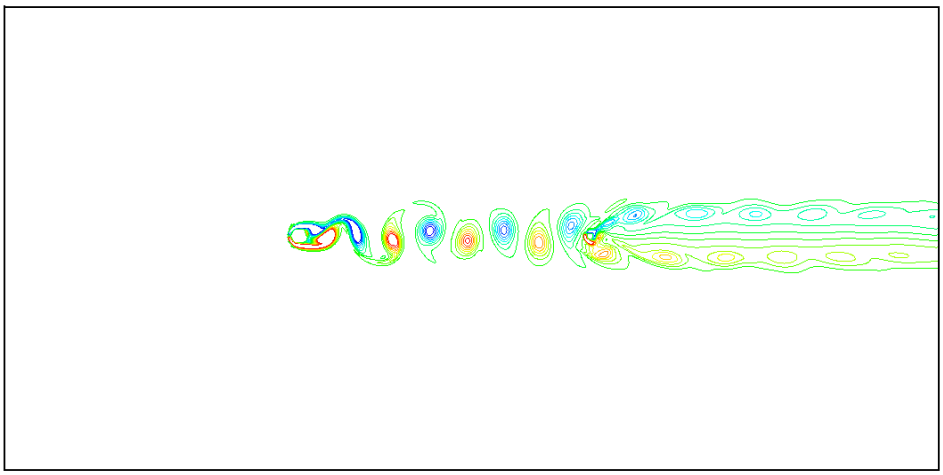

(a) σ = 34 Pa·s/m^2

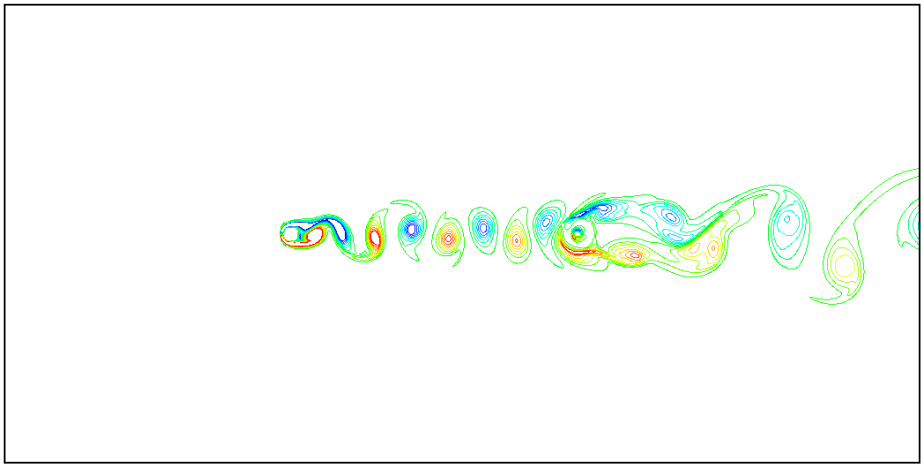

(b) σ = 340 Pa·s/m^2

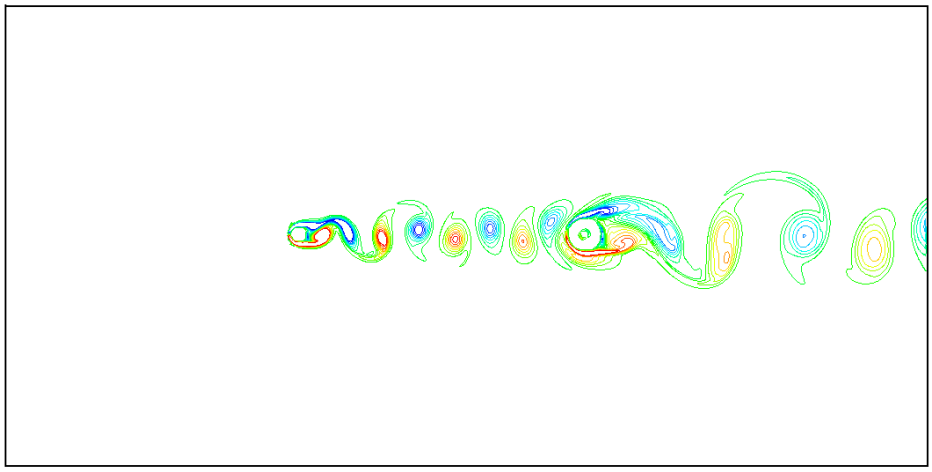

(c) σ = 3400 Pa·s/m^2

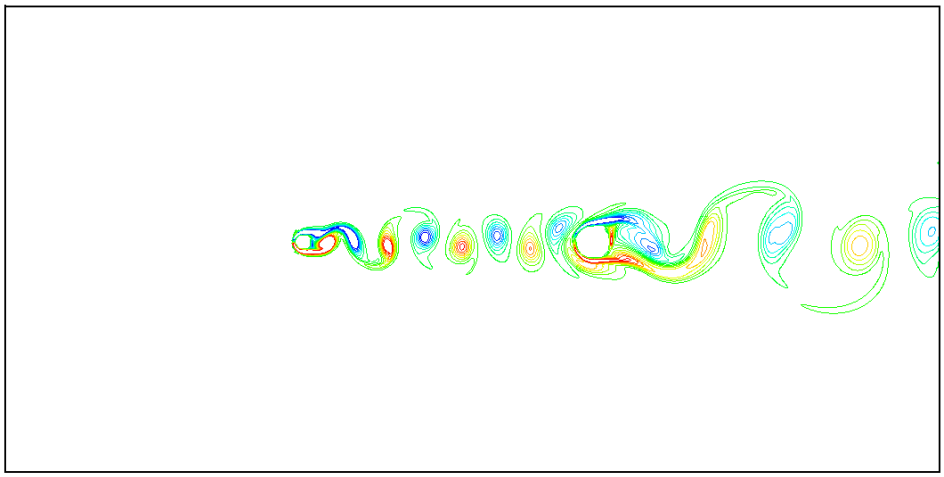

(d) σ = 34000 Pa·s/m^2

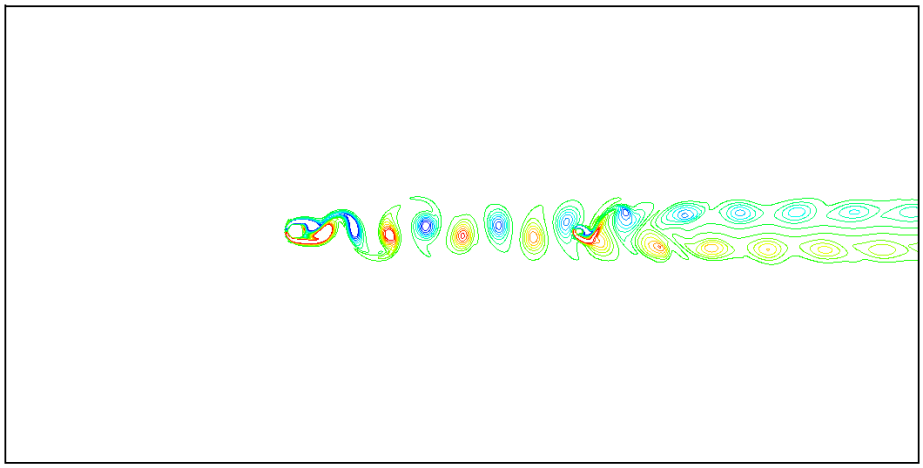

(e) unscreened

Figure 4-4 Vorticity contours of flow field (Re = 500, 0.5D case)

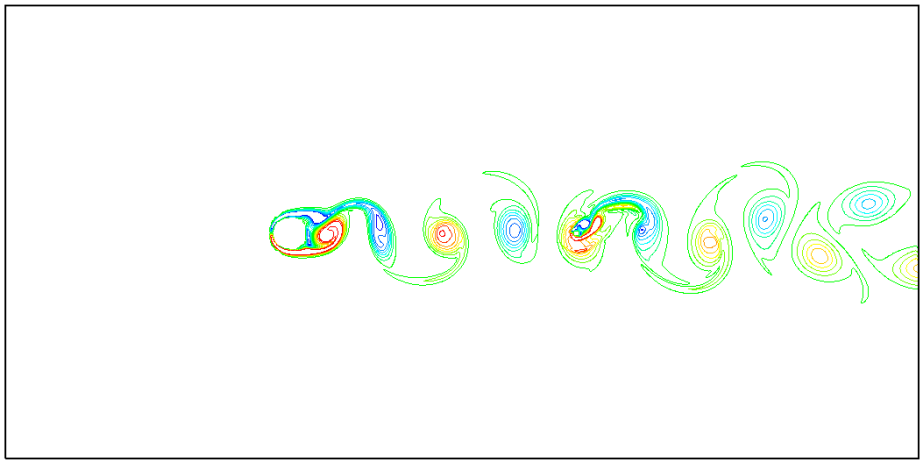

(a) σ = 34 Pa·s/m^2

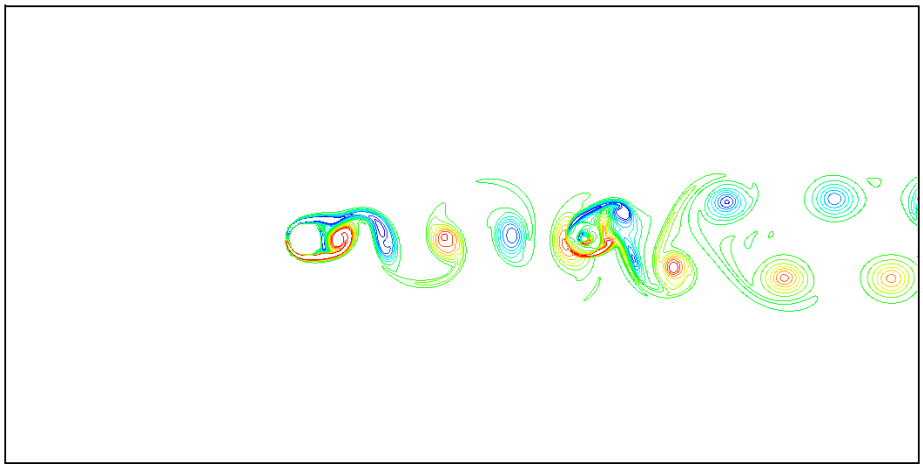

(b) σ = 340 Pa·s/m^2

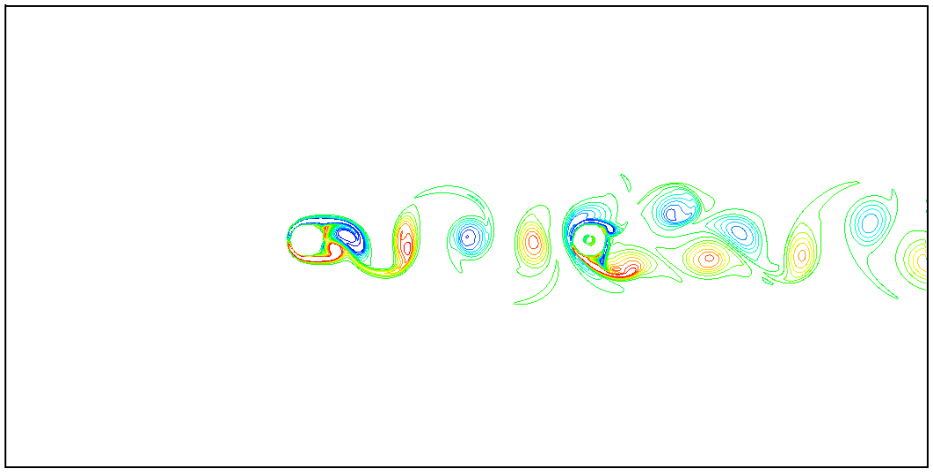

(c) σ = 3400 Pa·s/m^2

(d) σ = 34000 Pa·s/m^2

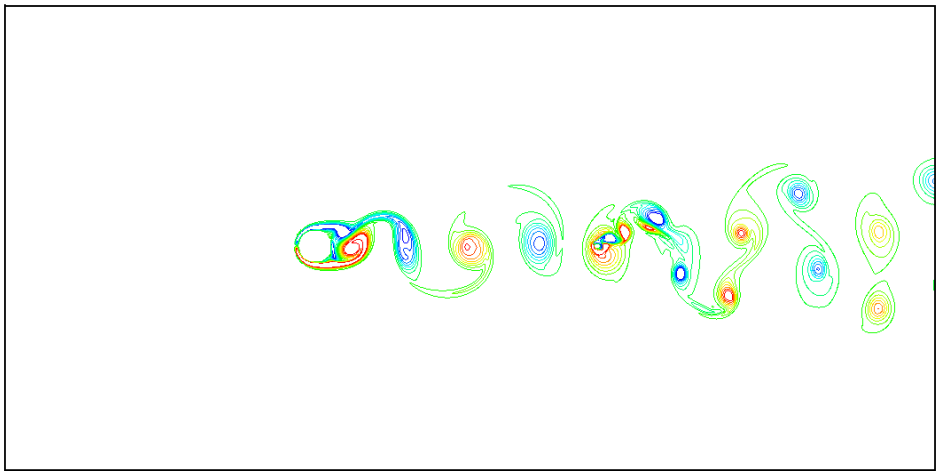

(e) unscreened

Figure 4-5 Vorticity contours of flow field (Re = 500, 1.0D case)

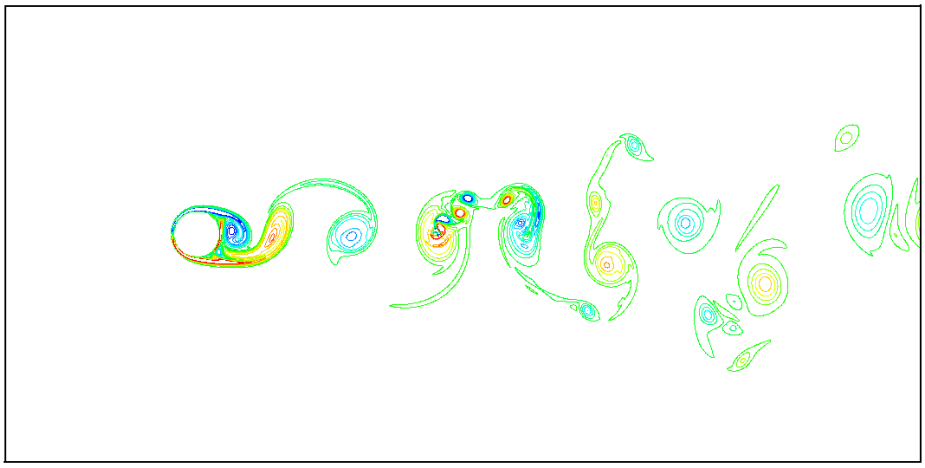

(a) σ = 34 Pa·s/m^2

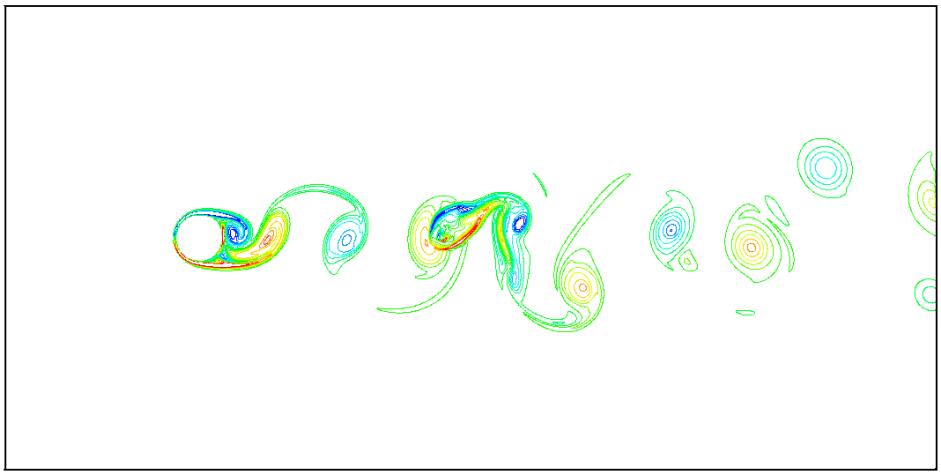

(b) σ = 340 Pa·s/m^2

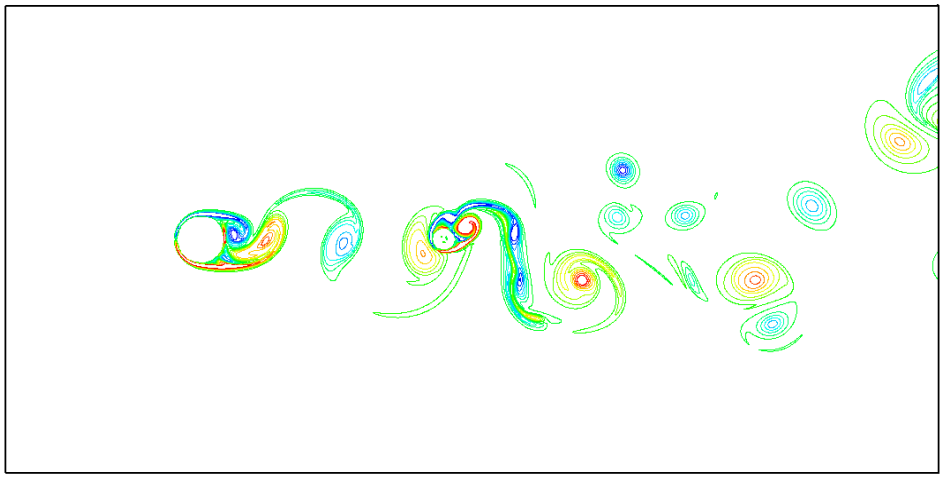

(c) σ = 3400 Pa·s/m^2

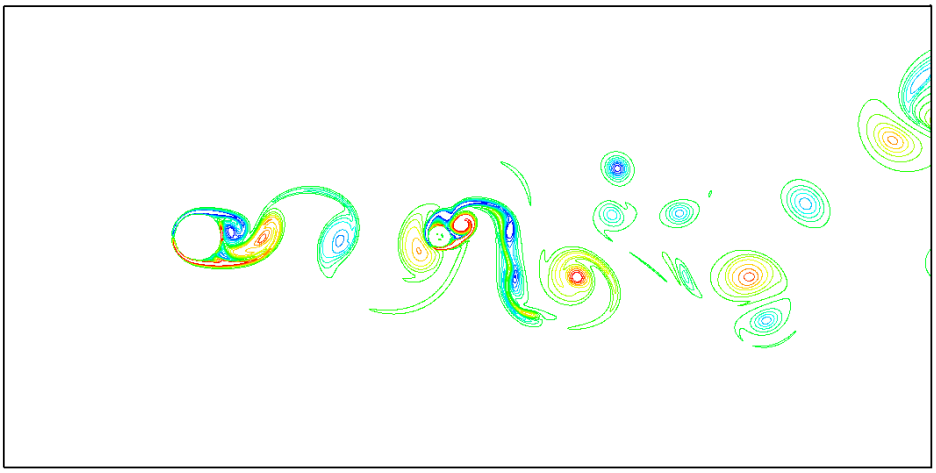

(d) σ = 34000 Pa·s/m^2

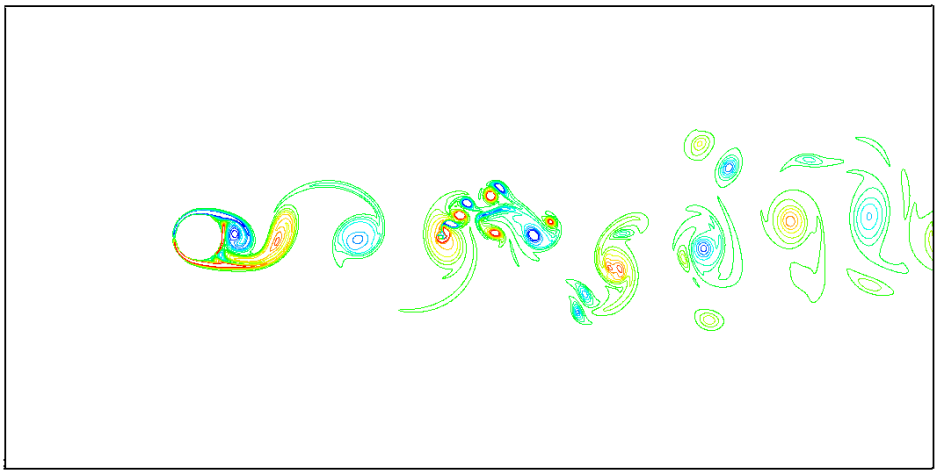

(e) unscreened

Figure 4-6 Vorticity contours of flow field (Re = 500, 2.0D case)

Figure 4-7 shows pressure histories at a downstream point after the upstream solid cylinder (σ = 340 Pa·s/m^2), specifically 4D away from the center of the upstream cylinder center. The four curves are for four different upstream cylinder size cases. The time histories show that each case reaches the steady state. Ostensibly, the smallest cylinder (0.2D) generates the highest frequency, and the largest cylinder (2.0D) generates the lowest frequency. Meanwhile, the power spectrum density (PSD) comparison is in Figure 4-8 clearly shows that the larger upstream cylinder generates smaller frequency perturbations in the flow field. The peak dimensionless

frequencies, for the cases of 0.2D, 0.5D, 1.0D, and 2.0D, are respectively 1.8, 0.9, 0.5, and 0.25, resulting in a Strouhal number (f D/U) ranging from 0.36 to 0.5. Also notable is that a larger upstream cylinder generates a higher magnitude of PSD because this cylinder has larger vortical structures (also shown in Figures 4-3 through 4-6). We also found that the same size upstream cylinder size generates almost the same downstream vortical structures regardless of the flow resistivity of the downstream windscreen cylinder. Therefore, with sufficient separation distance in this study, the upstream turbulence is not altered by the downstream condition.

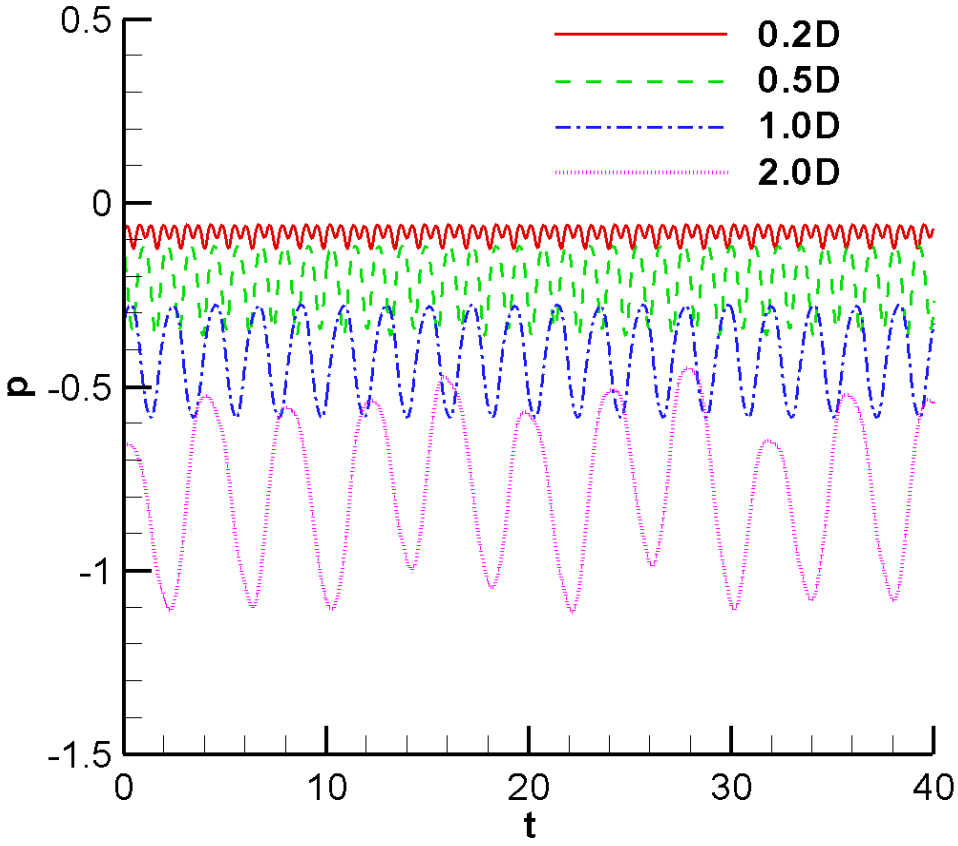

Figure 4-7 Pressure time histories of a downstream point of the first solid cylinder with a diameter of 0.2D, 0.5D, 1D, and 2D (The measurement point is 4D away from the first cylinder center, all values are dimensionless)

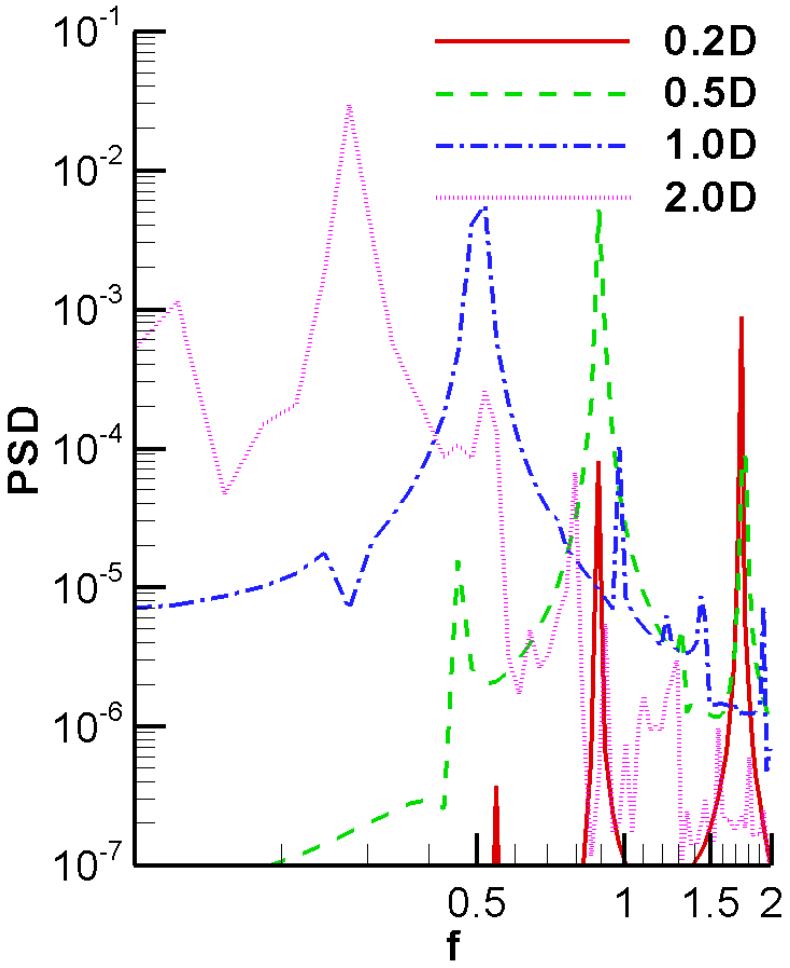

Figure 4-8 PSD of a downstream point of the first solid cylinder with a diameter of 0.2D, 0.5D, 1D, and 2D (the measurement point is 4D away from the first cylinder center; all values are dimensionless)

Figure 4-9 shows the pressure history of the center point of the microphone (measurement point in Figure 4-1) for all upstream cylinder cases (0.2D, 0.5D, 1.0D and 2.0D case). Obviously, the fluctuation magnitude of the unscreened center pressure is the highest of all the windscreened cylinder cases, which means the windscreen reduces wind noise. Also, for a long-duration simulation, the pressure time history reaches at least a quasi-steady state, which will be convenient for pressure signal post-processing. When upstream cylinder diameter

increases, the pressure fluctuation magnitude also increases, but the frequency seems to decrease. This tendency also conforms to our previous results for downstream pressure of the first solid cylinder as shown in Figure 4-7. Assuming the pressure time history at the microphone center as *p (t)* and its power spectral density as S_p *(f)*, the sound pressure level (SPL) for wind noise on the microphone can be computed as:

$$SPL = 10\log_{10}\frac{f_r S_p(f)}{p_r^2} \qquad \begin{matrix} f_r = 1Hz \\ p_r = 20\mu Pa \end{matrix} \tag{4.1}$$

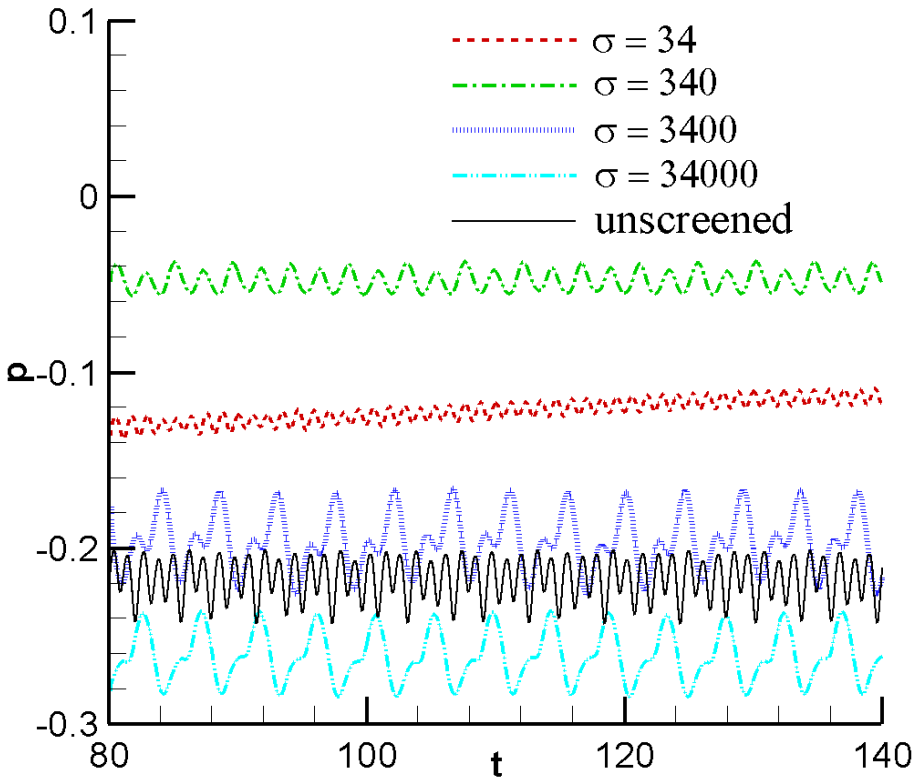

(a) 0.2D case

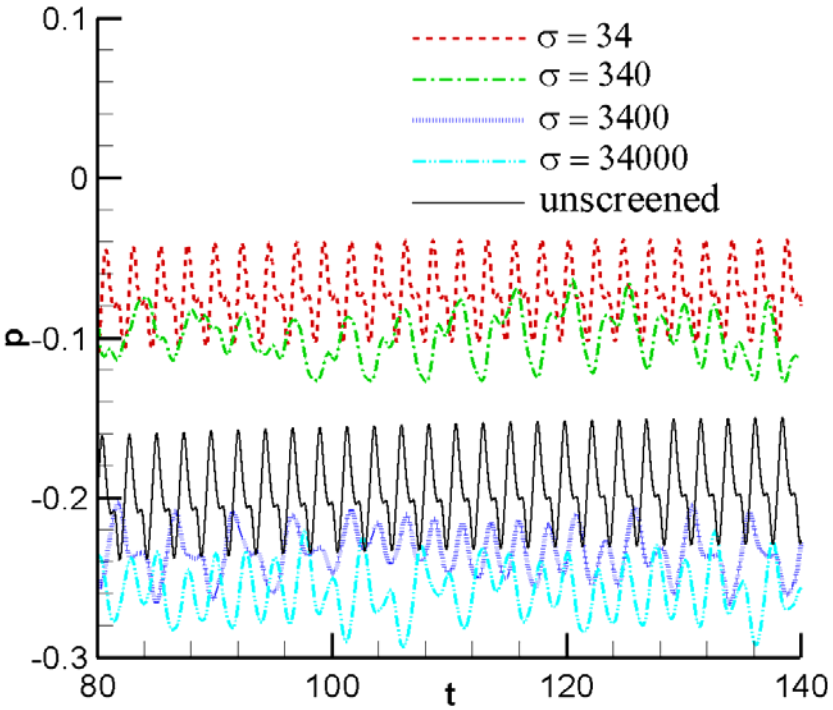

(b) 0.5D case

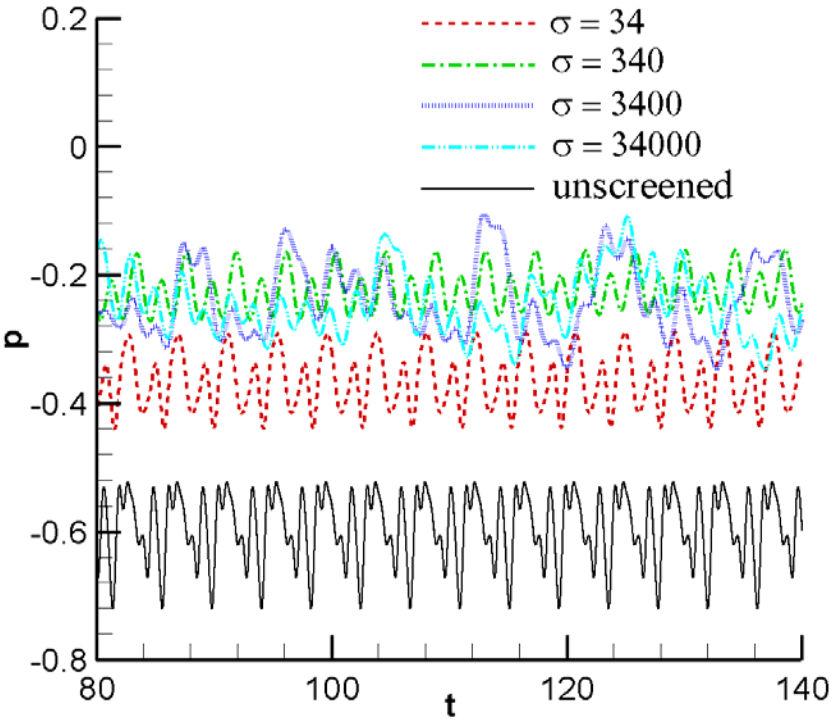

(c) 1.0D case

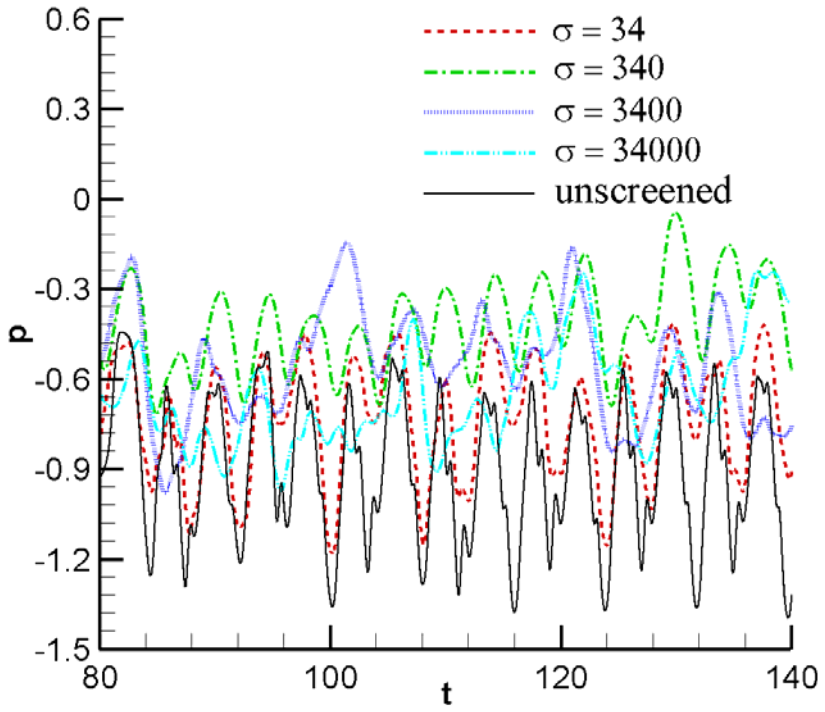

(d) 2.0D case

Figure 4-9 Pressure time histories at the center point of the microphone cylinder (all values are dimensionless, Re = 500)

Figure 4-10 shows the PSD of the pressure at the center of the windscreened microphone. It includes four different upstream cylinder cases (0.2D, 0.5D, 1.0D and 2.0D), and each case has five curves: one for the unscreened bare microphone case and the other four for the screened microphone with four different flow resistivities: 34, 340, 3400, and 34000 Pa·s/m^2 (corresponding to dimensionless values of 0.2, 2, 20 and 200, individually). Notably, all results showed in Figure 4-10 are dimensionless, which will be convenient for theoretical analysis. For case (a) with the upstream cylinder diameter 0.2D, it can be seen that the PSD with high flow resistivity (σ = 340, 3400 and 34000 Pa·s/m^2) is higher than that with the bare microphone case in the frequency range below 0.6, which means that there is no windscreen effect in this range. Furthermore, the windscreen is effective in the frequency range 0.75 to 2 for case (a). The most

distinctive PSD difference happens at the frequency of 0.85 and 1.9. An interesting finding here is that the high flow resistivity cases (σ = 340, 3400 and 34000 Pa·s/m^2) have some lower peak frequencies than the unscreened case, which is because the high flow resistivity porous windscreen is like a wall and has larger diameter than the unscreened microphone and will generate lower frequency turbulence than the unscreened microphone. For case (b) and case (c) with the upstream cylinder diameters 0.5D and 1.0D respectively, the two cases have similar windscreen effectiveness in the frequency range from 0.45 to 3. For case (d) with the upstream cylinder diameter 2.0D, the PSD shape trends are similar among all five curves and show windscreen effects in the frequency range from 0.8 to 3. Figure4-10 also shows that the PSD shape of the unscreened microphone case is very similar to that of the lowest windscreen flow resistivity case (σ = 34 Pa·s/m^2), which means that the low flow resistivity screen is similar to the unscreened (bare microphone) case.

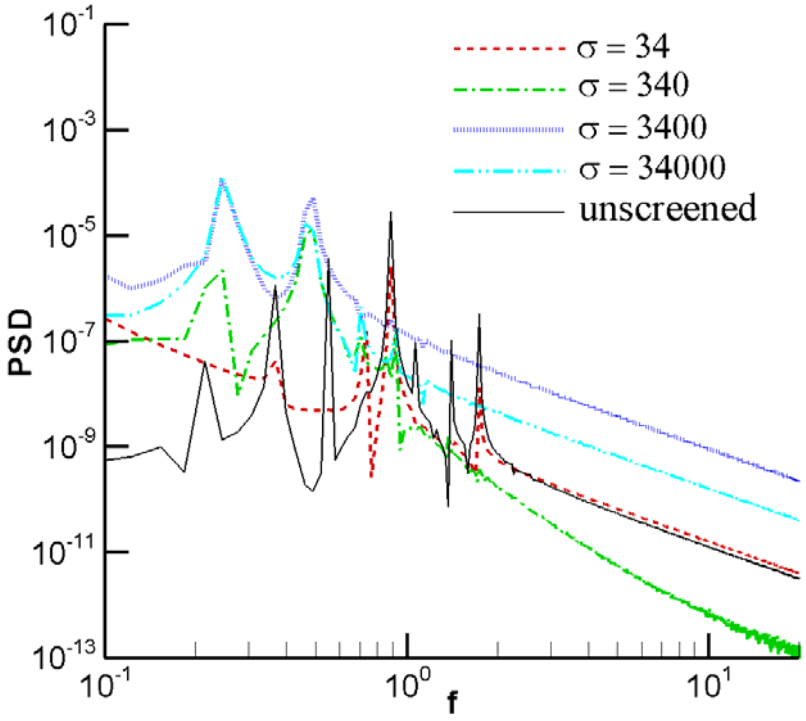

(a) 0.2D case

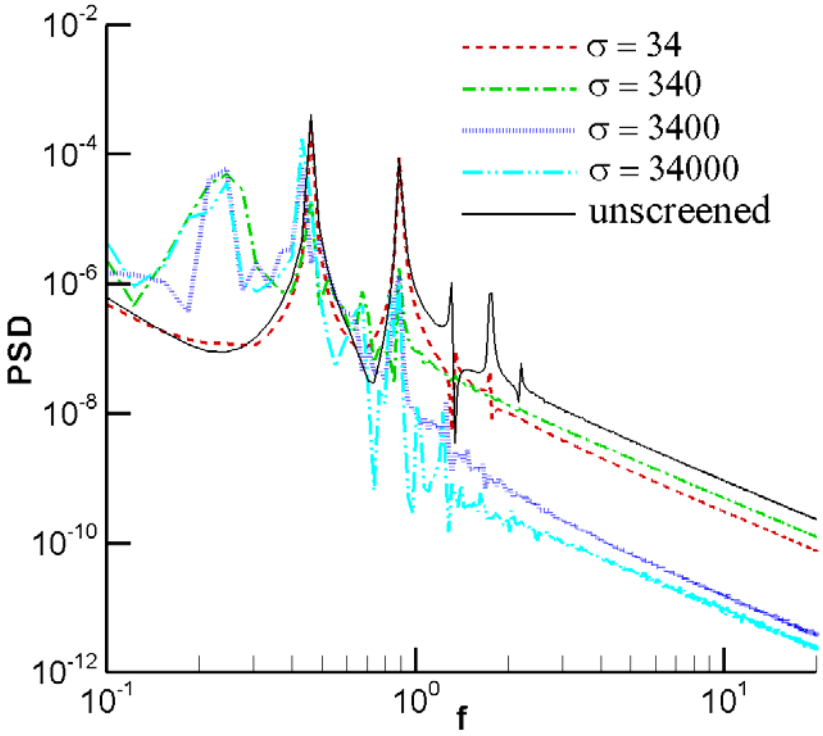

(b) 0.5D case

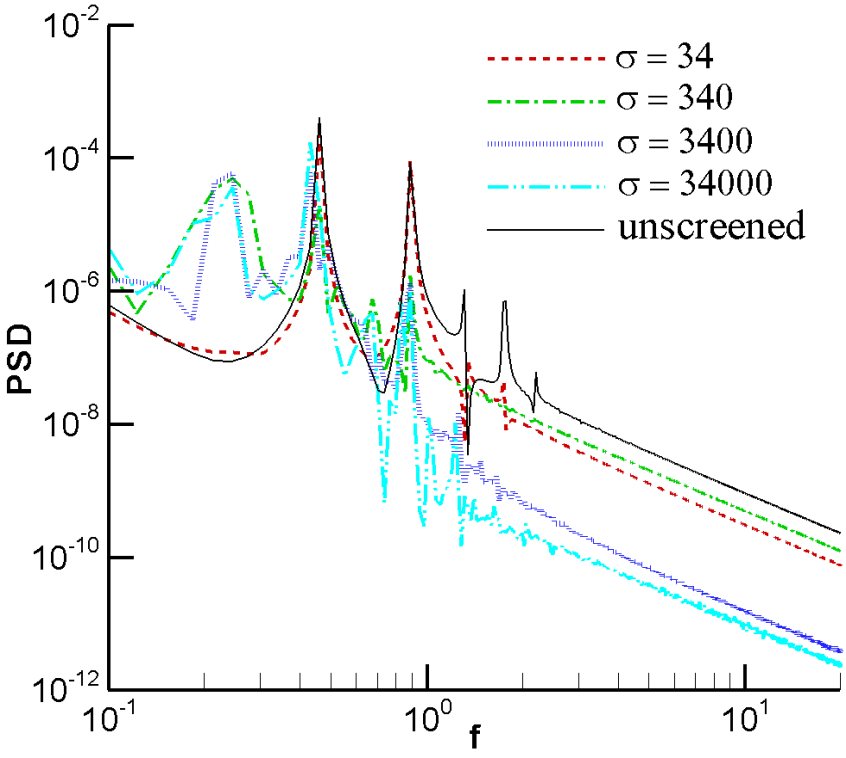

(c) 1.0D case

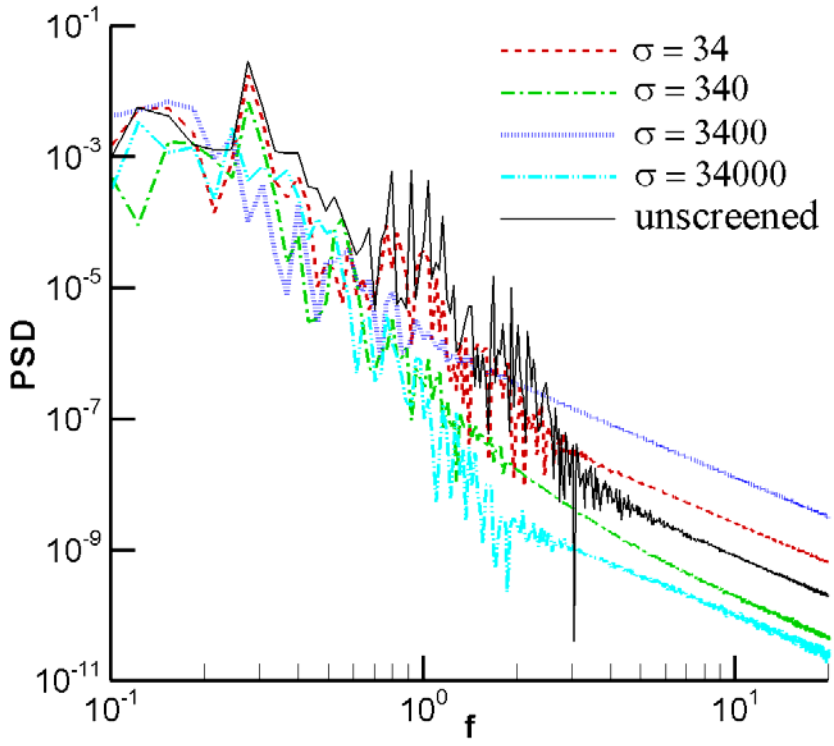

(d) 2.0D case

Figure 4-10 PSD at the center point of the microphone cylinder (all values are dimensionless, Re = 500)

Figure 4-11 shows the sound pressure level (SPL) at the center of the windscreened microphone which is calculated by Eq. (4.1). It has four different upstream cylinder cases (0.2D, 0.5D, 1.0D and 2.0D), and each case has five curves: one for the bare microphone case and the other four for the screened microphone cases with different flow resistivity: 34, 340, 3400, and 34000 Pa·s/m^2. It should be noted here that all the data in the Figure 4-11 are dimensional for real physical phenomena. For case (a) with the upstream cylinder diameter 0.2D, the SPL with large flow resistivity (σ = 340, 3400 and 34000 Pa·s/m^2) is higher than that with the bare microphone case in the frequency range below 80Hz, which means that there is no windscreen effect in this range. Also, the windscreen is effective in the range of 100Hz to 300Hz for case (a). Additionally, the remarkable SPL difference between the unscreened center and the screened

center lies at frequencies of 120Hz and 250Hz. For case (b) with the upstream cylinder diameter 0.5D, there are few windscreen effects below the frequency of 100Hz. but windscreen effects are in the range of 100Hz to 400Hz, especially at frequencies of 140Hz and 270Hz. For case (c) with the upstream cylinder diameter 1.0D, similar windscreen effects are as for case (b), with windscreens effective in the frequency range of 60Hz to 400Hz. For case (d) with the upstream cylinder diameter 2.0D, the SPL shape trend is not the same as for case (a), (b) and (c); instead, it shows more fluctuations at high frequencies, particularly, the windscreen effective at the frequencies of 70Hz to 300Hz. Figure 4-11 also shows that the SPL shape of the lowest windscreen flow resistivity case (σ = 34 Pa·s/m^2) is very similar to that of the unscreened microphone case, which means that the low flow resistivity screen is like the no windscreen (bare microphone) case.

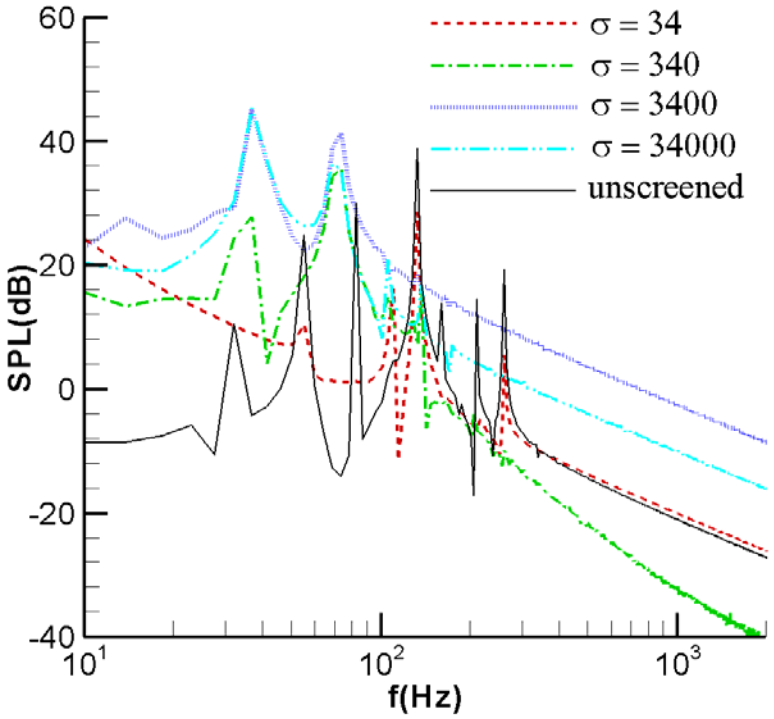

(a) 0.2D case

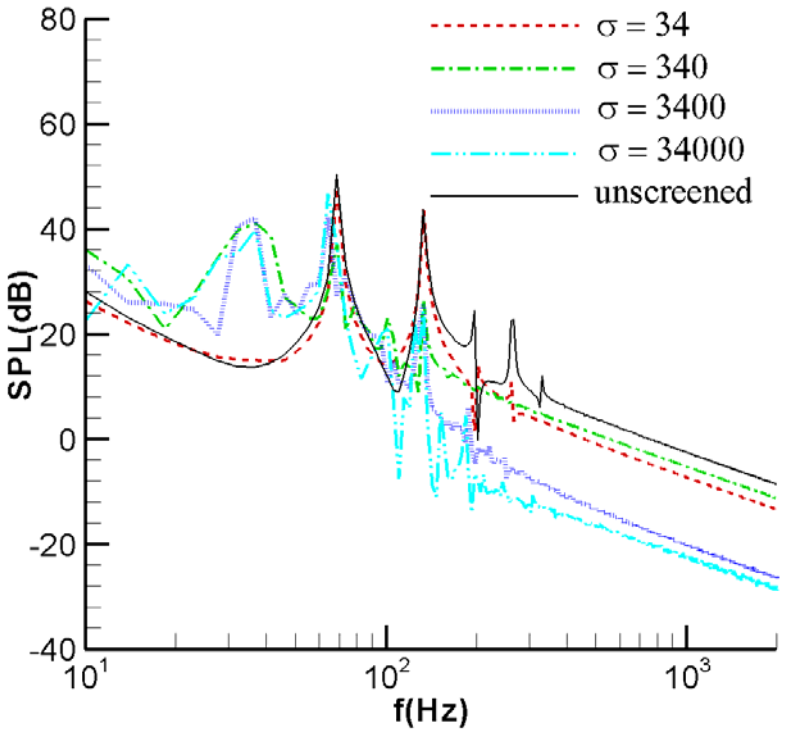

(b) 0.5D case

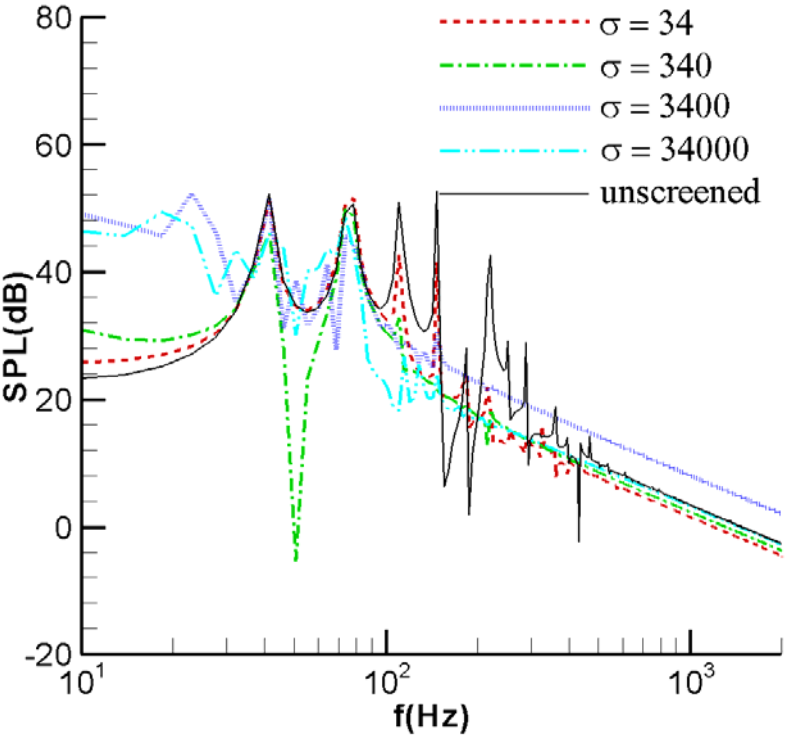

(c) 1.0D case

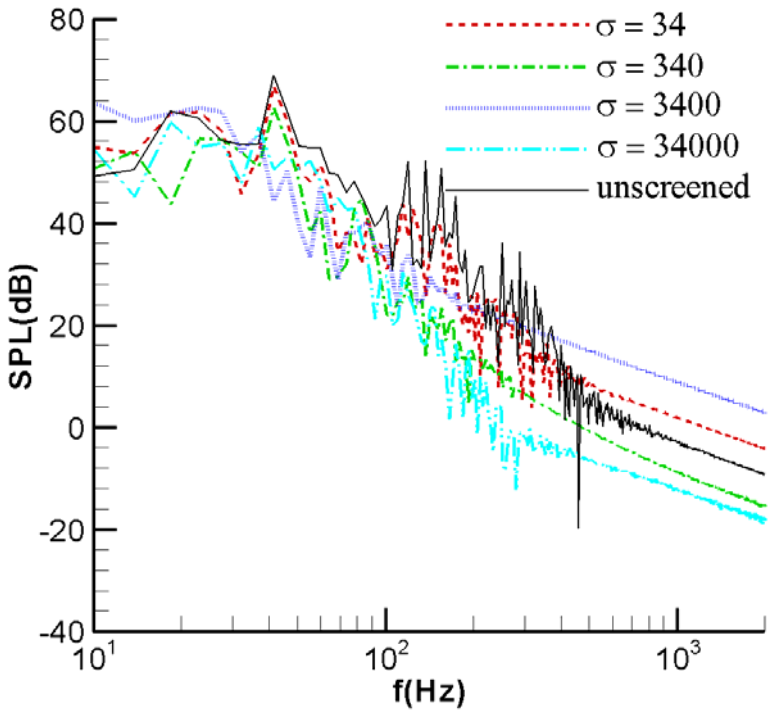

(d) 2.0D case

Figure 4-11 SPL at the center point of the microphone cylinder (a) 0.2D (b) 0.5D (c) 1.0D (d) 2.0D (all values are dimensional, Re = 500)

We further investigate wind noise reduction level (WNR) between the unscreened microphone and the screened microphone, $WNR = SPL_{unscreened\ \ center} - SPL_{screened\ \ center}$, by subtracting the SPL at screened microphone center from that at unscreened microphone center. Fig. 8 shows the WNR for four different upstream cylinder cases (0.2D, 0.5D, 1.0D and 2.0D), each with four curves showing results for the bare microphone minus results for each of the four screened microphones with varying flow resistivity (34, 340, 3400, 34000 Pa·s/m^2). It can be seen that the highest WNR is around 40dB, which is a very significant reduction. Clearly, the WNR between the unscreened microphone and the lowest flow resistivity (σ = 34 Pa·s/m^2, red dash line) case is smaller than the other three higher flow resistivity screens (σ = 340, 3400, 34000Pa·s/m^2). For Case (a), with the upstream cylinder diameter 0.2D, the

lowest flow resistivity windscreen (σ = 34 Pa·s/m^2) performs better around a few tens of H at 30-100 Hz, while the second lowest flow resistivity windscreen (σ =340 Pa·s/m^2) performs better around a few hundred Hz. For Case (b) with upstream cylinder diameter 0.5D, the medium flow resistivity windscreen (σ = 3400 Pa·s/m^2) performs better around 70 Hz and the highest flow resistivity windscreen (σ = 34000 Pa·s/m^2) performs better around a few hundred Hz. For Case (c) with upstream cylinder diameter 1.0D, the second lowest flow resistivity windscreen (σ = 340 Pa·s/m^2) performs better around 40 Hz, and the highest flow resistivity windscreen (σ = 34000 Pa·s/m^2) performs better at 100-200 Hz. For Case (d) with the upstream cylinder diameter 2.0D, the windscreen with σ = 340 Pa·s/m^2 is better around 20 Hz, the one with σ = 3400 Pa·s/m^2 does in the 50-60 Hz range, and the highest flow resistivity windscreen (σ = 34000 Pa·s/m^2) performs better in the 100-300 Hz range.

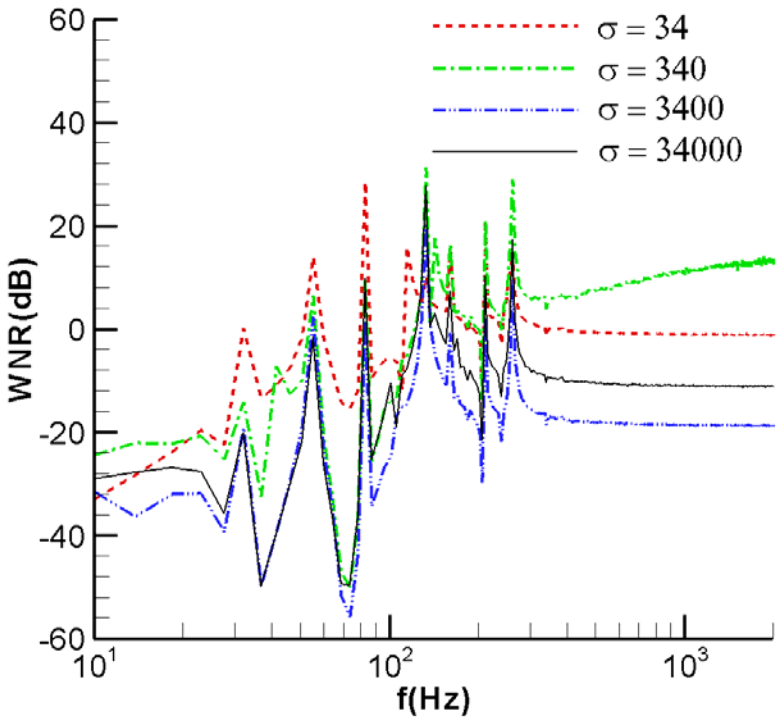

(a) 0.2D case

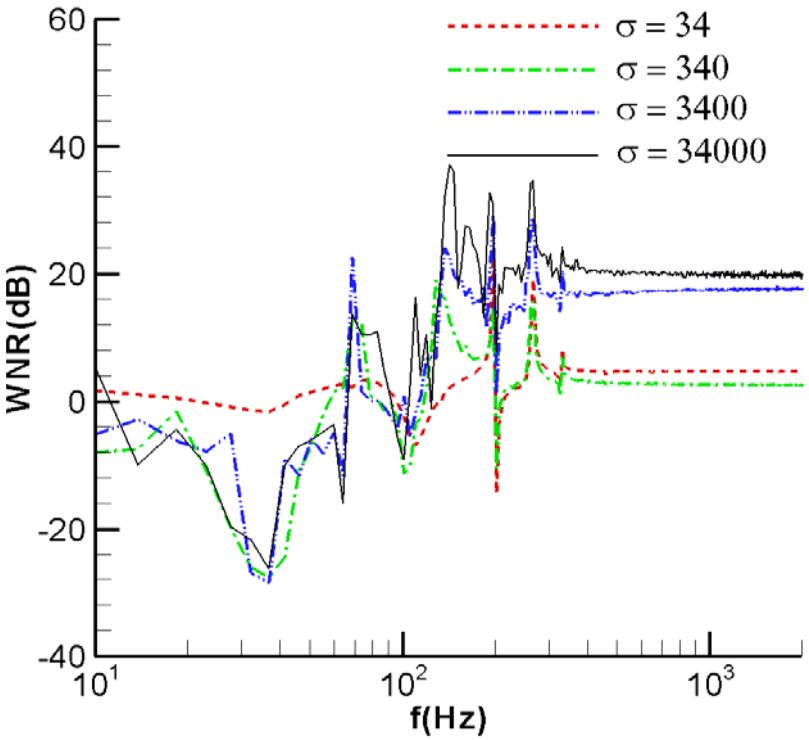

(b) 0.5D case

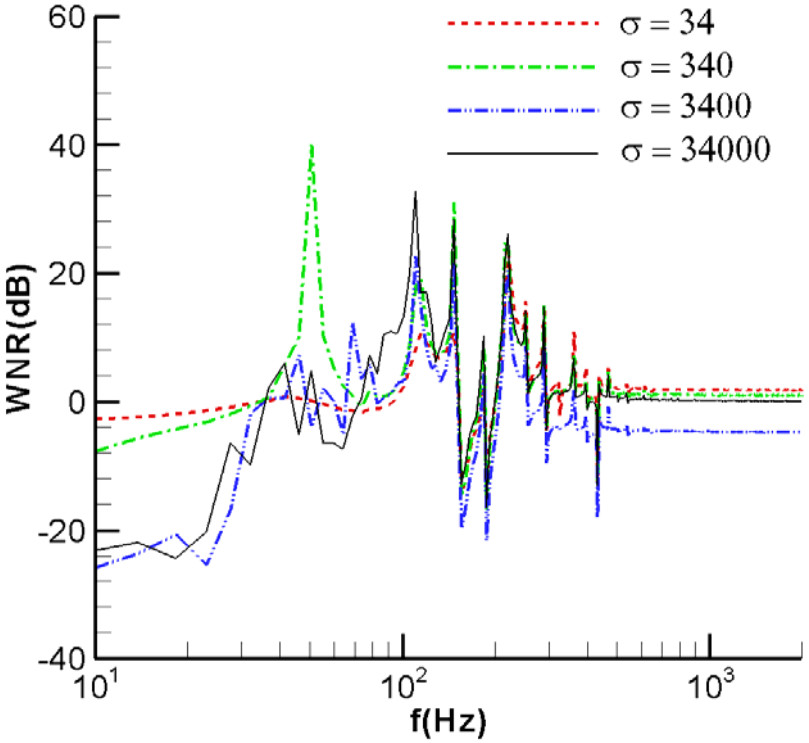

(c) 1.0D case

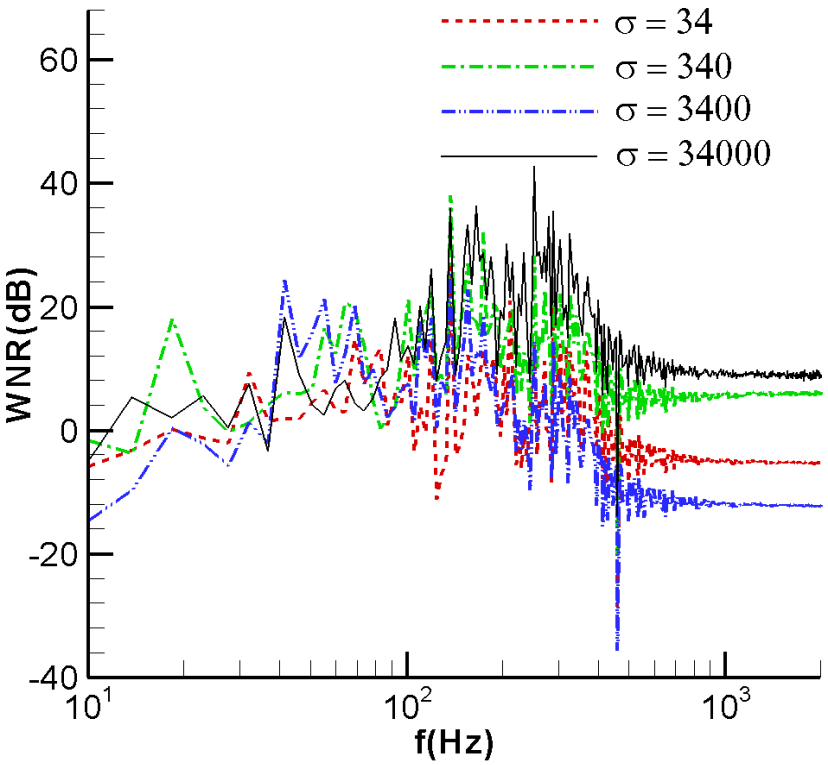

(d) 2.0D case

Figure 4-12 WNR between the unscreened microphone center and the screened microphone center (a) 0.2D (b) 0.5D (c) 1.0D (d) 2.0D (all values are dimensional, Re500)

To clarify the quantitative value for the wind noise reduction between the unscreened microphone center and the screened microphone center, Table 4-1 shows the most significant sound level reductions, the four sub-tables each define one case (0.2D, 0.5D, 1.0D and 2.0D cases). It should be noted that the symbol "-" used in Table 4-1 means negative values (no windscreen effects).

Table 4-1 WNR between the unscreened microphone center and the screened microphone center (2D cases, Re = 500)

(a) 0.2D case

Resistivity (Pa·s/m^2) / Frequency(Hz)	34	340	3400	34000
82.4	28.7	9.3	2.5	9.7
132.8	16.1	16.4	20.3	27.8
210.6	19.1	21.2	-	10.4
260.9	13.7	29.2	9.7	17.4

(b) 0.5D case

Resistivity (Pa·s/m^2) / Frequency(Hz)	34	340	3400	34000
73.2	3.4	12.9	22.7	13.7
141.9	2.7	19.1	24.1	37.0
196.8	22.9	15.1	29.2	32.8
265.5	19.2	15.8	28.9	34.7

(c) 1.0D case

Resistivity (Pa·s/m^2) / Frequency(Hz)	34	340	3400	34000
114.4	10.7	19.3	22.7	32.7
146.5	10.8	31.1	21.8	28.3
219.7	24.3	24.8	20.5	26.1
251.8	15.8	13.7	8.7	14.1

(d) 2.0D case

Resistivity (Pa·s/m^2) / Frequency(Hz)	34	340	3400	34000
119.0	14.8	22.5	18.3	26.1
137.3	26.6	38.1	25.7	35.9
251.8	14.1	28.3	14.5	42.6
366.2	13.0	16.4	-	24.8

Given that the real wind turbulence is a high Reynolds number flow composed of vortical structures spanning a large range of sizes, combining the four different upstream cylinder cases together yields the average WNR level for different levels of turbulence for each windscreen flow resistivity. The average WNR is computed as the arithmetic average of the WNR values from the four cases in Figure 4-12. Figure 4-13 shows the average wind noise reduction between the unscreened microphone and the screened microphone, where for the low flow resistivity (σ = 34 Pa·s/m^2), the highest WNR levels are about 7 dB at 80 Hz and 6dB at 300 Hz. For the second lowest flow resistivity (σ = 340 Pa·s/m^2), the highest WNR levels are about 6 dB at 50Hz, about 14 dB at 120Hz, and about 12dB at 300 Hz. For the medium flow resistivity (σ = 3400 Pa·s/m^2), the high WNR levels are about 10 dB at 120Hz, and 8 dB at 300 Hz. For the highest flow resistivity (σ = 34000 Pa·s/m^2), the highest WNR levels are about 16 dB at 120Hz and 14 dB at 300 Hz. This means that at the low frequency range (less than 100 Hz), windscreens of low flow resistivity are effective in reducing noise, while those with high flow resistivity are not. At the high frequency range (great than 100Hz), windscreens with high flow resistivity give more WNR than those with low flow resistivity.

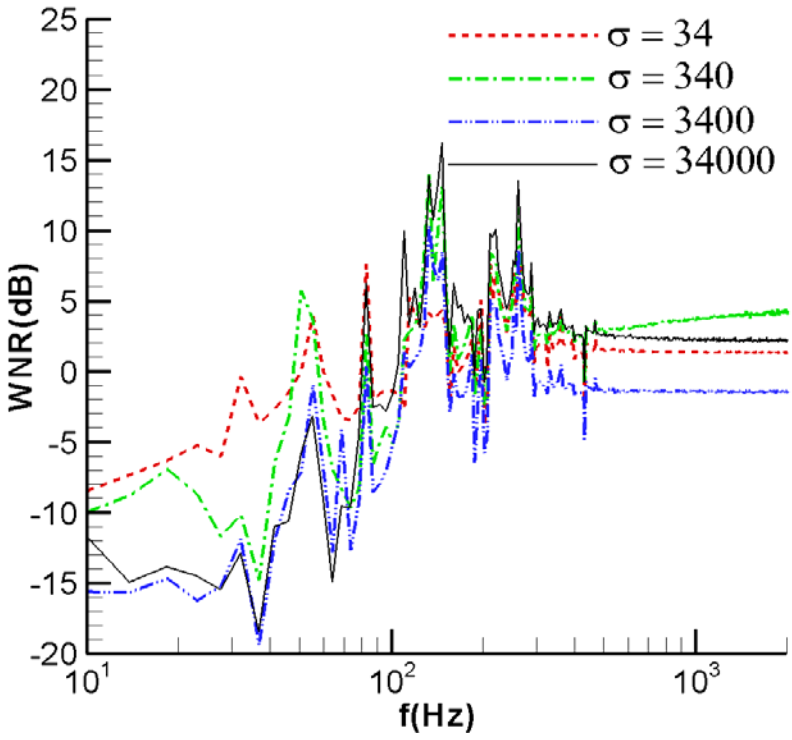

Figure 4-13 Average WNR between the unscreened microphone center and the screened microphone center (all values are dimensional, Re = 500)

4.3 High Reynolds Number (Re5000) Cases

For the cases with a high Reynolds number, $\mathrm{Re} = \frac{UD}{\nu} = \frac{1m/s \cdot 0.075m}{1.5 \times 10^{-5} m^2/s} = 5000$,

approximately characterizes a windscreen with a diameter of 7.5cm and a wind speed of 1m/s for the incoming air. Also, a bare microphone (unscreened) was set with diameter of 1.875cm. Next, four chosen values of dimensionless flow resistivity of the windscreen, 0.2, 2, 20 and 200, correspond to approximately 3.4, 34, 340 and 3400 Pa·s/m^2 of dimensional flow resistivity, respectively ($\sigma = \frac{\rho U}{D} = \frac{1.27kg/m^3 \cdot 1m/s}{0.075m} = 17 P_a \cdot s/m^2$). In this simulation, the grid size is 0.025 in both the x and y direction, and the time step is 0.0002 which satisfies the stability condition (detailed information see Zhang and Zheng, 2006).

For high Reynolds number cases (Re = 5000), it's more physical compared with Low Reynolds number (Re = 500) cases because high Reynolds number flow is more like a turbulence than low Reynolds number flow. This section has three different upstream cylinders 0.5D (Case (a)), 1.0D (Case (b)) and 2.0D (Case (c)) cases. As for the 0.2D case, the relative Reynolds number for the upstream cylinder is $\mathrm{Re} = \frac{UD}{\nu} = \frac{1m/s \cdot 0.2 * 0.075m}{1.5 \times 10^{-5} m^2/s} = 1000$. It is more the like laminar case, so we omitted the 0.2D case.

We first investigated the whole flow field as shown by vorticity contours in Figures 4-14 through 4-16 for the flow resistivity (σ = 3.4, 34, 340 and 3400 Pa·s/m^2 and also unscreened) with different upstream cylinder sizes (0.5D, 1.0D and 2.0D cases). The red color in the figures represents positive vorticity (in the counter clockwise sense, with the upper limit value of 10), the blue color represents negative vorticity (in the clockwise sense, with the lower limit value of -10). Clearly, the smaller upstream cylinders generate smaller but denser vortical structures compared with the larger upstream cylinders. Also, there is no flow inside the solid bare microphone, but some flow infiltrates the windscreened porous cylinder. When the flow resistivity reaches high enough values (σ = 3400 Pa·s/m^2) little flow permeates in the porous cylinder, similar to flow over the unscreened bare cylinder. With the flow resistivity very low, the flow permeates the porous cylinder as if the walls do not exist. Finally the flow field of the 0.5D case is much steadier than that of the 1.0D case and the 2.0D case. The reason is that the relative Reynolds number of 0.5D is $\mathrm{Re} = \frac{UD}{\nu} = \frac{1m/s \cdot 0.5 * 0.075m}{1.5 \times 10^{-5} m^2/s} = 2500$, while the relative Reynolds number of 2.0D is $\mathrm{Re} = \frac{UD}{\nu} = \frac{1m/s \cdot 2 * 0.075m}{1.5 \times 10^{-5} m^2/s} = 10000$, so Figure 4-16 shows more vortex fluctuation that does Figure 4-14 or Figure 4-15.

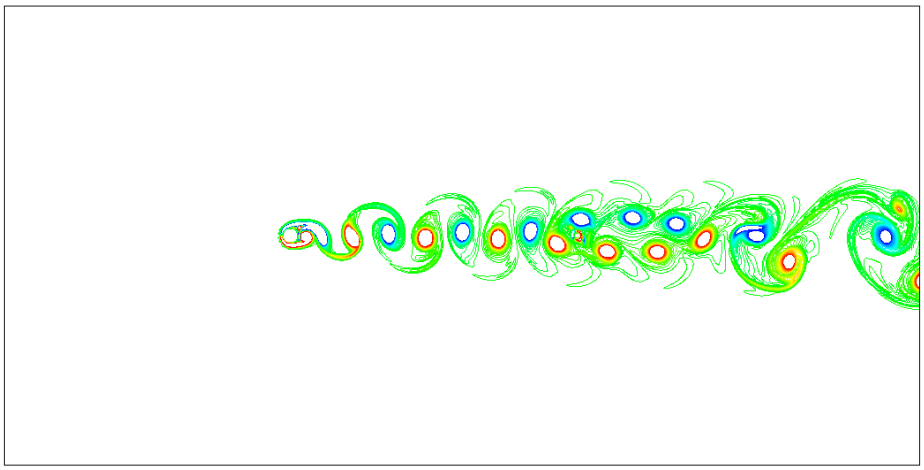

(a) σ = 3.4 Pa·s/m^2

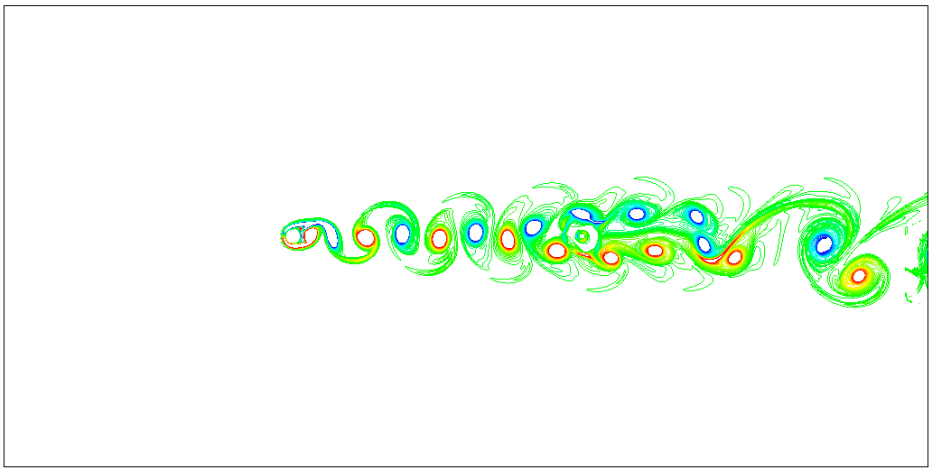

(b) σ = 34 Pa·s/m^2

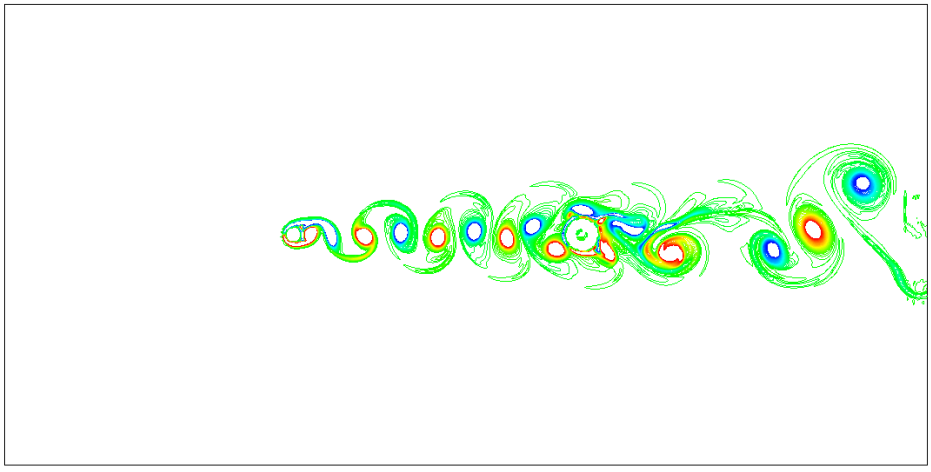

(c) σ = 340 Pa·s/m^2

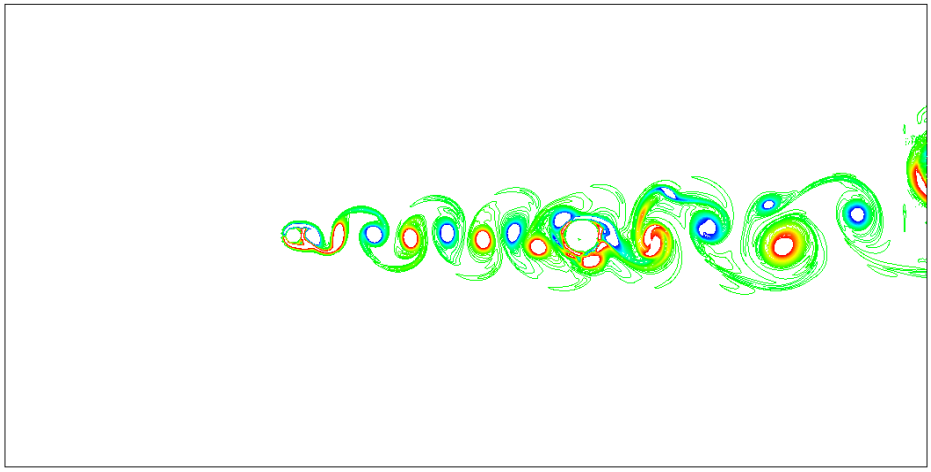

(d) σ = 3400 Pa·s/m^2

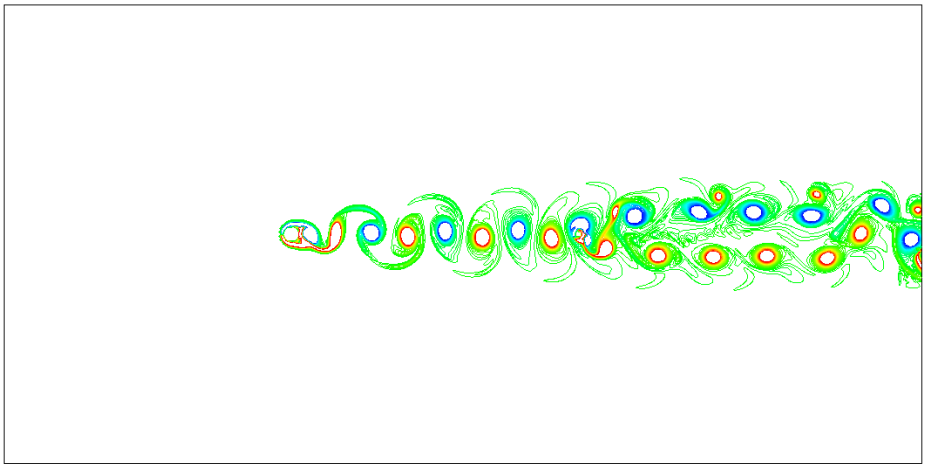

(e) unscreened

Figure 4-14 Vorticity contours of flow field (Re = 5000, 0.5D case)

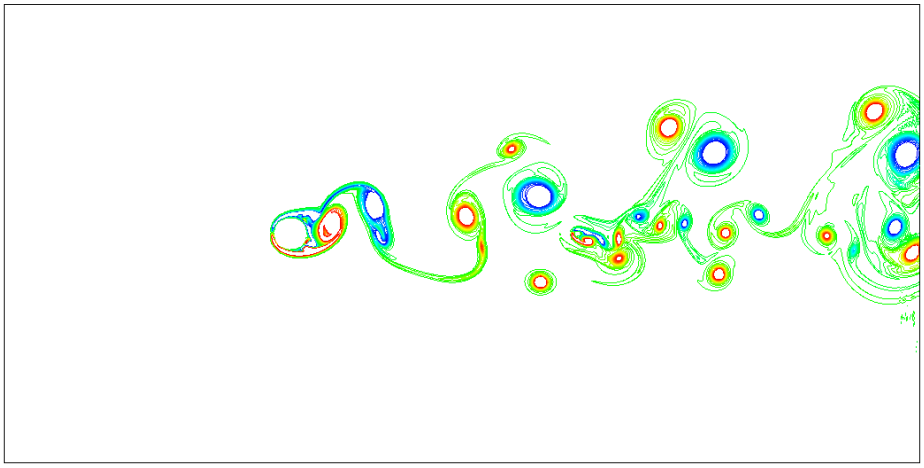

(a) σ = 3.4 Pa·s/m^2

(b) σ = 34 Pa·s/m^2

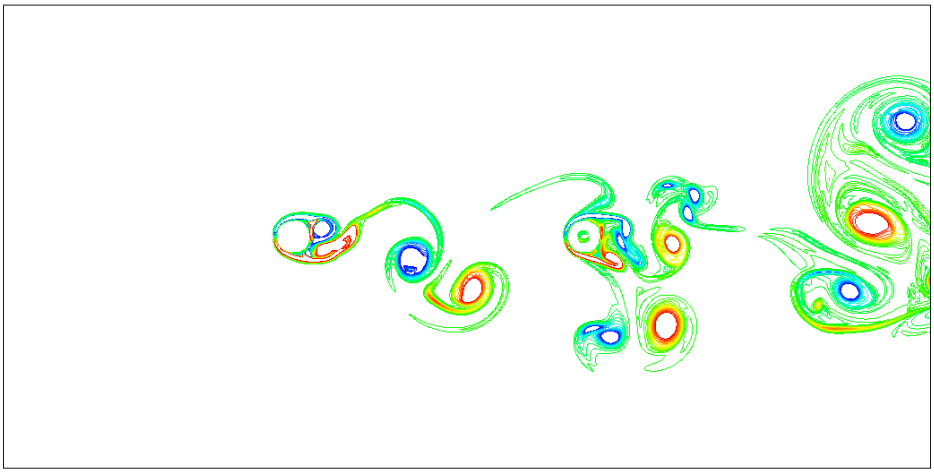

(c) σ = 340 Pa·s/m^2

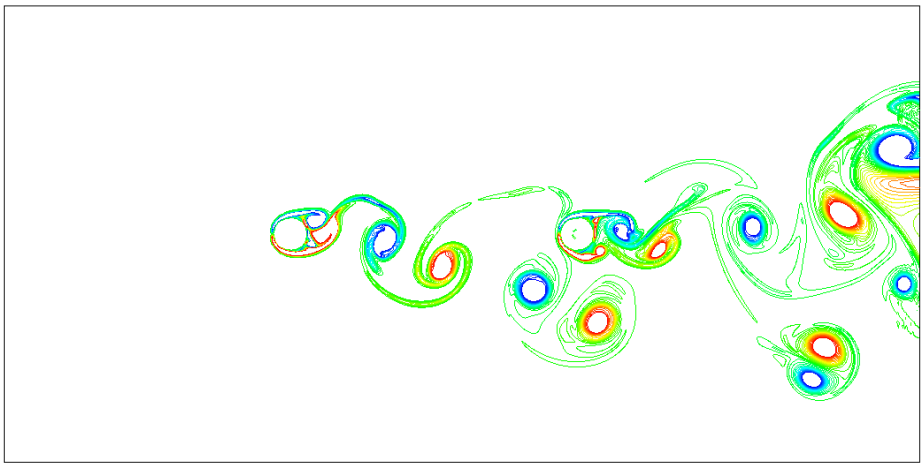

(d) σ = 3400 Pa·s/m^2

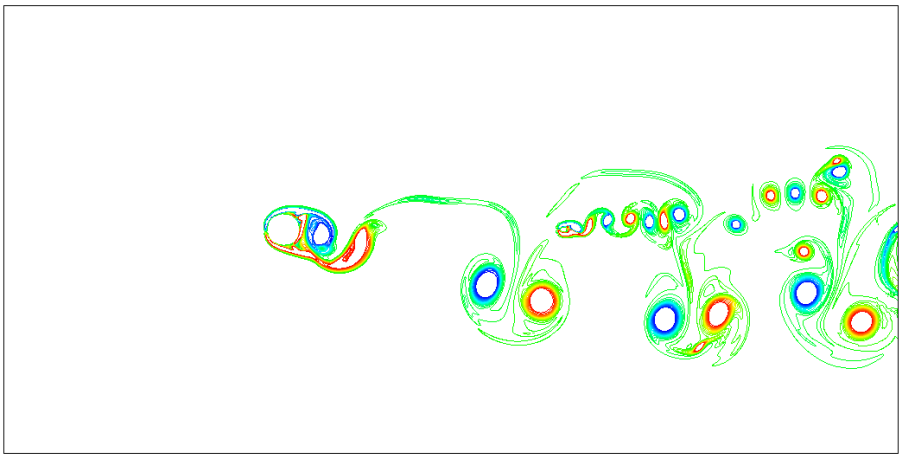

(e) unscreened

Figure 4-15 Vorticity contours of flow field (Re = 5000, 1.0D case)

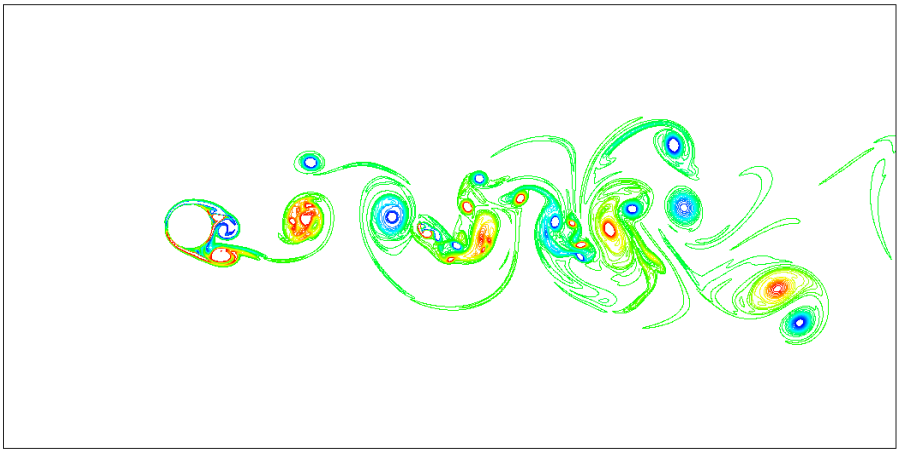

(a) σ = 3.4 Pa·s/m^2

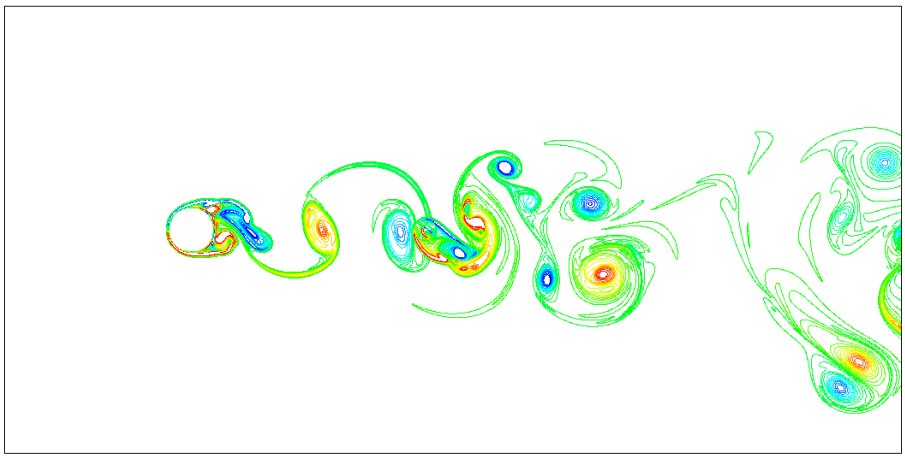

(b) σ = 34 Pa·s/m^2

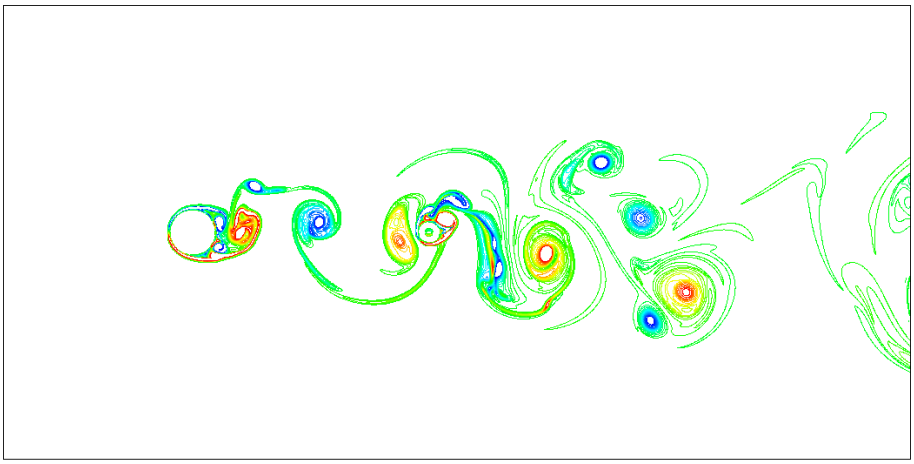

(c) σ = 340 Pa·s/m^2

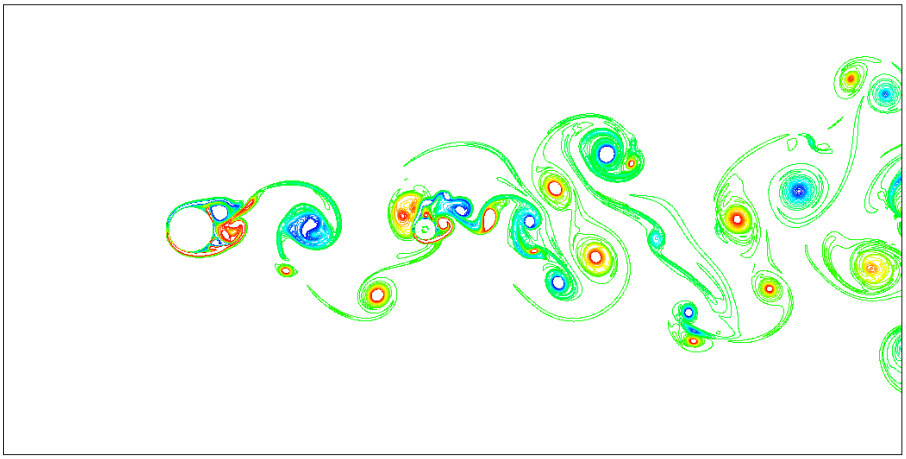

(d) σ = 3400 Pa·s/m^2

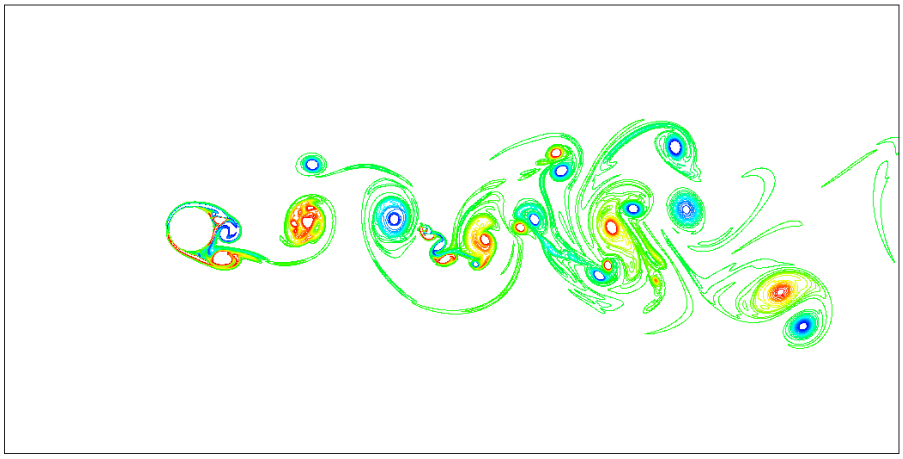

(e) unscreened

Figure 4-16 Vorticity contours of flow field (Re = 5000, 2.0D case)

Figure 4-17 shows the pressure time history of a downstream point of the first solid cylinder (4D far away from the center of the upstream solid cylinder) for all three cases (0.5D, 1.0D and 2.0D case). All five lines (each line represents one specific flow resistivity) behave similarly, which means the incoming vortex structure and intensity generated by the first solid cylinder is steady and consistent even though the downstream porous windscreens are different. Thus Figure 4-17 reveals greater fluctuations as the diameter of the upstream solid cylinder increases (which means the relative Reynolds number for the upstream cylinder is bigger as the diameter increases).

Figure 4-18 shows the pressure time history of the center point of the microphone, which reveals that the fluctuation magnitude of the unscreened bare microphone center pressure is higher than those of the windscreened microphone cases; this is the same trend as for those with previous low Reynolds number cases (Re = 500), although the trend is not so distinct as low Reynolds number cases. Also, for a long-duration simulation, the pressure time history reaches an almost quasi-steady state, but it looks more disturbing and chaotic than for previous low Reynolds number cases. For 2.0D cases, the pressure time history is more unstable and chaotic than for the1.0D case and the 0.5D case because the relative Reynolds number of the first solid cylinder increases (for 2.0D case, the relative Re = 10000; for 1.0D case, the relative Re = 5000; for 0.5D case, the relative Re = 2500) . Meanwhile, when the diameter of the upstream solid cylinder increases, the pressure fluctuation magnitude also increases, but the frequency seems to decrease.

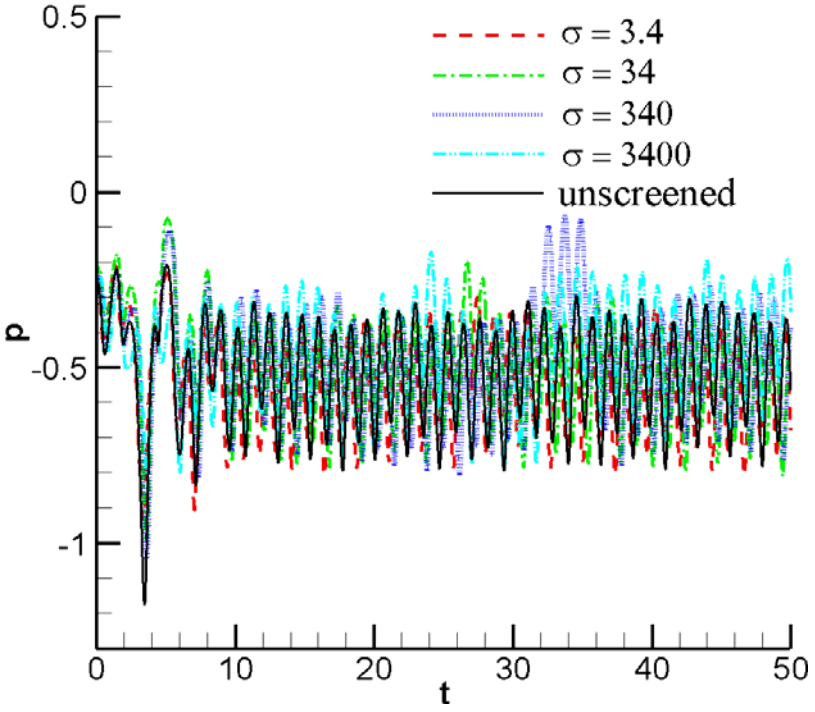

(a) 0.5D case

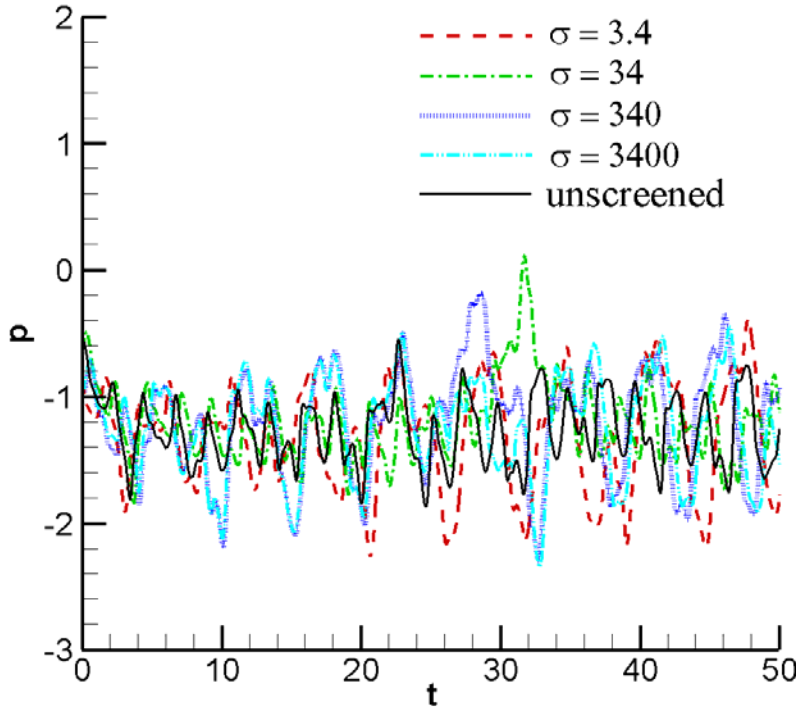

(b) 1.0D case

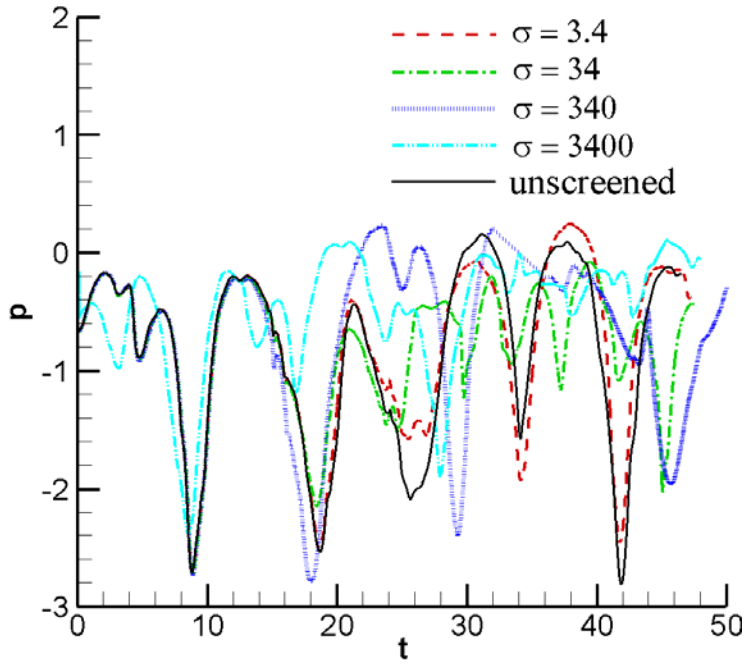

(c) 2.0D case

Figure 4-17 Pressure time histories at a downstream point of the first solid cylinder (The measurement point is 4D away from first cylinder center, all values are dimensionless, Re = 5000)

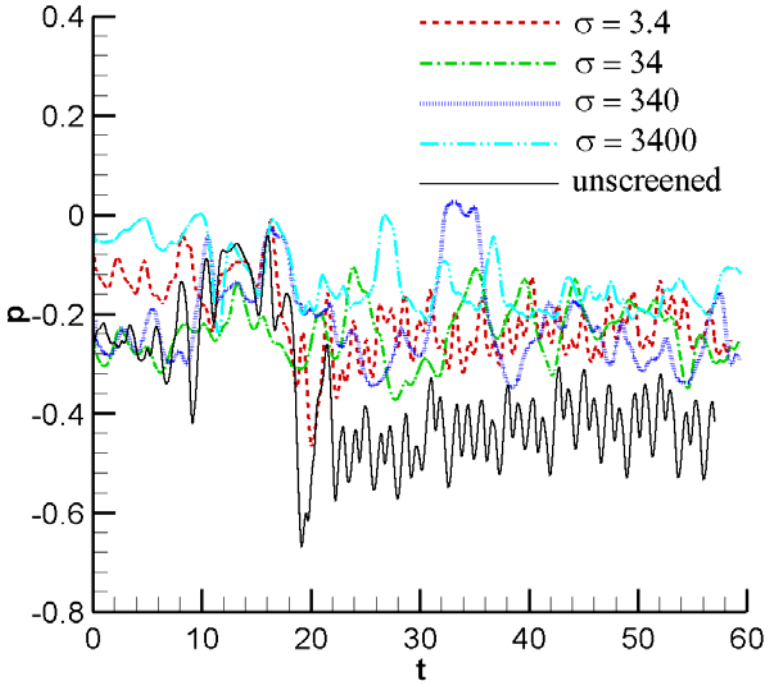

(a) 0.5D case

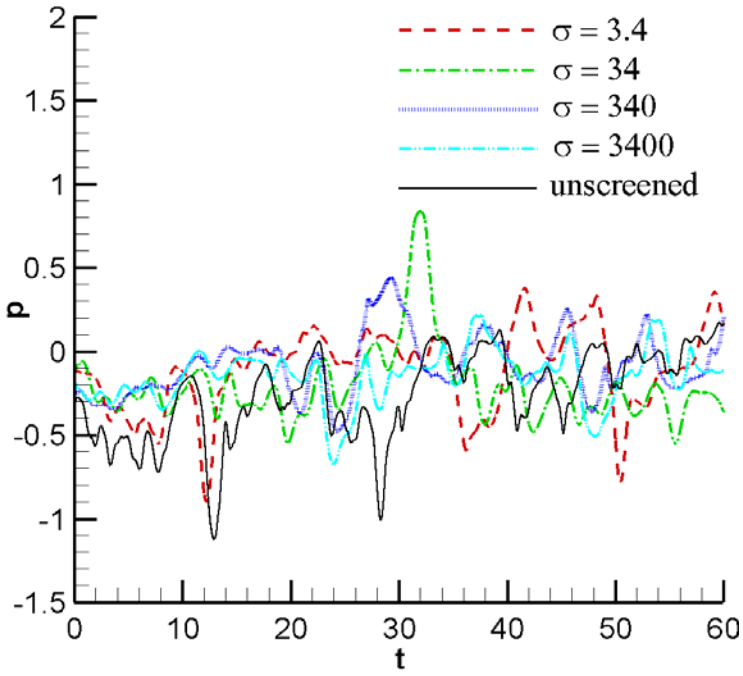

(b) 1.0D case

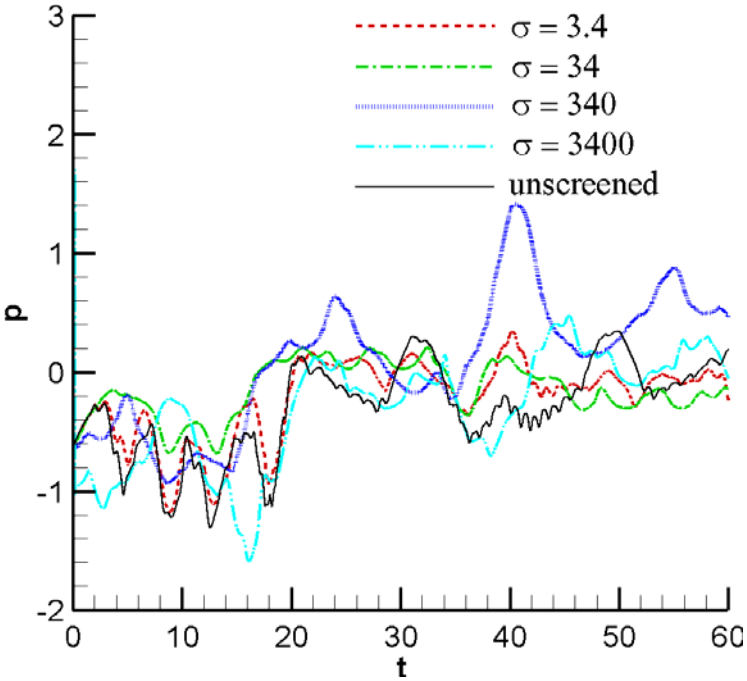

(c) 2.0D case

Figure 4-18 Pressure time histories at the center point of microphone cylinder (all values are dimensionless, Re = 5000)

Figure 4-19 shows the pressure power spectral density (PSD) at the center of the microphone (as the pressure time history is chaotic and random, we will use window functions to compute the PSD, more detail can be seen in Appendix A). It includes three different upstream cylinder cases (0.5D, 1.0D and 2.0D), and each sub-figure has five curves: one for the unscreened bare microphone case and the other four for the screened microphone with different flow resistivities: 3.4, 34, 340, and 3400 Pa·s/m^2 (corresponding to dimensionless values 0.2, 2, 20 and 200, separately). It should be noted here that all results shown in Figure 4-19 are dimensionless which will be convenient for theoretical analysis. Compared with previous low Reynolds number cases (Re = 500), the PSD line here is steeper, and it is more like realistic atmospheric turbulence (broad band spectrum). For case (a) with the upstream cylinder diameter 0.5D, the PSD of the unscreened microphone case is higher than those of windscreened microphone cases in the frequency range from 0.3 to 5, which means that the windscreen effect applies in this frequency range. The most distinctive PSD difference happens at the frequency range from 1.2 to 3. Also for case (a) the smallest resistivity case (σ = 3.4 Pa·s/m^2) has a similar trend with the unscreened case. For case (b) with the upstream cylinder diameter 1.0D, the windscreen is effective in the frequency range from 1.0 to 4. While for case (c) with the upstream cylinder diameter 2.0D, the PSD shape trend is similar to that in case (b) and has the windscreen effects in the frequency range from 0.8 to 4. Finally, Figure 4-19 shows that the PSD shape of the unscreened microphone case is more similar to that of the lowest windscreen flow resistivity windscreen case (σ = 3.4 Pa·s/m^2) comparing to the other three high flow resistivity windscreen cases (σ = 34, 340, 3400 Pa·s/m^2), which means that the low flow resistivity screen is similar to the unscreened (bare microphone) case.

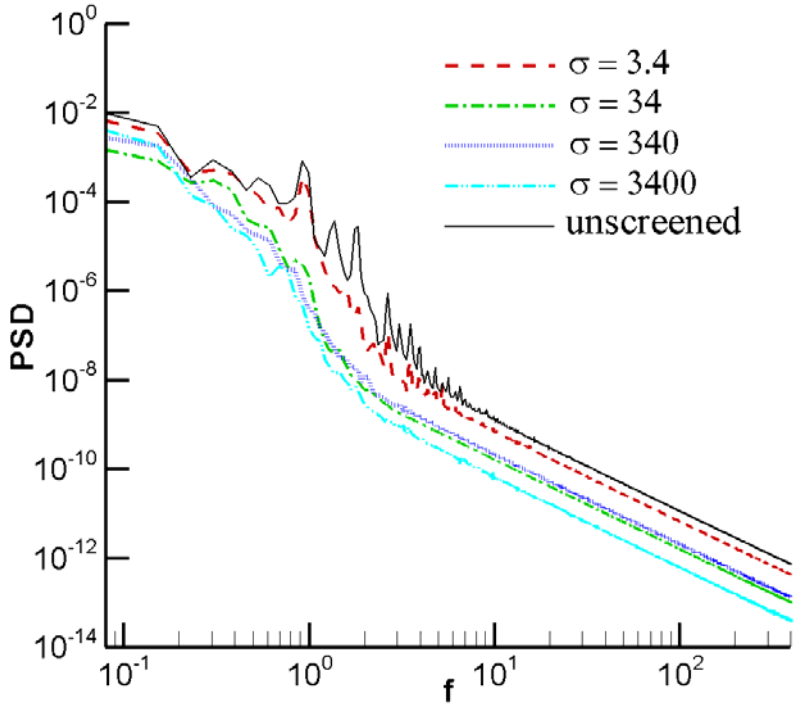

(a) 0.5D case

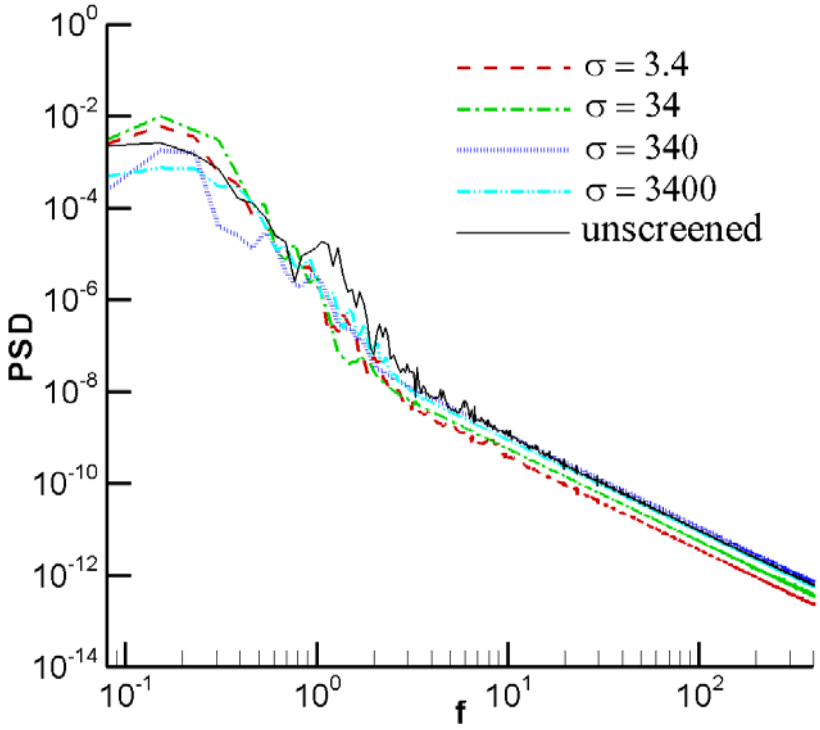

(b) 1.0D case

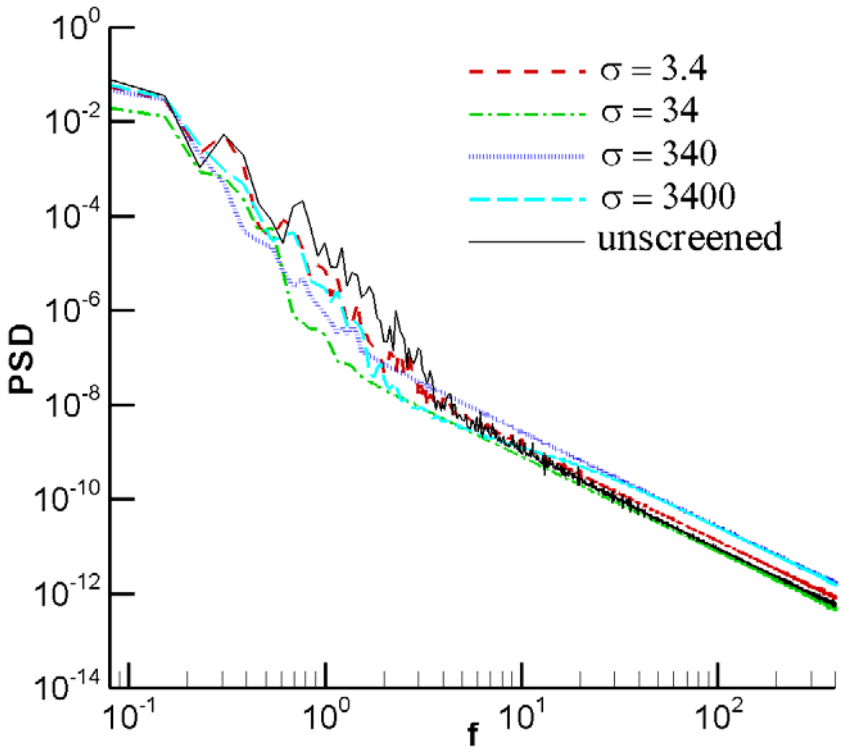

(c) 2.0D case

Figure 4-19 PSD at the center point of the microphone cylinder (all values are dimensionless, Re = 5000)

Next, Figure 4-20 shows the sound pressure level (SPL) at the center of the windscreened microphone for three different upstream cylinder cases (0.5D, 1.0D and 2.0D), and each case having five curves: one for the bare microphone case and the other four for the screened microphone with different flow resistivities: 3.4, 34, 340, and 3400 Pa·s/m^2. Notably all the data in Figure 4-20 are dimensional for real physical phenomena. First, case (a) with the upstream cylinder diameter 0.5D shows that the SPL shape of three large flow resistivity cases (σ = 34, 340 and 3400 Pa·s/m^2) is very similar with each other. Also, the unscreened case and smallest flow resistivity case (σ = 3.4 Pa·s/m^2) have similar SPL trend. The windscreen is effective in the range 4Hz to 60Hz for Case (a). Also, the remarkable SPL difference between the unscreened center and the screened center lies at frequencies of 16Hz and 40Hz. For case (b) with the

upstream cylinder diameter 1.0D, there are few windscreen effects below the frequency 10Hz, but windscreen effects are noted in the frequency range from 10Hz to 40Hz, especially at frequencies of 17Hz and 22Hz. In case (b) the SPL trend of three large flow resistivity cases (σ = 34, 340 and 3400 Pa·s/m^2) is very similar which is same trend as for case (a). Case (c) with the upstream cylinder diameter 2.0D shows a similar windscreen effects trend as for case (b), and also has distinct windscreen effective in the frequency range from 10Hz to 40Hz. Figure 4-20 also shows that the SPL shape of the lowest windscreen flow resistivity case (σ = 3.4 Pa·s/m^2) is very similar to that of the unscreened microphone case, which means that the low flow resistivity screen is like the no windscreen (bare microphone) case.

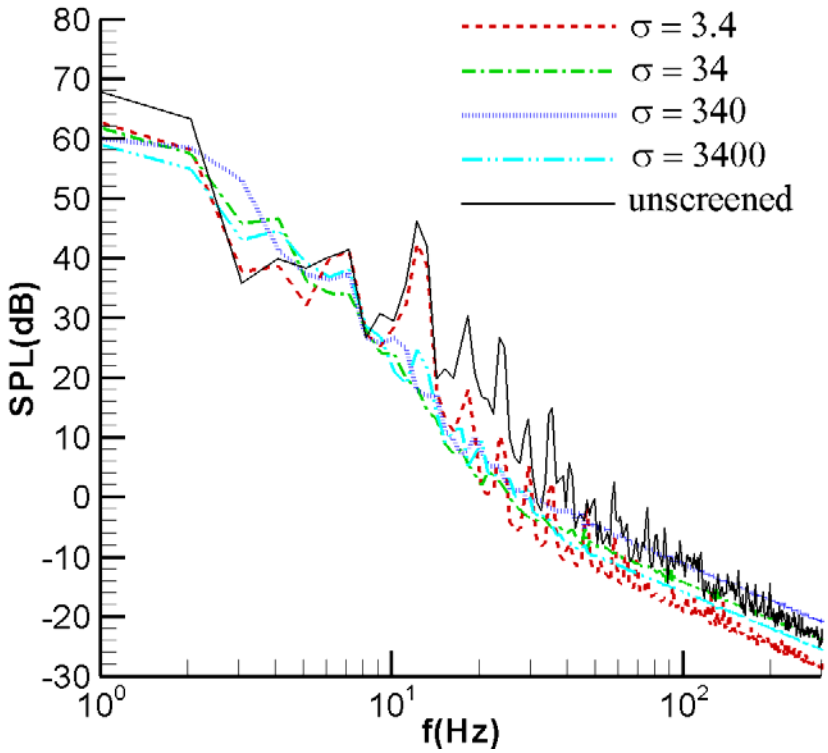

(a) 0.5D case

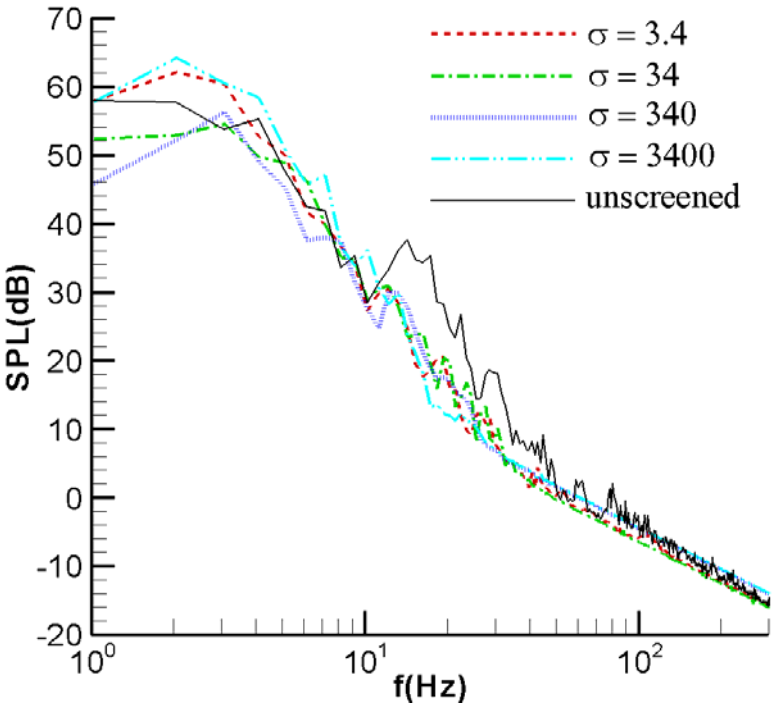

(b) 1.0D case

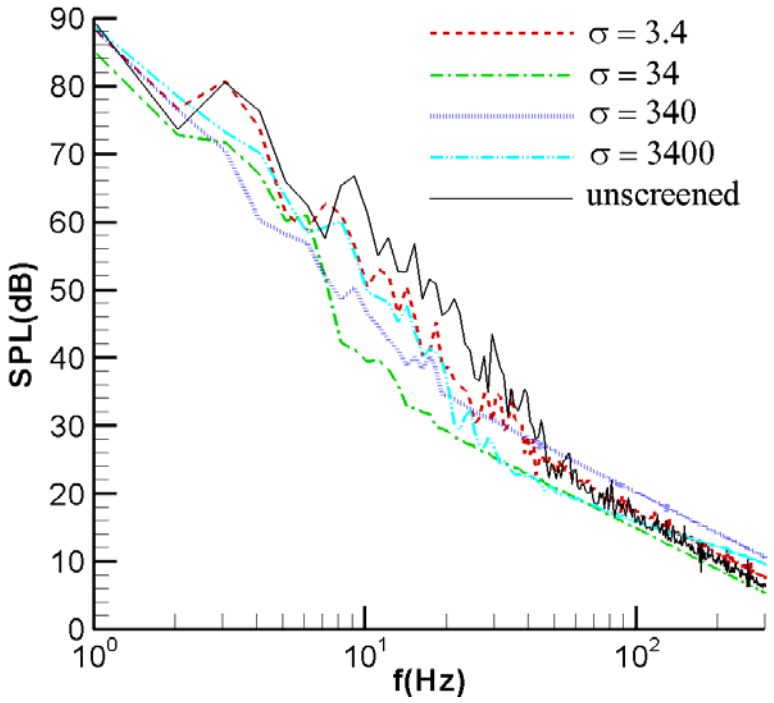

(c) 2.0D case

Figure 4-20 SPL at the center point of the microphone cylinder (all values are dimensionless, Re = 5000)

We further investigate wind noise reduction level (WNR) between the unscreened microphone and the screened microphone, defined as: $WNR = SPL_{unscreened\ \ center} - SPL_{screened\ \ center}$, by subtracting the SPL at screened microphone center from that at unscreened microphone center. Figure 4.21 shows the WNR comprising three different upstream cylinder cases (0.5D, 1.0D and 2.0D), each case with four curves: bare microphone minus four screened microphones with different flow resistivities (σ = 3.4, 34, 340 and 3400 Pa·s/m^2). Here, the highest WNR is around 25dB, which shows very significant windscreen effects. Clearly, the WNR between unscreened and lowest flow resistivity (σ = 3.4 Pa·s/m^2, red solid line) is the lowest compared with the other three higher flow resistivity screens (σ = 34, 340 and 3400 Pa·s/m^2). For case (a) with the upstream cylinder diameter 0.5D, there's little windscreen effect below the frequency of 10Hz. The lowest flow resistivity windscreen (σ = 3.4 Pa·s/m^2) has the smallest windscreen effect compared to higher flow resistivity windscreen cases (σ = 34, 340, 3400 Pa·s/m^2). For case (b) with upstream cylinder diameter 1.0D, the medium flow resistivity windscreen (σ = 34 Pa·s/m^2) performs best and has the highest reduction effects (around 23dB). Meanwhile, case (c) with upstream cylinder diameter 2.0D behaves similarly to case (b), while the medium flow resistivity windscreen (σ = 34 Pa·s/m^2) performs best and has the highest reduction effects (around 25dB). Figure 4-21 also shows that the lowest flow resistivity case (σ = 3.4 Pa·s/m^2) has few windscreen effects compared with the higher resistivity cases (σ = 34, 340 and 3400 Pa·s/m^2). Ultimately, the medium flow resistivity windscreen (σ = 34 Pa·s/m^2) performs best and has the highest wind noise reduction.

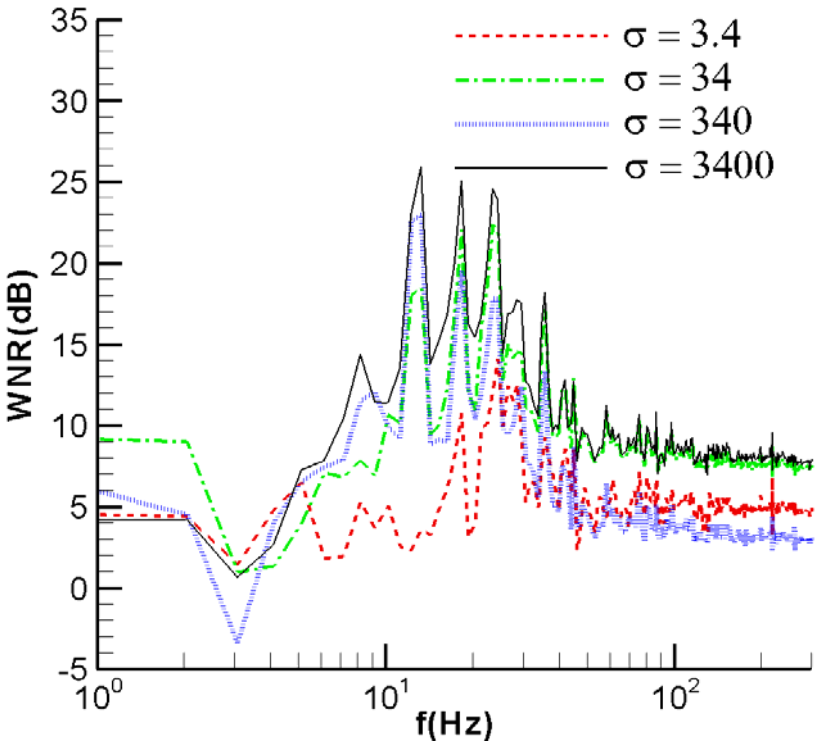

(a) 0.5D case

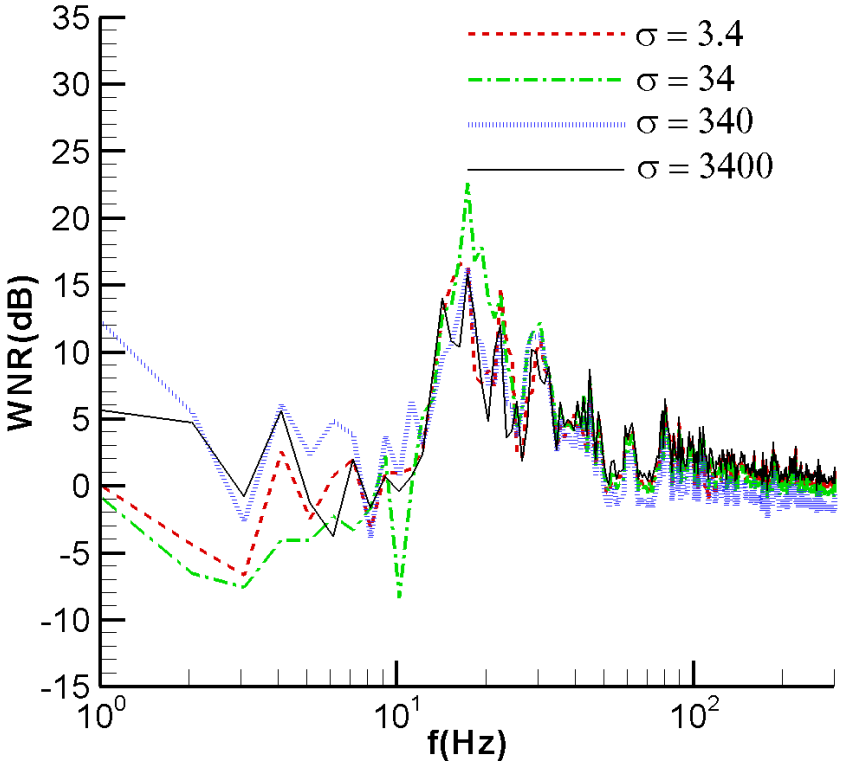

(b) 1.0D case

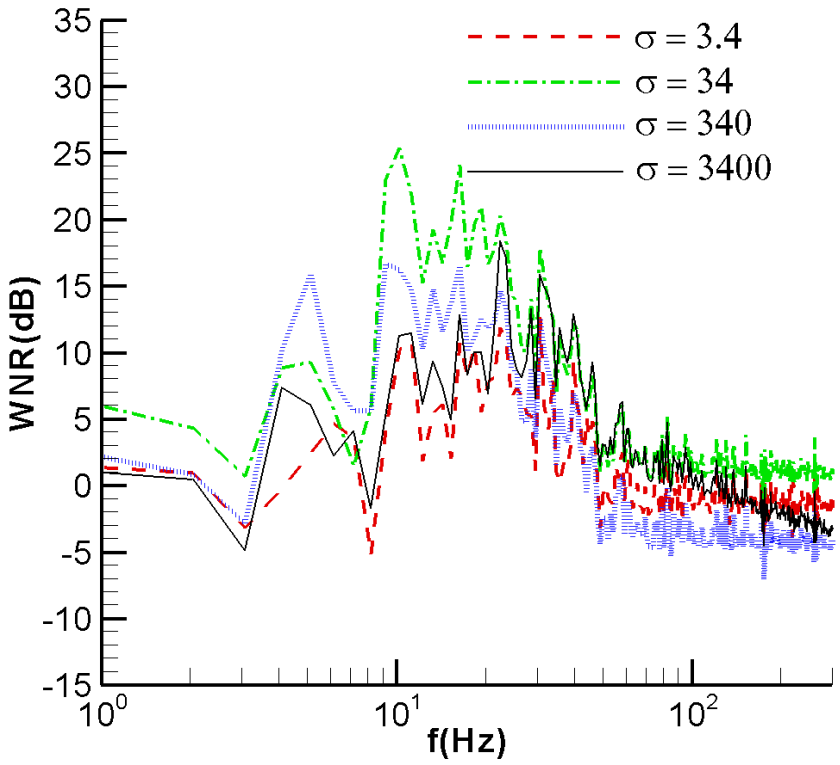

(c) 2.0D case

Figure 4-21 WNR between the unscreened microphone center and the screened microphone center (a) 0.2D (b) 0.5D (c) 1.0D (d) 2.0D (all values are dimensional, Re = 5000)

To clarify the quantitative value for the wind noise reduction between the unscreened microphone center and the screened microphone center, the significant sound level reductions are shown in Table 4-2 which includes three sub-tables with each describes one case (0.5D, 1.0D and 2.0D case).

Table 4-2 Wind noise reduction (WNR) between the unscreened microphone center and the screened microphone center (2D cases, Re = 5000)

(a) 0.5D case

Resistivity (Pa·s/m^2) / Frequency(Hz)	3.4	34	340	3400
13.2	2.5	18.6	23.1	25.6
18.3	10.8	22.1	19.6	25.1
24.4	14.2	22.4	17.8	23.9
35.6	9.3	17.2	13.4	18.2
44.7	8.5	12.9	8.7	12.7

(b) 1.0D case

Resistivity (Pa·s/m^2) / Frequency(Hz)	3.4	34	340	3400
17.3	16.7	22.6	16.3	15.8
22.4	14.8	14.3	11.6	12.0
30.5	10.9	12.2	11.3	10.0
44.7	7.6	7.8	6.5	6.2

(c) 2.0D case

Resistivity (Pa·s/m^2) / Frequency(Hz)	3.4	34	340	3400
11.2	10.9	25.4	16.2	11.5
16.3	10.7	24.1	16.6	12.8
22.4	11.9	20.3	14.7	18.4
30.5	12.8	17.9	12.6	15.9
39.7	9.4	12.2	7.0	12.9

4.4 Comparison of Low and High Reynolds Number Cases

The previous sections discussed the low Reynolds number cases and the high Reynolds number cases separately. However, this section compares cases in both categories (Re = 500 and Re = 5000).

In the low Reynolds number case, $\mathrm{Re} = \frac{UD}{\nu} = \frac{1m/s \cdot 0.0075m}{1.5 \times 10^{-5} m^2/s} = 500$, approximately characterizes a windscreen with a diameter of 0.75cm and a wind speed of 1m/s for the incoming air. Meanwhile, in the high Reynolds number case, $\mathrm{Re} = \frac{UD}{\nu} = \frac{1m/s \cdot 0.075m}{1.5 \times 10^{-5} m^2/s} = 5000$, approximately characterizes a windscreen with a diameter of 7.5cm and a wind speed of 1m/s for the incoming air. Clearly, the high Reynolds number case is more realistic and the low Reynolds number case is more theoretical.

Next, the following section compares the pressure between a downstream point of the first solid cylinder (4D away from the center of first solid cylinder, we call it P1 point) and a center point (the center point of the screened microphone, we call it P2 point) for these two cases (Re = 500 and Re = 5000). Accordingly, three different upstream solid cylinder cases (0.5D, 1.0D and 2.0D case) with the same resistivity (σ = 20, dimensionless value) are discussed here.

Figure 4-22 and 4-23 shows the comparison for the 0.5D case. Regarding pressure time history (see Figure 4-22), the high Reynolds number case (Re = 5000) has a greater magnitude of fluctuation than the low Reynolds number case (Re = 500). However, the pressure time history of P1 point for both cases is quasi-stable. Next, the pressure time history of P2 of the high Reynolds number case (Re = 5000) is not as stable as that of the low Reynolds number case (Re = 500) because there are more turbulent fluctuations for the high Reynolds number case. For the pressure power spectrum density (PSD) comparison (see Figure 4-23), both the low Reynolds

number case and the high Reynolds number case share an identical main peak frequency (around 1). However, the magnitude of PSD in the high Reynolds number case is much larger than that in the low Reynolds number case, which conforms to the pressure time history figure. Moreover, the PSD plot trend is different for the low Reynolds number case from than for the high Reynolds number case. In the low Reynolds number case, there are more peak frequencies before the main peak frequency (around 1), but in the high Reynolds number case, there is no peak frequency before the main peak.

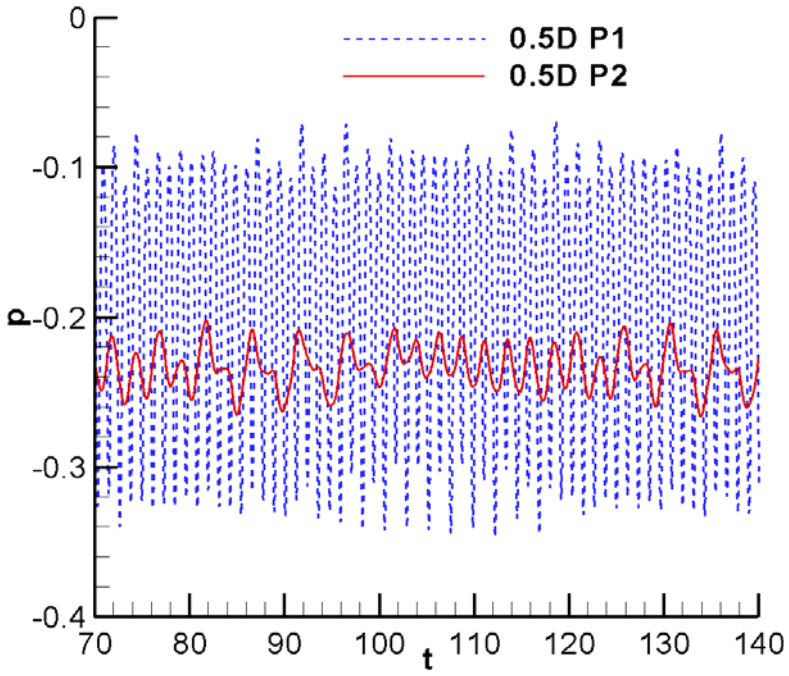

(a) Re = 500

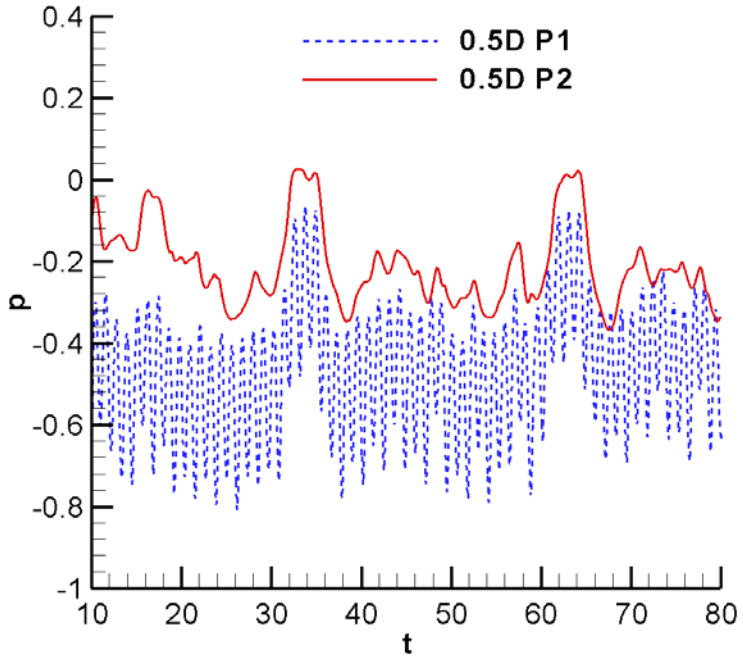

(b) Re = 5000

Figure 4-22 Pressure comparison between P1 point and the P2 point (Re = 500 and Re = 5000, 0.5D case, σ = 20, all values are dimensionless)

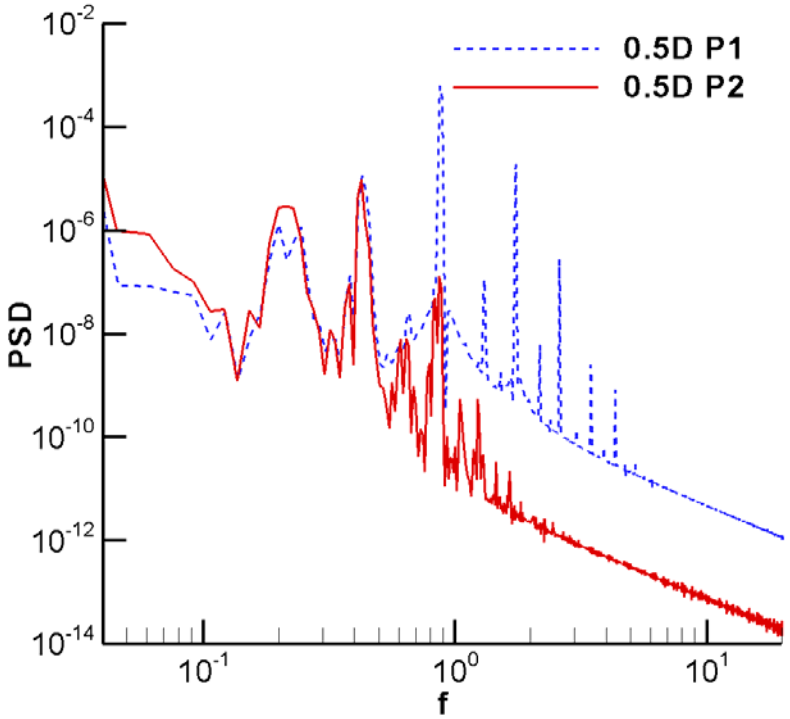

(a) Re = 500

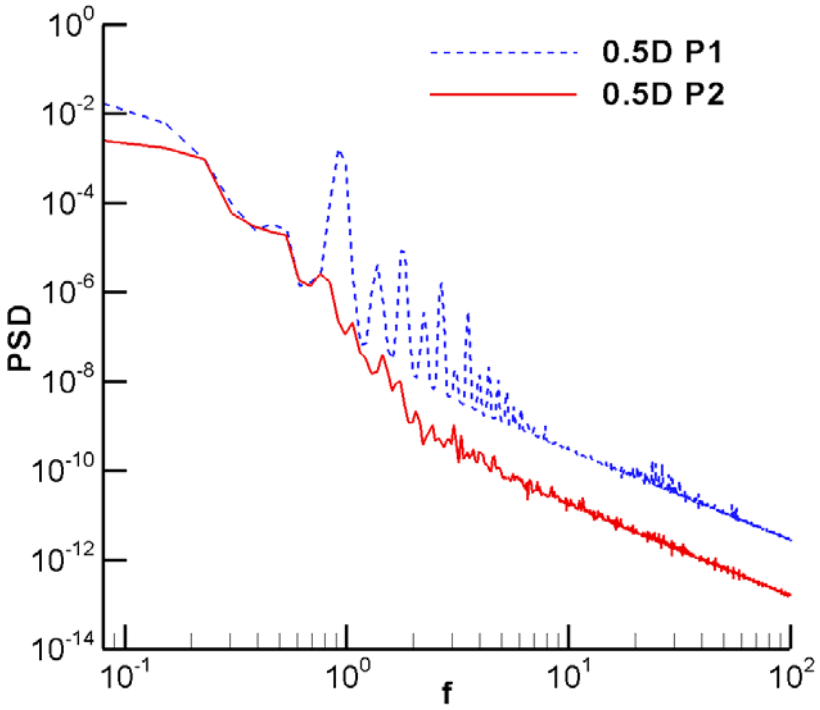

(b) Re = 5000

Figure 4-23 PSD comparison between P1 point and P2 point (Re = 500 and Re = 5000, 0.5D case, σ = 20, all values are dimensionless)

Figure 4-24 and 4-25 shows the comparison for the 1.0D case. For pressure time history (see Figure 4-24), the high Reynolds number case has a greater magnitude of fluctuation and is more unstable than the low Reynolds number case. Furthermore, both pressure time histories for P1 and P2 points for the low Reynolds case are stable, while the pressure time histories seem only quasi-stable for the high Reynolds number case. Next, the pressure PSD comparison (see Figure 4-25) shows an identical main peak frequency (around 0.5) between the low Reynolds number case and the high Reynolds number case. Again, the magnitude of PSD in the high Reynolds case is much larger than that in the low Reynolds case, which conforms to the pressure time history figure. Also, the PSD plot trend is different for the low Reynolds number case than for the high Reynolds number case. For the low Reynolds case there are more peak frequencies

before the main peak frequency (around 1), but for the high Reynolds case there is no peak frequency before the main peak. In fact, there is almost no distinct peak frequency in the PSD plot for the high Reynolds case.

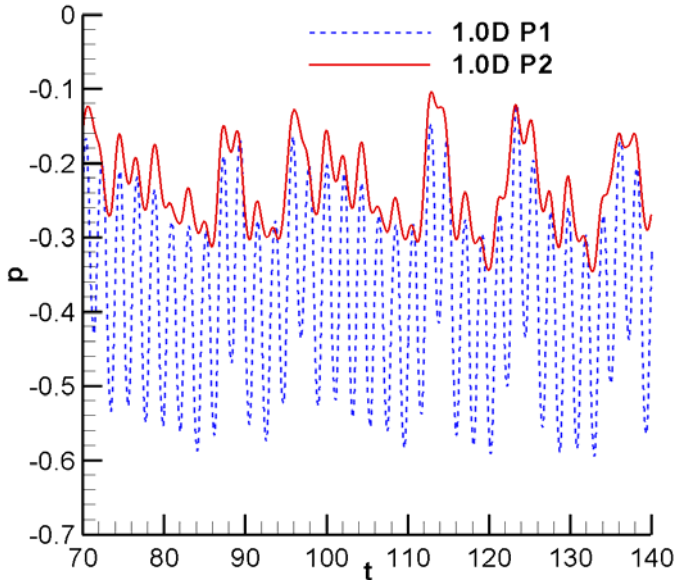

(a) Re = 500

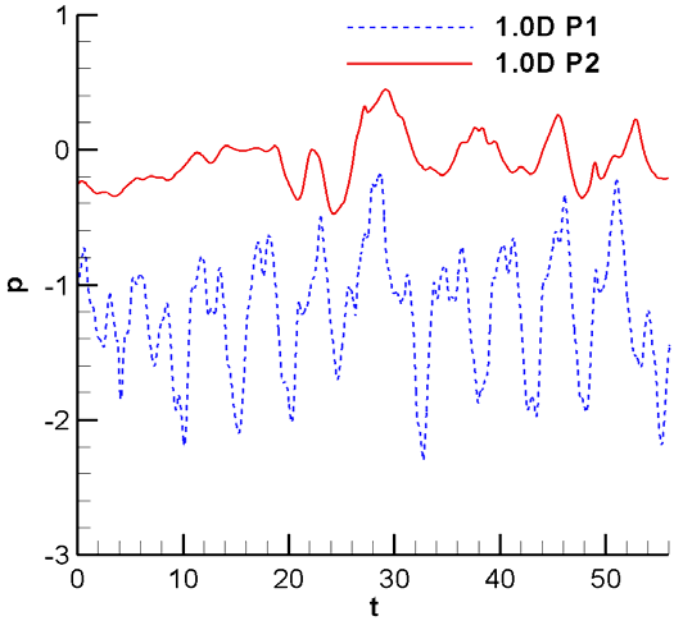

(b) Re = 5000

Figure 4-24 Pressure comparison between P1 point and the P2 point (Re = 500 and Re = 5000, 1.0D case, σ = 20, all values are dimensionless)

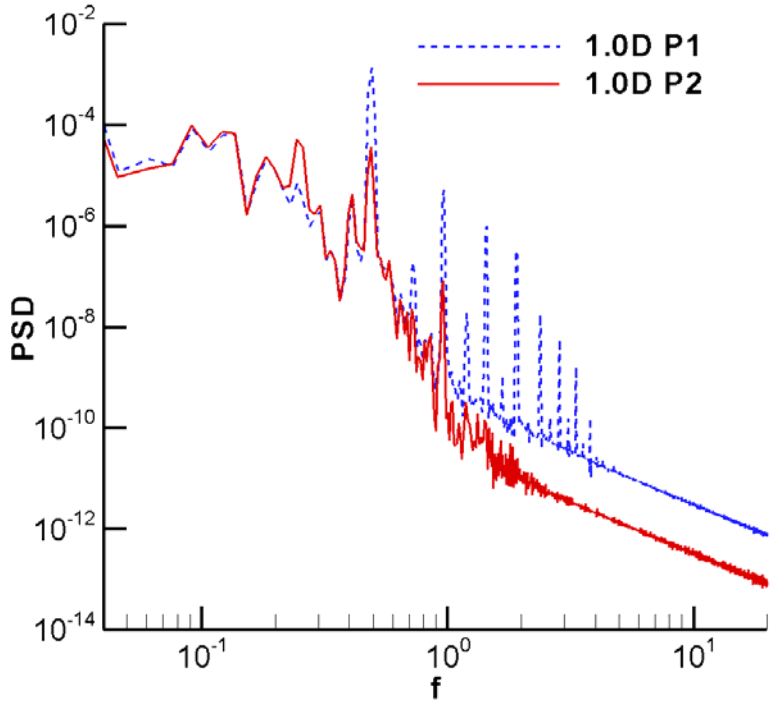

(a) Re = 500

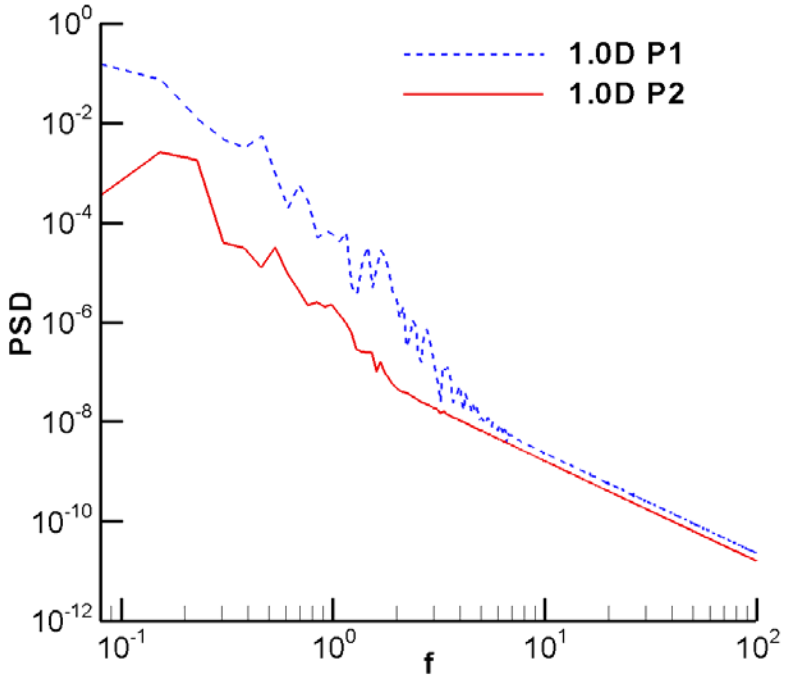

(b) Re = 5000

Figure 4-25 PSD comparison between P1 point and the P2 point (Re = 500 and Re = 5000, 1.0D upstream solid cylinder, σ = 20, all values are dimensionless)

Figure 4-26 and 4-27 shows the comparison for the 2.0D case. The pressure time history shows that the high Reynolds number case has a greater magnitude of fluctuation and is more chaotic than the low Reynolds number case. Also, both pressure time histories for P1 and P2 points for the low Reynolds case are not as stable as for the 0.5D and 1.0D cases. The pressure time history for P1 point in the low Reynolds number case seems only quasi-stable, and the pressure time history of P2 point looks more chaotic than that of P1 point. Regarding the pressure PSD comparison, there is no identical main peak frequency between the low Reynolds number case and the high Reynolds number case. Instead, for the low Reynolds number case, the main peak frequency is 0.25, and for the high Reynolds number case, it is around 0.6 and not so distinct compared to the low Reynolds number case. Indeed, the magnitude of PSD in the high Reynolds case is much larger than that in the low Reynolds number case, which conforms to the pressure time history figure.

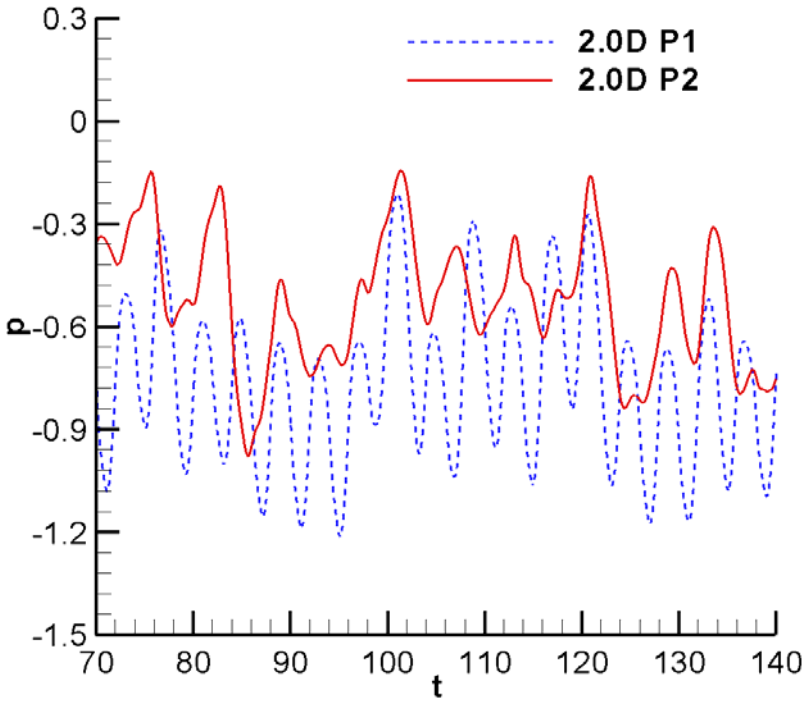

(a) Re = 500

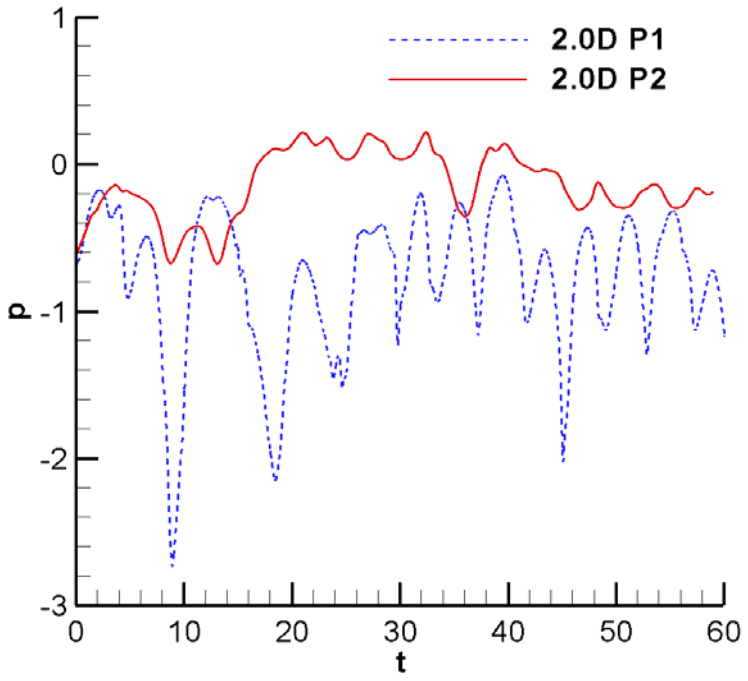

(b) Re = 5000

Figure 4-26 Pressure comparison between a downstream point and the center point (Re = 500 and Re = 5000, 2.0D case, σ = 20, all values are dimensionless)

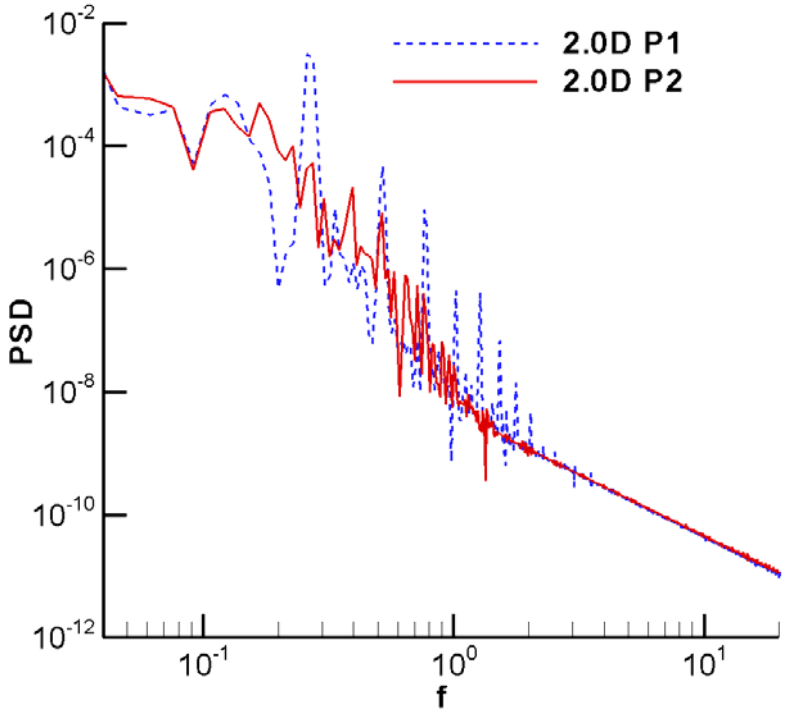

(a) Re = 500

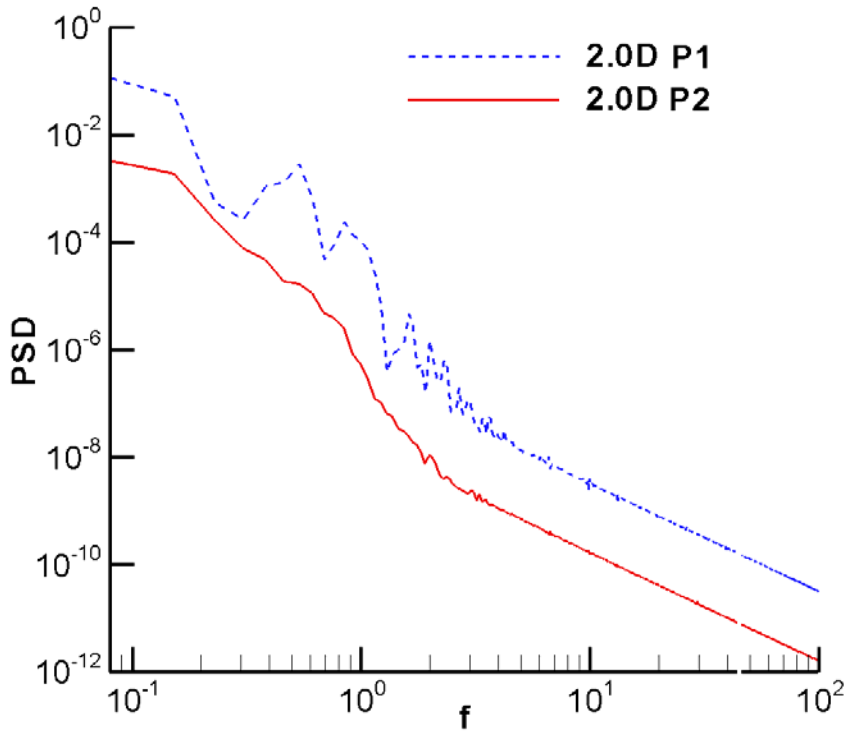

(b) Re = 5000

Figure 4-27 PSD comparison between P1 point and P2 point (Re = 500 and Re = 5000, 2.0D upstream solid cylinder, σ = 20, all values are dimensionless)

4.5 Different Shape Cases

We define the diameter of the upstream circular cylinder as D in Figure 4-28; the diameter of the bare microphone is 0.25D. The windscreen shape is represented by the ellipse equation, $x^2/a^2 + y^2/b^2 = 1$. We selected three typical windscreen shapes: the first case is a circular cylinder with a=0.5D, b=0.5D; the second case is a horizontally-oriented elliptical cylinder with a=1.0D, b=0.5D; the third case is a vertically-oriented elliptical cylinder with a=0.5D, b=1.0D. In the following discussion, we will call the circular windscreen case as Case C, the horizontal ellipse windscreen case as Case E1, and the vertical ellipse windscreen case as

Case E2. The distance, L, between the first cylinder center and the second windscreen center, is 8D. With the geometrical parameters, the region to implement the WENO scheme is thus selected as a rectangular region of 12D-long and 4D-high contouring the two cylinders, with 2D ahead of the center of the upstream solid cylinder.

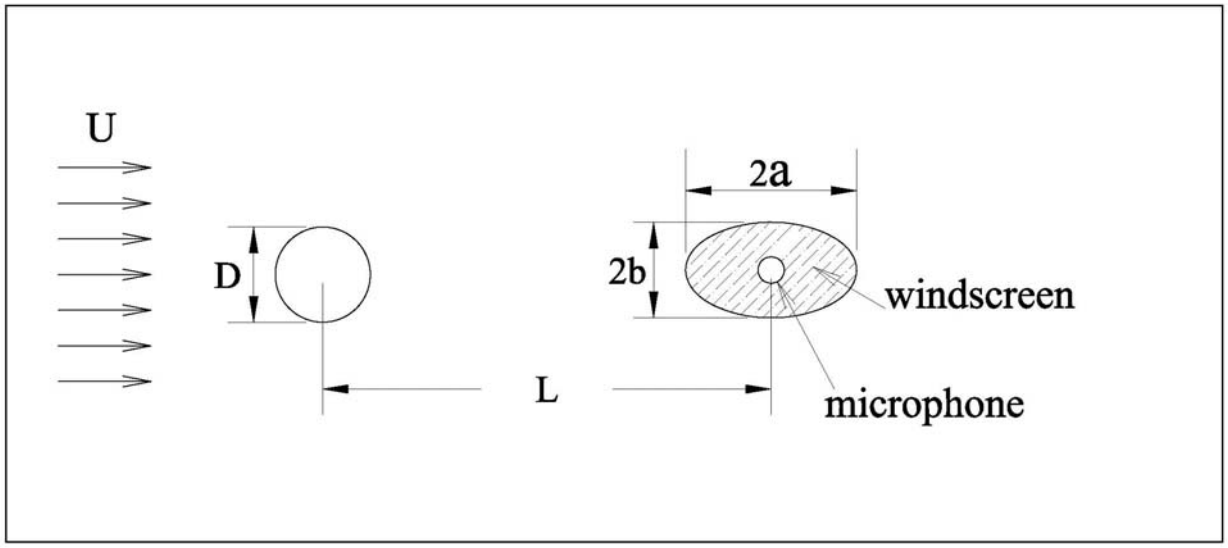

Figure 4-28 Illustration of the incoming wind turbulence generation with an upstream solid cylinder for different shape windscreens.

The Reynolds number for the cases presented here is 5000, which approximately corresponds to a windscreen with a diameter of 7.5cm, a bare microphone with a diameter of 1.875cm, and a wind speed of 1m/s for the incoming air. At this high Reynolds number, a relatively broad spectrum of pressure fluctuations is generated with flow over the upstream circular cylinder, contrary to a low Reynolds number flow where only very tonal pressure fluctuations are generated related to the von Karman vortex shedding frequency. The three chosen values of dimensionless flow resistivity of the windscreen, 1, 10 and 100, correspond to dimensional flow resistivity values of approximately 17, 170, and 1700 Pa·s/m^2, respectively

($1\sigma = \frac{\rho U}{D} = \frac{1.27kg/m^3 \cdot 1m/s}{0.075m} = 17P_a \cdot s/m^2$). In the simulation here, the grid size is 0.025 in both the *x* and *y* directions, and the time step is 0.0005, which satisfies the grid convergence and stability requirements on the computational scheme.

We first investigate the whole flow field as shown by vorticity contours in Figures 4-29 through 4-31 for three different flow resistivities, σ = 17, 170 and1700 Pa·s/m^2 with three different windscreen shapes (C, E1, and E2). The red color in figure represents positive vorticity (in the counter clockwise sense, with the upper limit value of 10); the blue color represents negative vorticity (in the clockwise sense, with the lower limit value of -10). Clearly, there is no flow inside the solid objects, but some flow infiltrates the windscreen porous cylinder. The vortical structures shed from the upstream cylinder are diffused by the porous medium windscreen. When the flow resistivity is high (σ = 1700Pa·s/m^2), little flow permeates the porous windscreen. When the flow resistivity is low (σ = 17Pa·s/m^2), the flow permeates the porous windscreen more easily.

In comparing different shapes among Figures 4-29 through 4-31, it can be seen that the least amount of vortices are generated in the wake of the horizontal ellipse, while the most amount of vortices are generated in the wake of the vertical ellipse. The amount of vortices in the wake of the circular windscreen is in between these two cases. This is because the horizontal ellipse has the smallest area projected in the flow direction, while the vertical ellipse has the largest one so that stronger wakes are generated. This directly affects the pressure fluctuations detected at the microphone as shown in following time history figures.

(a) σ = 17 Pa·s/m^2

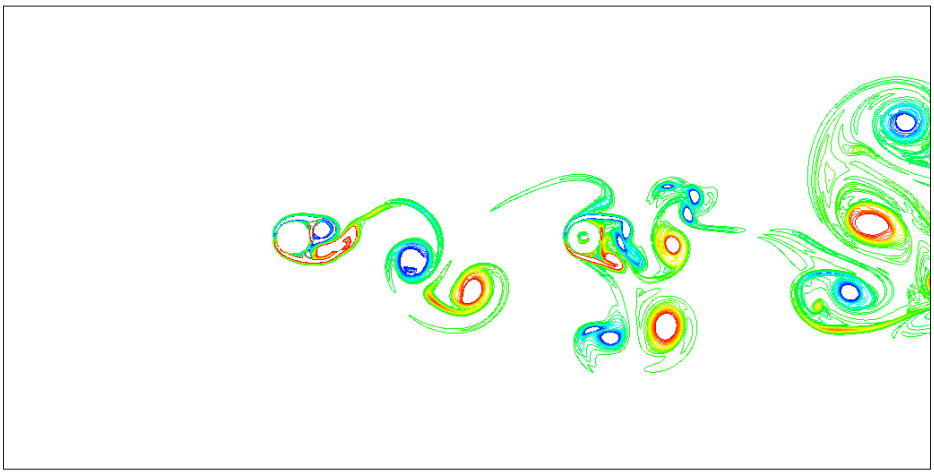

(b) σ = 170 Pa·s/m^2

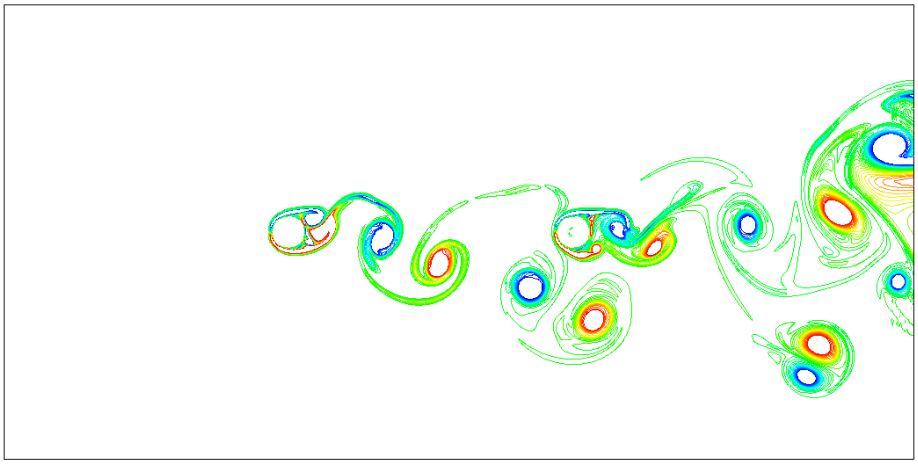

(c) σ = 1700 Pa·s/m^2

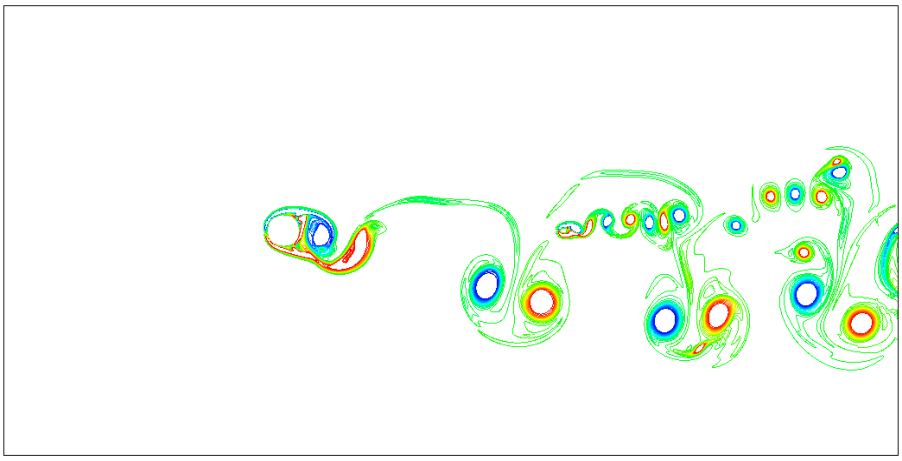

(d) unscreened

Figure 4-29 Vorticity contours of flow field (Re = 5000, C case)

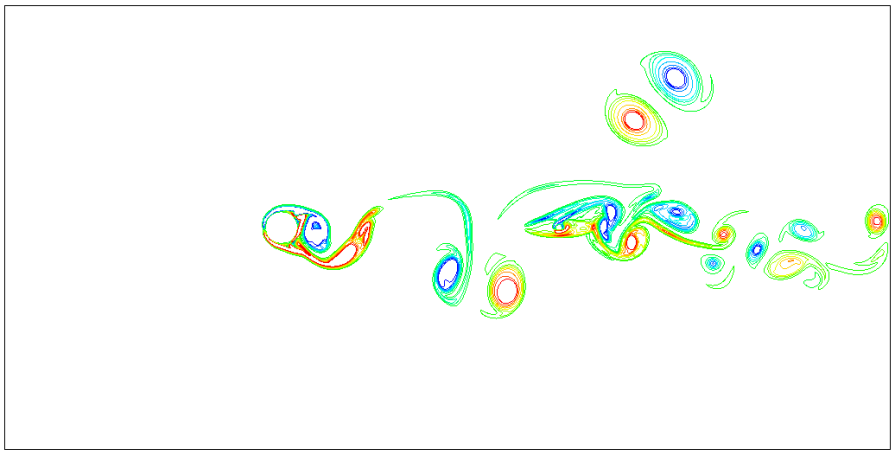

(a) σ = 17 Pa·s/m^2

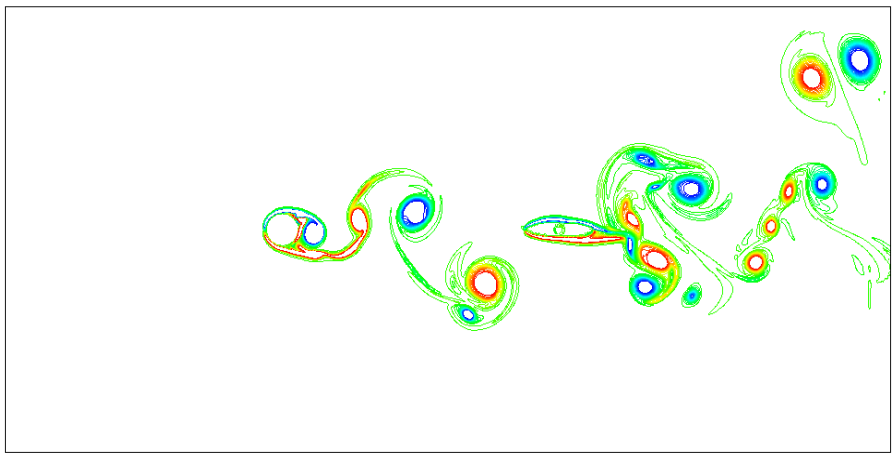

(b) σ = 170 Pa·s/m^2

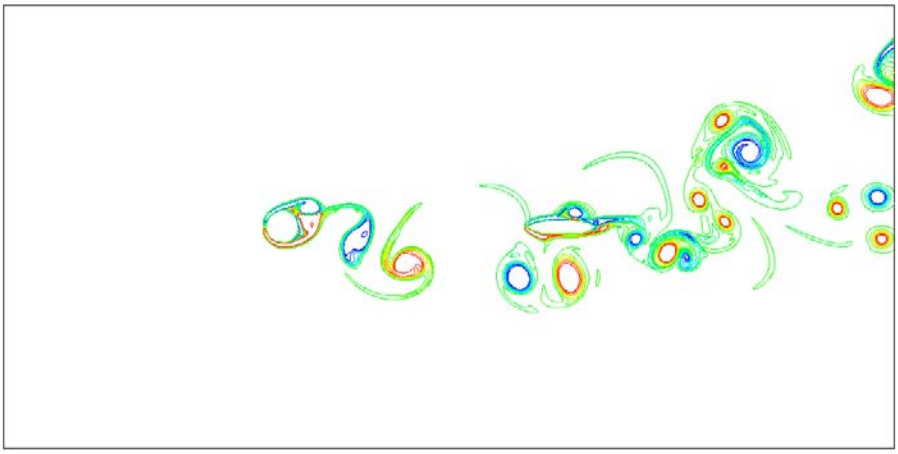

(c) σ = 1700 Pa·s/m^2

Figure 4-30 Vorticity contours of flow field (Re = 5000, E1 case)

(a) σ = 17 Pa·s/m^2

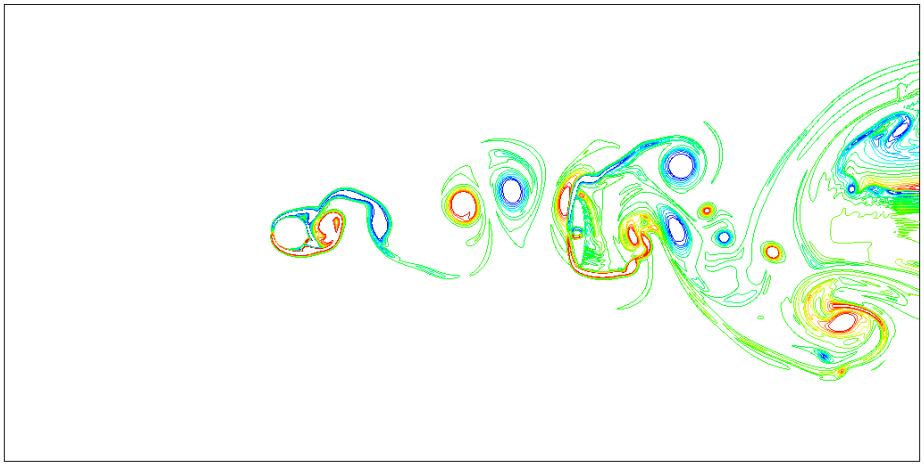

(b) σ = 170 Pa·s/m^2

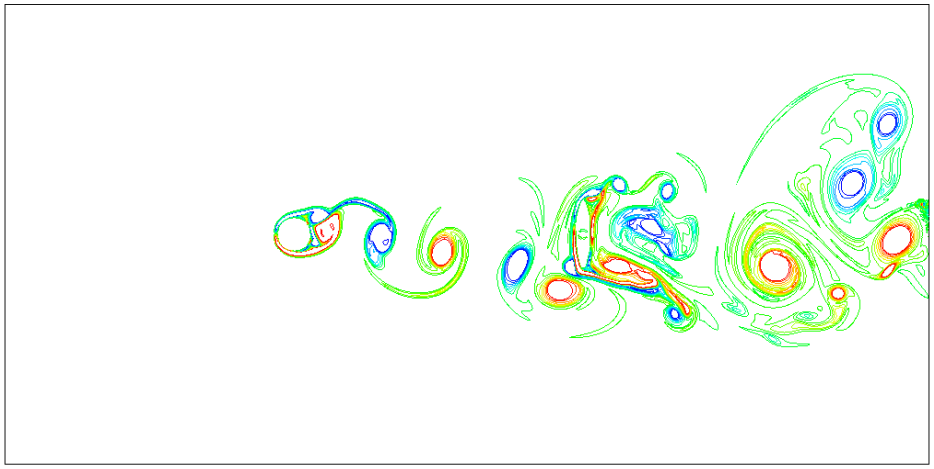

(c) σ = 1700 Pa·s/m^2

Figure 4-31 Vorticity contours of flow field (Re = 5000, E2 case)

Figure 4-32 presents the pressure time histories of the center point of the microphone. We compare the histories of each one of the three shapes of windscreens under different flow resistivities (σ = 17, 170 and 1700 Pa·s/m^2), along with the unscreened case in sub figures 4-32(a-c), and compare the histories of the same flow resistivity under different windscreen shapes in sub figures 4-32(d-f).

The pressure time histories in sub figures 4-32 (a) and (b) show that the fluctuation magnitude of the unscreened center pressure is the highest comparing all the C and E1 cases. This means for the circular and horizontal ellipse windscreens, there is some wind noise reduction effect, more or less. Although it is difficult to recognize the quantity of the reduction from the time histories (which will be clear when we plot these results in the spectral domain in the following sections), it is still discernable that the medium flow resistivity material (σ = 170 Pa·s/m^2) provides more noise reduction than the low or high flow resistivity materials. For the E2 cases in sub figure 4-32 (c), only the low resistivity windscreen shows some noise reduction effect. In this case, the medium resistivity windscreen maybe only has a little noise reduction

effect, while the high resistivity windscreen even increases the pressure fluctuation magnitudes, which means a lot of interaction between the upstream turbulence structure and the vertical ellipse windscreen in the E2 cases, as evident in the flow fields shown in figures from 4-29 through 4-31.

For the low resistivity cases in sub figure 4-32 (d), the pressure fluctuation magnitudes are very similar on the average among these three different shapes, showing low resistivity windscreens have some, but not significant, wind noise reduction effects. For the medium and high resistivity cases in sub figures 4-32 (e) and (f), the C and E1 shapes reduce the pressure fluctuations significantly in comparison to the unscreened case; the E2 shape cases show large magnitudes of pressure fluctuations, which means the wind noise is increased by the vertical ellipse windscreen.

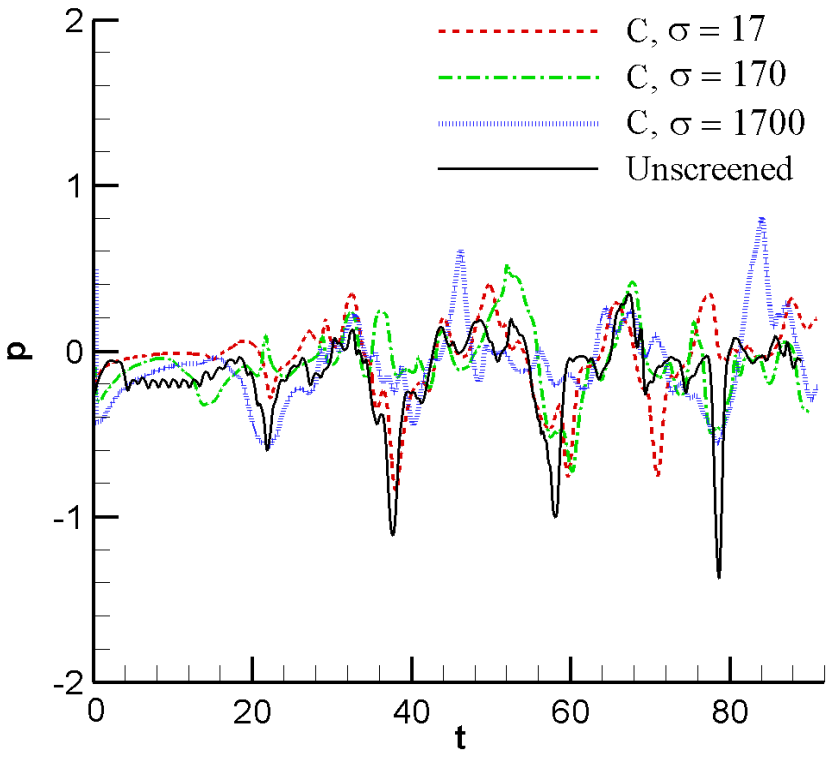

(a) C cases, different flow resistivities

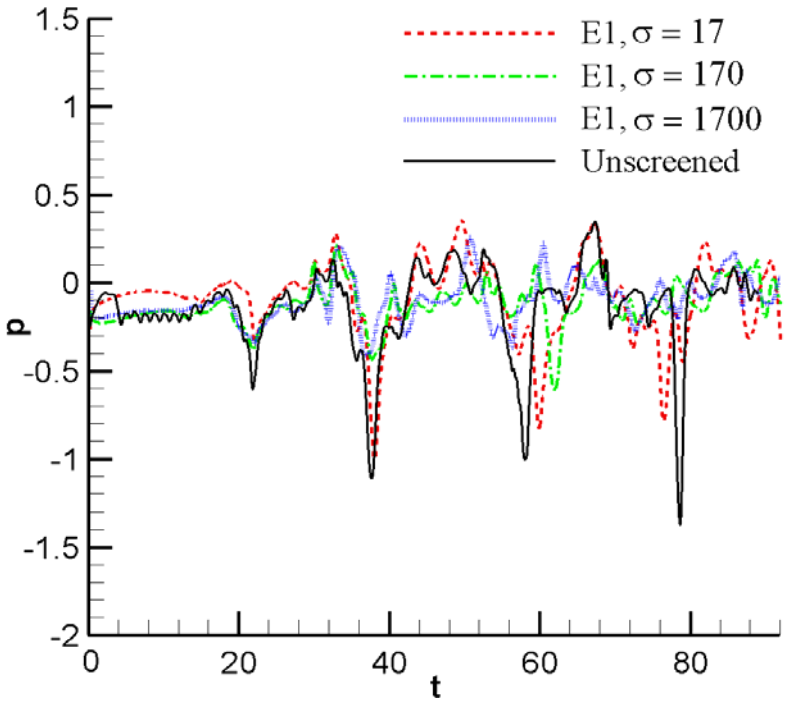

(b) E1 cases, different flow resistivities

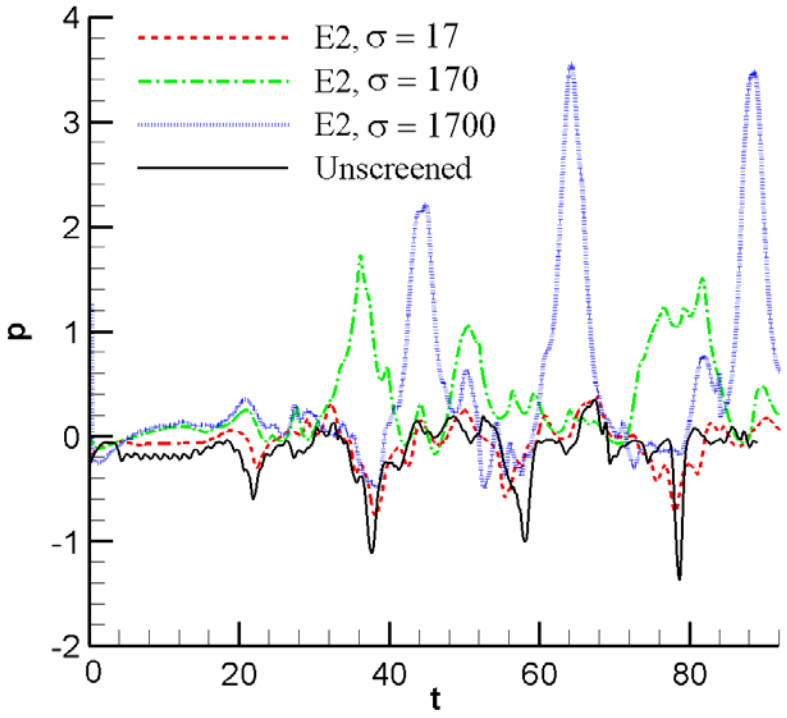

(c) E2 cases, different flow resistivities

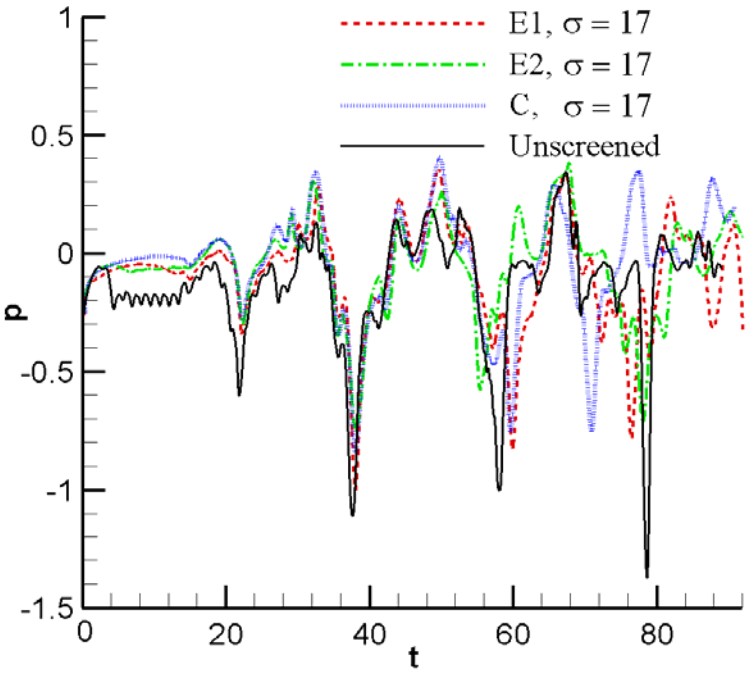

(d) σ = 17 Pa·s/m^2, different shapes

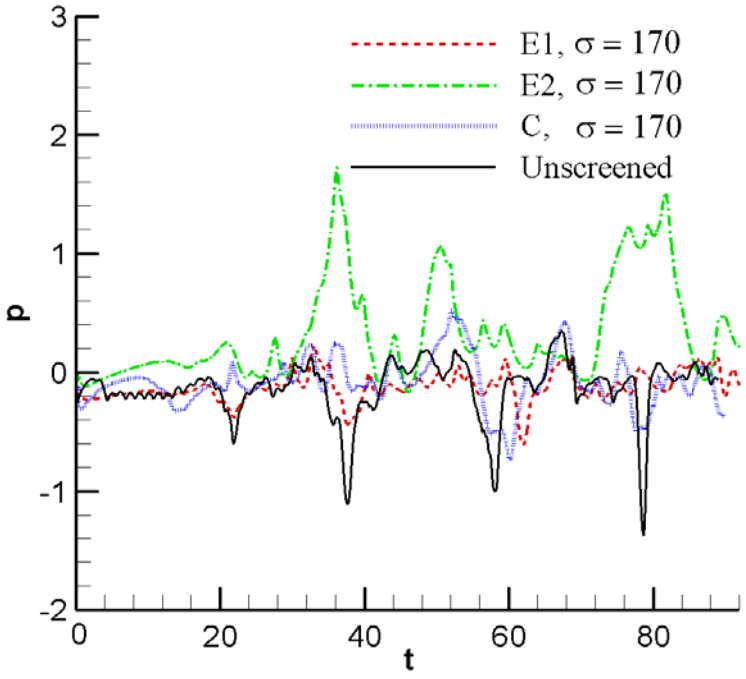

(e) σ = 170 Pa·s/m^2, different shapes

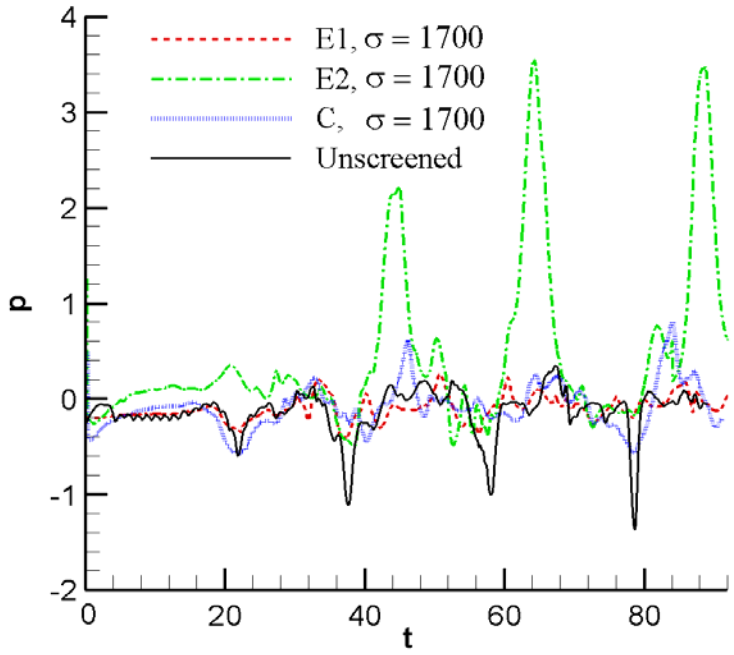

(f) σ = 1700 Pa·s/m^2, different shapes

Figure 4-32 Pressure time histories at the center point of microphone (all values are dimensionless, Re = 5000)

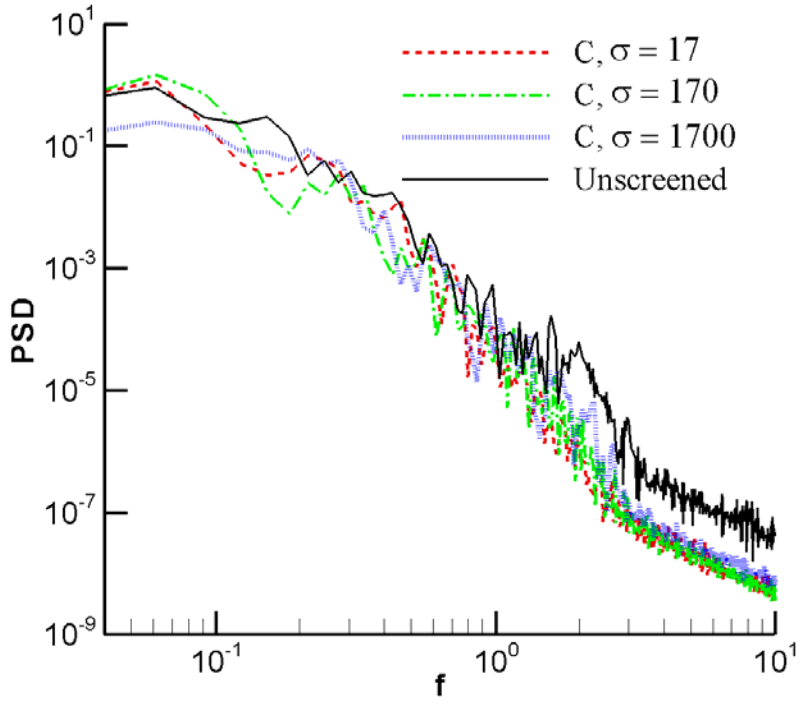

(a) C cases, different flow resistivities

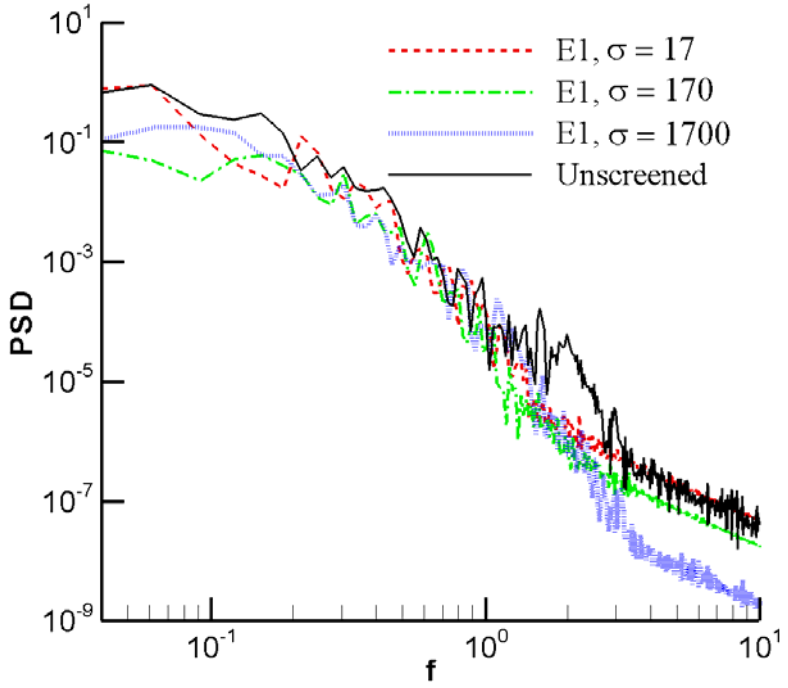

(b) E1 cases, different flow resistivities

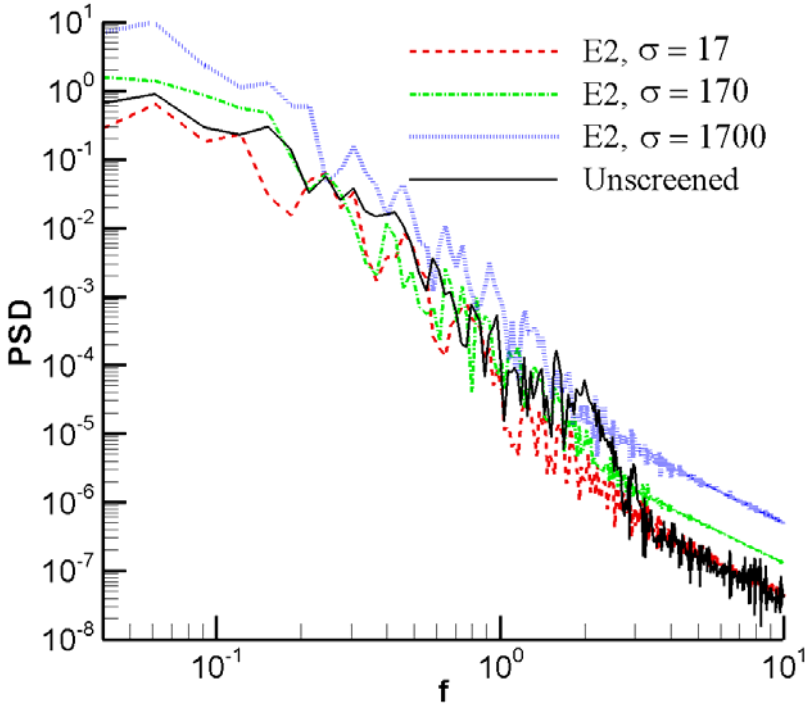

(c) E2 cases, different flow resistivities

Figure 4-33 PSD at the center point of the microphone (all values are dimensionless, Re = 5000)

Figure 4-33 shows the pressure PSD at the center of the windscreened microphone for different windscreen shapes and different resistivities. Each case has four curves: one for the unscreened microphone case and the other three for the screened microphone with different flow resistivity: 17, 170, and1700 Pa·s/m^2 (corresponding to dimensionless 1, 10 and 100 separately). It should be noted here that all results shown in Figure 4-32 are dimensionless, which will be convenient for theoretical analysis. In the cylinder and the ellipse 1 cases the PSD line for the unscreened case is higher than that of the windscreened microphone, which means there are windscreen effects. Mainly the windscreen effective frequency range is around 1-4. Also, there are some distinct peak frequencies between the frequencies 1.5 and 3, but maybe not so clear as in the low Reynolds cases. Another interesting finding is that for the E2 cases, the PSD line for the unscreened microphone case is not as high as for the high flow resistivity case (σ = 1700 Pa·s/m^2), which means the there are a lot of interactions between the upstream turbulence structure and the vertical ellipse windscreen in E2 cases.

Next, we look at the corresponding sound pressure level (SPL) comparisons. The SPL is defined as: $SPL = 10\log_{10}(f_r S_p(f)/P_r^2$, where f_r equals 1Hz, Pr equals 20 μPa, $Sp(f)$ is the power spectral density (PSD) of the pressure at the microphone center which is shown in Figure 4-34. Sub figures 4-34(a-c) are the SPL for each of the three windscreen shapes, respectively, and each figure contains four curves: one for the bare microphone case and the other three for the screened microphone cases (σ = 17, 170, and 1700 Pa·s/m^2). Sub figures 4-34(d-f) are the SPL for each of the three flow resistivities of windscreen materials with different windscreen shapes, respectively. All the data in Figure 4-24 have been converted to dimensional data according to the physical parameters. It should be noted that all these SPL curves are of broad spectrum, very close to the spectrum of realistic wind turbulence. While

we put a 1D-diameter circular cylinder for generating turbulence in this paper, we also tested other sizes of circular cylinders. Unless the circular cylinder size is small that reduces the effective Reynolds, turbulence generated by cylinders larger than 1D is always of broad-band spectrum and very similar to the spectra shown here.

For the circular cylinder and horizontal ellipse windscreens, there is little noise windscreen effect below the frequency of 4Hz for the low flow resistivity (σ =17 Pa·s/m^2), as shown in sub figures 4-24(a), (b) and (d). However, there are distinct noise reduction effects between frequencies of 10Hz and 30Hz. Furthermore, for the C and E1 cases within the 10Hz to 40 Hz range, Figures 4-24(a-b) and 4(d-f) also show that the three different resistivities for the porous windscreen material do not seem to make much difference in the noise reduction effects. When the flow resistivity increases to medium and high (σ = 170 and 1700 Pa·s/m^2), Figures 4-24(a) and (b) show that the noise reduction effect improves in all the frequency range in this study. This trend is more significant for the E1 cases.

In contrast, the E2 cases in sub figures 4-24(c) and (e-f) with the medium and high resistivities show very poor noise reduction behavior and, in fact, increase the noise levels than those of the bare microphone. For the low flow resistivity (sub figures 4-24(c)-(d)), the vertical ellipse windscreen provides a small amount of noise reduction in the low frequency range.

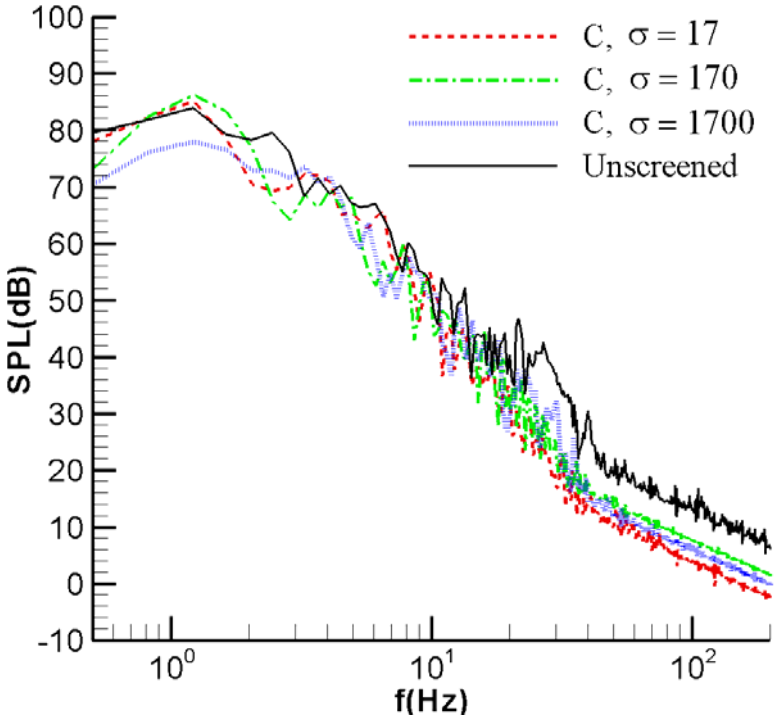

(a) C cases, different flow resistivities

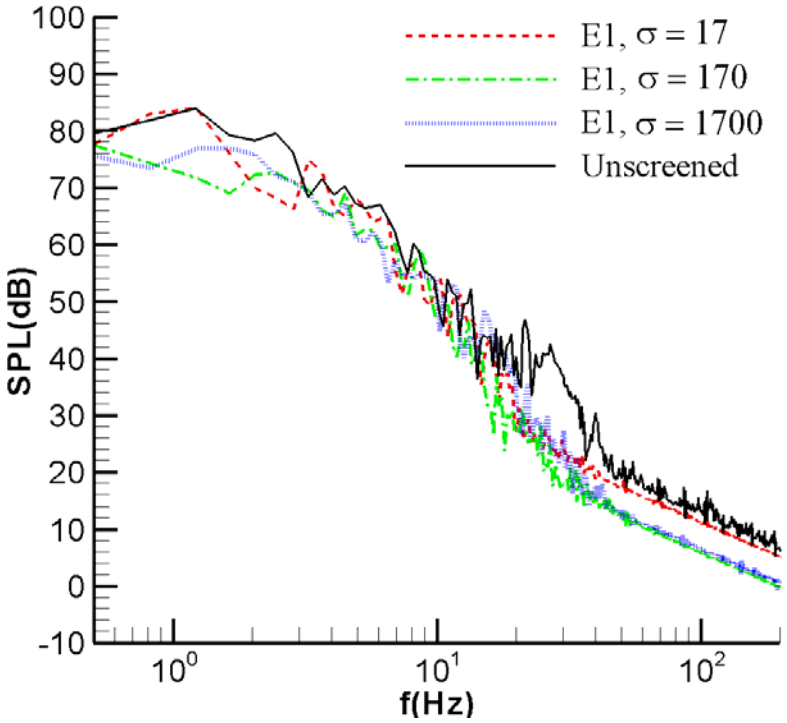

(b) E1 cases, different flow resistivities

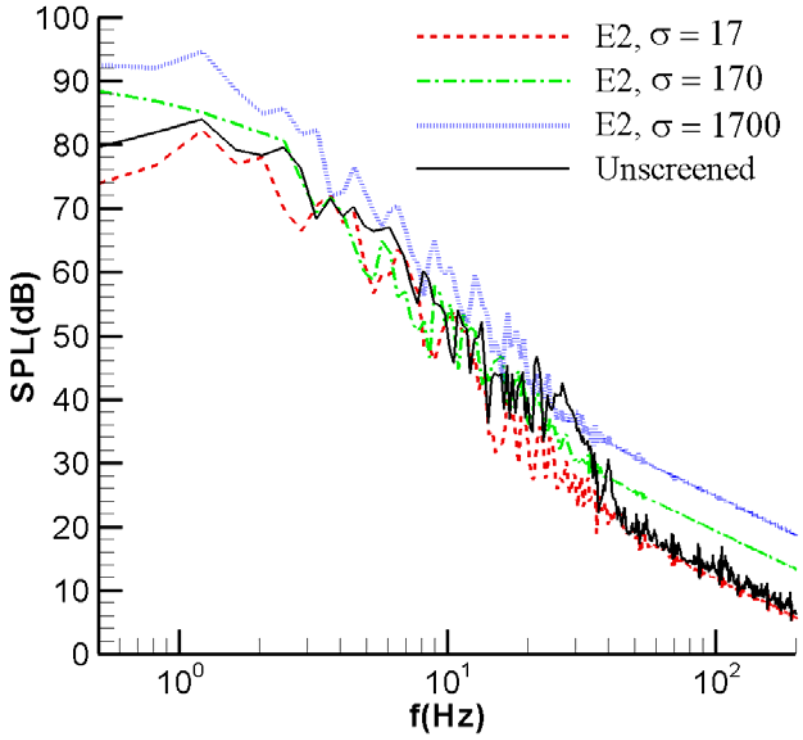

(c) E2 cases, different flow resistivities

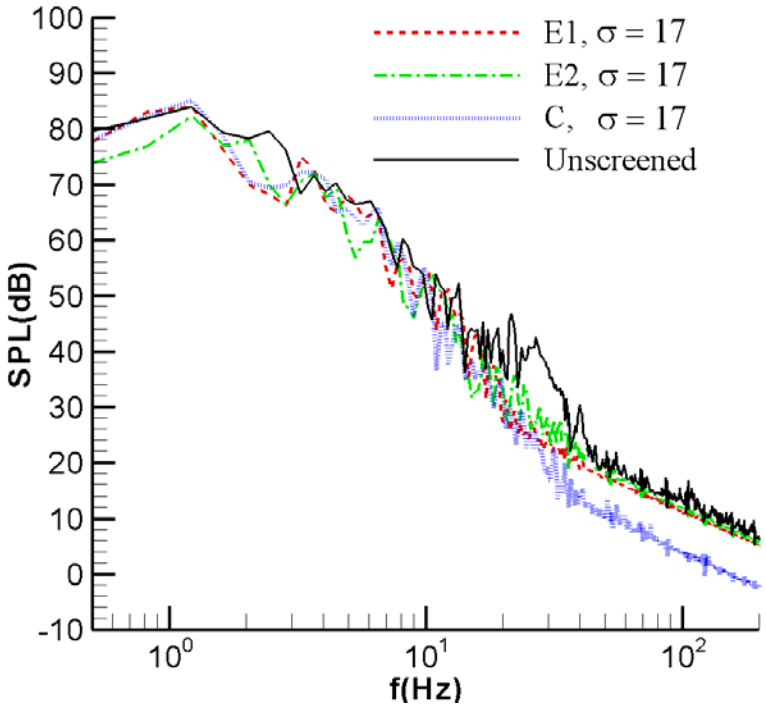

(d) σ = 17 Pa·s/m^2, different shapes

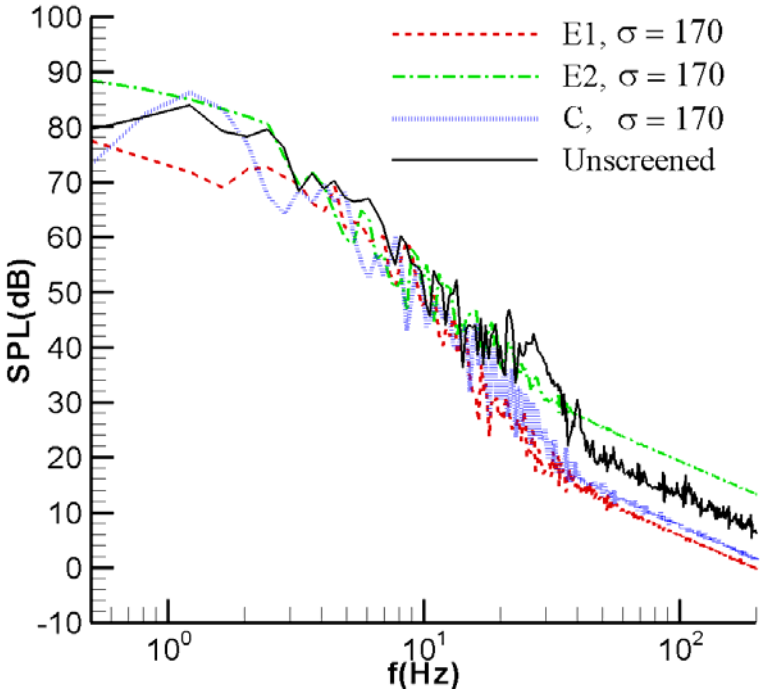

(e) σ = 170 Pa·s/m^2, different shapes

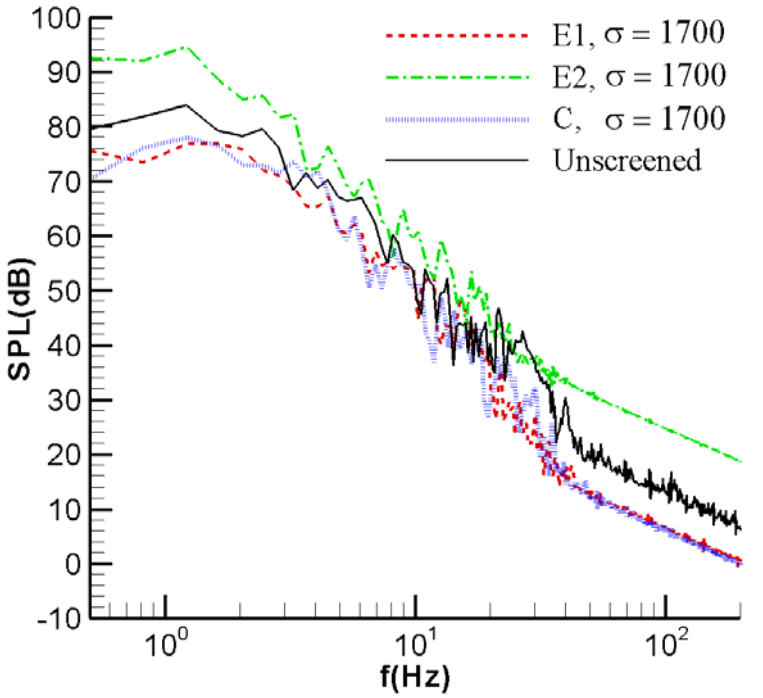

(f) σ = 1700 Pa·s/m^2, different shapes

Figure 4-34 SPL at the center point of the microphone (all values are dimensionless, Re = 5000)

Finally, in order to clearly quantify the wind noise reduction effect, we investigate wind noise reduction (WNR) levels between the unscreened microphone and the screened microphone, defined as: $WNR = SPL_{unscreened\ \ center} - SPL_{screened\ \ center}$, by subtracting the SPL at the screened microphone center from that at the unscreened microphone center. In Figure 4-35, the WNR for comparing different resistivities with the same windscreen shape is plotted in sub figures 4-35(a-c), and the WNR for comparing different windscreen shapes with the same flow resistivity windscreen is plotted in sub figures 4-35(d-f). It can be seen among all the cases, the highest WNR is around 22dB, which is a very significant wind noise reduction in a case of E1 with the medium flow resistivity in the frequency around 30 Hz. On the other hand, significant noise increase, with a negative WNR level of approximately 16 dB, can occur by using a vertical elliptical (E2) windscreen with a high flow resistivity porous material in the frequency range of a few Hz to 15 Hz. Therefore the windscreen shape influences the WNR behavior significantly, although flow resistivity and frequency range also have influence.

The overall behaviors of the WNR between the circular cylinder and horizontal ellipse windscreens are similar, for which the lowest flow resistivity windscreens (σ = 17 Pa·s/m^2) have less noise reduction than the other two higher flow resistivity screens (σ = 170 and 1700 Pa·s/m^2); the horizontal ellipse windscreens work a little better than the circular windscreens. The vertical ellipse windscreens are not effective, especially for the high flow resistivity cases when additional self-noise is generated to cause negative WNR.

For the circular cylinder cases in sub figure 4-35(a), the medium and high resistivity materials are more effective in the lower frequency range (f < 10Hz) while the low resistivity material has more effect in the higher frequency range (f > 10Hz). For the horizontal ellipse cases in sub figure 4-35(b), the medium resistivity is the most effective one among the three

resistivities in almost all the frequency range. For the vertical ellipse cases in Fig. 5(c), the low resistivity resistivity has more effect in most frequency ranges than the other two, while the high resistivity windscreen has even adverse effects in noise reduction.

Here we point out more detailed numbers of some high WNR levels for each case from sub figures 4-35(d-f). For the low flow resistivity windscreens in sub figures 4-35(d) (σ = 17 Pa·s/m^2), the high WNR levels for the C case are about 17 dB at 10 Hz, about 20 dB at 20 Hz and 30 Hz; the highest WNR levels for the E1 case are about 10 dB at 10 Hz, about 20 dB at 20 Hz, and about 18 dB at 30 Hz; the high WNR levels for the E2 case are about 12 dB at 10 Hz, about 15 dB at 20 Hz and 30 Hz. For the medium flow resistivity windscreens in sub figure 4-35 (e) (σ = 170 Pa·s/m^2), the high WNR levels for the C case are about 17 dB at 20Hz, about 19 dB at 30Hz, and about 13 dB at 40 Hz; the high WNR levels for the E1 case are about 20 dB at 20 Hz, about 24 dB at 27 Hz, and about 18 dB at 31 Hz; the high WNR levels for the E2 case are about 9 dB at 10 Hz, and about 6 dB at 27 Hz. For the large flow resistivity windscreens in sub figure 4-35 (f) (σ = 1700 Pa·s/m^2), the high WNR levels for the C case are about 14 dB at 10 Hz, about 17 dB at 20 Hz, and about 15 dB at 40 Hz; the high WNR levels for the E1 case are about 9 dB at 20 Hz, about 19 dB at 30 Hz, and about 15 dB at 40 Hz; the high WNR levels for the E2 case are about 4 dB at 20 Hz, and about 6 dB at 27 Hz. In summary, the medium flow resistivity windscreens (σ = 170 Pa·s/m^2) perform best and achieve the highest wind noise reduction level. The circular cylinder and the horizontal ellipse windscreens behave similarly overall, while the vertical ellipse windscreens do not provide significant WNR and, in fact, if made with high flow resistivity materials, they increase the wind noise in most frequency range.

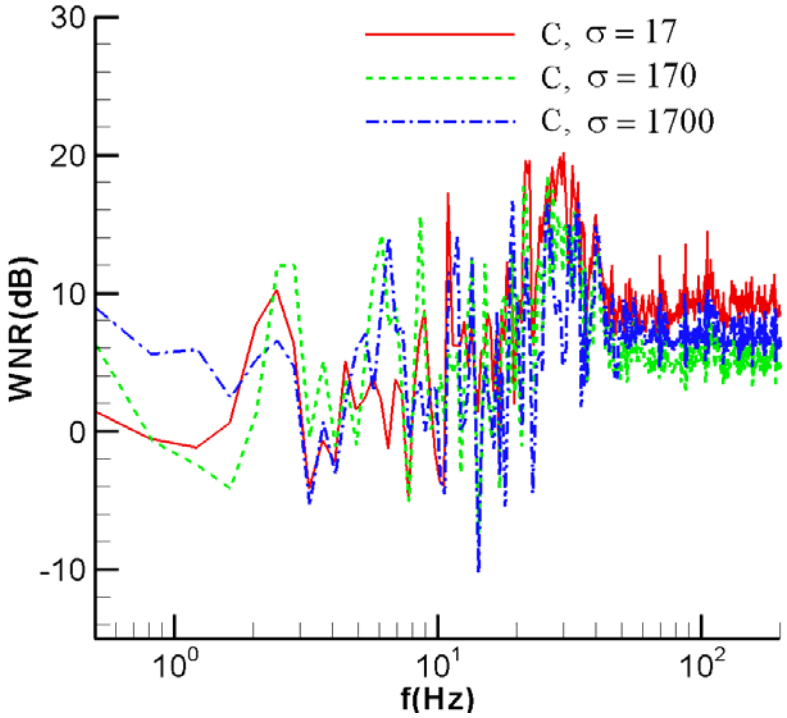

(a) C cases, different flow resistivities

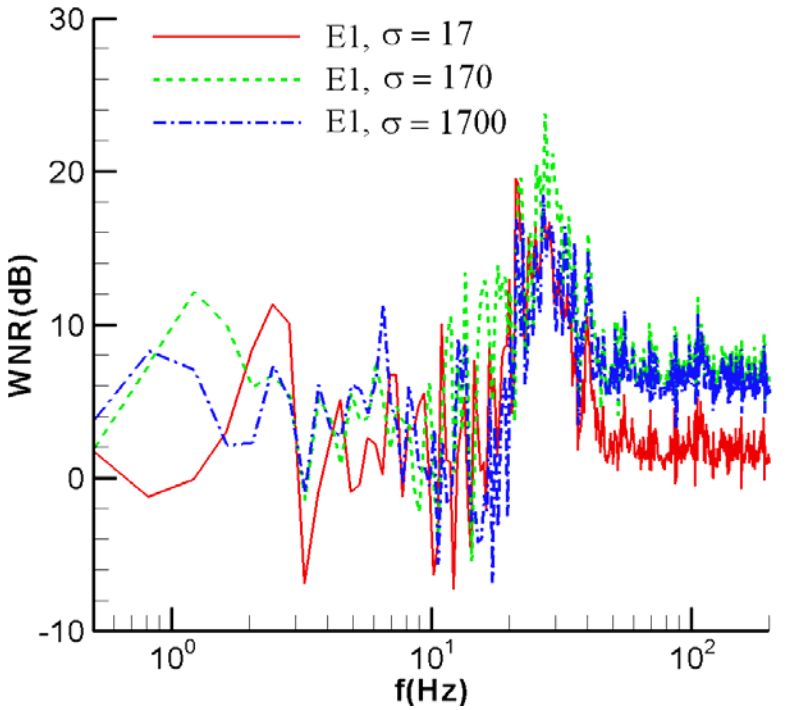

(b) E1 cases, different flow resistivities

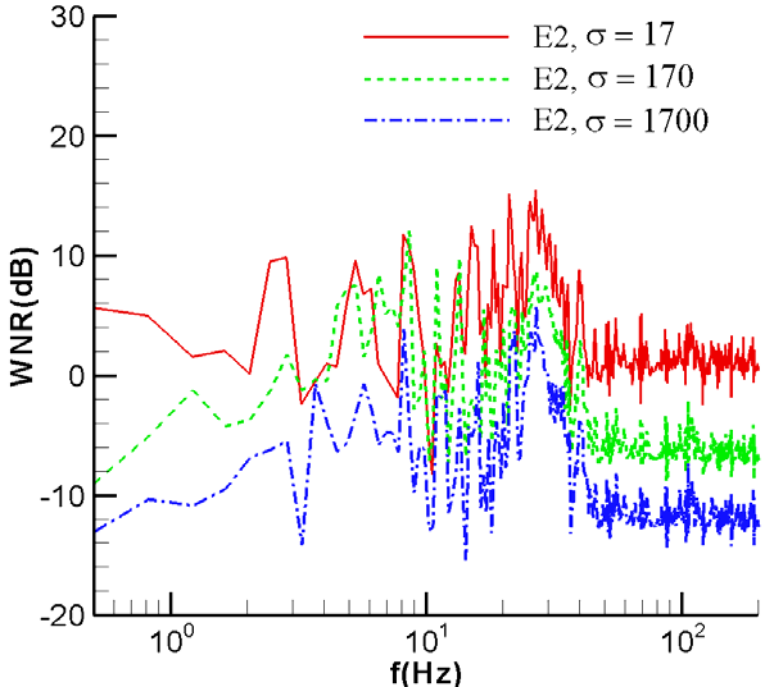

(c) E2 cases, different flow resistivities

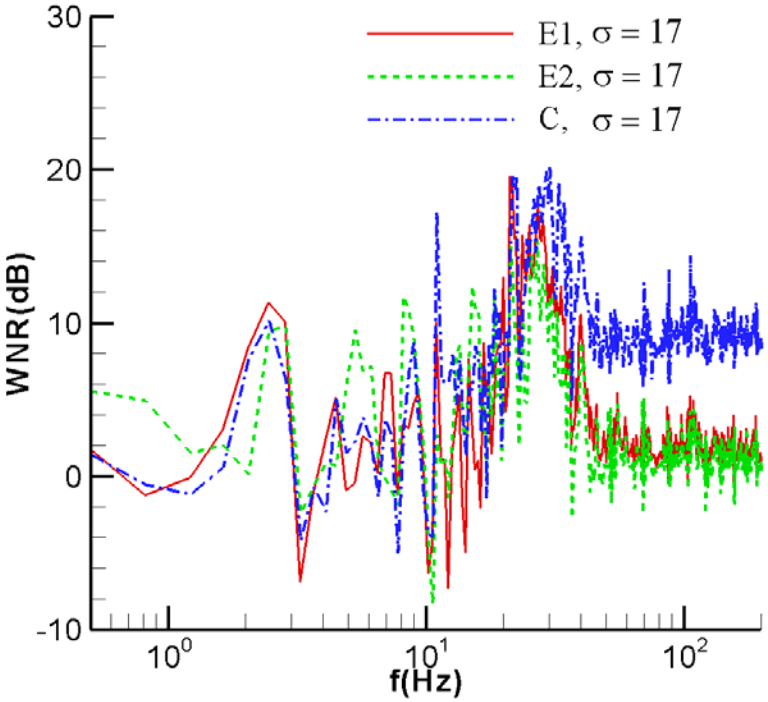

(d) σ = 17 Pa·s/m^2, different shapes

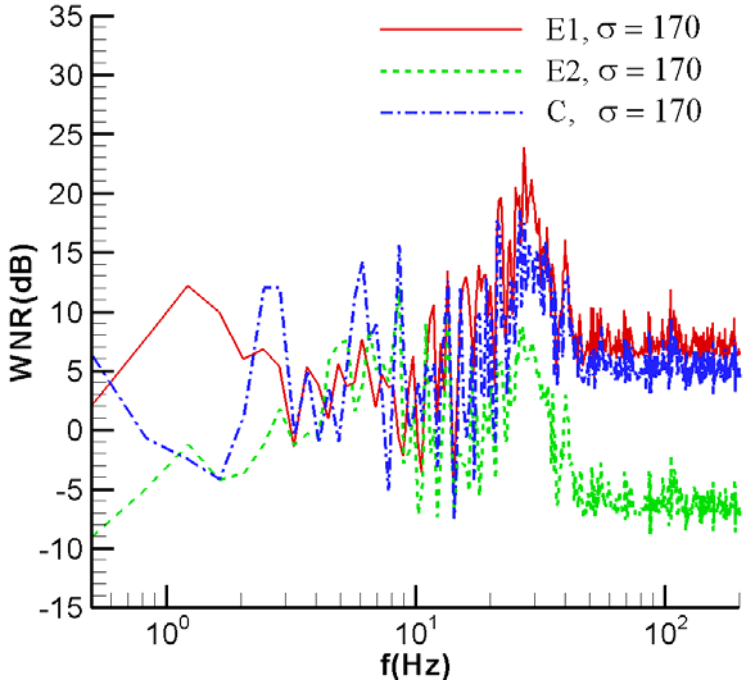

(e) σ = 170 Pa·s/m^2, different shapes

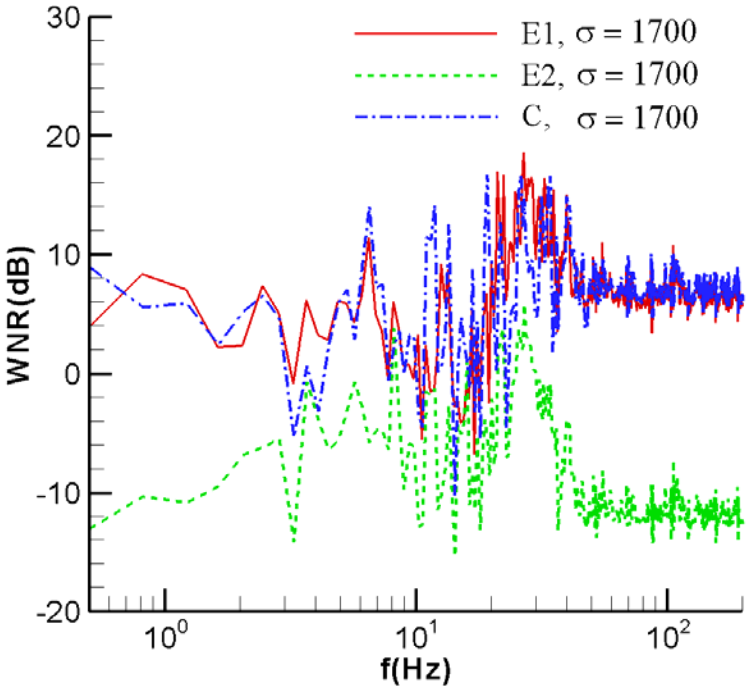

(f) σ = 1700 Pa·s/m2, different shapes

Figure 4-35 WNR between the unscreened microphone center and the screened microphone center (all values are dimensionless, Re = 5000)

To clarify the quantitative value for wind noise reduction between the unscreened microphone center and the screened microphone center, table 4-3 offers the most significant sound level reductions. In particular, the three-sub tables document the same resistivity but using different windscreen shapes (C, E1, and E2). It should be noted that the symbol "-" used in Table 4-1 means negative values (no windscreen effects).

Table 4-3 WNR between unscreened microphone center and screened microphone center (Different shape cases, Re = 5000)

(a) Resistivity σ = 17 Pa·s/m^2

Shape / Frequency(Hz)	C	E1	E2
11.0	17.3	10.0	11.8
16.7	12.2	8.7	12.1
21.6	19.6	19.5	15.1
27.3	19.1	17.5	15.4
30.9	20.2	13.6	9.4
40.0	15.7	10.6	8.7

(b) Resistivity σ = 170 Pa·s/m^2

Shape / Frequency(Hz)	C	E1	E2
11.0	5.7	10.5	9.1
16.7	7.3	12.9	5.5
21.6	17.0	19.7	5.8
27.3	18.6	23.8	6.0
30.9	15.1	17.8	5.2
40.0	13.1	6.0	3.1

(c) Resistivity σ = 1700 Pa·s/m^2

Shape / Frequency(Hz)	C	E1	E2
11.0	14.2	9.1	-
16.7	12.2	9.2	-
21.6	16.7	16.9	3.8
27.3	14.7	18.5	5.9
30.9	14.9	14.6	2.4
40.0	14.7	14.8	-

CHAPTER 5 - 3D Simulation and Results

This chapter discusses the three-dimensional simulation and mainly includes two parts. The first part introduces and discusses the flow over a screened microphone under a low Reynolds number (Re = 500) will be introduced and discussed; the second part introduces and discusses the flow over a screened microphone under a high Reynolds number (Re = 5000).

5.1 Problem Description

The three-dimensional model problem is shown in Figure 5-1, where a stream of unsteady and/or turbulent flow approaches a cylindrical unscreened or screened microphone. The windscreen, when present, is made of a porous material. Because of the unsteadiness and surface conditions, flow fluctuations and vortical structures are generated around the surface and in the wake region. The pressure fluctuations sensed by the microphone, which are assumed to be at the center of the screen, result from near-field, incompressible disturbances. The flow fluctuations, both internal and external to the windscreen, are investigated based on coupled flow simulation between the outside and inside of the windscreen. We have developed an immersed-boundary (IB) computational method suitable for simulations in which a windscreen is immersed in a background flow. The important issue is to study the wind noise reduction (WNR) effect of the windscreen. Specially, we want to know the sound pressure level (SPL) difference between the unscreened microphone center (measurement point in the sub-figure (a) in Figure 5-1) and the screened microphone center (measurement point in the bottom sub-figure (b) in Figure 5-1) for different windscreen under different wind turbulence. The detailed computational scheme can be referenced in chapter 2 and 3.

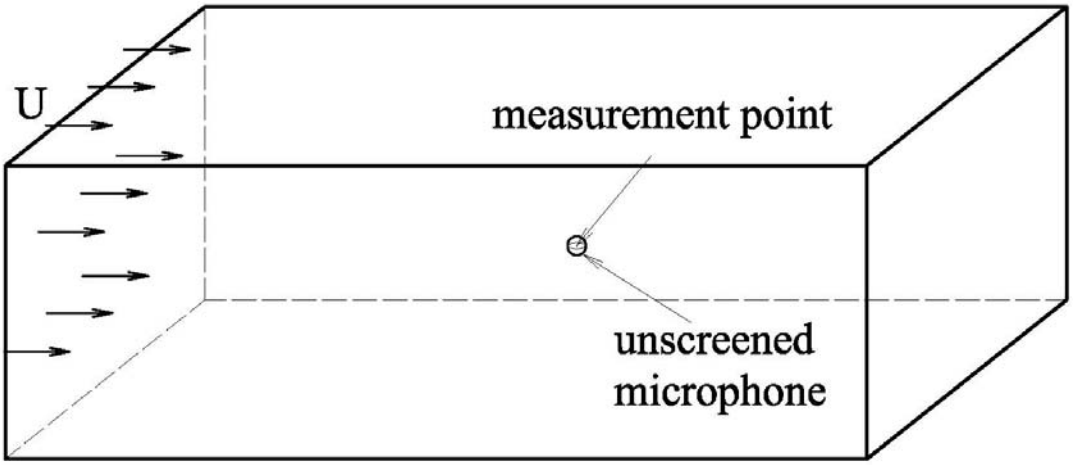

(a) unscreend microphone

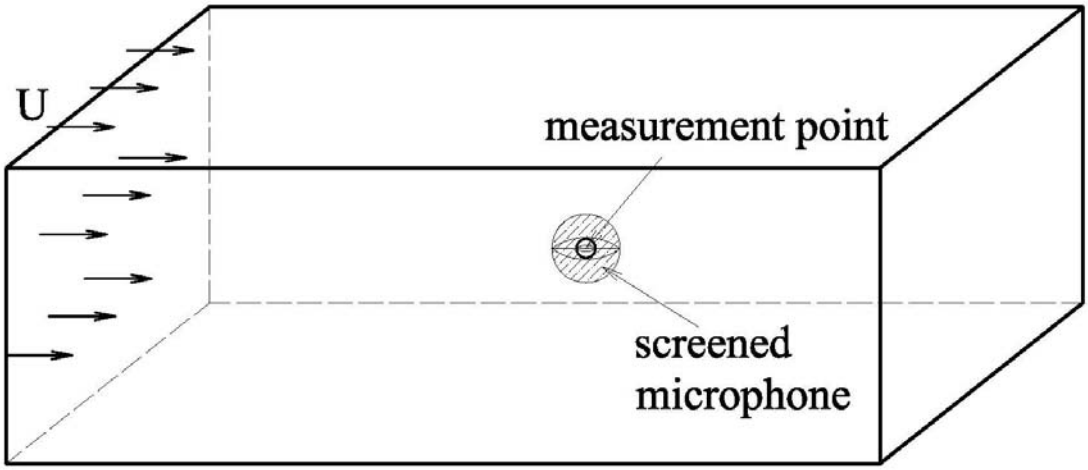

(b) screend microphone

Figure 5-1 Illustration of the model problem

The model equation is the Momentum equation for incompressible flow outside the porous microphone:

$$\frac{\partial \vec{\mathrm{v}}}{\partial t} + (\vec{\mathrm{v}} \cdot \nabla)\vec{\mathrm{v}} = -\nabla p + \frac{1}{\mathrm{Re}} \nabla^2 \vec{\mathrm{v}} \tag{5.1}$$

A modified ZK equation models the flow inside the windscreen (The windscreen is considered to be a porous medium with the porosity and the structure constant set to 1 for simplicity):

$$\frac{\partial \vec{\mathrm{v}}}{\partial t} + (\vec{\mathrm{v}} \cdot \nabla)\vec{\mathrm{v}} = -\nabla p + \frac{1}{\mathrm{Re}} \nabla^2 \vec{\mathrm{v}} - \sigma \vec{\mathrm{v}} \tag{5.2}$$

Notably, although we are studying acoustic phenomena, and therefore the fluid is compressible, the pressure fluctuations that we are interested in are near the surface of an object or inside a porous medium. These pressure fluctuations are considered in the near field to be caused by flow fluctuations, such as the surface pressure fluctuations produced by a turbulent boundary layer over the surface addressed by Kraichnan (1956), where the incompressible flow assumption is well justified.

Figure 5-2 shows the numerical model for the three dimensional case. The wind turbulence is generated by placing a solid sphere upstream of the microphone. The diameter of the sphere is D and the free-stream velocity as U. We selected 1.0D diameter sphere to generate the flow field. The distance, L, between the first sphere center and the second windscreen sphere is 6D.

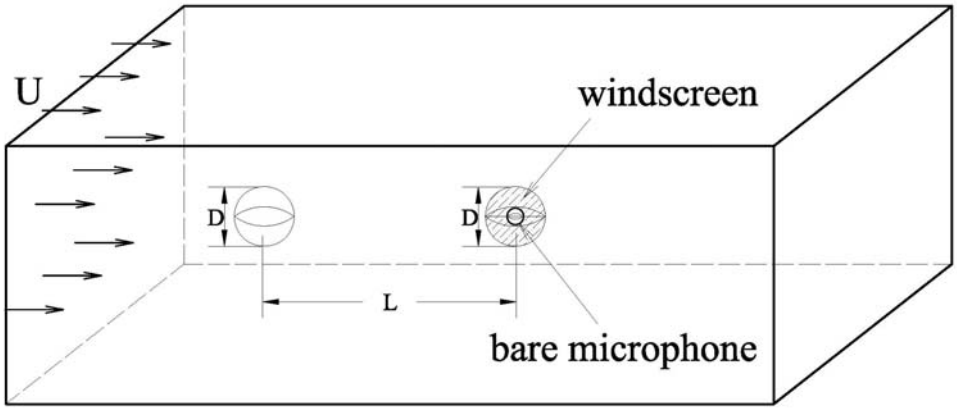

Figure 5-2 Illustration of the incoming wind turbulence generation

The computation is performed on a staggered Cartesian grid mesh. For the boundary conditions, at the inlet, $u = 1$, $v = w = 0$, and $\partial p / \partial x = 0$. For the bottom and top, $\partial u / \partial y = 0$, $v = w = 0$, and $\partial p / \partial y = \partial p / \partial z = 0$. For the outlet, $\partial u / \partial x = 0$, $\partial v / \partial x = \partial v / \partial x = 0$, and $p = 0$. The domain size is 19.2X4.8X4.8 (L*W*H), and the grid size dx = dy = dz = 0.05. The center of the first solid sphere is located a 4D unit length from the inlet boundary.

The following sections investigates the flow over the windscreen problem first under a low Reynolds number (Re = 500) and then with a high Reynolds number (Re = 5000).

5.2 Low Reynolds Number (Re = 500) Cases

For the cases with a low Reynolds number, $\mathrm{Re} = \frac{UD}{\nu} = \frac{1m/s \cdot 0.0075m}{1.5 \times 10^{-5} m^2/s} = 500$, approximately characterizes a windscreen with a diameter of 0.75cm and a wind speed of 1m/s for the incoming air. Also, the bare microphone (unscreened) is set with a diameter of 0.1875cm. Finally, the four values of dimensionless flow resistivity of the windscreen are 0.2, 2, 20 and 200, corresponding to approximately 34, 340, 3400 and 34000 Pa·s/m^2 of dimensional flow resistivity, respectively.

We first investigated the whole flow field as shown by the Z-direction vorticity contours in Figure 5-3 for different flow resistivity cases (34, 340, 3400, 34000 Pa·s/m^2 and also unscreened). The incoming free stream is X direction and normal to YZ plane. The Z-direction vorticity contour is chosen at the XY plane with Z = 0 (through microphone sphere center). The red color in the figures represents positive vorticity (in the counter clockwise sense, with the upper limit value of 5), the blue color represents negative vorticity (in the clockwise sense, with the lower limit value of -5). Next, Figure 5-4 shows the iso-surface of vorticity magnitude of the whole flow field (the selected iso-surface value is 2). Clearly, there is no flow inside the solid bare

microphone, but some flow infiltrates the windscreened porous sphere. When the flow resistivity reaches high enough values (σ = 34000 Pa·s/m^2) little flow permeates the porous sphere, as with a solid sphere. However, when the flow resistivity is small (σ = 34 Pa·s/m^2) much flow permeates the porous sphere, as if there is no windscreen. Finally, with the flow resistivity very low (less than 10 Pa·s/m^2), the flow permeates the porous cylinder as if the walls do not exist.

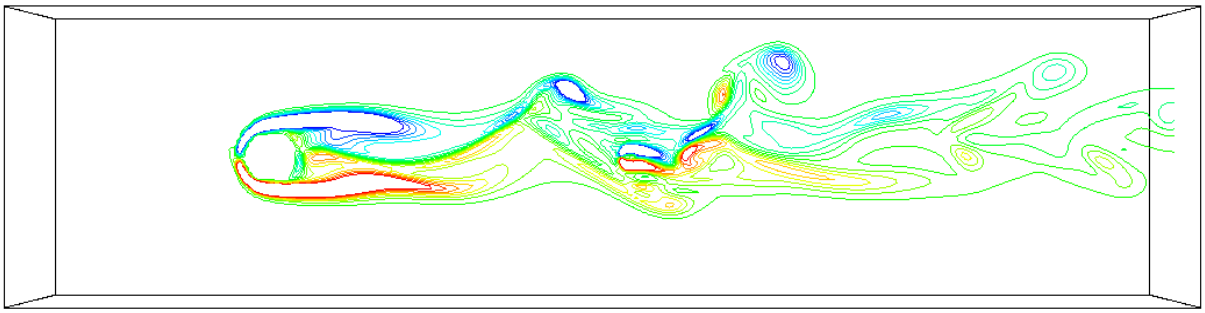

(a) σ = 34 Pa·s/m^2

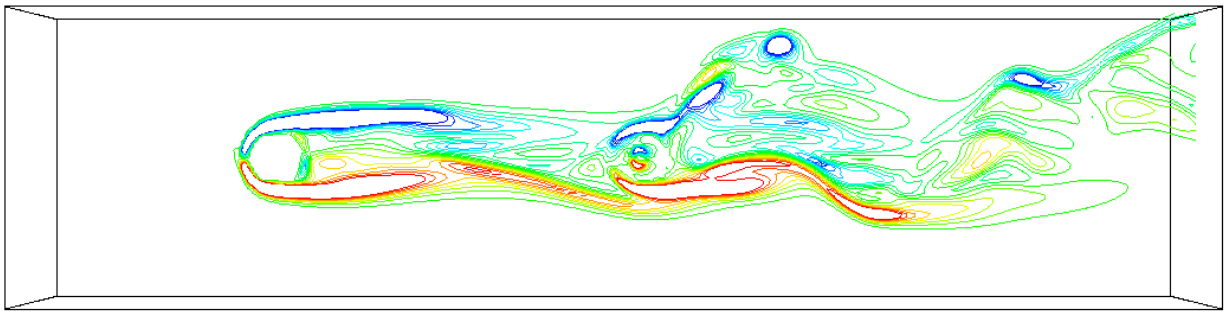

(b) σ = 340 Pa·s/m^2

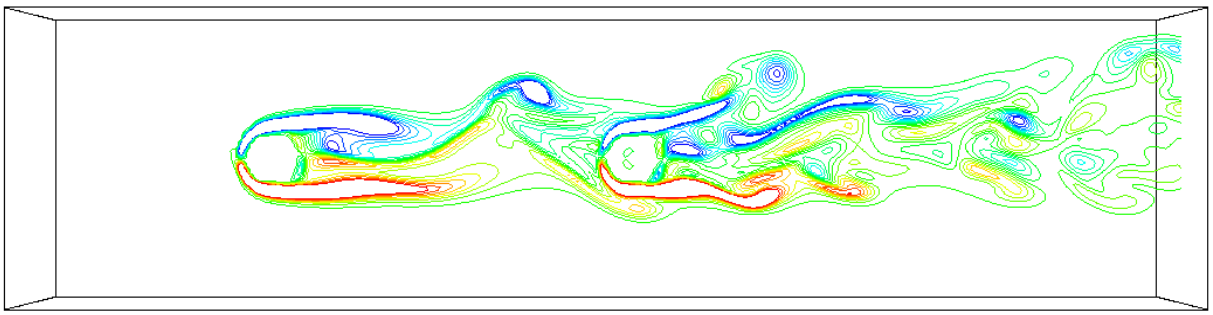

(c) σ = 3400 Pa·s/m^2

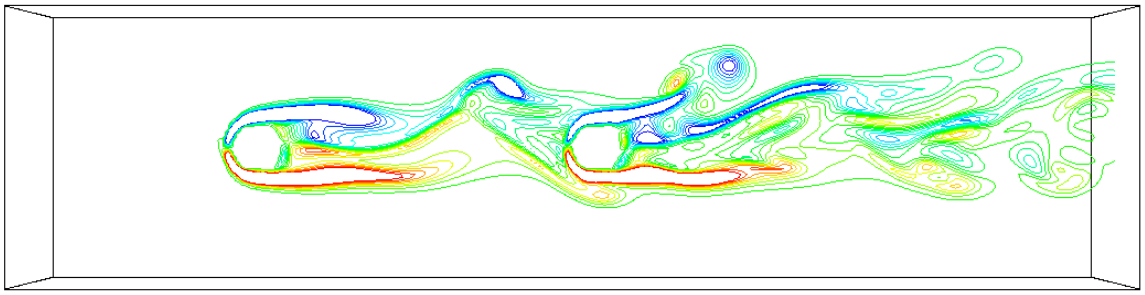

(d) σ = 34000 Pa·s/m^2

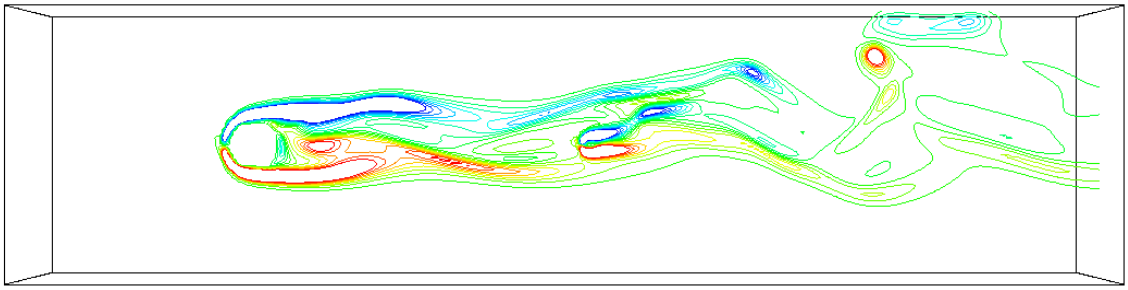

(e) unscreened

Figure 5-3 Z-Vorticity contours of flow field (Re = 500)

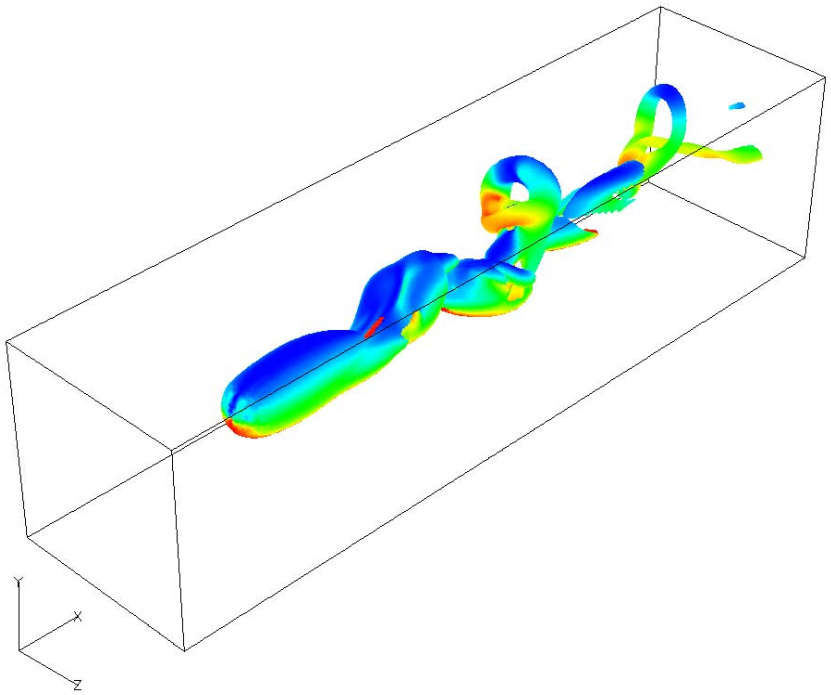

(a) σ = 34 Pa·s/m^2

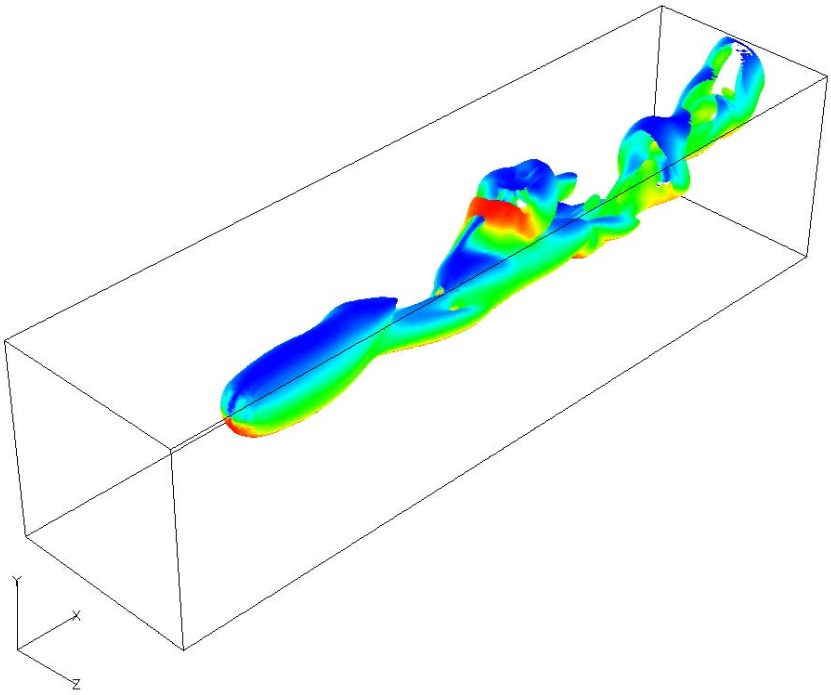

(b) σ = 340 Pa·s/m^2

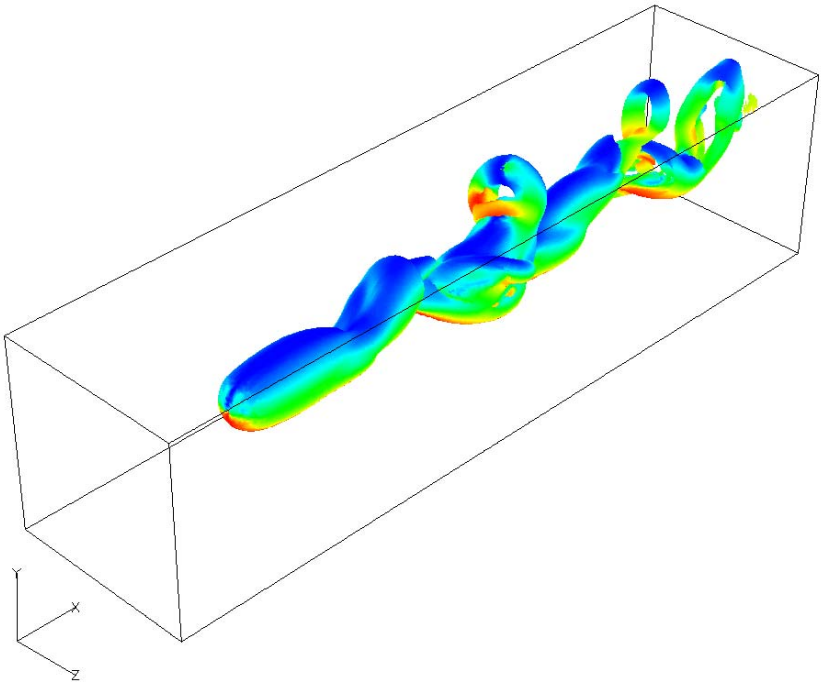

(c) σ = 3400 Pa·s/m^2

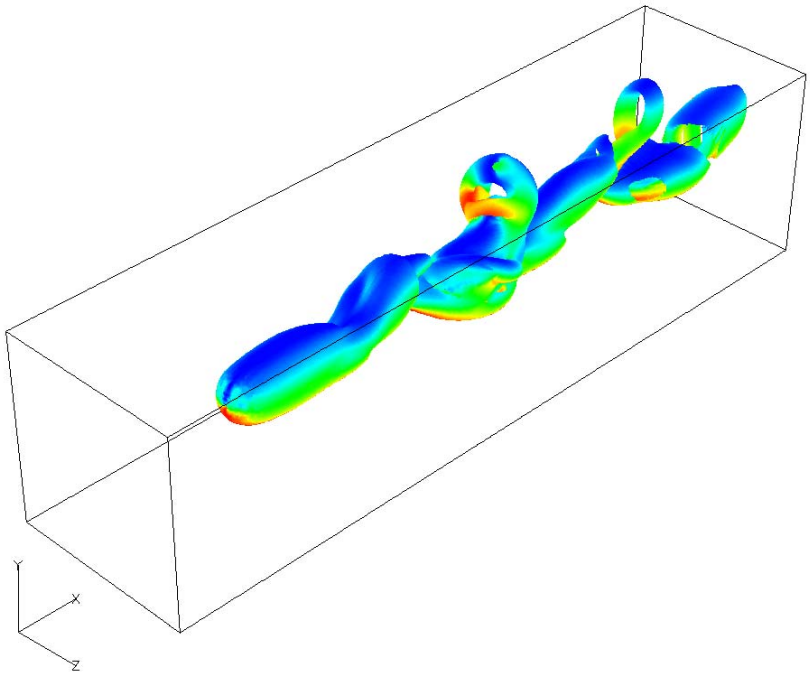

(d) σ = 34000 Pa·s/m^2

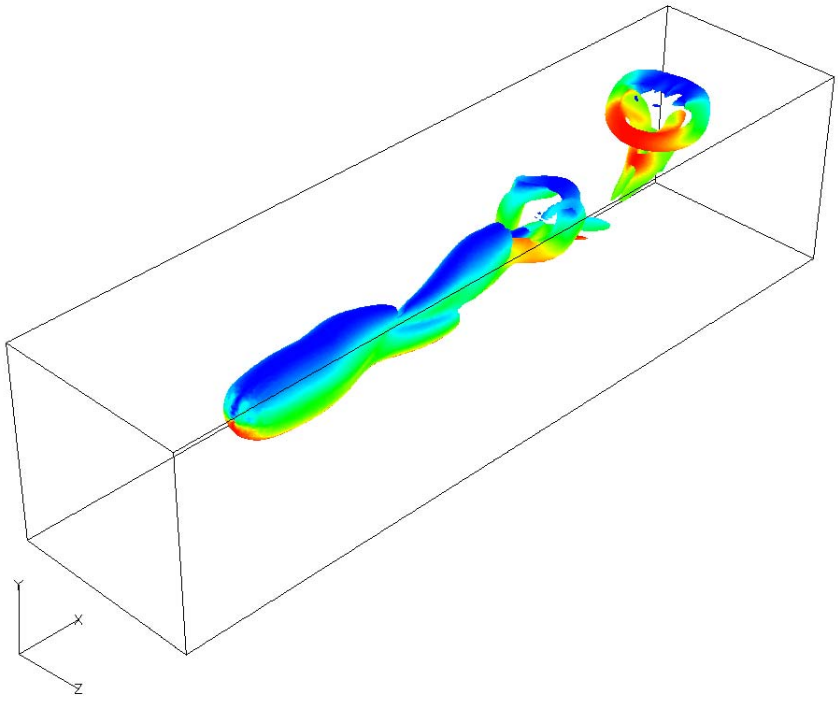

(e) unscreened

Figure 5-4 Iso-surface of Vorticity Magnitude of flow field (Re = 500)

Figure 5-5 shows the pressure time history of the center point of the microphone (measurement point in Figure 5-1). Obviously, the fluctuation magnitude of the unscreened center pressure is the highest compared to the windscreened sphere cases, which means the windscreen has the effect of wind noise reduction (WNR). Also, for a long-duration simulation, the pressure time history reaches a quasi-steady state, which will be convenient for pressure signal post-processing. The figure also clarifies that the shape trend of the lowest flow resistivity case (σ = 34 Pa·s/m^2, red dash line) is similar to that of the unscreened case (black solid line), which means as the resistivity goes very small, the windscreen effect will disappear as if there is no windscreen. Finally, the pressure fluctuation of the medium resistivity case (σ = 3400 Pa·s/m^2, cyan dotted line) seems the smallest for all windscreened cases.

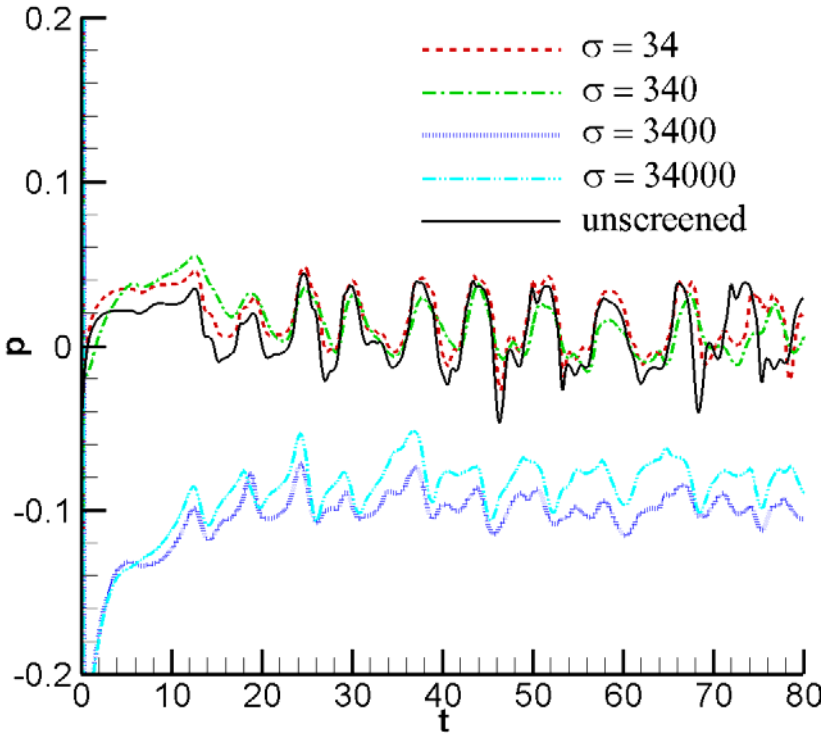

Figure 5-5 Pressure time histories at center point of the microphone sphere (all values are dimensionless, Re = 500)

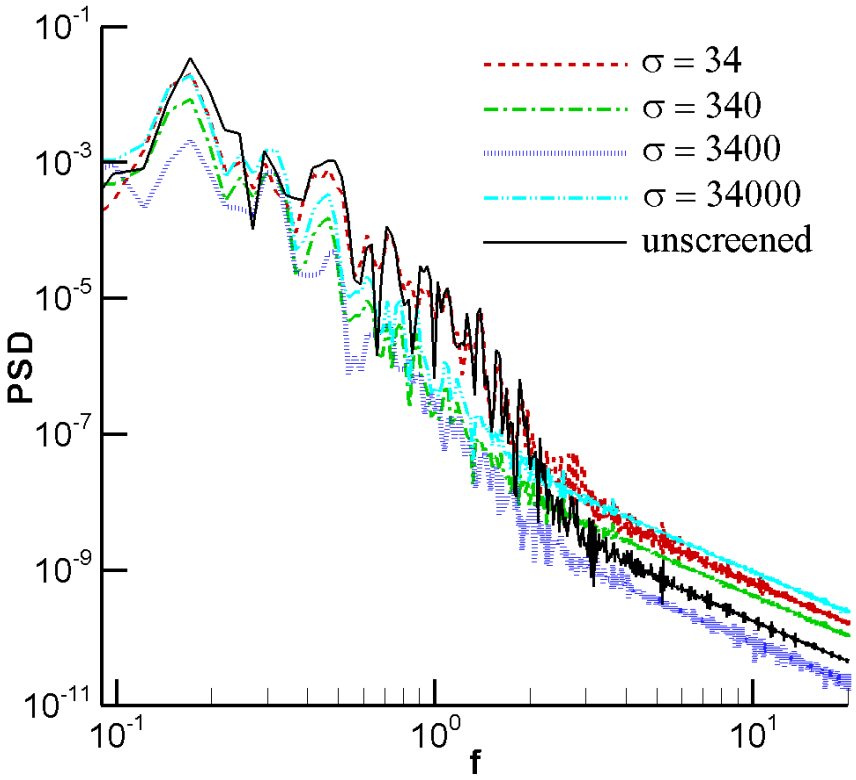

Figure 5-6 PSD at the center point of microphone sphere (all values are dimensionless, Re = 500)

Figure 5-6 shows the pressure PSD at the center point of the microphone. It includes five curves: one for the unscreened bare microphone case and for the other windscreened cases with four flow resistivities: 34, 340, 3400, and 34000 Pa·s/m^2 (corresponding to dimensionless values 0.2, 2, 20 and 200 separately). It should be noted here that all results in Figure 5-6 are dimensionless. The first frequency peak for all cases is around 0.2, which conforms to the Strouhal theory (for spheres in uniform flow the Strouhal number is attributed to the large-scale instability of the wake and is independent of the Reynolds number and is approximately equal to 0.2). In this figure, the black solid line represents the unscreened case, and obviously the unscreened case has the highest PSD level compared to the windscreened cases, which is easily understandable given the windscreen effects. It also shows that the windscreen effect is distinct

in the dimensionless frequency range between 0.2 and 2. It also can be seen from Figure 5-6 that the PSD shape of the unscreened microphone case is very similar to that of the lowest windscreen flow resistivity case (σ =34 Pa·s/m^2), which conforms to the previous investigation of pressure time history in Figure 5-5. Specifically, Fgure5-6 shows that the medium resistivity case (σ = 3400 Pa·s/m^2, blue dotted line) has the smallest PSD level for all five cases, which also conforms to the previous discussion of Figure 5-5.

Figure 5-7 shows the sound pressure level (SPL) at the center point of the microphone. It has five curves: one for the bare microphone case and the other four for the screened microphone cases with different flow resistivities: 34, 340, 3400, and 34000 Pa·s/m^2. It should be noted here that all the data in Figure 5-7 are dimensional for real physical phenomena. It shows that the windscreen effect happens mostly in the frequency range of 25Hz to 300Hz. In this range, the SPL value of the screened cases (σ = 340, 3400 and 34000 Pa·s/m^2) is remarkably smaller than that of the unscreened case. Also, the SPL shape of the lowest windscreen flow resistivity case (σ = 34 Pa·s/m^2) is very similar to that of the unscreened microphone case, which means the windscreen effect is pretty small as the flow resistivity of porous material is very small. Additionally, the screened cases (σ = 340, 3400 and 34000 Pa·s/m^2) all have a similar SPL shape in Figure 5-7. In particular, the medium resistivity case (σ = 3400 Pa·s/m^2, purple dotted line) has the smallest SPL value in most frequency range which means the biggest SPL difference between the unscreened microphone and the screened microphone should happen in the medium resistivity case.

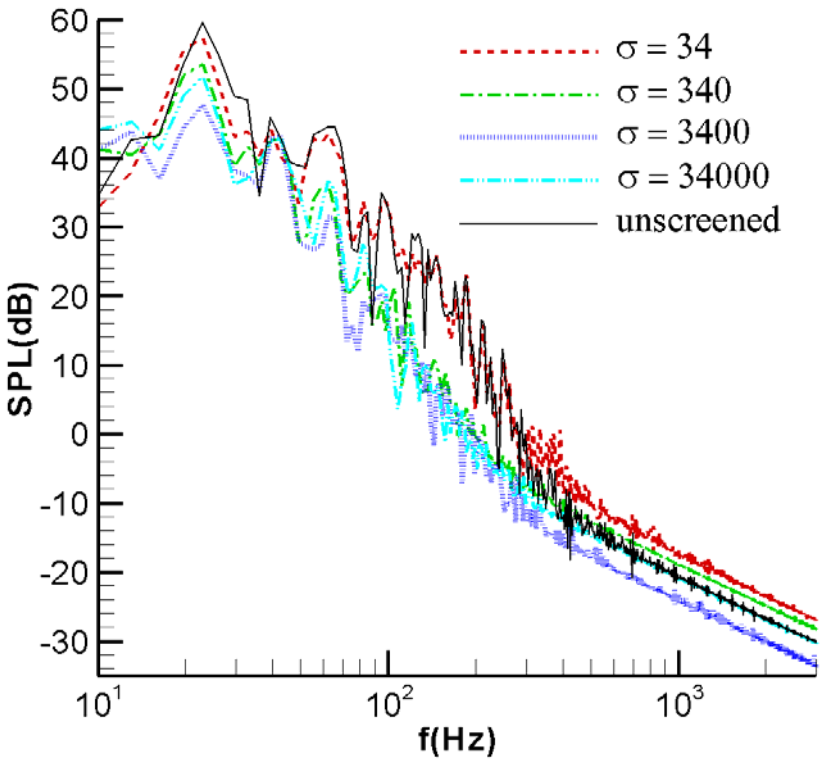

Figure 5-7 SPL at the center point of the microphone sphere (all values are dimensional, Re = 500)

Next, we investigate wind noise reduction level (WNR) between the unscreened microphone and the screened microphone, defined as: $WNR = SPL_{unscreened\ \ center} - SPL_{screened\ \ center}$, by subtracting the SPL at screened microphone center from that at unscreened microphone center. Figure 5-8 shows the WNR, which comprises four curves: bare microphone minus four screened microphones with different flow resistivities (σ = 34, 340, 3400 and 34000 Pa·s/m^2). Here, the highest WNR is around 26dB, which shows very significant windscreen effects. Moreover, the WNR between the unscreened and lowest flow resistivity (σ = 34 Pa·s/m^2, red solid line) is lower than the other three higher flow resistivity screens (σ = 340, 3400 and 34000 Pa·s/m^2), which means there is little windscreen effect as the flow resistivity is very small. Apparently, the medium flow resistivity windscreen (σ = 3400 Pa·s/m^2) performs best in the frequency range

from 25Hz to 300Hz, and its WNR value is the highest among the three windscreened cases (σ = 340, 3400 and 34000 Pa·s/m^2). The highest flow resistivity windscreen (σ = 34000 Pa·s/m^2) also performs well, and it has similar WNR shape compared to the medium flow resistivity windscreen (σ = 3400 Pa·s/m^2). Also, the value is a little smaller than for the medium flow resistivity windscreen.

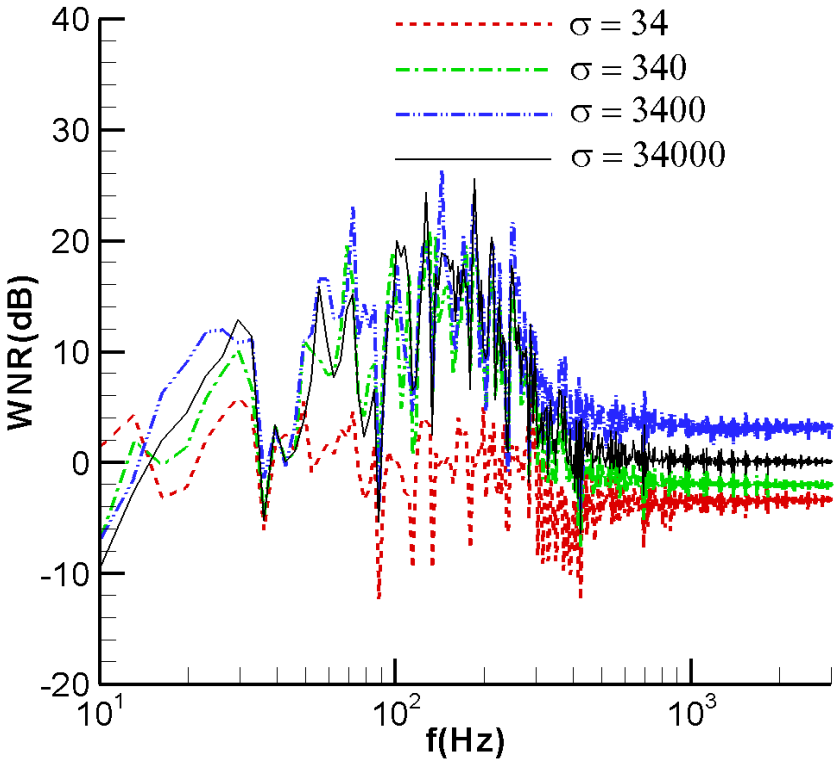

Figure 5-8 WNR between unscreened microphone center and screened microphone center (all values are dimensional, Re = 500)

To clarify the quantitative value for the wind noise reduction between the unscreened microphone center and the screened microphone center, Table 5-1 shows the most significant wind noise reductions.

Table 5-1 WNR between unscreened microphone center and screened microphone center (3D cases, Re = 500)

Resistivity (Pa·s/m^2) / Frequency(Hz)	34	340	3400	34000
26.0	5.9	10.1	11.9	12.1
55.3	5.5	11.1	16.6	15.5
71.6	4.6	19.5	23.1	15.2
143.2	3.2	15.9	26.4	24.3
182.3	4.9	18.9	23.3	20.0
250.7	1.6	15.3	21.6	16.9
296.2	2.9	7.5	11.8	9.8

Table 5-1 shows that for the low flow resistivity case (σ = 34 Pa·s/m^2), the highest WNR levels are about 6 dB at 26 Hz. For the medium flow resistivity (σ = 340 Pa·s/m^2), the highest WNR levels are about 19.5 dB at 71.6Hz, and about 18.9 dB at 182.3Hz. For the medium flow resistivity (σ = 3400 Pa·s/m^2), the high WNR levels are about 23.1 dB at 71.6Hz, 26.4 dB at 143.3 Hz, and 23.3 dB at 182.3Hz. For the highest flow resistivity (σ = 34000 Pa·s/m^2), the highest WNR levels are about 24.3 dB at 143.2Hz, and 20.0 dB at 182.3 Hz. Generally speaking, the lowest flow resistivity windscreen (σ = 34 Pa·s/m^2) has very little wind noise reduction and seems to have no windscreen effects; the medium flow resistivity windscreen (σ=3400 Pa·s/m^2) has the highest wind noise reduction and seems to have the most windscreen effects; finally, the largest flow resistivity windscreen (σ = 34000 Pa·s/m^2) has similar but fewer windscreen effects compared to the medium resistivity case (σ = 3400 Pa·s/m^2).

5.3 High Reynolds Number (Re = 5000) Cases

For the cases for a high Reynolds number, $\mathrm{Re} = \frac{UD}{\nu} = \frac{1m/s \cdot 0.075m}{1.5 \times 10^{-5} m^2/s} = 5000$,

approximately characterizes a windscreen with a diameter of 7.5cm and a wind speed of 1m/s for the incoming air. Also a bare microphone (unscreened) is set with a diameter of 1.875cm. Four values of dimensionless flow resistivity of the windscreen are 0.2, 2, 20 and 200, corresponding to approximately 3.4, 34, 340 and 3400 Pa·s/m^2 of dimensional flow resistivity, respectively.

We first investigated the whole flow field as shown by the Z-direction vorticity contours in Figure 5-9 for different flow resistivity cases (3.4, 34, 340, 3400 Pa·s/m^2 and also unscreened). The incoming free stream is X direction and normal to YZ plane. The Z-direction vorticity contour is chosen at the XY plane with Z = 0 (through microphone sphere center). The red color in the figures represents positive vorticity (in the counter clockwise sense, with the upper limit value of 10), the blue color represents negative vorticity (in the clockwise sense, with the lower limit value of -10). Next, Figure 5-10 shows the iso-surface of vorticity magnitude of the whole flow field (the selected iso-surface value is 2). There is no flow inside the solid bare microphone, but some flow infiltrates the windscreened porous sphere. When the flow resistivity reaches high enough values (σ = 3400 Pa·s/m^2), little flow permeates the porous sphere, as if it is like a solid wall boundary. When the flow resistivity is low (σ = 3.4 Pa·s/m^2), much flow permeates the porous sphere, as if there is no windscreen. Compared to previous low Reynolds number cases (Re = 500), the high Reynolds number cases generate stronger structural vortices, especially around the zone of the windscreened sphere.

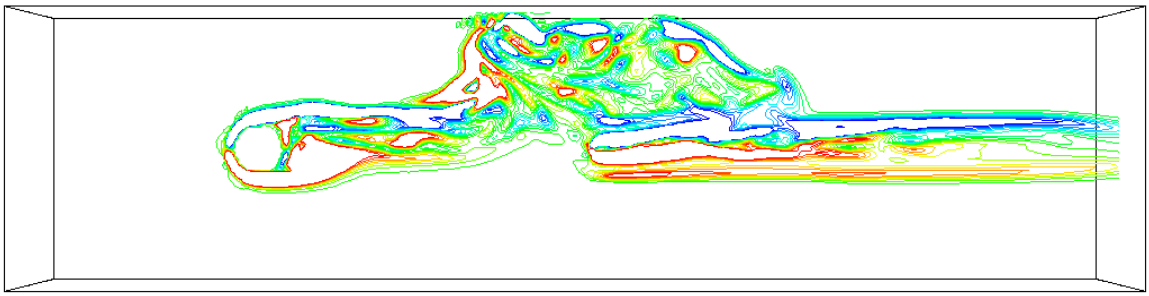

(a) σ = 3.4 Pa·s/m^2

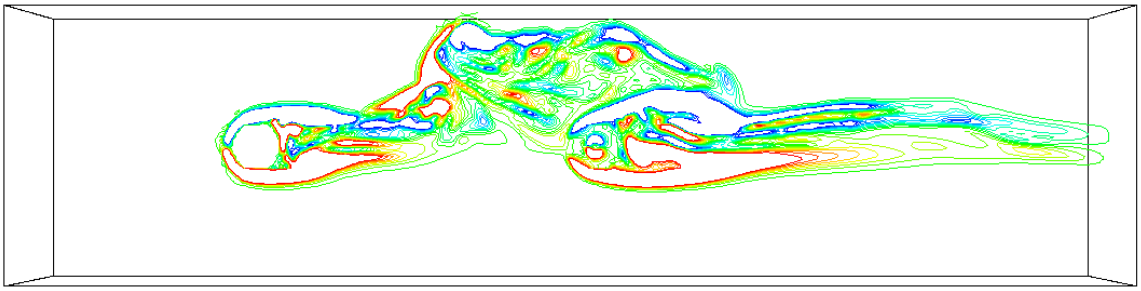

(b) σ = 34 Pa·s/m^2

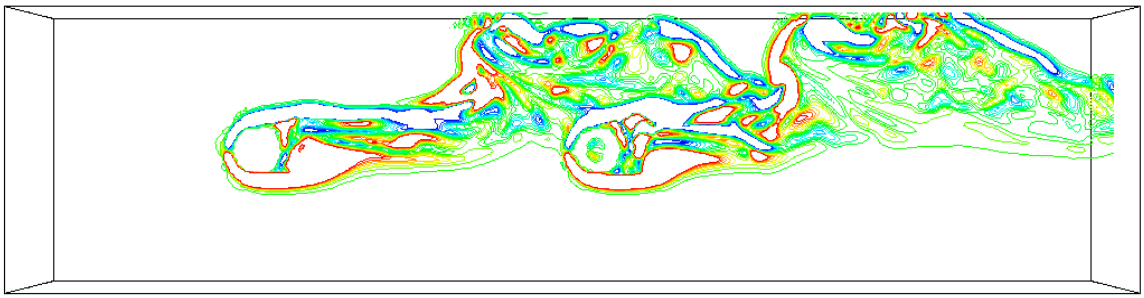

(c) σ = 340 Pa·s/m^2

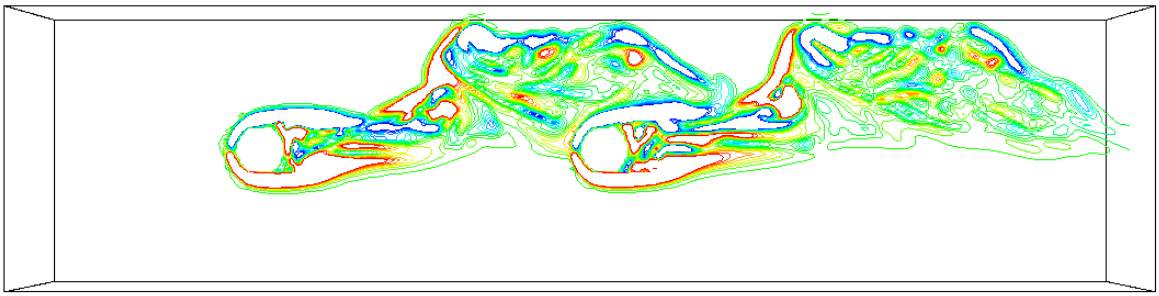

(d) σ = 3400 Pa·s/m^2

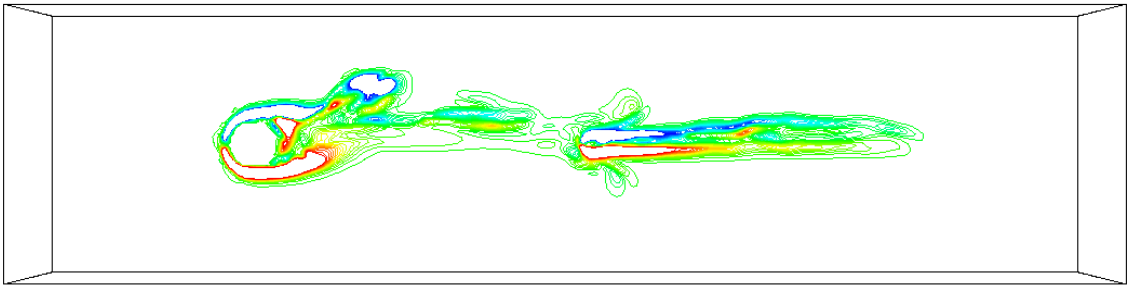

(e) unscreened

Figure 5-9 Z-Vorticity contours of flow field (Re = 5000)

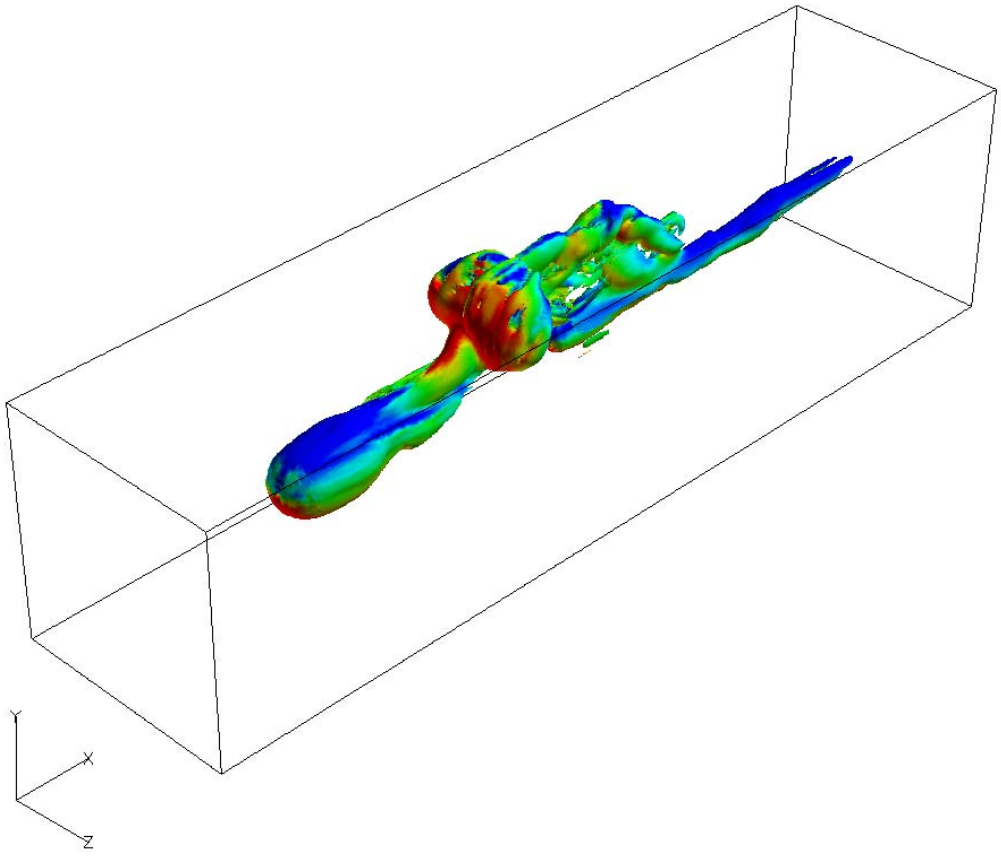

(a) σ = 3.4 Pa·s/m^2

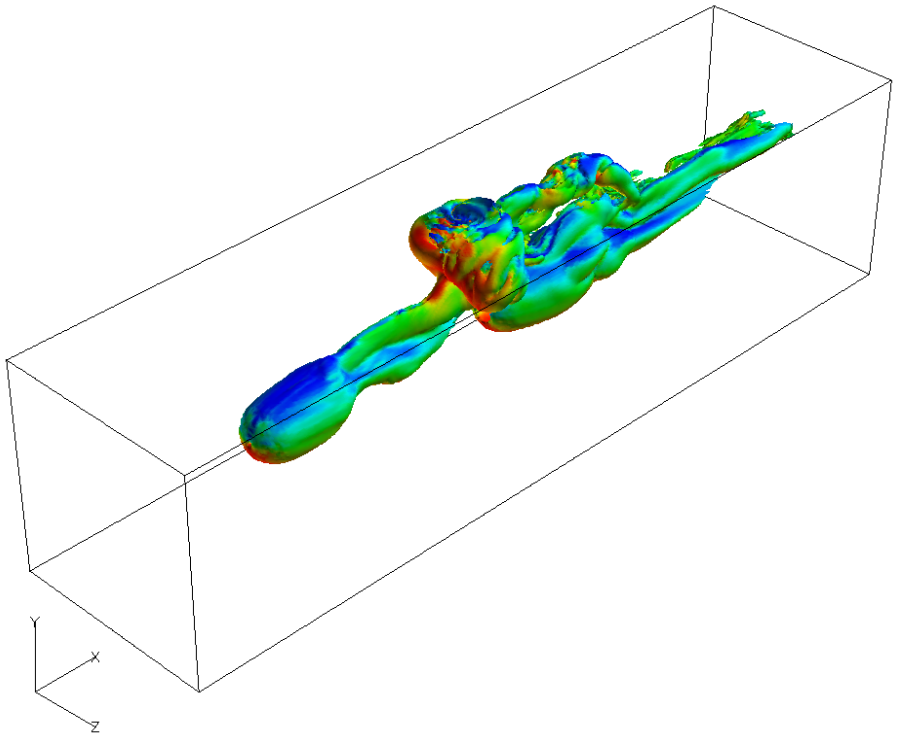

(b) σ = 34 Pa·s/m^2

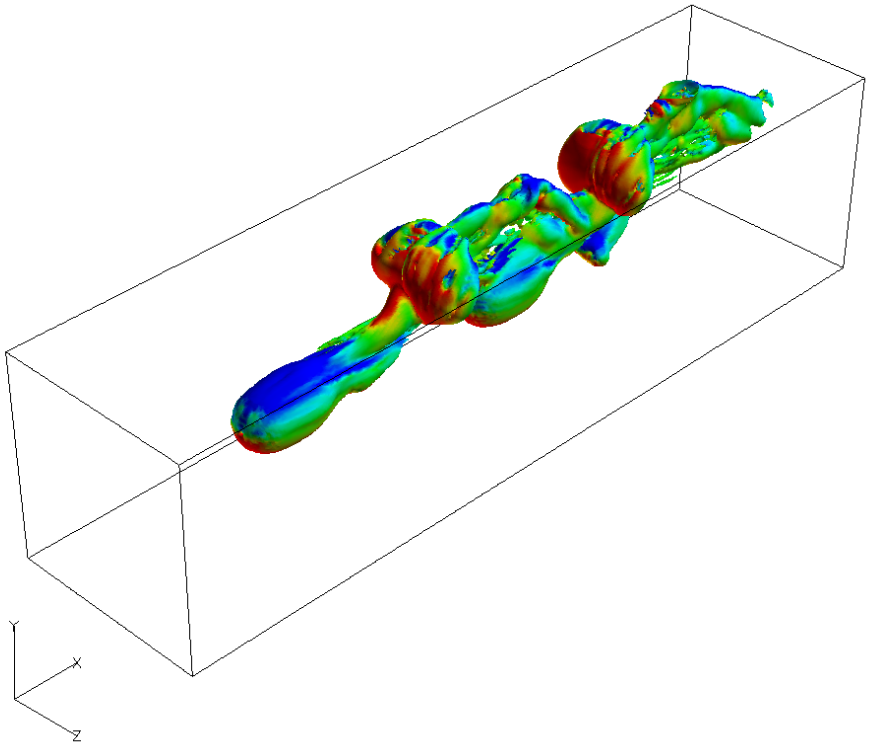

(c) σ = 340 Pa·s/m^2

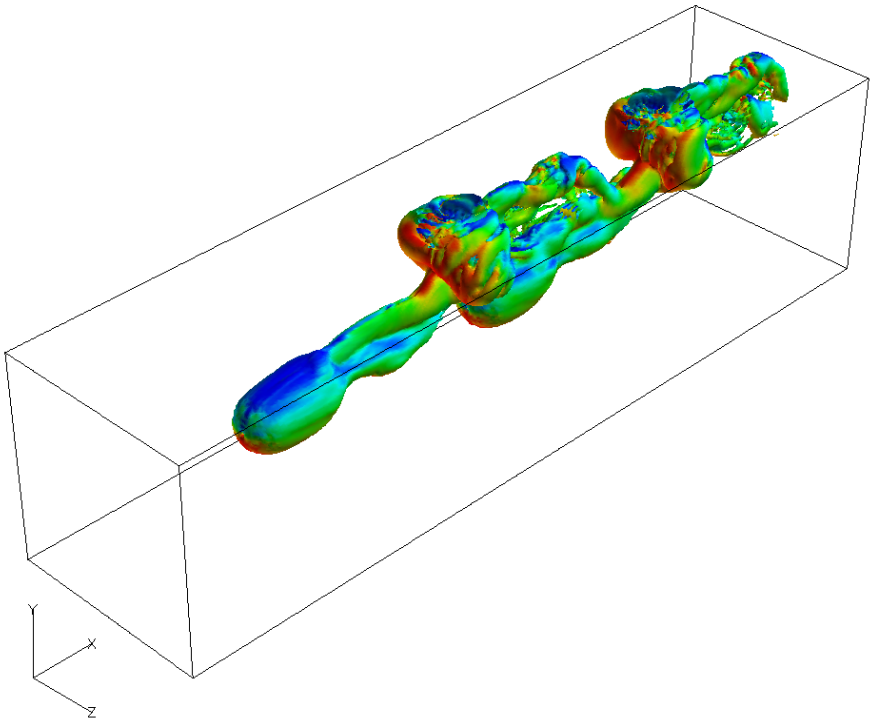

(d) σ = 3400 Pa·s/m^2

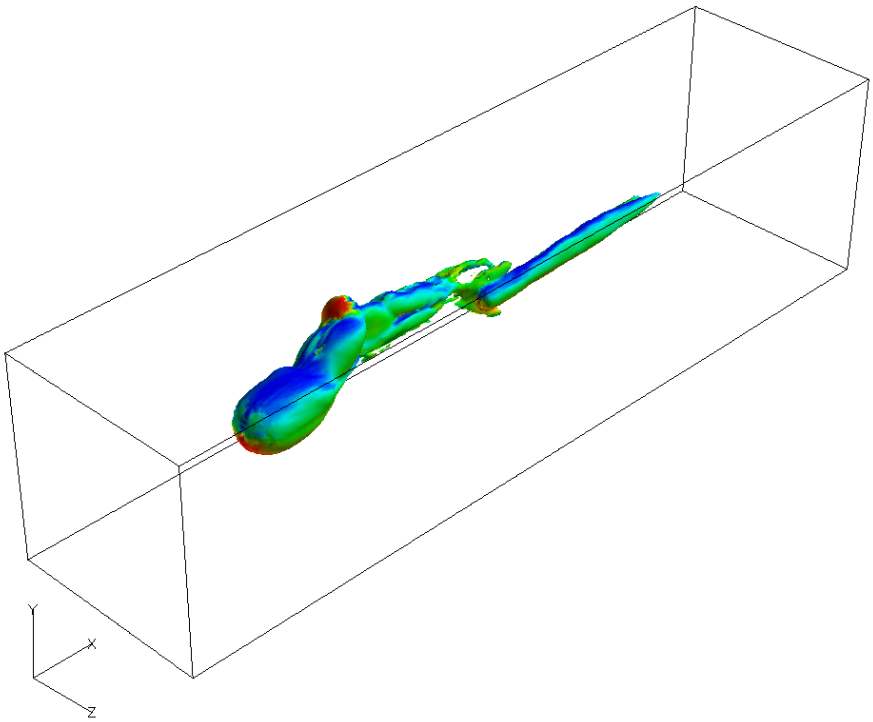

(e) unscreened

Figure 5-10 Iso-surface of Vorticity Magnitude of flow field (Re = 5000)

Figure 5-11 shows the pressure time history of the center point of the microphone sphere (measurement point in Figure 5-1). And specifically it shows that the fluctuation magnitude of the unscreened center pressure is the highest of the windscreened sphere cases, which means the windscreen has the WNR effects. Also, for a long-duration simulation, the pressure time history reaches a kind of quasi-steady state although the trend is not as good as that of the previous low Reynolds number cases (Re = 500). Additionally, Figure 5-11 shows the pressure time history trend of the lowest flow resistivity case (σ = 3.4 Pa·s/m^2, red dash line) is most similar to that of the unscreened case (black solid line). Moreover, the pressure fluctuation magnitude of the medium resistivity case (σ = 340 Pa·s/m^2, blue dotted line) seems the smallest for all windscreened cases.

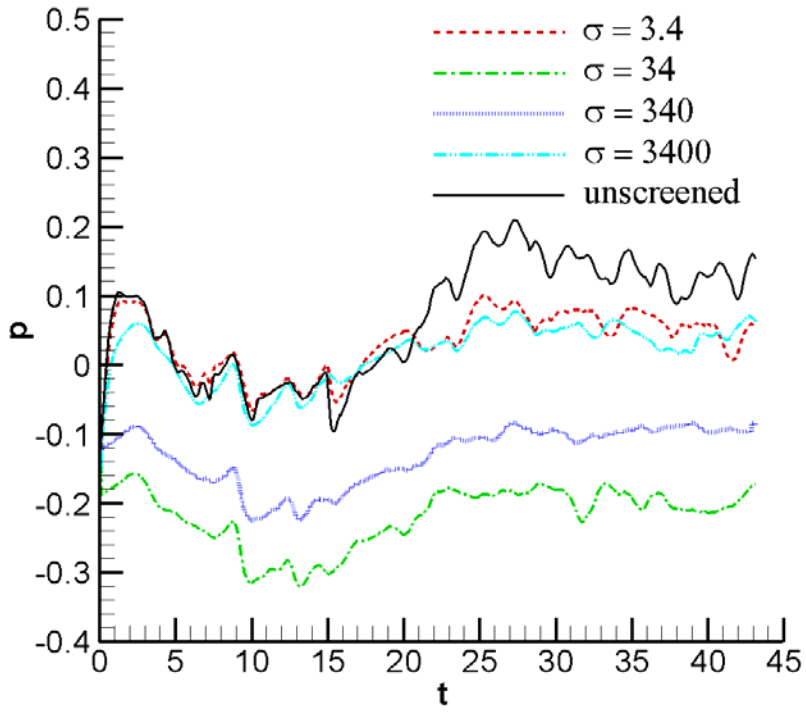

Figure 5-11 Pressure time histories at center point of the microphone sphere (all values are dimensionless, Re = 5000)

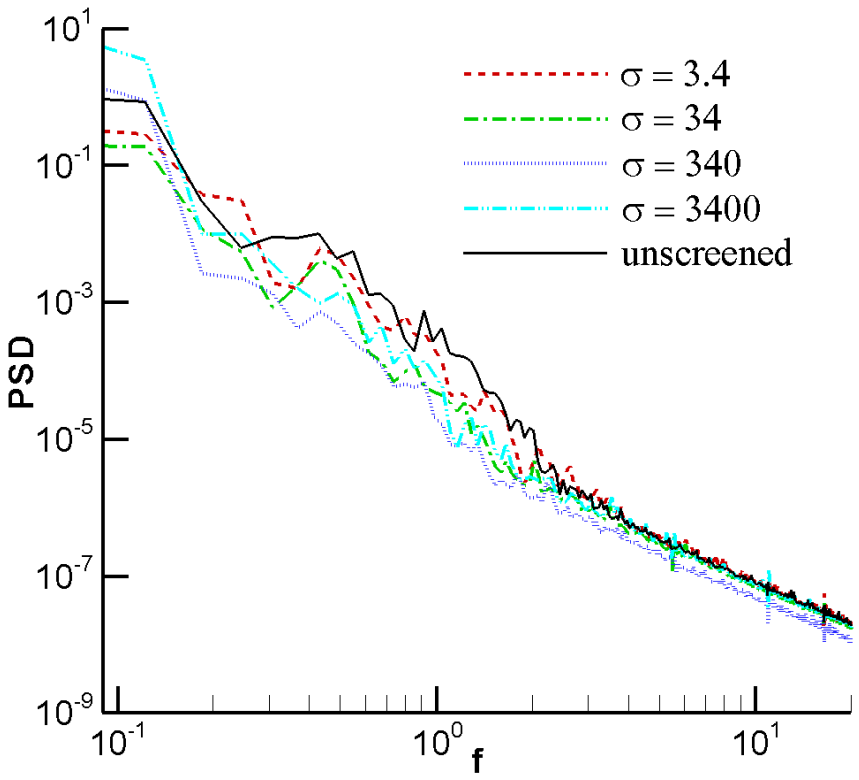

Figure 5-12 PSD at the center point of microphone sphere (all values are dimensionless, Re = 5000)

Figure 5-12 shows the pressure power spectral density (PSD) at the center point of the microphone sphere. It includes five curves: one for the unscreened bare microphone case and four other windscreened cases with flow resistivities: 34, 340, 3400, and 34000 Pa·s/m^2 (corresponding to dimensionless 0.2, 2, 20 and 200 separately). It should be noted here that all results shown in Figure 5-12 are dimensionless. Comparing to previous low Reynolds number cases (Re = 500), the peak frequency for all cases is not so clear. The distinct peak frequencies are about 0.4 and 0.9. In this figure, the black solid line represents the unscreened case clearly showing it has the highest PSD level compared to other four windscreened cases. Also, Figure 5-12 shows that the lowest resistivity case (σ = 3.4 Pa·s/m^2) has the most similar shape trend to that of the unscreened case because the windscreen effect will be pretty small as flow resistivity

is pretty small. The trend here conforms to the previous investigation of pressure time history in Figure 5-11. Figure 5-12 also shows that the windscreen effect is distinct in the dimensionless frequency range between 0.4 and 2. Additionally, it shows that that the medium resistivity case (σ = 340 Pa·s/m^2, blue dotted line) has the smallest PSD level compared to other windscreened cases, which means this medium flow resistivity windscreen has the largest WNR effect.

Figure 5-13 shows SPL at the center point of the microphone sphere with five curves: one for the bare microphone case and four for the screened microphone with different flow resistivities: 3.4, 34, 340, and 3400 Pa·s/m^2. Notably, all the data in Figure 5-13 are real dimensional values for physical phenomena. It shows that the windscreen effect happens mostly in the frequency range from 5Hz to 30Hz, where the SPL level of the screened cases (σ = 34, 340 and 3400 Pa·s/m^2) is clearly smaller than that of the unscreened case. Also the SPL shape of the lowest flow resistivity windscreen case (σ = 3.4 Pa·s/m^2) is most similar to that of the unscreened microphone case compared to the other windscreened cases. This trend is also verified by the previous pressure history in Figure 5-11 and the PSD in Figure 5-12, which means the windscreen effect is pretty small as the flow resistivity of windscreen reaches a very low value. Furthermore, the windscreened cases (σ = 34, 340 and 3400 Pa·s/m^2) have a similar SPL shape trend. In these three cases, the medium resistivity case (σ = 340 Pa·s/m^2, blue dotted line) has the smallest SPL value in the most common frequency range which means the biggest SPL difference between the unscreened microphone and the screened microphone should happen in the medium resistivity case.

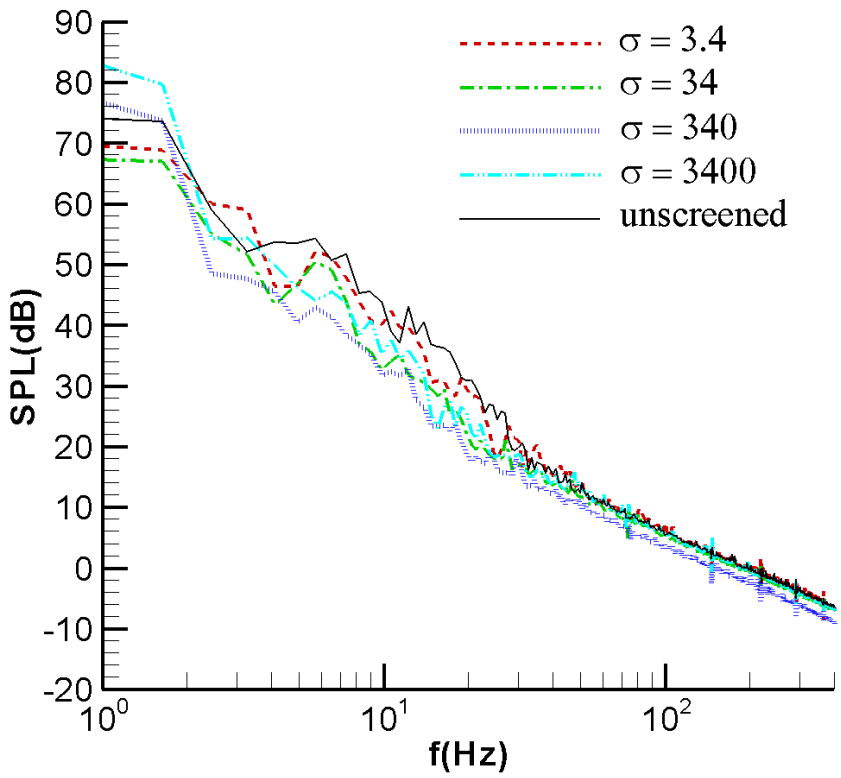

Figure 5-13 SPL at the center point of the microphone (all values are dimensional, Re = 5000)

Next, we investigate wind noise reduction level (WNR) between the unscreened microphone and the screened microphone, defined as: $WNR = SPL_{unscreened\ \ center} - SPL_{screened\ \ center}$, by subtracting the SPL at screened microphone center from that at unscreened microphone center. Figure 5.14 shows the WNR for different cases that comprises four curves: bare microphone minus four screened microphones with different flow resistivities (σ = 3.4, 34, 340 and 3400 Pa·s/m^2). The highest WNR is around 15dB, which shows significant wind noise reduction effects. Figure 5-14 clearly shows that the WNR between the unscreened and the lowest flow resistivity (σ = 3.4 Pa·s/m^2, red solid line) is the lowest compared to the other three higher flow resistivity screens (σ = 34, 340 and 3400 Pa·s/m^2)) which means little windscreen effect as flow

resistivity is very small. Apparently, the medium flow resistivity windscreen (σ = 340 Pa·s/m^2) performs best in the frequency range from 5Hz to 30Hz, and its WNR value is the highest among the three windscreened cases (σ = 34, 340 and 3400 Pa·s/m^2). The highest flow resistivity windscreen (σ = 3400 Pa·s/m^2)) also performs well, and it has similar WNR shape to that of the medium flow resistivity windscreen (σ = 340 Pa·s/m^2) while the value is a little smaller than that of the medium flow resistivity windscreen.

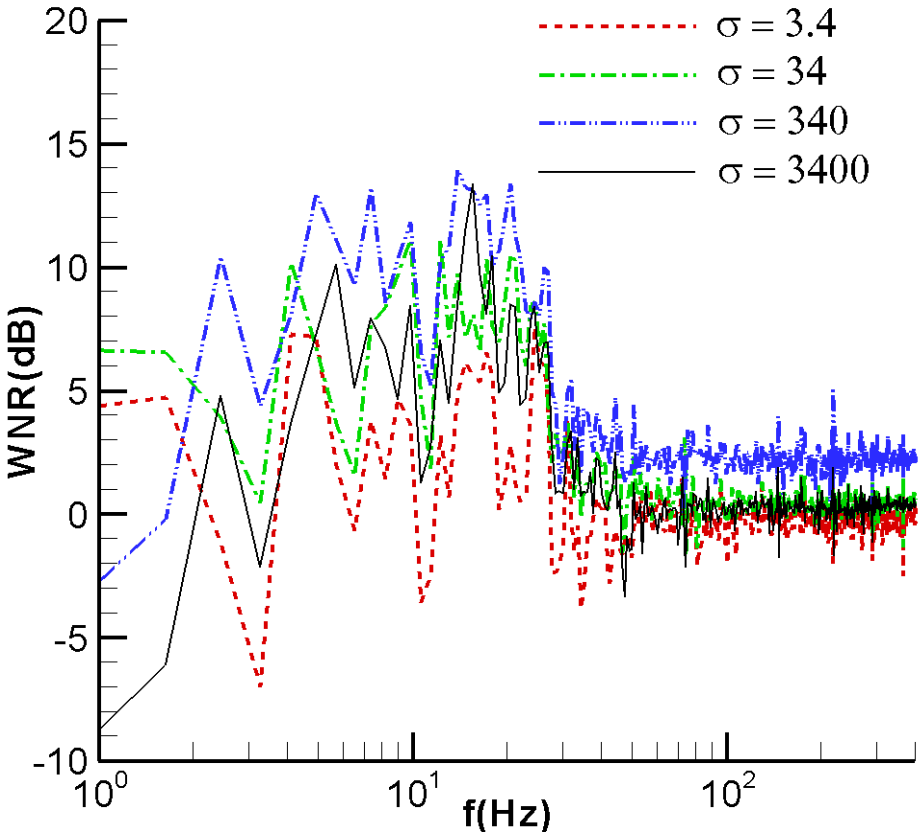

Figure 5-14 WNR between unscreened microphone center and screened microphone center (all values are dimensional, Re = 5000)

To clarify the quantitative value for the wind noise reduction between the unscreened microphone center and the screened microphone center, Table 5-2 offers the most significant wind noise reductions values. It should be noted that the symbol "-" used in Table 4-1 means negative values (no windscreen effects).

Table 5-2 WNR between unscreened microphone center and screened microphone center (3D cases, Re = 5000)

Resistivity (Pa·s/m^2) / Frequency(Hz)	3.4	34	340	3400
2.4	-	3.9	10.5	4.8
4.9	7.2	10.2	13.2	10.0
9.8	4.7	11.2	11.9	8.4
15.5	6.2	8.2	14.2	13.3
17.9	6.6	10.4	12.8	10.5
24.4	7.6	8.6	8.6	8.4

In Table 5-2, for the low flow resistivity case (σ = 3.4 Pa·s/m^2), the highest WNR levels are about 7.2 dB at 4.9Hz, and 7.6 dB at 24.4Hz. For the medium flow resistivity (σ = 34 Pa·s/m^2), the highest WNR levels are about 11.2 dB at 9.8Hz, and 10.4 dB at 17.9Hz. For the medium flow resistivity (σ = 340 Pa·s/m^2), the high WNR levels are about 13.2 dB at 4.9Hz, and 14.2dB at 15.5Hz. For the highest flow resistivity (σ = 3400 Pa·s/m^2), the highest WNR levels are about 10.0dB at 4.9Hz, and 13.3dB at 15.5Hz. Generally speaking, the lowest flow resistivity windscreen (σ = 3.4 Pa·s/m^2) has very little wind noise reduction and seems not to have the windscreen effect; the medium flow resistivity windscreen (σ = 340 Pa·s/m^2) has the highest wind noise reduction and seems to have the most windscreen effects; the largest flow

resistivity windscreen (σ = 3400 Pa·s/m^2) has similar but less windscreen effect comparing with the medium resistivity case (σ = 340 Pa·s/m^2).

CHAPTER 6 - QW Background Turbulence Simulation

This chapter investigates the flow/acoustic interaction in the porous medium (windscreen) under background wind turbulence generated by the Quasi-Wavelet (QW) Method.

6.1 Quasi-Wavelet Method

The atmospheric velocity field can be decomposed into mean and fluctuation parts:

$$\vec{v} = \bar{\vec{v}} + \vec{v}' \tag{6.1}$$

where $\vec{v}$ is the total velocity, $\bar{\vec{v}}$ is the mean background flow velocity, and $\vec{v}'$ is the turbulent velocity fluctuation. In Chapter 4 and Chapter 5, we put different sizes of solid cylinder or sphere in the upstream of the microphone to generate the wind turbulence. In fact, these kinds of generated wind turbulence are not real atmospheric turbulence. They are different types wake vortices generated by solid cylinder or sphere. Atmospheric turbulence, however, is external to the wake vortices, which does not include the part of the turbulence generated by the wake vortices themselves. Such turbulence is on a different scale and usually is larger than wake-generated turbulence. However, the scale of the background turbulence can be comparable to that of the "mean" behavior of the wake vortices (Garratt, 1992). For example, the length scale of atmospheric turbulence near the inertial subrange, and the energy containing subrange, can be in the range of a few meters to several hundred meters (Lenschow and Stankov, 1986). Apparently, given this size of the length scale, atmospheric turbulence is able to directly transport wake vortices, in both horizontal and vertical directions, with its velocity fluctuations at the magnitude possibly comparable to the mean wind speed.

From a theoretical point of view, velocity fluctuations of turbulence can be calculated by direct numerical simulation of atmospheric turbulent flow, but this is not a practical approach

even with today's state-of-the-art computing power. Instead, a practical approach is to use measured information, such as the eddy dissipation rate (EDR), to approximately construct velocity fluctuations based on known turbulence spectra, such as the von Karman spectrum. Therefore, we use a quasi-wavelet (QW) method to develop a random velocity field for wake vortex simulation.

In a quasi-wavelet representation of turbulence, self-similar, eddy-like structures are used with random orientations and positions in space. Such a representation is based on a spatially localized parent function that is related to the turbulent kinetic energy spectrum. The orientations and positions of the Qws are randomly generated and the QW basis functions are not required to be mutually orthogonal or to form a mathematically complete set.

In the QW method, each of the QW can be viewed as a random "eddy." The fluctuation velocity field, created by the QWs (or the QW ensembles), is found at a spatial location, r, by superposition of these "eddies":

$$\vec{\mathrm{v}}'(\vec{r}) = \sum_{\alpha=1}^{N} \sum_{n=1}^{N_\alpha} \vec{\mathrm{v}}^{\alpha n}(\vec{r}) \tag{6.2}$$

where N is the number of size classes and N_α is the number of QWs for the size class α, and the velocity field associated with each QW is

$$\vec{\mathrm{v}}^{\alpha n}(\vec{r}) = \vec{\Omega}^{\alpha n} \times f(\vec{r} - \vec{b}^{\alpha n}) \tag{6.3}$$

where $\vec{\Omega}^{\alpha n}$ is the angular velocity vector of the QW, and $\vec{b}^{\alpha n}$ is the center of the QW, and f is the QW parent function to be determined by the expression of turbulence energy spectrum. The randomness of the resultant velocity fluctuations is that the orientation of the QWs, the direction of vectors $\vec{\Omega}^{\alpha n}$, and their eddy centers, $\vec{b}^{\alpha n}$, are random variables. They are generated

using random-number generators in the computer. The strength of the eddy is determined by the size of eddy and the EDR in the inertial subrange. Notably, turbulence generated by the QW method is a solenoidal field and therefore satisfies the incompressible flow condition.

We use the von Karman spectrum to represent atmospheric turbulence, because it contains the Kolmogorov spectrum (inertial subrange) in the high-wavenumber limit and is also valid for the lower wavenumbers comprising the energy subrange. The expression for the von Karman energy spectrum is

$$E(k) = C\frac{\sigma_v^2 k^4 L_v^5}{(1+k^2 L_v^2)^{17/6}} \tag{6.4}$$

where C is a von Karman spectrum constant, v is the velocity scale, and Lv is the length scale near the transition between the energy and inertial subranges, and is proportional to the distance from the ground in shear turbulence.

The detailed mathematical derivation of the QW representation of the von Karman spectrum can be found in papers by Goedecke et al. (2004) and Wilson et al. (2004), and a typical resultant eddy structure is shown in Figure 6-1. The z-direction is the vertical distance from the ground and the structure is represented by vorticity iso-surface with the color representing the velocity magnitude of eddies. The color represents the velocity magnitude. The size of the simulation box is 15m (x) by 50m (y) by 15m (z). Meanwhile, the length scale of the turbulence becomes larger when the vertical distance from the ground increases. The figure also shows that the eddies can sometimes be fairly strong, shown as “hot spots” of atmospheric turbulence. When a wake vortex system is immersed in these eddies, they transport and deform the vortices in a random fashion.

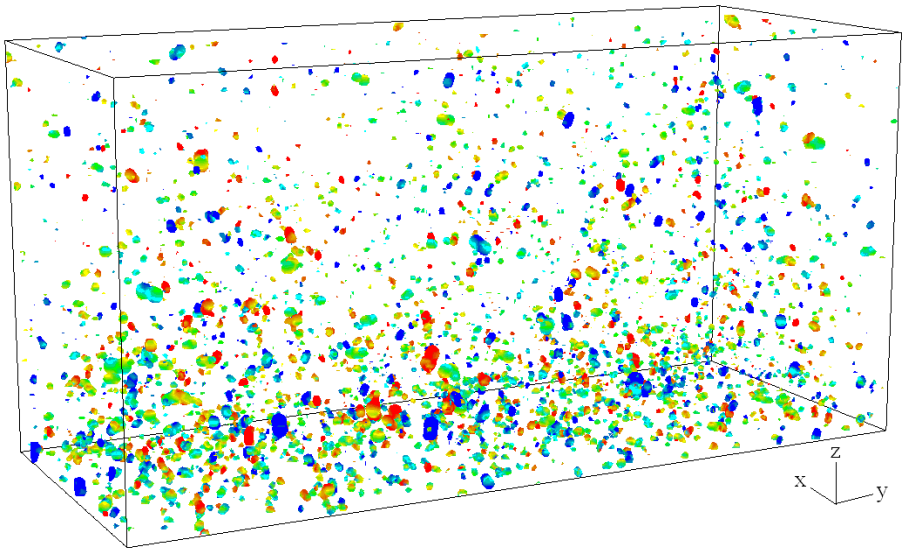

(a) Vorticity iso-surface

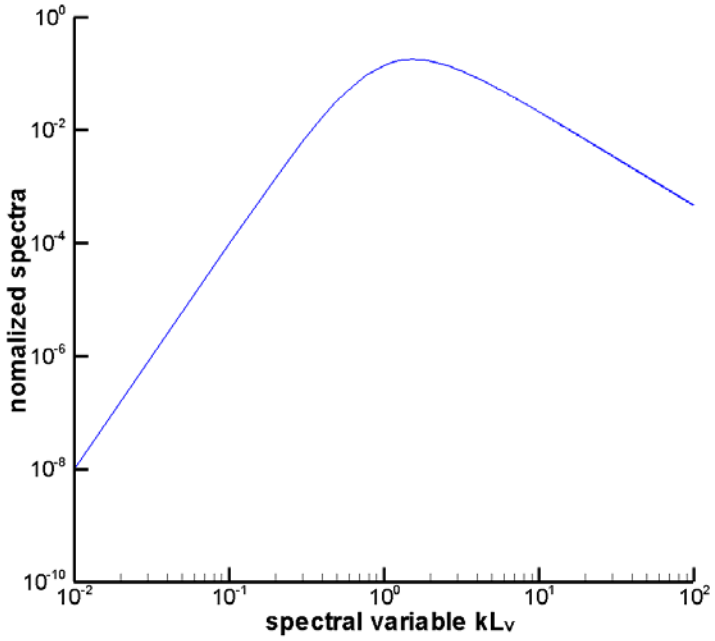

(b) Energy spectrum

Figure 6-1 QW generated atmospheric turbulence with the von Karman energy spectrum.

Figure 6-2 shows the dimensionless continuity iso-surface of generated wind turbulence using the following equation:

$$\left(\frac{\partial u}{\partial x}\frac{L}{U}+\frac{\partial v}{\partial y}\frac{L}{U}+\frac{\partial w}{\partial z}\frac{L}{U}\right)=\left(\frac{\partial u}{\partial x}+\frac{\partial v}{\partial y}+\frac{\partial w}{\partial z}\right)\frac{h}{u^{*}} \tag{6.5}$$

where h is the grid size, u^{*} is the mean velocity in the flow field.

The color in Figure 6-2 represents the velocity magnitude. Most continuity values in the flow field are lower than 0.2, although there are some 'hot spots' in the field. The biggest continuity value in the generated flow filed is around 5. Therefore, most of the flow field conforms to the incompressible condition which is the basic assumption of the simulation of flow over porous medium, but some 'hot spots' make the 3D simulation difficult to converge. The way to deal with this problem is to separate the 3D flow fields into different 2D slices and select the generally smoother slice as the background flow in 2D simulation.

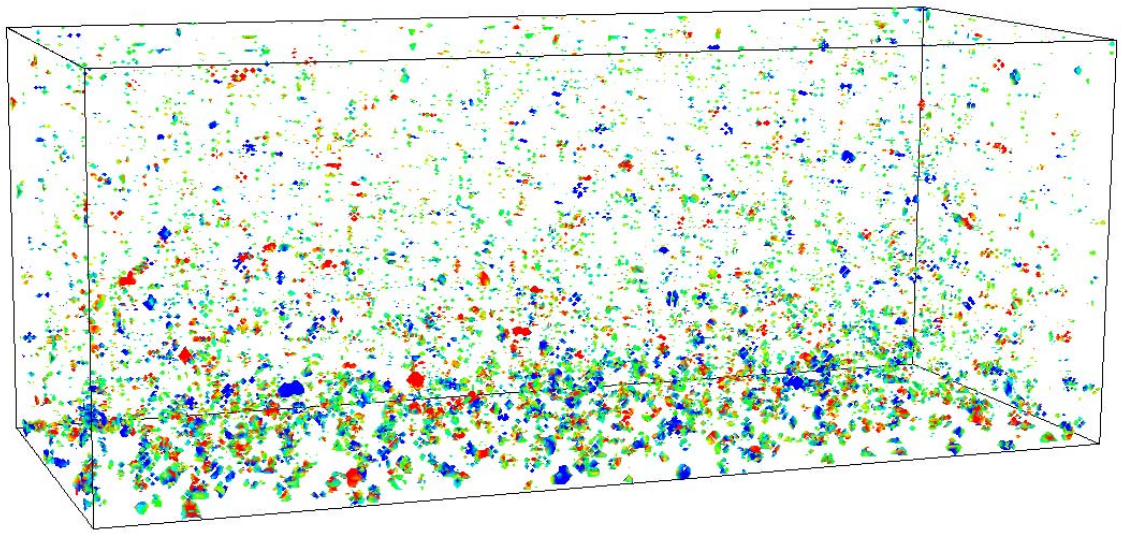

Figure 6-2 Continuity iso-surface of QW generated atmospheric turbulence with the von Karman energy spectrum.

6.2 Test Cases

This section uses QW generated wind turbulence as background flow to simulate the flow/acoustic interaction around the microphone so we could test some cases using two-dimensional simulations.

The two-dimensional model problem is in Figure 6-3, where a stream of unsteady turbulent flow approaches a cylindrical windscreen of porous material. The flow fluctuations, both internal and external to the windscreen, are investigated based on a coupled flow simulation between the outside and the inside of the windscreen. The important issue is to study the noise reduction effect of the windscreen. In Figure 6-3, we want to know the sound pressure level (SPL) difference between the unscreened microphone center and the screened microphone center. The detailed computational equation and algorithm can be found in Chapter 3.

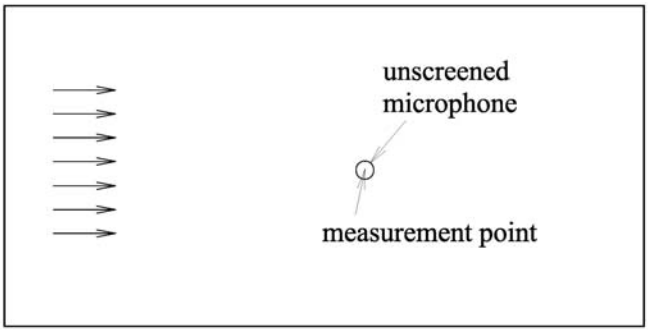

(a) unscreened microphone

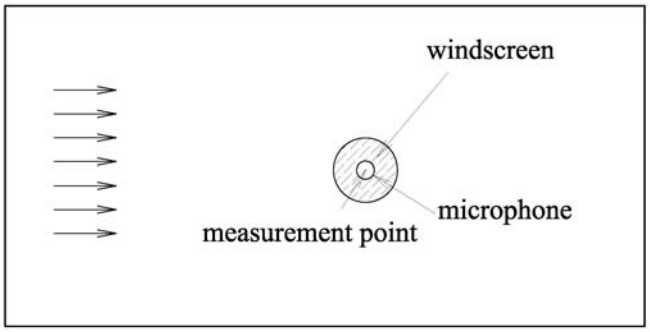

(b) screened microphone

Figure 6-3 Schematic illustration of the model problem

The Reynolds number for the test cases presented here is 5000, approximately characterizing a windscreen with a diameter of 7.5cm and a mean wind speed of 1m/s for the incoming air adding to generated wind turbulence. Also a bare microphone (unscreened) is set with diameter of 1.875cm. Three values of dimensionless flow resistivity of the windscreen, 2, 20, and 200, correspond to approximately 34, 340, and 3400 Pa·s/m^2 of dimensional flow resistivity, respectively ($\sigma = \frac{\rho U}{D} = \frac{1.27kg/m^3 \cdot 1m/s}{0.075m} = 17 P_a \cdot s/m^2$). In this simulation, the grid size is 0.025 in both the x and y directions, and the time step is 0.001.

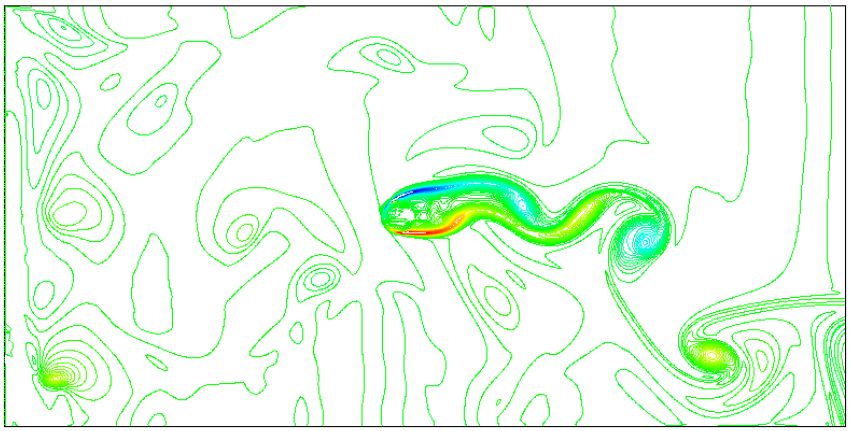

(a) σ = 34 Pa·s/m^2

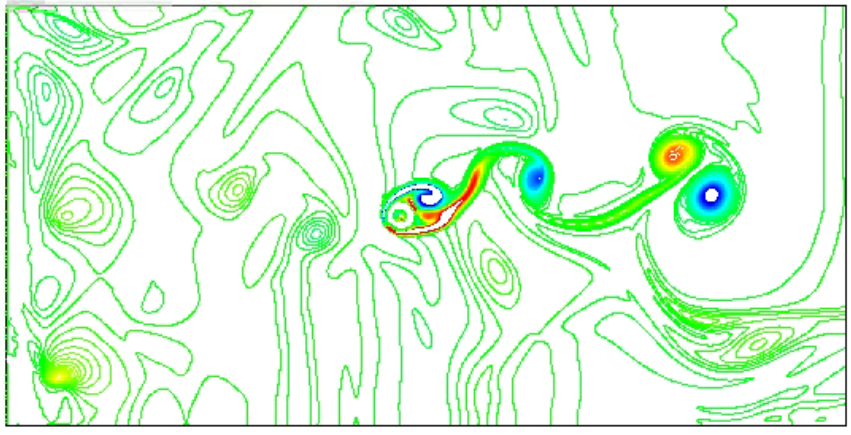

(b) σ = 340 Pa·s/m^2

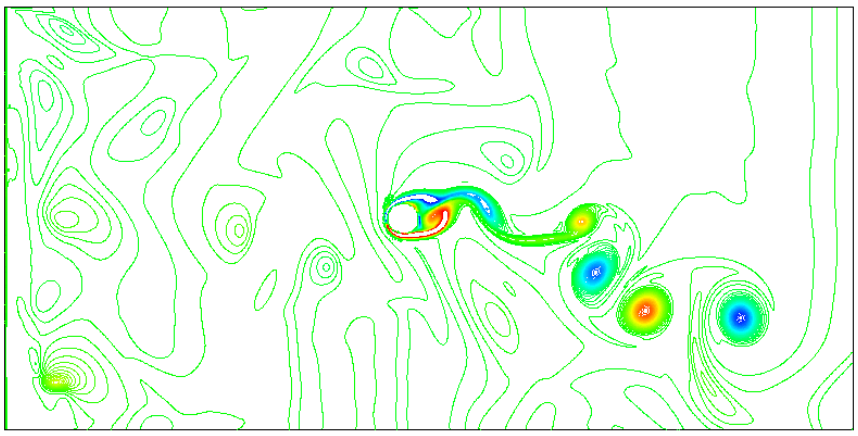

(c) σ = 3400 Pa·s/m^2

Figure 6-4 Vorticity contours of flow field with background wind turbulence (background turbulence slice 1)

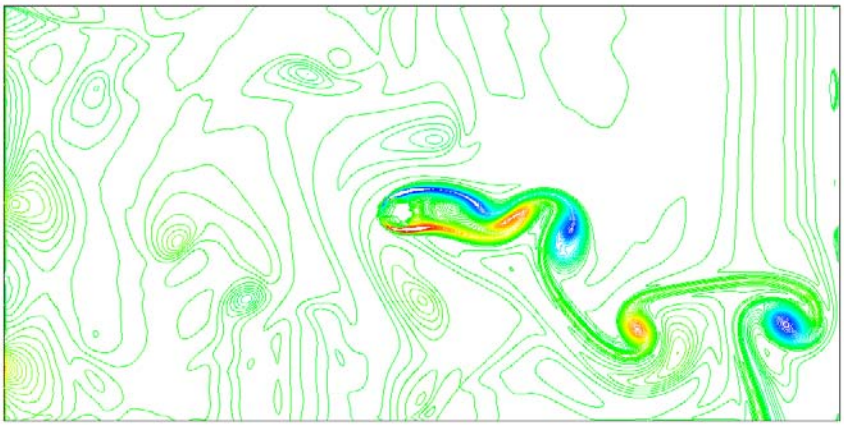

(a) σ = 34 Pa·s/m^2

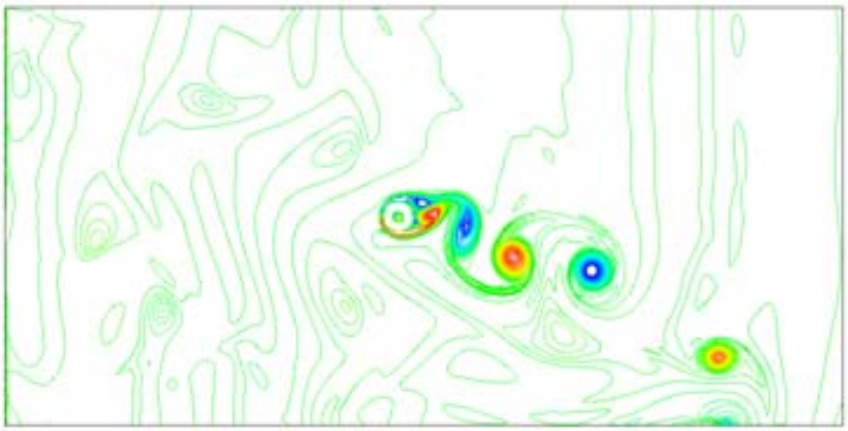

(b) σ = 340 Pa·s/m^2

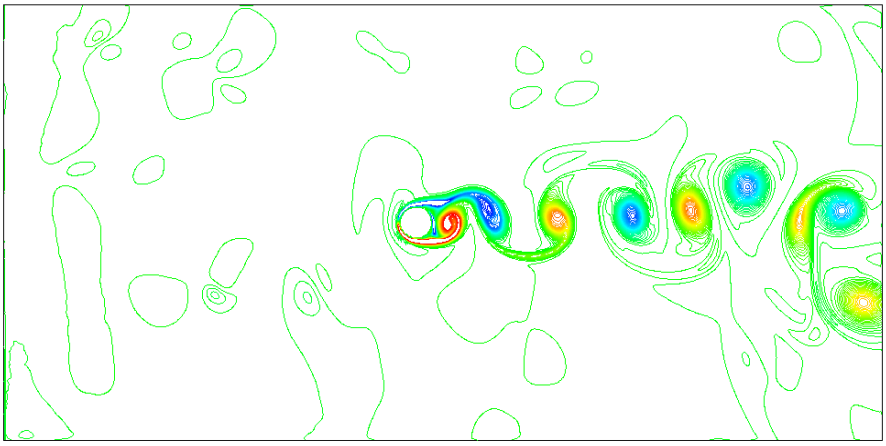

(c) σ = 3400 Pa·s/m^2

Figure 6-5 Vorticity contours of flow field with background wind turbulence (background turbulence slice 2)

Figures 6-4 through 6-5 show the vorticity contours of flow field with two different QW generated background wind turbulence slices (because wind turbulence generated is three dimensional, we cut it into many planes to get the flow field of each slice). The red color in vorticity figures represents positive vorticity (in the counter clockwise sense, with the upper limit value of 10); the blue color represents negative vorticity (in the clockwise sense, with the lower limit value of -10). Also there are lots of different sized structural vortices in the background turbulence. With the low flow resistivity case, much flow permeates the windscreen; and with high flow resistivity case, little flow infiltrates the windscreen.

As mentioned, we select two different wind turbulence slices as background flow in this simulation; Figures 6-6 through 6-9 represents one case (slice 1) and Figures 6.10 through 6.13 represents the other case (slice 2). First Figure 6-6 shows the pressure time history of the center point of the microphone showing the fluctuation magnitude of unscreened center pressure is the highest compared to the windscreened cylinder cases, which shows a similar trend with the

results from previous chapters (upstream cylinder and sphere cases), although the trend is not so clear as for those upstream solid cylinder cases.

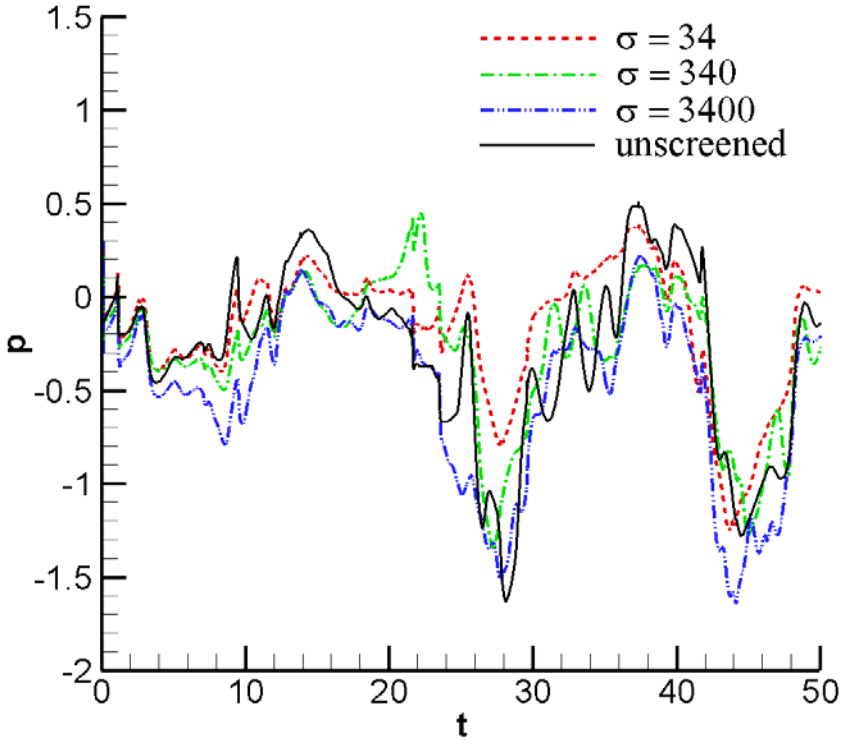

Figure 6-6 Pressure time histories at center point of the microphone (all values are dimensionless, background turbulence slice 1)

Figure 6-7 shows the PSD at the center of the windscreened microphone. It includes four curves: one for the unscreened bare microphone case and the other three for the windscreened microphone cases with three different flow resistivities: 34, 340, and 3400 Pa·s/m^2 (corresponding to dimensionless 2, 20 and 200, separately). It is noted here that all results in Figure 6-7 are dimensionless, which will be convenient for theoretical analysis. Compared with previous high Reynolds number cases (Re = 5000, detailed in chapter 4), the PSD line trend here is similar and more like a realistic atmospheric turbulence. Furthermore, the PSD of the unscreened case is higher than that of screened microphone cases in the frequency range from

0.3 to 5, which means that there is windscreen effect in this frequency range. The most distinctive PSD difference happens at the frequency range from 0.5 to 1.

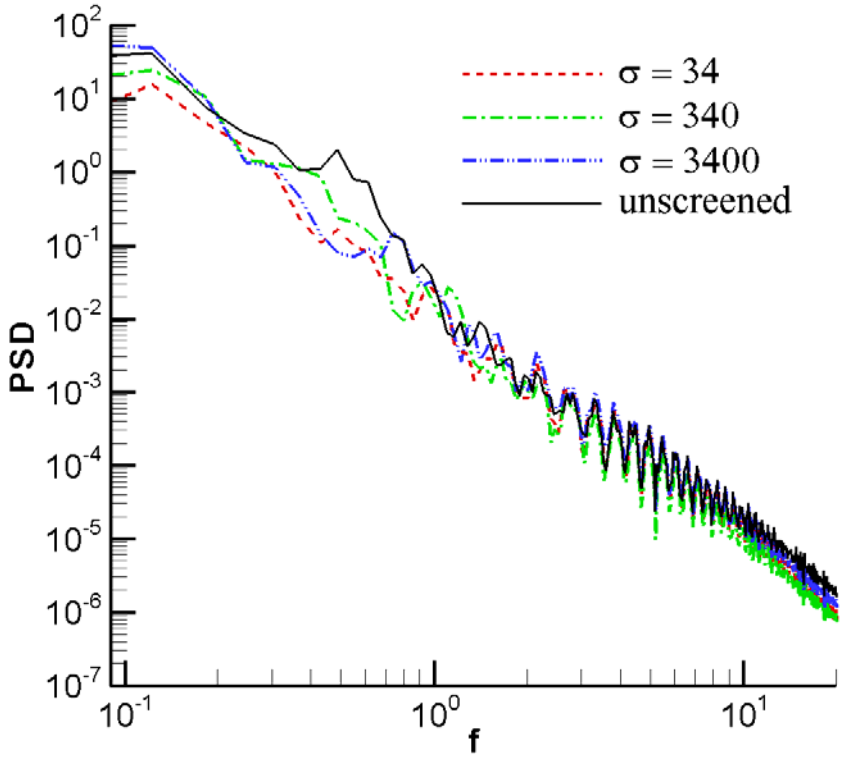

Figure 6-7 PSD at center point of the microphone (all values are dimensionless, background turbulence slice 1)

Figure 6-8 shows the sound pressure level (SPL) at the center of the windscreened microphone. This figure has four curves: one for the bare microphone case and the other three for the screened microphone cases with three different flow resistivities: 3.4, 34, 340, and 3400 Pa·s/m^2. Notably, all the data in the Figure 6-8 are dimensional for real physical phenomena. Next, the SPL trend for all four lines is similar, and the peak frequency is not so distinct. Also, the SPL of the unscreened case is higher than that of the windscreened case. The remarkable SPL difference between the unscreened center and the windscreened center lies at frequencies of 6Hz and 30Hz. The figure also shows very few windscreen effects over the frequency 30Hz.

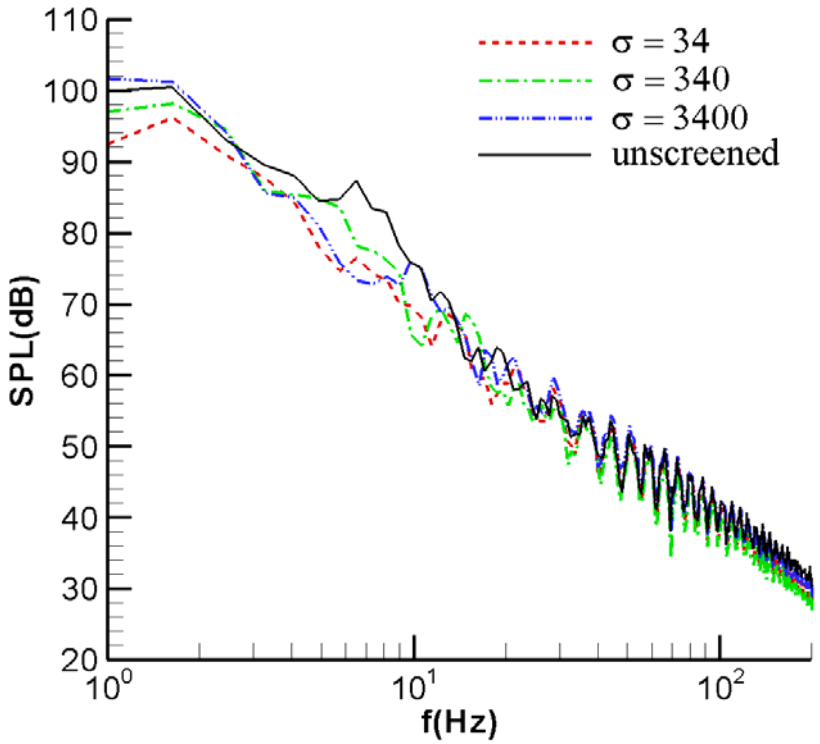

Figure 6-8 SPL at center point of the microphone (all values are dimensionless, background turbulence slice 1)

We further investigated wind noise reduction level (WNR) between the unscreened microphone and the windscreened microphone for different cases. Figure 6-9 shows the WNR which is computed from Figure 6-8 using the SPL of unscreened case minus the SPL of the windscreened case. The figure has three curves: bare microphone case minus three windscreened microphone cases with different flow resistivities (σ = 34, 340, 3400 Pa·s/m^2). The highest WNR is around 14dB, which shows significant windscreen effects. Apparently, the medium flow resistivity windscreen (σ = 340 Pa·s/m^2) performs best and has the most distinct wind noise reduction effects in the whole range, which is the same trend as for the previous upstream solid cylinder and sphere cases (chapter 4 and chapter 5).

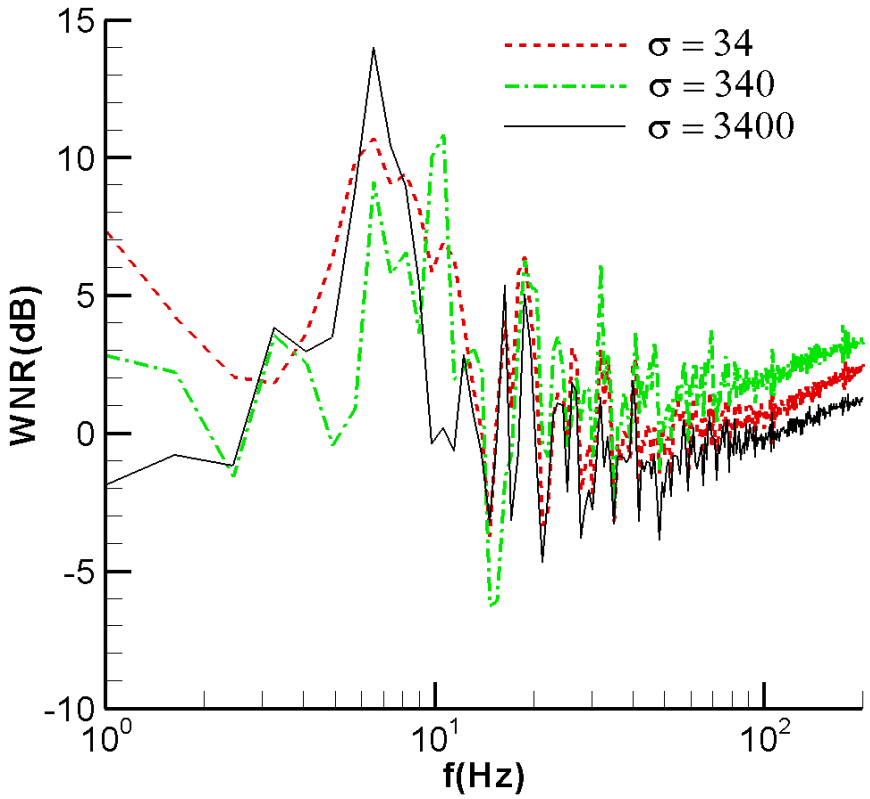

Figure 6-9 WNR between unscreened microphone center and screened microphone center (all values are dimensional, background turbulence slice 1)

Figures 6-10 through 6-13 show the slice 2 case, representing pressure time history, PSD, SPL, and WNR separately. The figure's trend is similar with that of slice 1 cases, although some values are different. For instance, the highest WNR is around 12dB at 16Hz, and the medium flow resistivity windscreen (σ = 340 Pa·s/m^2) performs best and has the best wind screen effects in the whole frequency range. The interesting finding is that the windscreen effect also happens over the frequency of 100 Hz (around 5dB), which is not shown in the slice 1 case. The reason may be due to the signal processing error or wind turbulence difference between slice 1 and slice 2 in the wind turbulence flow field.

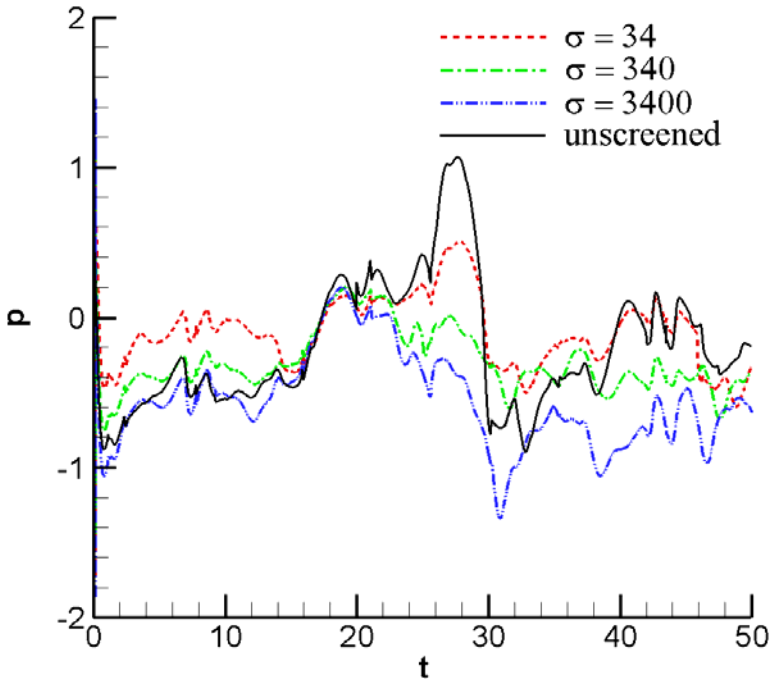

Figure 6-10 Pressure time histories at center point of the microphone (all values are dimensionless, background turbulence slice 2)

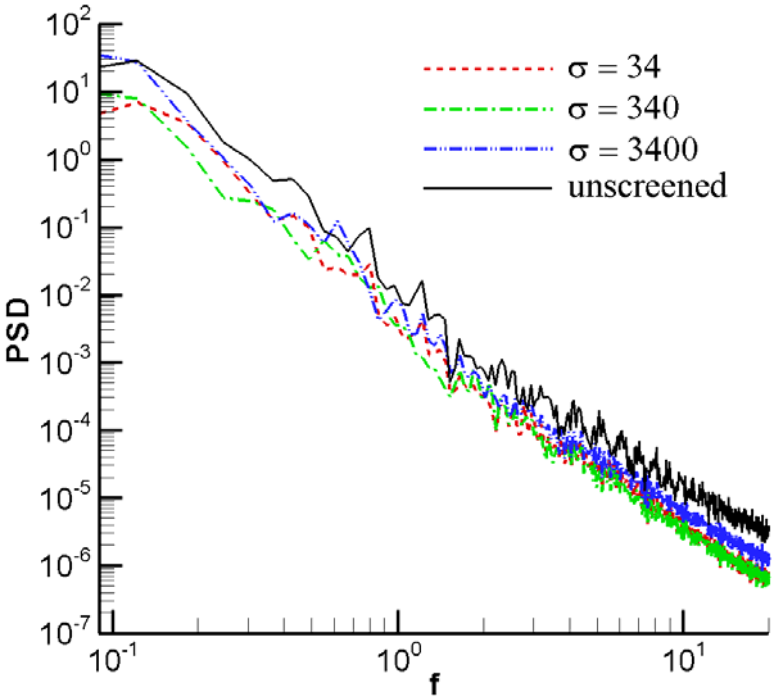

Figure 6-11 PSD at center point of the microphone (all values are dimensionless, background turbulence slice 2)

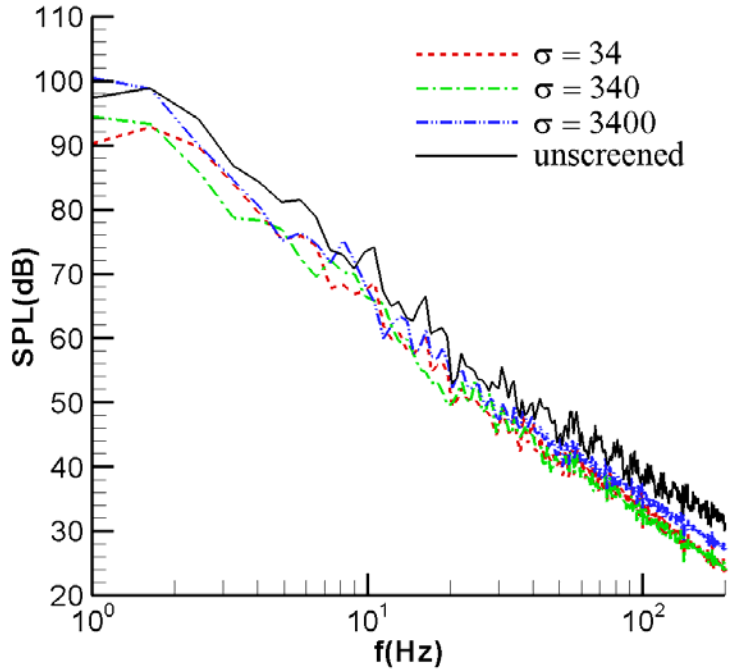

Figure 6-12 SPL at center point of the microphone (all values are dimensionless, background turbulence slice 2)

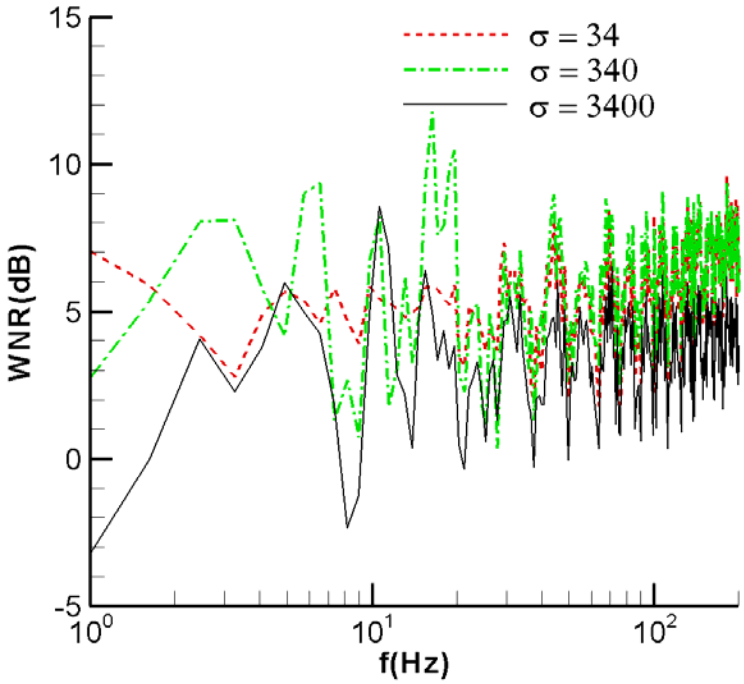

Figure 6-13 WNR between unscreened microphone center and screened microphone center (all values are dimensional, background turbulence slice 2)

For Quasi-wavelet (QW) generated background wind turbulence, some hot points exist that have big numbers of continuity, although the continuity in Figure 6-2 shows that most regions have good incompressible condition. However, the simulation with QW background flow is not so stable, which can be seen from the pressure time history. In future work, this part needs more research.

CHAPTER 7 - Conclusion

During this research, we investigated the flow/acoustic interaction in the porous medium (windscreen) under Low Reynolds number cases (Re = 500) and High Reynolds number cases (Re = 5000) in two-dimensional flows and three-dimensional flows.

Table 7-1 Case summary

	Upstream cylinder or sphere cases				QW cases
	2D cases		3D cases		2D cases
Reynolds number	500	5000	500	5000	5000
Microphone diameter (cm)	0.1875	1.875	0.1875	1.875	1.875
Windscreen diameter (cm)	0.75	7.5	0.75	7.5	7.5
Flow resistivity ($Pa \cdot s/m^2$)	34, 340, 3400, 34000	3.4, 34, 340, 3400	34, 340, 3400, 34000	3.4, 34, 340, 3400	34, 340, 3400
Highest WNR (dB)	40	25	26	15	14
Windscreen effect	low flow resistivity more effective for low turbulence, high flow resistivity more effective for high turbulence	medium flow resistivity windscreen more effective comparing with low and high flow resistivity			

To do this, we use different sizes of upstream cylinders or spheres to generate the different wind turbulence flow fields. Also we use a QW method to generate the background wind turbulence to simulate real physical phenomena. With different wind turbulence interacting

with different porous windscreened microphones, we want to find the windscreen properties and effects for different porous media. Most simulated cases were summarized in the table 7-1.

Ultimately, the previous chapters have yielded some specific conclusions:

1) The modified immersed boundary method can be applied to the flow/acoustic simulation for different porous media.

2) The modified Zwikker-Kosten Equation can be used to simulate the flow motion in the porous medium and can be easily numerically implemented using sophisticated solvers, and also good consistent matches can be reached compared to the results from other papers and software.

3) The fifth-order WENO scheme has been successfully implemented in the interface area between flow field and porous field.

4) Physical mechanism for windscreen effects can be described as: large vortical structures are diffused, diffracted, and averaged out by the porous medium windscreen.

5) For 2D low Reynolds number cases (Re = 500), the windscreen effect was very significant, and the highest WNR was around 40dB. Apparently, the low flow resistivity windscreen (σ = 340 Pa·s/m^2) performed better in the few ten Hz range, and the highest flow resistivity windscreen (σ = 34000 Pa·s/m^2) performed better in the few hundred Hz range. Generally, low flow resistivity windscreens were more effective for low frequency turbulence; whereas high flow resistivity windscreens were more effective for high frequency turbulence.

6) For 2D high Reynolds number cases (Re = 5000), the windscreen effect was significant, and the highest WNR was around 25dB. Clear windscreen effects are evident in the frequency range between10Hz and 40Hz. Compared with low flow resistivity windscreen (σ = 3.4 Pa·s/m^2) and high flow resistivity windscreen (σ = 3400 Pa·s/m^2), the medium flow resistivity windscreen (σ = 34 Pa·s/m^2) performed best and had the highest wind noise reduction.

7) We investigated WNR between the unscreened microphone and the windscreened microphone for three different windscreen shapes (cylinder, horizontal ellipse and vertical ellipse) under the high Reynolds number case (Re = 5000). The WNR levels between a cylinder shape windscreen and a horizontal ellipse shape windscreen were similar, while a vertical ellipse windscreen in fact increases the wind noise. Again, the medium flow resistivity windscreen (σ = 170 Pa·s/m^2) performed best for all flow resistivity cases and had the highest wind noise reduction.

8) For 3D Low Reynolds number cases (Re = 500), the windscreen effect was significant, and the highest WNR was around 26dB. The medium flow resistivity windscreen (σ = 3400 Pa·s/m^2) performed best in the whole frequency domain whether with low flow resistivity cases (σ = 34 and 340 Pa·s/m^2) or with high resistivity cases (σ = 34000 Pa·s/m^2).

9) For 3D high Reynolds number cases (Re = 5000), the windscreen effect was significant, and the highest WNR was around 15dB. The medium flow resistivity windscreen (σ = 340 Pa·s/m^2) performed best in most common frequency range

compared with low flow resistivity cases (σ = 3.4 and 34 Pa·s/m^2) and high flow resistivity cases (σ = 3400 Pa·s/m^2).

10) With background wind turbulence (generated by a QW method) added into the flow field, the simulation results show that the medium flow resistivity windscreen (σ = 340 Pa·s/m^2) performs best in the whole frequency domain compared with low flow resistivity (σ = 34 Pa·s/m^2) case and high flow resistivity case (σ = 3400 Pa·s/m^2).

In future work, a fine-grid three-dimensional simulation using parallel code could be implemented. However, the current single-processor simulation scheme would require too much computational time for 3D fine-grid simulation. Instead, parallel technology could shorten the simulation time considerably and increase efficiency and accuracy.

In addition, future research should also explore the three-dimensional simulation of wind turbulence over a porous medium under real background wind turbulence. There are many ways (models and software) to generate the background wind turbulence, including the Dryden Wind Turbulence Model (Tatom et al., 1981), LES Boundary Layer Model (Koutmos and Mavridis, 1997), Quasi-Wavelet (QW) Model (Wilson et al., 2004) and the Vortex Method (Benhamadouche et al., 2006) etc. Which model is the best one to fit with our simulation is yet to be determined.

References

Adams, J. (1989). "MUDPACK: Multigrid Fortran software for the efficient solution of linear elliptic partial differential equations," Applied Mathematics and Computation, 34, 113-146.

Addad, Y., Laurence, D., Talotte, C., and Jacob, M. C. (2003). "Large eddy simulation of a forward-backward facing step for acoustic source identification," International Journal of Heat and Fluid Flow, 24, 562-571.

Aldoss, T. K., Jarrah, M. A., and AlShaer, B. J. (1996). "Mixed convection from a vertical cylinder embedded in a parous medium: Non-Darcy model," International Journal of Heat and Mass Transfer, 39, 1141-1148.

Al-Hajeri, M. H., Aroussi, A., and Witry, A. (2009). "Numerical simulation of flow past multiple porous cylinders," Journal of Fluids Engineering, 131, 1101-1110.

Antonia, R. A., Zhou, T., and Romano, G. P. (2002). "Small-scale turbulence characteristics of two-dimensional bluff body wakes," Journal of Fluid Mechanics, 459, 67-92.

Avancha, R. V. R., and Pletcher, R. H. (2002). "Large eddy simulation of the turbulent flow past a backward-facing step with heat transfer and property variations," International Journal of Heat and Fluid Flow, 23, 601-614.

Batycky, R. P., and Brenner, H. (1997). "Thermal macrotransport processes in porous media. A review," Advances in Water Resources, 20, 95-110.

Benhamadouche, S., Jarrin, N., Addad, Y., and Laurence, D. (2006). "Synthetic turbulent inflow conditions based on a vortex method for large-eddy simulation," Progress in Computational Fluid Dynamics, 6, 50-57.

Benhamadouche, S., and Laurence, D. (2003). "LES, coarse LES, and transient RANS comparisons on the flow across a tube bundle," International Journal of Heat and Fluid Flow, 24, 470-479.

Berthelsen, P. A., and Faltinsen, O. M. (2008). "A local directional ghost cell approach for incompressible viscous flow problems with irregular boundaries," Journal of Computational Physics, 227, 4354-4397.

Bhattacharyya, S., Dhinakaran, S., and Khalili, A. (2006). "Fluid motion around and through a porous cylinder," Chemical Engineering Science, 61, 4451-4461.

Bose, N.K. and Rao, C.R. (1993) “Signal processing and its applications,” North-Holland publisher, New York

Brook, D. and Wynne, R.J. (1988) “Signal processing: principles and applications,” E. Arnold publisher, London

Chen, C.H. (1988) “Signal processing handbook,” Dekker publisher, New York

Chen, X. B., Yu, P., Winoto, S. H., and Low, H. T. (2008). "Numerical analysis for the flow past a porous square cylinder based on the stress-jump interfacial-conditions," International Journal of Numerical Methods for Heat & Fluid Flow, 18, 635-655.

Chen, X. B., Yu, P., Winoto, S. H., and Low, H. T. (2009). "Numerical analysis for the flow past a porous trapezoidal-cylinder based on the stress-jump interfacial-conditions," International Journal of Numerical Methods for Heat & Fluid Flow, 19, 223-241.

Chester, S., Meneveau, C., and Parlange, M. B. (2007). "Modeling turbulent flow over fractal trees with renormalized numerical simulation," Journal of Computational Physics, 225, 427-448.

Chidambaram, N., and Pletcher, R. H. (2000). "A colocated-grid, fully coupled algorithm for large eddy simulation of incompressible and compressible flows," Numerical Heat Transfer Part B-Fundamentals, 37, 1-23.

Cho, Y., Chopra, J., and Morris, P., J. (2007). "Immersed boundary method for compressible high-reynolds number viscous flow around moving bodies," 45th AIAA Aerospace Sciences Meeting, January 9-11, 2007, Reno, NV

Clarke, D., Salas, M., and Hassan, H. (1986). "Euler calculations for multielement airfoils using Cartesian grids," AIAA Journal, 24, 353-358

Deka, R. K., Gupta, A. S., and Das, S. K. (2007). "Stability of viscous flow driven by an azimuthal pressure gradient between two porous concentric cylinders with radial flow and a radial temperature gradient," Acta Mechanica, 189, 73-86.

Dolezal, A., and Wong, S. S. M. (1995). "Relativistic hydrodynamics and essentially nonoscillatory shock capturing schemes," Journal of Computational Physics, 120, 266-277.

Dong, P., Feng, S. D., and Zhao, Y. (2004). "Numerical analysis of fluid flow through a cylinder array using a lattice Boltzmann model," Chinese Physics, 13, 434-440.

Edwards, D. A., Shapiro, M., and Brenner, H. (1993). "Dispersion and reaction in two dimensional model porous media," Physics of Fluids A-Fluid Dynamics, 5, 837-848.

Flekkoy, E. G., Oxaal, U., Feder, J., and Jossang, T. (1995). "Hydrodynamic dispersion at stagnation points - simulations and experiments," Physical Review E, 52, 4952-4962.

Garratt, J. R. (1992). “The atmospheric boundary layer,” Cambridge University Press London

Goedecke, G. H., Ostashev, V. E., Wilson, D. K., and Auvermann, H. J. (2004). "Quasi-wavelet model of von Karman spectrum of turbulent velocity fluctuations," Boundary-Layer Meteorology, 112, 33-56.

Goedecke, G. H., Wilson, D. K., and Ostashev, V. E. (2006). "Quasi-wavelet models of turbulent temperature fluctuations," Boundary-Layer Meteorology, 120, 1-23.

Graham, D. R., and Higdon, J. J. L. (2002). "Oscillatory forcing of flow through porous media. Part 1. Steady flow," Journal of Fluid Mechanics, 465, 213-235.

Harten, A., Engquist, B., Osher, S., and Chakravarthy, S. R. (1987). "Uniformly high-order accurate essentially nonoscillatory schemes .3," Journal of Computational Physics, 71, 231-303.

Kaimer, J.C. and Finnigan J.J. (1994). "Atmospheric boundary layer flows," Oxford University, New York

Jarrin, N., Prosser, R., Uribe, J. C., Benhamadouche, S., and Laurence, D. (2009). "Reconstruction of turbulent fluctuations for hybrid RANS/LES simulations using a synthetic-eddy method," International Journal of Heat and Fluid Flow, 30, 435-442.

Hinze, JO. (1975). "Turbulence," 2nd edition, McGraw- Hill, New York

Kim, K. J. and Durbin, P. A. (1988) "Observations of the frequencies in a sphere wake and drag increase by acoustic excitation," Physics of Fluids, 31, 3260-3265

Kirsh, V. A. (2006). "Stokes flow in periodic systems of parallel cylinders with porous permeable shells," Colloid Journal, 68, 173-181.

Kirsh, V. A. (2006). "Stokes flow past periodic rows of porous cylinders," Theoretical Foundations of Chemical Engineering, 40, 465-471.

Kohr, M., Wendland, W. L., and Sekhar, G. P. R. (2009). "Boundary integral equations for two-dimensional low Reynolds number flow past a porous body," Mathematical Methods in the Applied Sciences, 32, 922-962.

Kondo, K., Murakami, S., and Mochida, A. (1997). "Generation of velocity fluctuations for inflow boundary condition of LES," Journal of Wind Engineering and Industrial Aerodynamics, 67, 51-64.

Koutmos, P., and Mavridis, C. (1997). "A computational investigation of unsteady separated flows," International Journal of Heat and Fluid Flow, 18, 297-306.

Kraichnan, R. H. (1956). "Pressure fluctuations in turbulent flow over a flat plate," Journal of the Acoustical Society of America, 28, 378-390.

Kraichnan, R. H. (1957). "Noise transmission from boundary layer pressure fluctuations," Journal of the Acoustical Society of America, 29, 65-80.

Kundu, P. (1990). "Fluid mechanics," Academic Press, New York

Ladeinde, F. (1995). "Supersonic flux-split procedure for 2nd moments of turbulence," AIAA Journal, 33, 1185-1195.

Lenschow, D.H. and Stankov, B. B. (1986). “Length scales in the convective boundary layer,” Journal of the Atmospheric Sciences, 43, 1198-1209

Lessard, Charles S. (2006) “Signal processing of random physiological signals,” Morgan & Claypool Publishers, New Jersey

Liu, K. L., and Pletcher, R. H. (2006). "Inflow conditions for the large eddy simulation of turbulent boundary layers: A dynamic recycling procedure," Journal of Computational Physics, 219, 1-6.

Liu, X. D., Osher, S., and Chan, T. (1994). "Weighted essentially nonoscillatory schemes," Journal of Computational Physics, 115, 200-212.

Min, K., and Lueptow, R. M. (1994). "Hydrodynamic stability of viscous-flow between rotating porous cylinders with radial flow," Physics of Fluids, 6, 144-151.

Morgan, S., and Raspet, R. (1992). "Investigation of the mechanisms of low-frequency wind noise generation outdoors," Journal of the Acoustical Society of America, 92, 1180-1183.

Morgan, M. S. (1993) "An investigation of the sources and attenuation of wind noise in measurement microphones," Ph.D. dissertation, Department of physics and Astronomy, Universtiy of Mississippi, PARGUM Report, 93-101.

Nazar, R., Amin, N., Filip, D., and Pop, I. (2003). "The Brinkman model for the mixed convection boundary layer flow past a horizontal circular cylinder in a porous medium," International Journal of Heat and Mass Transfer, 46, 3167-3178.

Neale, G., and Nader, W. (1974). "Formulation of boundary-conditions at surface of a porous-medium," Society of Petroleum Engineers Journal, 14, 434-436.

Nield, D.A., and Bejan, A. (1998), “Convection in porous media,” 2nd edition, Springer, New York

Ochoatapia, J. A., and Whitaker, S. (1995). "Momentum-transfer at the boundary between a porous-medium and a homogeneous fluid 1. theoretical development," International Journal of Heat and Mass Transfer, 38, 2635-2646.

Ochoatapia, J. A., and Whitaker, S. (1995). "Momentum-transfer at the boundary between a porous-medium and a homogeneous fluid 2. comparison with experiment," International Journal of Heat and Mass Transfer, 38, 2647-2655.

Orfanidis, S. (1995). “Introduction to signal processing,” Prentice Hall, New Jersey

Ostashev, V. E., Wilson, D. K., Liu, L. B., Aldridge, D. F., Symons, N. P., and Marlin, D. (2005). "Equations for finite-difference, time-domain simulation of sound propagation in moving inhomogeneous media and numerical implementation," Journal of the Acoustical Society of America, 117, 503-517.

Peskin, CS. (1972), "Flow patterns around heart valves: a digital computer method for solving the equations of motion," PhD thesis, Physiology, Albert Einstein College of Medicine University

Raspet, R., Webster, J., and Dillion, K. (2006). "Framework for wind noise studies," Journal of the Acoustical Society of America, 119, 834-843.

Panton, R.L. (1996). "Incompressible flow," 2nd edition, John Wiley & Sons, New York

Pollock, D. S. G. (1999) "A handbook of time-series analysis, signal processing and dynamics," Academic, San Diego

Saada, M. A., Chikh, S., and Campo, A. (2007). "Natural convection around a horizontal solid cylinder wrapped with a layer of fibrous or porous material," International Journal of Heat and Fluid Flow, 28, 483-495.

Sabine, H. J. (1950). "Sound absorbing materials," Journal of the Society of Motion Picture & Television Engineers, 55, 332-333.

Shu, C. W., and Osher, S. (1988). "Efficient implementation of essentially non-oscillatory shock-capturing schemes," Journal of Computational Physics, 77, 439-471.

Shu, C. W., and Osher, S. (1989). "Efficient implementation of essentially non-oscillatory shock-capturing schemes .2," Journal of Computational Physics, 83, 32-78.

Siginer, D. A., and Bakhtiyarov, S. I. (2001). "Flow in porous media of variable permeability and novel effects," Journal of Applied Mechanics, 68, 312-319.

Silva, A. L. F. L. E., Silveira-Neto, A., and Damasceno, J. J. R. (2003). "Numerical simulation of two-dimensional flows over a circular cylinder using the immersed boundary method," Journal of Computational Physics, 189, 351-370.

Siyyam, H., Merabet, N., and Hamdan, M. H. (2007). "Standard numerical schemes for coupled parallel flow over porous layers," Applied Mathematics and Computation, 194, 38-45.

Strasberg, M. (1979). "Non-acoustic noise interference in measurements of infrasonic ambient noise," Journal of the Acoustical Society of America, 66, 1487-1493.

Strasberg, M. (1988). "Dimensional analysis of windscreen noise," Journal of the Acoustical Society of America, 83, 544-548.

Tachie, M. F., James, D. F., and Currie, I. G. (2003). "Velocity measurements of a shear flow penetrating a porous medium," Journal of Fluid Mechanics, 493, 319-343.

Tanino, Y., and Nepf, H. M. (2008). "Lateral dispersion in random cylinder arrays at high Reynolds number," Journal of Fluid Mechanics, 600, 339-371.

Tatom, F. B., Smith, S. R., Fichtl, G. H., and Campbell, C. W. (1982). "Simulation of atmospheric turbulent gusts and gust gradients," Journal of Aircraft, 19, 264-271.

Tseng, Y. H., and Ferziger, J. H. (2003). "A ghost-cell immersed boundary method for flow in complex geometry," Journal of Computational Physics, 192, 593-623.

Udaykumar, H. S., Shyy, W., and Rao, M. M. (1996). "ELAFINT: A mixed Eulerian-Lagrangian method for fluid flows with complex and moving boundaries," International Journal for Numerical Methods in Fluids, 22, 691-712.

Van den Berg, G. P. (2006). "Wind-induced noise in a screened microphone," Journal of the Acoustical Society of America, 119, 824-833.

Von Wolfersdorf, L., and Monch, W. (2000). "Potential flow past a porous circular cylinder," Zeitschrift Fur Angewandte Mathematik Und Mechanik, 80, 457-471.

White, B. L., and Nepf, H. M. (2003). "Scalar transport in random cylinder arrays at moderate Reynolds number," Journal of Fluid Mechanics, 487, 43-79.

Wilson, D. K. (1993). "Relaxation-matched modeling of propagation through porous-media, including fractal pore structure," Journal of the Acoustical Society of America, 94, 1136-1145.

Wilson, D. K. and White, M.J. "Numerical simulation of turbulence induced pressure fluctuations around a porous microphone windscreen," 12th Long Range Sound Propagation Symposium, June, 2006, New Orleans, LA

Wilson, D. K., Collier, S. L., Ostashev, V. E., Aldridge, D. F., Symon, N. P., and Marlin, D. H. (2006). "Time-domain modeling of the acoustic impedance of porous surfaces," Acta Acustica United with Acustica, 92, 965-975.

Wilson, D. K., Ostashev, V. E., Collier, S. L., Symons, N. P., Aldridge, D. F., and Marlin, D. H. (2007). "Time-domain calculations of sound interactions with outdoor ground surfaces," Applied Acoustics, 68, 173-200.

Wilson, D. K., Ostashev, V. E., and Goedecke, G. H. (2009). "Quasi-wavelet formulations of turbulence and other random fields with correlated properties," Probabilistic Engineering Mechanics, 24, 343-357.

Wilson, D. K., Ostashev, V. E., Goedecke, G. H., and Auvermann, H. J. (2004). "Quasi-wavelet calculations of sound scattering behind barriers," Applied Acoustics, 65, 605-627.

Wilson, D. K., Ott, S., Goedecke, G. H., and Ostashev, V. E. (2009). "Quasi-wavelet formulations of turbulence and wave scattering," Meteorologische Zeitschrift, 18,

237-252.

Wu, Q., Weinbaum, S., and Andreopoulos, Y. (2005). "Stagnation-point flows in a porous medium," Chemical Engineering Science, 60, 123-134.

Ye, T., Mittal, R., Udaykumar, H. S., and Shyy, W. (1999). "An accurate Cartesian grid method for viscous incompressible flows with complex immersed boundaries," Journal of Computational Physics, 156, 209-240.

Zhang, N., and Zheng, Z. C. (2007). "An improved direct-forcing immersed-boundary method for finite difference applications," Journal of Computational Physics, 221, 250-268.

Zheng, Z. C., and Tan, B. K. (2003). "Reynolds number effects on flow/acoustic mechanisms in spherical windscreen," Journal of the Acoustical Society of America, 113, 161-166.

Zheng, Z. C. "A computational study of the flow/acoustic mechanisms in screened microphones," Proceedings of the ASME 2001 Fluids Engineering Division Summer Meeting, FEDSM2001-18204, May 29-June 1, 2001, New Orleans, LA

Zheng, Z. C., Xu, Y., and Wilson, D. K. (2009). "Behaviors of vortex wake in random atmospheric turbulence," Journal of Aircraft, 46, 2139-2144.

Zheng, Z. C., and Xu, Y. "Behaviors of vortex wake in random atmospheric turbulence," 47th AIAA Aerospace Sciences Meeting and Exhibits, Paper number AIAA2009-0347, January 5-8, 2009, Orlando, FL

Zheng, Z. C., and Xu, Y. "Wind noise reduction for outdoor measurement microphones with windscreens," Proceedings of ASME NCAD2008, Paper number NCAD2008-73084, July 28-30, 2008, Dearborn, MI

Zwikker, C., and Kosten, C. W. (1949). "Sound absorbing materials" Elsevier, New York

Appendix A - Spectral Analysis Using Hamming Window

The power spectral of a random signal describes the energy characteristics of the signal in the frequency domain. Suppose an available time history series *x(t)* for the time duration of the record, T, the Fourier transform relation can be expressed as (Pollock, 1999):

$$x(t) = \int_{-\infty}^{+\infty} X(f) e^{j2\pi \frac{kt}{T}} df \tag{A.1}$$

The power spectral density (PSD) can be calculated in terms of the Fourier transform, *X(f)* of the signal, *x(t)* as:

$$PSD(f) = \frac{|X(f)|^2}{T} \tag{A.2}$$

For the periodic time series *x(t)* (i.e. Figure 4-7), it is not difficult to calculate the PSD of the signal *x(t)*. Otherwise, if the signal *x(t)* is more turbulent and chaotic (i.e. Figure 4-32), we will do the spectral analysis using some window functions.

A.1 Window Function

Spectral leakage occurs during the conversion process from a time domain signal into frequency domain. It is important to know that this leakage is not an artifact but in fact a perfect sinusoidal representation of what the Fourier Transform has analyzed. The Fourier Transform expects truly periodic measured signal intervals in order to build the frequency domain representation of a perceived repetitive never ending signal. When the signal is not periodic in nature, the Fourier Transform will introduce sharp discontinuities into the signal (Bose and Rao, 1993, Brook and Wynne1988).

Windowing is a process by which the sampled data points are “weighted” in the time domain. The effect is smoothing of the signal at the beginning and end of the record to prevent

the occurrence of discontinuities in the data. (Lessard, 2006) There are numerous window functions that can be applied.

Hamming window is one of most widely-used window functions and it was proposed by Richard W. Hamming.

$$w(n) = 0.54 - 0.46\cos(\frac{2\pi n}{N-1}) \tag{A.3}$$

where the window length is N, 0≤n <N.

If window length N equals 1024, the hamming window shape is shown in Figure A-1.

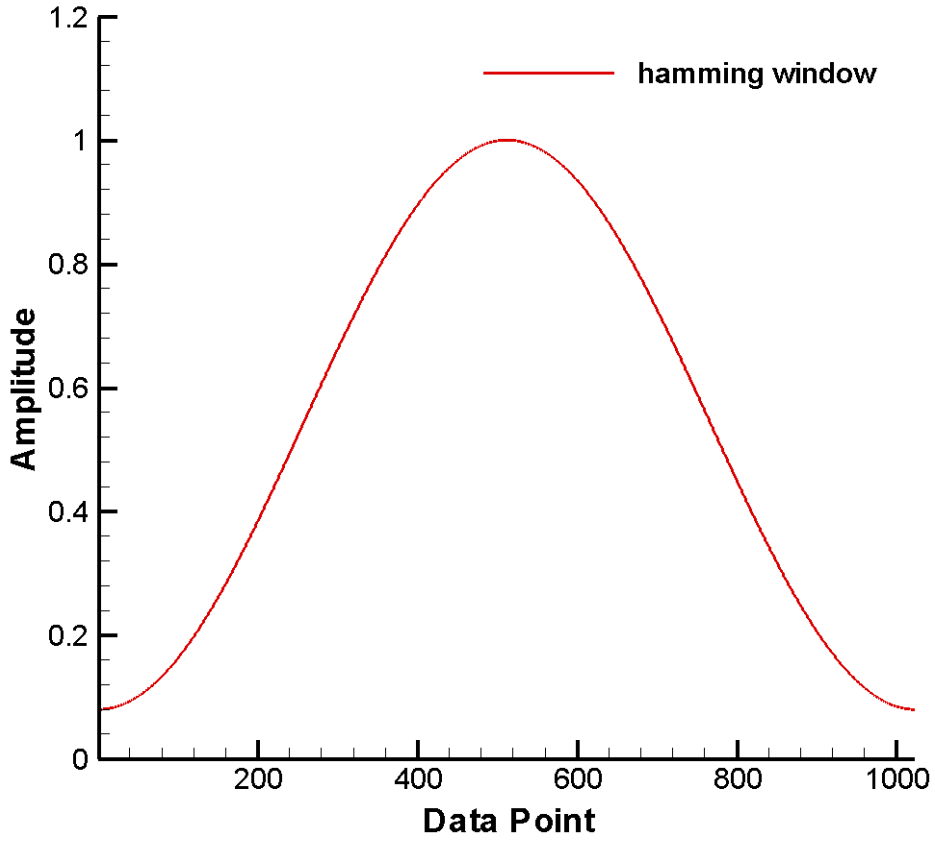

Figure A-1 Hamming window

A.2 Algorithm for Using Window Function

The idea for spectral analysis in our research is to break the input signal data into overlapping segments, perform the FFT on each block using hamming window, and then do average for all segments.

The detailed algorithm is as follows:

(1) We will split the input signal data into overlapping segments. The overlapping percentage will be 90%, and make sure that each segment data length (nfft) equals to a power of 2.

(2) Multiply each segment data with the pre-computed hamming window values w(n) (calculated from Eq. (A-3)).

(3) Calculate the magnitude of the FFT of each segment.

(4) Scale the FFT of each segment so it is not a function of the input length.

(5) Calculate the square of the magnitude of the scaled FFT to get PSD (calculated from Eq. (A-2))

(6) Average the PSD from all segments to get the final PSD result.

A.3 MATLAB Pwelch Function

In MATLAB there is a function called 'pwelch' which could be used to implement the algorithm shown in A.2. The function is defined as follows:

[Pxx,f] = pwelch(*x, nwin, noverlap, nfft, fs*)

where *x* is a vector with the time series, *nwin* is an integer (then a Hamming window of nwin length is used), *noverlap* is an integer (a fraction of the FFT length) that indicates the desired

overlap, *nfft* is an integer giving the length of the FFT (normally, *nfft* should be the same as the length of the window *nwin*), and fs is the sampling frequency.

The results are Pxx, a vector with the power spectral density (PSD), and f, a vector with the corresponding frequencies. If y is the unit of the input time series, the output Pxx has the unit y^2/Hz.

For example, looking at the pressure time history *x(t)* shown in Figure A-2 (a), we have total 200000 data points ($dt = 0.0005$, $fs = 2000$, total time 0.0005*200000=100). The post-processed time period is chosen from 24 to 96, total points of the processing data is $N = 144000$, the overlapping percentage *noverlap* is 90% (the default overlapping percentage in Matlab is 50%, we set here for 90% because there will be more window processing with more overlapping percentage which will make the spectral curves much smoother), *nfft* is 65536, *nwin* is 58982. We can call Matlab function, [Pxx,f] = pwelch(*x,nwin,noverlap,nfft,fs*), to get the PSD. The PSD result can be seen in Figure A-2 (b).

The resolved frequency range of the set of data with window size (*nwin* points in each window) is from $1/(dt \cdot nwin)$ to $1/(2 \cdot dt)$. However, the accurate high frequency limit for the whole set of processing data (N points) is not able to reach the highest frequency, $1/(2 \cdot dt)$, because of the overlapping of the windows (Kaimer and Finnigan, 1994). The highest resolvable frequency can be estimated based on the time step, dt, the window size, *nwin*, and the overlapping percentage, *noverlap*. The number of windowed data sets for the entire data set (with N points) is $r = N/[(1-noverlap) \cdot nwin] - 1$. And then the highest frequency limit can possibly be reduced to $1/(2 \cdot r \cdot dt)$, because of the *r*-times of average.

For the example case mentioned above, the parameters are the following: the number of the total time series data points is $N = 144000$, the window size is $nwin = 65536$, the time step is $dt = 0.0005$, and the overlapping $noverlap = 90\%$. Therefore, the number of windows is $r = 144000/(1-0.9)/65536 - 1 = 21$. The lowest accurate frequency in this case is $f_a = 1/(0.0005 \cdot 65536) = 0.0305$, and the highest accurate frequency is $f_b = 1/(2 \cdot 21 \cdot 0.0005) = 47.6$.

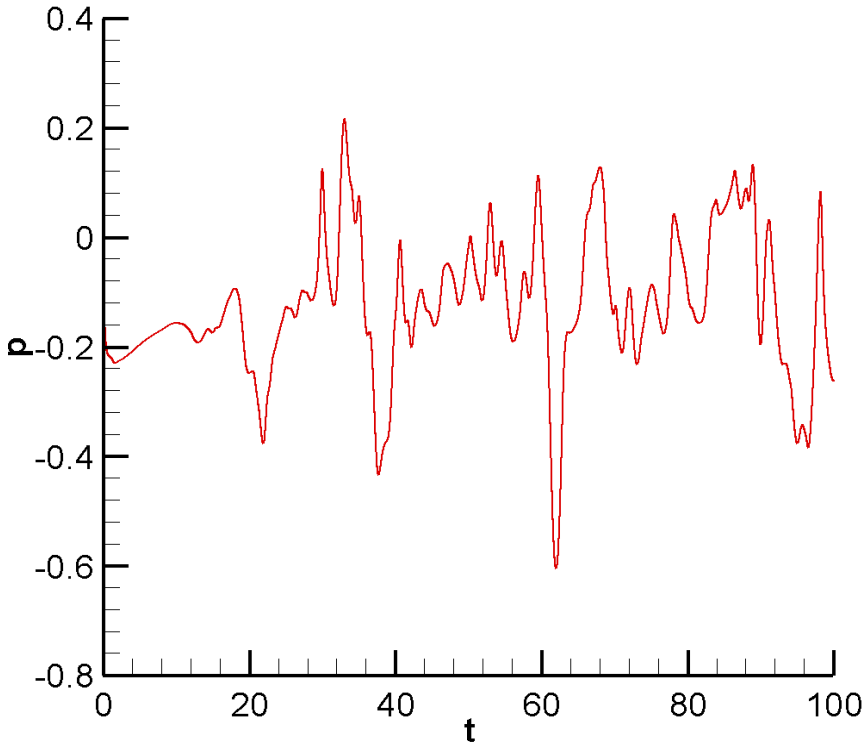

(a) time history

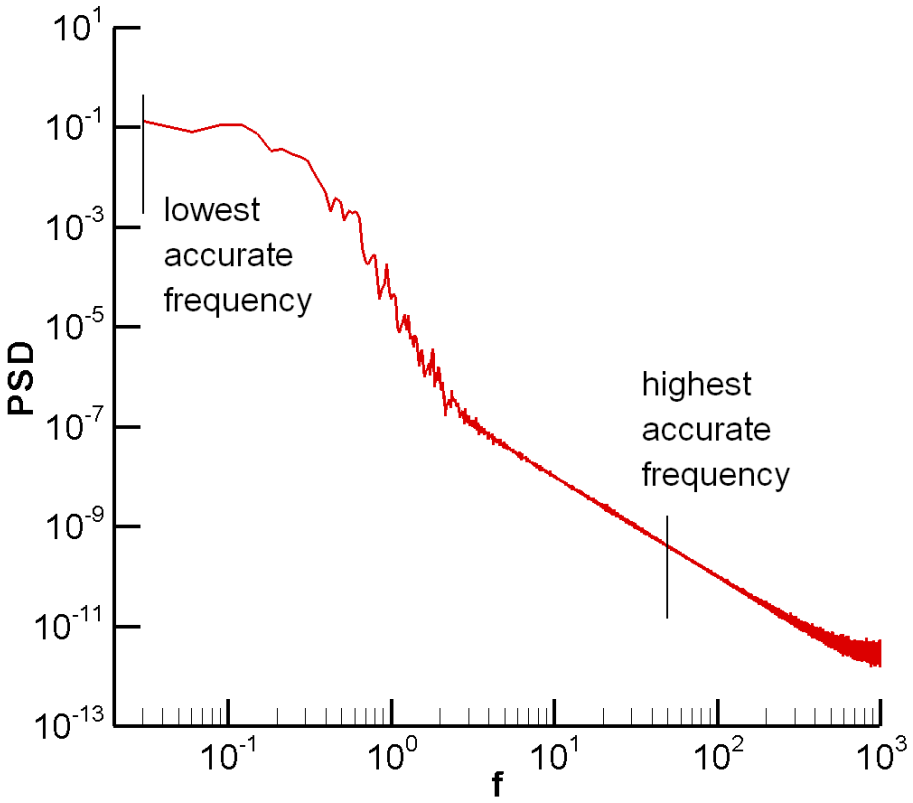

(b) PSD

Figure A-2 Spectral analysis example using pwelch

List of Publications during Ph.D. Study

Xu, Y., Zheng, Z. C., and Wilson, D. K., 2010, "Simulation of Turbulent Wind Noise Reduction by Porous Windscreens Using High-order Schemes," (Journal of Computational Acoustics, accepted for publication)

Zheng, Z. C., Tan, B. K., and Xu, Y., 2010, "Near-Field Fluctuations and Far-Field Noise of a Three-Element Airfoil System by a Discrete Vortex Method," Applied Mathematics and Computation, Vol. 216, Issue 4, pp. 1072-1086.

Xu, Y., and Zheng, Z. C., 2009, " Application of High-order Scheme for Flow/acoustic Simulation at the Interface between Air and Porous Medium", 2009 ASME International Mechanical Engineering Congress & Exposition, Paper number IMECE2009-11694, Nov. 13~19, 2009, Lake Buena Vista, Florida

Zheng, Z. C., Xu, Y., and Wilson, D. K., 2009, "Behaviors of Vortex Wake in Random Atmospheric Turbulence," Journal of Aircraft, Vol. 46, No. 6, pp. 2139-2144.

Zheng, Z. C., and Xu, Y., 2008, "Behaviors of Vortex Wake in Random Atmospheric Turbulence," 47th AIAA Aerospace Sciences Meeting and Exhibits, Paper number AIAA2009-0347, January 5-8, 2009, Orlando, FL.

Zheng, Z. C., and Xu, Y., 2008, "Wind Noise Reduction for Outdoor Measurement Microphones with Windscreens," Proceedings of ASME NCAD2008, Paper number NCAD2008-73084, July 28-30, 2008, Dearborn, MI.

Zheng, Z. C., and Xu, Y., 2008, "A Visualized Wake Hazard Assessment," 46th AIAA Aerospace Sciences Meeting and Exhibits, Paper number AIAA2008-467, January 7-10, 2008, Reno, NV.

Li, W., Zheng, Z. C., and Xu, Y., 2007, "Flow/Acoustic Mechanisms in Three-Dimensional Vortices undergoing Sinusoidal-Wave Instabilities," Proceedings of ASME 2007 International Mechanical Engineering Congress & Exposition, Paper number IMECE2007-43163, November 11-15, 2007, Seattle, WA.

Zheng, Z. C., and Xu, Y., 2006, "Effects of Reynolds Stress in Flow Noise from Vortex/Hydrofoil Interactions," Journal of Hydrodynamics, Vol. 18, No. 3, Supplement 1, pp. 381-385

Zheng, Z. C., 2006, and Xu, Y., 2006, "A Combined RANS/Vortex Method for Predicting Noise from Vortex/Airfoil Interactions," 12th AIAA/CEAS Aeroacoustics Conference, AIAA2006-2512, Cambridge, MA, May 8-10, 2006.